The Effectiveness of Axial Flow Fans in A-Frame Plenums

Sarel Jacobus Venter

Dissertation presented for the degree of Doctor of Philosophy (Mechanical Engineering) at the University of Stellenbosch.

Thesis Supervisor: Prof. D.G. Kröger

Department of Mechanical Engineering
University of Stellenbosch
March 1990

Declaration

I, Sarel Jacobus Venter, the undersigned, hereby declare that the work contained in this thesis is my own original work and has not previously, in its entirety or in part, been submitted at any university for a degree.

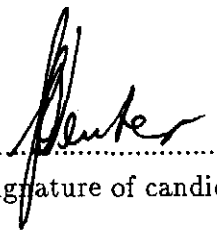

.....
Signature of candidate

30... day of NOVEMBER 1990.

Abstract

The ultimate goal of this project is to ensure a better understanding of the governing mechanisms present when flow distorting components are installed in close proximity of an axial flow fan.

The effect of different parameters on the operation of axial flow fans is investigated. These parameters are divided into flow enhancing and flow reduction effects. The performance of an axial flow fan can be enhanced by changing the tip clearance, by adding a solid disc to the hub of the fan or by varying the number of fan blades. Flow reductions are caused by components such as inlet grids, walkways and their supporting structures, heat exchangers and windwalls.

The effects of flow enhancing components are measured and compared to the results of other authors. The sensitivity of these effects to parameters such as the type of fan rotor and the specific system in which the rotor is installed is highlighted.

The system effect (the interaction between the fan rotor and flow resistances in close proximity of each other) of individual components, as well as the combination of different components, is predicted both theoretically and experimentally. These predictions are compared to measured data relevant to the components in an installation where the system effects are present. The results are correlated to the kinetic energy flux coefficient of the flow at different locations within the installation.

Experimental data obtained from a full scale unit (inlet shroud diameter of 9,216 m) are used to compare to scaled data from the model (inlet shroud diameter of 1,542 m). The hub to tip ratio of the axial flow fans investigated is 0,15.

The most important conclusions are that the performance of the type of axial flow fan under investigation can be improved by reducing its tip clearance and by installing a solid disc to the downstream side of the rotor. An increase in the number of blades of the fan leads to only marginal improvements in the fan performance. The overall performance of the system can also be improved by removing some of the flow resisting components, or by changing their relative positions. All these conclusions are based on the assumption that the power input to the fan rotor remains constant.

Opsomming

Die uiteindelike doel van hierdie projek is om te verseker dat die beherende meganismes wat teenwoordig is wanneer vloeiversteurende komponente in die nabyheid van 'n aksiaalwaaier geïnstalleer word, beter verstaan word.

Die effek van verskillende parameters op die werkverrigting van aksiaalwaaiers word ondersoek. Hierdie parameters word verdeel in vloeiverbeterings- en vloeiverminderingseffekte. Die werkverrigting van 'n aksiaalwaaier kan verbeter word deur die lempuntspeling te verstel, deur 'n soliede skyf aan die naaf van die waaierrotor te installeer, of deur die aantal lemme te verander. Die vloeiverminderings word veroorsaak deur inlaatsiwwe, loopvlakke en hul onderteuningsstrukture, warmteruilers en windwande.

Die effekte van vloeiverbeteringskomponente word gemeet en vergelyk met die resultate van ander outeurs. Die sensitiwiteit van hierdie effekte op parameters soos die tipe rotor en die spesifieke stelsel waarin die rotor geïnstalleer is, word uitgelig.

Die stelseleffek (die interaksie tussen die rotor van die waaier en vloeiweerstande wat naby mekaar geïnstalleer is) van individuele, sowel as 'n kombinasie van verskillende komponente, word teoreties en eksperimenteel voorspel. Hierdie voorspellings word dan vergelyk met eksperimentele data wat van toepassing is op die komponente in 'n installasie waar stelseleffekte voorkom. Die resultate word gekoppel aan die kinetiese energievloedkoëffisiënt van die vloei by verskillende posisies binne die installasie.

Eksperimentele data, verkry vanaf 'n volskaaleenheid (inlaatmondstukdiameter van 9,216 m), word met die geskaleerde data van die model (inlaatmondstukdiameter van 1,542 m) vergelyk. Die naaf- tot hulsverhouding van die aksiaalwaaiers wat ondersoek word is 0,15.

Die belangrikste gevolgtrekkings is dat die werkverrigting van die tipe aksiaalwaaier wat ondersoek word verbeter kan word deur die lempuntspeling te verminder en deur 'n soliede skyf te installeer by die stroomaf kant van die rotor. 'n Toename in die aantal lemme van die waaier lei slegs tot marginale verbeterings in die werkverrigting van die waaier. Die totale werkverrigting van die stesel kan ook verbeter word deur sommige vloeiweerstandskomponente te verwyder, of deur hulle relatiewe posisies te verander. Al hierdie gevogtrekkings is gebasseer op gie aanname dat die drywingsinset na die waaierrotor konstant bly.

Aknowledgements

The author wishes to express his gratitude towards the following individuals and institutions for contributing towards this study.

- The CSIR, BMI and Harry Crossley Foundation for financial support in the form of bursaries and grants.

- GEA (SA) and Howden-Safanco for contributing to the manufacturing of the fan test facility.

- ESKOM for making available the full scale unit for exhaustive experimental investigations.

- Prof. D.G. Kröger for prolonged assistance and guidance during the course of the project.

- All co-workers for their contributions, especially J.G.J. Visser and D.J. van Aarde for their support in the design of the fan test facility and the generation of experimental data pertaining to the five hole probe calibration and the full scale unit.

Contents

List of Tables

List of Figures

Nomenclature

Symbols

$\bar{A}$	Vector perpendicular to the area	$[m^2]$
A	Area	$[m^2]$
A	Constant in correlation	[-]
B	Constant in correlation	[-]
C_d	Drag coefficient	[-]
C_p	Specific heat capacity at constant pressure	$[J/kg^oK]$
C_v	Specific heat capacity at constant volume	$[J/kg^oK]$
c	Constant of straight line correlation	[-]
D	Fan diameter	$[m]$
d	Diameter	$[m]$
E	Stored energy of the fluid, comprising thermal, kinetic and potential energies	$[J]$
e	Stored energy per unit mass	$[J/kg]$
g	Gravitational acceleration	$[m/s^2]$
h	Enthalpy	$[J/kg]$
k	Loss coefficient in terms of volume flow	[-]
K	Pressure loss coefficient	[-]
K_p	Coefficient of compression	[-]
L	Length	$[m]$
l	Length	$[m]$
M	Mach number	[-]
$\dot{m}$	Mass flow rate	$[kg/s]$
m	Gradient of straight line correlation	[-]
m	Mass of the system or body	$[kg]$
N	Rotational speed	$[rpm]$
n	Polytropic expansion coefficient	[-]
P	Power consumption	$[W]$
p	Pressure	$[N/m^2]$
p_{sF}	Fan static pressure	$[N/m^2]$
Q	Heat loss from the system to the environment	$[J]$
R	Inner radius of conical inlet	$[m]$
R	Universal gas constant	$[J/kg^oK]$
r	Radius	$[m]$
r	Ratio	[-]
r^*	Dimensionless radius	[-]
s	Entropy	$[J/kg^oK]$
s	Local tip clearance gap	$[m]$

T	Temperature	$[^oK]$
T	Torque	$[N.m]$
t	Time	$[s]$
U	Thermal energy of the system	$[J]$
u	Thermal energy per unit mass	$[J/kg]$
V	Volume flow rate	$[m^3/s]$
V	Volume of the control volume	$[m^3]$
v	Velocity	$[m/s]$
$\bar{v}$	Average velocity	$[m/s]$
$\bar{v}$	Velocity vector	$[m/s]$
v^*	Dimensionless velocity	[–]
W	Work done by the system on the environment	$[J]$
w	Width	$[m]$
w	Work per unit mass	$[J/kg]$
X	Downstream distance from fan rotor	$[m]$
z	Elevation	$[m]$
z	Compressibility factor	[–]

Greek Symbols

α	Kinetic energy flux coefficient	[–]
α	Flow coefficient	[–]
α	Yaw angle	$[^o]$
β	Blade angle	$[^o]$
ϵ	Expansibility factor	[–]
Δ	Differential	[–]
δ	Change or variation in the parameter	[–]
η	Efficiency	[%]
η_{sF}	Fan static efficiency	[%]
γ	Specific heat ratio	[–]
λ	Pitch angle	$[^o]$
μ	Dynamic viscosity	$[Ns/m^2]$
ν	Kinematic viscosity	$[m^2/s]$
ρ	Density	$[kg/m^3]$
σ_{21}	Solidity ratio	[–]
σ_c	Contraction area ratio	[–]
θ	Angle	$[^o]$

Subscripts

0	Stagnation/total conditions
0	No steam pipe conditions
1	Upstream/inlet conditions
2	Downstream/outlet conditions
$1-5$	Component number
$1-5$	Five hole probe - hole number
amb	Ambient conditions
avg	Average
ax	Axial
b	Distance between steam pipes in A-frame
beam	Structural support beams for inlet safety grid
bell	Inlet bellmouth
C	Combined effects
c	Contraction
cond	Condenser
d	Downstream losses
d	Dynamic pressure
deph	Dephlegmator
dn	Downstream
e	Expansion
F	Fan
F	Frontal
f	Friction
fan	Fan
he	Heat exchanger
HX	Heat exchanger
hx	Heat exchanger
IS	Inlet shroud
i	Inlet
id	Ideal operating conditions
j	Jetting losses
m	Corrected angle
o	Outlet
o	Outlet losses
P	Power
pd	probe diameter
pitch	Pitch angle
pitot	Pitot tube traverse
press	Pressure forces

probe	Probe
R	Reversible process
R	Shaft input
r	r-coordinate
rad	Radial
red	Reduced values
S	System
SG	Safety grid
s	Static pressure
sett	Settling chamber
shear	Shearing forces
support	Support beams
stat	Static pressure
t	Total pressure
tang	Tangential
tot	Total frontal area
tot	Total pressure
tot	Total to total conditions
U	Unit
up	Upstream
V	Volume flow rate
w	Bundle width
walk	Walkway
ww	Including windwalls
x	x-coordinate
y	y-coordinate
yaw	Yaw angle
z	z-coordinate (Axial direction)
Δp_{sF}	Fan static pressure
η_{sF}	Fan static efficiency
θ	Oblique flow conditions
θ	θ-coordinate

Groups

Re	Reynolds number	[-]
Ry	Reynolds number per unit length	$[1/m]$

Chapter 1 - Introduction

Research relevant to this study is directed towards a better understanding of the effect of different flow resistances and flow distorting components on the overall performance of axial flow fans. These flow resisting components include inlet safety grids, walkways, supporting beams and heat exchangers. The effects of additional parameters which influence the overall fan performance such as fan tip clearance and sealing discs are also evaluated. Finally the measured data obtained from the scale model is compared to data generated for a full scale cooling unit to illustrate the effect of scaling on the system effect.

Fan selection is based upon matching of ideal fan characteristic curves to the empirical resistance correlations of the components in the system. The fan characteristics as measured according to certain standards are normally available from the fan manufacturer. The system resistances are determined from published data for the drag forces acting on different bodies immersed in a flow field, or from the characteristics of certain duct components. The experimental data for both these cases is measured under idealized flow conditions [61JO1]. Ideal flow conditions are achieved when both the upstream and downstream velocity distributions approach a one dimensional uniform velocity profile. The total pressure losses for the individual components of the system are assumed to be related to the square of the average velocity approaching the specific component (refer to section 2.7). They are expressed in terms of a total pressure loss coefficient (K). Many publications concern themselves with the listing of pressure loss coefficients for a selection of different components and immersed bodies [61JO1, 72AS1, 80AS2, 73EC1, 78DA1, 83WA1, etc.].

The specific problem addressed in this work involves the case where, due to space limitations and others, the fan and flow resistances are installed in close proximity of each other. The flow resistances consist mainly of heat exchangers and support structures. It can be appreciated that the inlet and outlet velocity distributions, through both the fan and the flow resisting components, are affected by such an installation. This renders the previously mentioned published data irrelevant under these conditions. The magnitude of these deviations from the published data forms the nucleus of this study.

The influence of the fan and the system on one another (known as the system or installation effect) has been recognized and investigated by a number of authors [79NO1, 81GR1, 82CO1, 83OC1]. Available literature is only relevant to a certain sector of the complete range of fan applications in industry. Beard [80BE2] and Hay et al. [72HA1] explored the system effects associated with inlet shrouds and the distance between radiator and fan in vehicle cooling systems. A number of authors, concerning themselves with the system effect associated with elbows, diffusers and contractions, both at fan inlet and outlet, presented papers at a conference sponsored by the Institution of Mechanical Engineers [84DA1, 84DE1, 84RO1]. Studies by Coward [83CO1] and Cory [82CO1] covers the same range of fan applications. The effect of fan plenums on the fan performance is described by

authors such as Lambert et al. [72LA1], Stone and Yeh [73ST2] and Russell and Berryman [78RU1].

The primary concern of this study is to determine the magnitude of the system effects present in an industrial scale air cooled heat exchanger (ACHE).

Gunter and Shipes [72GU1] give an extensive account of the development of dry air cooling equipment. Initially the units consisted of vertical heat exchangers through which air flow was achieved utilizing axial flow fans. This arrangement changed to horizontal fin tubes towards 1935. The "A" and "V" configurations evolved to save plot plan area and were operational before 1940. Some smaller industrial units, where the covered area is relatively small, still utilize the horizontal arrangement [79MO1, 87BE1]. One disadvantage of inclined finned tubes is that the system pressure losses increase due to the oblique flow at inlet to and outlet from the heat exchangers. "A" and "V" configurations are also more sensitive to wind effects than horizontal tubes [79HU1, 79MO1].

Another distinction which can be made for industrial scale units is between forced and induced draft modes of operation. Forced draft systems are recognized by having internal pressures in excess of atmospheric pressure. This means that the air passes through the fan before exiting through the system resistances. Induced draft units are the opposite, where the internal system pressure is maintained below atmospheric pressure by the suction of air through the system [72GU1, 79HU1].

The full scale unit available for testing in this work entails a forced draft cooling system, with the finned tubes installed in the "A" frame arrangement (figures F.1.1 and F.1.2). This is a typical example of the recent trend in large scale ACHE's. The semi apex angle of the "A" frame is 28°. The fan inlet shroud diameter is 9,216 m. The cooling system is connected to a power plant consisting of six 660 MWe power generation units. Each unit is served by its own air cooled condenser, consisting of 40 condenser and 8 dephlegmator units.

The range of tests which can be carried out on the full scale unit is limited by a number of factors. Exposure to the elements means that local atmospheric wind and temperature conditions influence the performance of the unit. The size of the unit increases the financial burden involved in any attempted modifications. This means that even relatively simple adjustments, such as variation of tip clearance, can become very costly. Structural supports and safety measures are integral parts of the full scale unit and cannot be removed or adjusted without major implications to the operation of the fan. The measurement of fan static pressure and volume flow rate through the fan is also inaccurate due to the non axial inlet flow conditions [87BE1]. The solution is to manufacture a scale model without the limitations of the full scale unit.

A scale model of the fan system, approximating a single unit in the array of full scale

condensers, was designed and manufactured. Limitations associated with the scaling down of such a unit are stated in chapter 3. The model is attached to a standard fan test facility to improve the quality of the experimental work.

The system effects associated with the various flow resisting components are measured. These components include an inlet safety grid, supporting beams, a walkway and the finned tubes. The effect of each individual component is isolated, but the effects of different combinations of these components installed in the same system are also investigated.

Parametric studies into the effect of tip clearance, sealing discs, wind walls and different fan rotors also receive attention. The position of the walkway and supporting beams relative to the fan is adjusted and the effect on system losses monitored. The pressure losses associated with the heat exchanger are compared to data from the literature pertaining to systems with ideal flow conditions at the inlet to the "A" frame arrangement.

All system losses are compared to the commonly accepted method of fan selection. The influence of volume flow rate on system losses is accounted for in all tests.

Relevant data generated using the scale model is extrapolated to approximate operating conditions of the full scale unit. The effect of scaling is limited to measurable quantities such as overall system performance and velocity distributions at fan inlet and outlet from the full scale unit. The velocity profiles at the outlet from the cooling unit (between the steam ducts) and parallel to the heat exchanger surfaces are also measured and scaled.

The successful completion of the study provides basic flow information for possible numerical modelling and the industry with some data to be used for design calculations. It will also fill a void in the literature surrounding the system effects associated with industrial size air cooled heat exchangers.

Chapter 2 - Theoretical analysis of axial flow fans

The theoretical analysis which is performed in this chapter is aimed at validating the generally accepted methods of presenting fan characteristics. These methods are summarized in all the relevant fan test codes [66VD1, 74AM1, 75AS1, 80BS1, 85DE1]. The three basic parameters used to present the fan characteristics as a function of volumetric flow rate through the fan are:

- fan pressure
- fan power consumption
- fan efficiency

The fan efficiency is the ratio between the ideal power input to the air stream and the actual fan power consumption. The efficiency is therefore an indication of the power losses exhibited by the fan operating system. The ideal power input to the air stream will be determined from first principles before investigating the origin of the fan efficiency.

2.1 Energy considerations in axial flow fans

The principle law from which the energy equation evolves is the first law of thermodynamics which can be presented for a system by [76ZU1, 78VA1, 78EA1]

$$dE = \delta Q - \delta W \tag{2.1}$$

where δQ - heat loss term which has a positive sign in the event of heat being transferred to the system.

δW - work done by the system having a positive sign in the event of work being done on the surroundings. This term includes the work due to normal stresses or pressure work.

The change in stored energy associated with the fluid (dE) is assumed to comprise only thermal, kinetic and potential energies, resulting in the following relation [76ZU1, 78VA1]

$$E = U + \frac{1}{2}mv^2 + mgz \tag{2.2}$$

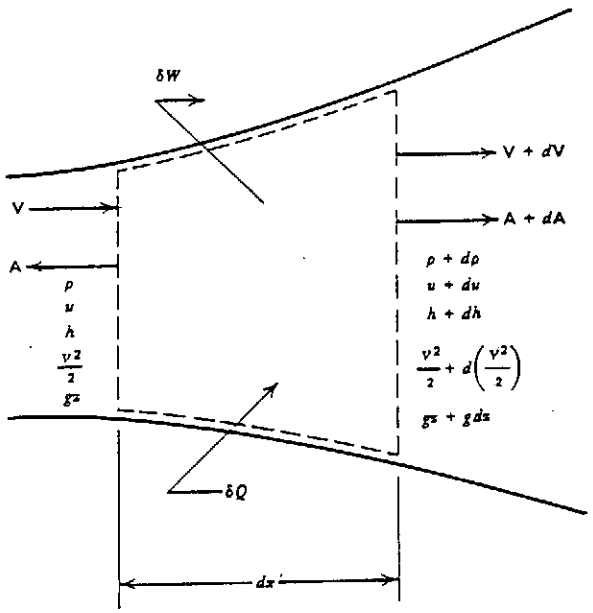

Figure 2.1: One-dimensional control volume

where U - internal energy of the system in $[J]$

$\frac{1}{2}mv^2$ - kinetic energy of the system in $[J]$

mgz - potential energy of the system in $[J]$

m - total mass of the system in $[kg]$

The time rate of change in stored energy for a control volume (see figure 2.1) follows from the substantial derivative of equation (2.1) [76ZU1].

$$\frac{DE}{Dt} = \dot{Q} - \dot{W} \tag{2.3}$$

This substantial derivative can be rewritten as [76ZU1]

$$\frac{DE}{Dt} = \int_V \frac{\partial e}{\partial t}\rho dV + \int_A e\rho\bar{v}.d\bar{A} \tag{2.4}$$

with $e = \frac{E}{m} = u + \frac{v^2}{2} + gz$ from equation (2.2).

The complete energy equation can now be derived after substituting equation (2.4) into equation (2.3).

$$\int_V \left(\frac{\partial e}{\partial t}\rho\right) dV + \int_A (e\rho)\,\bar{v}.d\bar{A} = \dot{Q} - \dot{W} \tag{2.5}$$

Research in this study is aimed at predicting steady state fan characteristics. This implies that the time derivatives can be neglected in the energy equation, resulting in:

$$\dot{W} - \dot{Q} + \int_A \rho \left(u + \frac{v^2}{2} + gz\right) \bar{v}.d\bar{A} = 0 \tag{2.6}$$

The work done by the control volume on the environment is divided into two components

- shaft work i.e. input power to the fan
- flow work which includes shear work due to forces acting tangentially on the surface of the control volume and pressure forces due to forces perpendicular to the control volume surface.

The components are all added together to obtain the total work, i.e.

$$\dot{W} = \dot{W}_{id} + \dot{W}_{shear} + \dot{W}_{press} \tag{2.7}$$

where $\delta\dot{W}_{press} = p\bar{v}.d\bar{A}$

$$\text{thus } \dot{W}_{press} = \int_A p\bar{v}.d\bar{A} \tag{2.8}$$

Equations (2.7) and (2.8), substituted into equation (2.6) gives

$$\dot{W}_{id} + \dot{W}_{shear} - \dot{Q} + \int_A \rho \left(u + \frac{p}{\rho} + \frac{v^2}{2} + gz\right) \bar{v}.d\bar{A} = 0 \tag{2.9}$$

2.2 The second law of thermodynamics

The change in entropy of a system is defined as [78VA1, 78EA1]

$$ds \equiv \frac{\delta Q_R}{T} \tag{2.10}$$

where s - entropy of the system in $[J/kg^{\circ}K]$

Q_R - theoretical heat supplied to a reversible process in $[J/kg]$

T - temperature of the system in $[^{\circ}K]$

Equation (2.10) can be expanded to represent all processes by introducing an inequality. The result is known as the inequality of Clausius [78EA1] and also summarizes the second law of thermodynamics.

$$ds \leq \frac{\delta Q}{T} \tag{2.11}$$

A relation, attributed to Maxwell [87VA1], gives the change in specific entropy as a function of the changes in specific internal energy and density, and of the pressure of the control volume.

$$Tds = du + pd\left(\frac{1}{\rho}\right) \tag{2.12}$$

2.3 Ideal flow through a fan (Compressible)

The assumptions incorporated into the derivation of relevant equations for ideal flow conditions through a fan are :

- The compression process is adiabatic which means that $\delta Q = 0$ for ideal conditions. The relation representing an isentropic compression of a perfect gas follows from Boyle's law [79MA1]

$$p_0\left(\frac{1}{\rho_0}\right)^{\gamma} = constant = C_1 \tag{2.13}$$

  where γ is the ratio of specific heat capacity at constant pressure to specific heat capacity at constant volume for a perfect gas $\left(\frac{C_p}{C_v}\right)$ [78EA1]. The subscripts 0 refer to stagnation (total) properties which correspond to the static value of the property in an infinitely large reservoir from which the flow is accelerated isentropically to its actual speed (v) [76ZU1].

- The friction losses across the fan are negligible implying that $W_{shear} = 0$.
- The change in elevation across the fan is small enough for the change in potential energy to be assumed zero.
- All properties of the flow at entrance to and exit from the control volume are uniform and one-dimensional.

Apply equation (2.9) now to the control volume presented by figure 2.1 for which the above assumptions hold true.

$$\delta\dot{W}_{id} + \int_A \rho \left(h + \frac{v^2}{2} + gz \right) \bar{v}.d\bar{A} = 0 \tag{2.14}$$

where the enthalpy (h) is defined as [78VA1]

$$h = u + \frac{p}{\rho} \tag{2.15}$$

The differential form for one-dimensional flow is obtained by applying equation (2.14) to the control volume in figure 2.1 and dividing by the mass flow rate.

$$\delta w_{id} + dh + d\left(\frac{v^2}{2}\right) + gdz = 0 \tag{2.16}$$

which is transformed by assuming an isentropic evolution and negligible potential energy changes.

$$-\delta w_{id} = dh + vdv \tag{2.17}$$

From the definition of the coefficient of compression for a perfect gas through a constant pressure process (C_p), it follows that [78EA1]

$$dh = C_p dT \tag{2.18}$$

Equation (2.18) is substituted into equation (2.17) followed by integration to obtain

$$\begin{aligned} -{}_1w_2 &= \int_1^2 C_p dT + \int_1^2 vdv \\ &= C_p(T_2 - T_1) + \frac{1}{2}\left(v_2^2 - v_1^2\right) \\ &= C_p\left(T_2 + \frac{1}{2C_p}v_2^2\right) - C_p\left(T_1 + \frac{1}{2C_p}v_1^2\right) \\ &= C_p(T_{02} - T_{01}) \end{aligned} \tag{2.19}$$

where the total (stagnation) temperature is [76ZU1, 79MA1]

$$T_0 = T + \frac{1}{2C_p}v^2 \tag{2.20}$$

Two relations for a perfect gas undergoing an isentropic compression process that are derived in almost any handbook on basic thermodynamics [78EA1, 78VA1, 79MA1], are

$$\frac{T_{02}}{T_{01}} = \left(\frac{p_{02}}{p_{01}}\right)^{\frac{\gamma-1}{\gamma}} = \left(\frac{\rho_{02}}{\rho_{01}}\right)^{\gamma-1} \tag{2.21}$$

$$\text{and } C_p = \frac{\gamma R}{\gamma - 1} \tag{2.22}$$

where R, the universal gas constant is 287,08 J/kg^oK.

Substituting equations (2.21) and (2.22) into equation (2.19) results in

$$\begin{aligned} -_1w_2 &= \frac{\gamma R T_{01}}{\gamma - 1}\left(\frac{T_{02}}{T_{01}} - 1\right) \\ &= \frac{\gamma\, p_{01}}{(\gamma-1)\rho_{01}}\left[\left(\frac{p_{02}}{p_{01}}\right)^{\frac{\gamma-1}{\gamma}} - 1\right] \end{aligned} \tag{2.23}$$

where $\frac{p_{01}}{\rho_{01}} = R\,T_{01}$ from the ideal gas law for isentropic flow. Equation (2.23) can be rewritten in terms of the total pressure drop across the fan $(p_{02} - p_{01})$ and the total pressure ratio $\left(r = \frac{p_{02}}{p_{01}}\right)$

$$-_1w_2 = \frac{\gamma}{(\gamma-1)\rho_{01}}\left(\frac{r^{\frac{\gamma-1}{\gamma}} - 1}{r - 1}\right) \times (p_{02} - p_{01}) \tag{2.24}$$

The continuity equation for one-dimensional flow is presented by [76ZU1]

$$\dot{m}_1 = \dot{m}_2 = \rho_1 A_1 v_1 = \rho_2 A_2 v_2 = \rho_1 V_1 = \rho_2 V_2 \tag{2.25}$$

The ideal power input to the fan rotor is determined from the rate of energy input to the fan and is equated to be [78EA1]

$$P_{id} = \dot{m} \times (-_1w_2) \tag{2.26}$$

Upon substitution of equations (2.24) and (2.25) into equation (2.26), a general relation to determine the ideal input power to the fan rotor is obtained.

$$P_{id} = \frac{\gamma \rho_1 V_1}{(\gamma - 1)\rho_{01}} \left(\frac{r^{\frac{\gamma-1}{\gamma}} - 1}{r - 1} \right) \times (p_{02} - p_{01}) \tag{2.27}$$

The ultimate objective of this theoretical evaluation is to obtain a relationship between the power input to the air stream and the actual shaft power input to the fan rotor (fan efficiency). The power input to the air stream is the ideal power input to the fan rotor for a small stage (polytropic) pressure evolution [61JO1, 66VD1, 80BS1]. A small stage process is a better approximation of the actual flow work supplied to the air stream as it accounts for diverging pressure lines on the Mollier diagram [78DI1, 72CO1]. Equation (2.27) can now be rewritten to be valid for a small stage process and becomes

$$P_{id} = \frac{n \rho_1 V_1}{(n - 1)\rho_{01}} \left(\frac{r^{\frac{n-1}{n}} - 1}{r - 1} \right) \times (p_{02} - p_{01}) \tag{2.28}$$

where it can be shown that for a compressor or fan [72CO1, 78DI1]

$$\frac{n}{n-1} = \eta_{tot} \frac{\gamma}{\gamma - 1} \tag{2.29}$$

The small stage efficiency (or fan total efficiency) can be presented by

$$\eta_{tot} = \frac{P_{id}}{P_R} \tag{2.30}$$

Equations (2.29) and (2.30) are substituted into equation (2.28) to give

$$\begin{aligned} \eta_{tot} P_R &= \frac{n \rho_1 V_1}{(n - 1)\rho_{01}} \left(\frac{r^{\frac{n-1}{n}} - 1}{r - 1} \right) \times (p_{02} - p_{01}) \\ &= K_p \left(\frac{\rho_1}{\rho_{01}} \right) (p_{02} - p_{01}) V_1 \end{aligned} \tag{2.31}$$

where, according to Jorgensen [61JO1]

$$K_p = \frac{\frac{n}{n-1} \left(r^{\frac{n-1}{n}} - 1 \right)}{(r - 1)} \tag{2.32}$$

Equations (2.29) and (2.31) are substituted into equation (2.32) resulting in an alternative representation of K_p.

$$K_p = \frac{\frac{\eta_{tot}\gamma}{\gamma-1}\left(r^{\frac{\gamma-1}{\gamma\eta_{tot}}}-1\right)}{(r-1)} \tag{2.33}$$

$$= \frac{K_p\left(r^{\frac{z}{K_p}}-1\right)}{z(r-1)}$$

$$\text{where } z = \left(\frac{\gamma-1}{\gamma}\right)\frac{\rho_{01}P_R}{\rho_1 V_1(p_{02}-p_{01})} \tag{2.34}$$

The parameter z is used to simplify equation (2.33). This is a common parameter in a number of publications [61JO1, 78DA1, 80BS1] known as the compressibility factor.

$$K_p = \frac{z log_{10}(r)}{log_{10}[1+z(r-1)]} \tag{2.35}$$

The small stage efficiency of the fan is represented by rewriting equation (2.31) to be

$$\eta_{tot} = \frac{K_p(p_{02}-p_{01})V_1}{P_R}\left(\frac{\rho_1}{\rho_{01}}\right) \tag{2.36}$$

with K_p determined according to equation (2.35)

2.4 Ideal flow through a fan (Incompressible)

The equations derived in section 2.3 are all valid for the compressible flow regime which includes the incompressible region. Before investigating incompressible flow conditions, it is necessary to describe the stagnation or total pressure at a specific location within the flow field. By definition total pressure corresponds to the static pressure in an infinite reservoir from which the gas is accelerated isentropically to its actual speed v [76ZU1]. This assumption is incorporated into the energy equation and the definition can then be presented by [76ZU1, 80BE1]

$$\frac{p_0}{p} = \left(1+\frac{\gamma-1}{2}M^2\right)^{\frac{\gamma}{\gamma-1}} \tag{2.37}$$

or after a series expansion of equation (2.37) [80BE1]

$$p_0 = p + \frac{\rho v^2}{2}\left(1 + \frac{M^2}{4} + \frac{(2-\gamma)M^4}{24} + \cdots\right) \tag{2.38}$$

Equation (2.38) is simplified by assuming the higher order terms of Mach number to be negligible if the flow is incompressible:

$$\frac{p_0}{\rho} = \frac{p}{\rho} + \frac{v^2}{2} \tag{2.39}$$

Equations (2.12) and (2.15) are combined to obtain an alternative expression for dh in the case of adiabatic flow.

$$Tds = 0 = du + pd\left(\frac{1}{\rho}\right) = dh - \frac{dp}{\rho} \tag{2.40}$$

$$\text{thus } dh = \frac{dp}{\rho} \tag{2.41}$$

Incompressible flow is characterized by a constant density throughout. Assuming this to be the case in and substituting equation (2.41) into equation (2.17), the ideal power input to a fan is solved from:

$$\begin{aligned} -_1w_2 &= \frac{1}{\rho}\int_1^2 dp + \int_1^2 v dv \\ &= \frac{1}{\rho}(p_2 - p_1) + \frac{1}{2}\left(v_2^2 - v_1^2\right) \\ &= \frac{1}{\rho}(p_{02} - p_{01}) \end{aligned} \tag{2.42}$$

From equation (2.26) it follows that

$$P_{id} = V(p_{02} - p_{01}) \tag{2.43}$$

where V is the volumetric flow rate through the fan which remains constant due to the constant density term for incompressible flow in equation (2.25). Equation (2.43) is similar to equation (2.31) if the value of $K_p = 1$ is substituted.

2.5 Standard fan test codes

The fan application which is relevant to the fan installation investigated in this study, is a fan with free inlet and free outlet (type A installation of the British fan test codes [80BS1]). According to Wallis [83WA1] it is desirable to employ fan static conditions as opposed to fan total conditions to describe the fan characteristics of such an installation. A complete experimental illustration of the differences between fan static and total considerations is attached in the introduction to chapter 4. In light of these statements, only the equations relevant to fan static conditions for type A fan installations are extracted from the fan test codes and used to determine the fan characteristics.

Referring to figure 3.1, the complete fan characteristic can be described once the ambient conditions (p_{amb}, T_{amb} and ρ_{amb}) have been determined. Note that the settling chamber is attached to the fan inlet.

The mass flow rate of air through the installation is determined from [84BS1, 84BS2]

$$\dot{m} = \alpha\epsilon \frac{\pi d_{bell}^2}{4} \sqrt{2\rho_{amb}\Delta p_{bell}} \tag{2.44}$$

The product of the flow coefficient (α) and the expansibility factor (ϵ) is known as the compound calibration constant. It is determined by calibrating the inlet bellmouth against flow measurements using pitot static tube traverses according to BS 1042 [83BS1] (see section D.1). The calibration constant ($\alpha\epsilon$) accounts for flow losses due to the actual flow conditions not being isentropic.

The ideal gas law is used to calculate the density of air inside the settling chamber.

$$\rho_{sett} = \rho_{amb} \frac{(p_{amb} + \Delta p_{sett})}{p_{amb}} \tag{2.45}$$

The air velocity within the settling chamber approaches zero due to the large cross sectional area ratio between the settling chamber and the fan inlet. The flow within the settling chamber is therefore assumed to be incompressible. Combining equations (2.25) and (2.39) gives

$$\Delta p_{t_{sett}} = \Delta p_{s_{sett}} + p_{d_{sett}} \tag{2.46}$$

$$\text{where } p_{d_{sett}} = \frac{1}{2}\rho_{sett} v_{sett}^2 = \frac{\dot{m}^2}{2\rho_{sett} A_{sett}^2} \tag{2.47}$$

The fan static pressure (Δp_{sF}) can be calculated by subtracting the total pressure (gauge) at fan inlet from the static pressure (gauge) at fan outlet.

$$\Delta p_{sF} = -\Delta p_{t_{sett}} \tag{2.48}$$

If the flow through the fan cannot be assumed incompressible the compressibility coefficient (K_p) is determined from equations (2.34) and (2.35). The boundary between compressible and incompressible flow is assumed to be where $\Delta p_{sF} = 2500\ N/m^2$ according to BS 848 [80BS1]. Note the following differences between these equations and those proposed by BS 848.

- The constant z used to define the compressibility coefficient (K_p) in equation (2.36) is different from the one proposed by BS 848 (z_{BS}). The difference can be presented as

  $$z_{BS} = z \times \left(\frac{\rho_1}{\rho_{01}}\right) \tag{2.49}$$

  The ratio between ρ_1 and ρ_{01} approaches 1 as the velocity approaches zero. At a velocity through the fan of 50 m/s ($M \approx 0,15$) the error introduced by using the assumption suggested by BS 848 will only be approximately 1%. This implies that for low Mach numbers z_{BS} can also be used.

- The total pressure at fan outlet used to determine the compression coefficient as proposed by BS 848 is p_{amb}. This corresponds to the suggestions of other authors [61JO1, 72CO1] who argue that all the kinetic energy present in the air stream at exit to atmosphere is dissipated and cannot be utilized.

The shaft power input to the fan is calculated from the measured torque and rotational speeds.

$$P_R = \frac{2\pi N}{60} T \tag{2.50}$$

where N - rotational speed in $[rpm]$

T - input torque to fan shaft in $[N.m]$

By definition, fan static pressure is fan total pressure less one dynamic pressure component. The total pressure differential present in equation (2.36) is replaced by fan static pressure to result in the fan static efficiency. Due to the incompressibility assumption, K_p is assumed equal to 1.

$$\eta_{sF} = \frac{\Delta p_{sF} V}{P_R} \times 100 \tag{2.51}$$

$$\text{where } V = \frac{\dot{m}}{\rho_{sett}} \tag{2.52}$$

The final step is to scale the results to a representative density (ρ') and rotational speed (N'). The fan laws are utilized to derive the following equations [73EC1, 77OS1, 78DA1, 80BS1].

$$V' = V \left(\frac{N'}{N}\right) \left(\frac{D'}{D}\right)^3 \tag{2.53}$$

$$\Delta p'_{sF} = \Delta p_{sF} \left(\frac{N'}{N}\right)^2 \left(\frac{\rho'}{\rho_{sett}}\right) \left(\frac{D'}{D}\right)^2 \tag{2.54}$$

$$P'_R = P_R \left(\frac{N'}{N}\right)^3 \left(\frac{\rho'}{\rho_{sett}}\right) \left(\frac{D'}{D}\right)^5 \tag{2.55}$$

$$\eta'_{sF} = \eta_{sF} \tag{2.56}$$

2.6 Distorted flow patterns

Flow distortions relevant to this study are mainly evident in the non-uniformity of the velocity and pressure distributions directly downstream of the fan rotor. The theoretical implications of these non-uniform distributions can be evaluated by considering the theoretical energy equation which has been derived for uniform one-dimensional flow as equation (2.16). Referring to equation (2.9), the kinetic energy term in applying equation (2.16) to non-uniform three-dimensional incompressible flow fields can be presented by [77DA1]

$$\frac{\text{Kinetic energy}}{\text{Unit mass}} = \alpha_{tot} \frac{1}{2} v_{avg}^2 \tag{2.57}$$

where α_{tot} is known as the kinetic energy flux coefficient defined as

$$\alpha_{tot} = \frac{\int_A |\bar{v}|^2 \bar{v}.d\bar{A}}{v_{avg}^2 \int_A \bar{v}.d\bar{A}} \tag{2.58}$$

This kinetic energy flux coefficient can be subdivided into kinetic energy flux coefficients associated with the individual velocity components [84DA1]. These velocity components are the axial, radial and tangential components in a cylindrical system of coordinates. The cylindrical coordinate system is relevant to axial flow fan characterization. The representation of these components is directly derived from equation (2.58).

$$\begin{aligned}
\alpha_{tot} &= \frac{\int_A |\bar{v}|^2 \bar{v}.d\bar{A}}{v_{avg}^2 \int_A \bar{v}.d\bar{A}} \\
&= \frac{\int_A \left[(v_{ax})^2 + (v_{rad})^2 + (v_{tang})^2\right] \bar{v}.d\bar{A}}{v_{avg}^2 \int_A \bar{v}.d\bar{A}} \\
&= \frac{\int_A (v_{ax})^2 \bar{v}.d\bar{A}}{v_{avg}^2 \int_A \bar{v}.d\bar{A}} + \frac{\int_A (v_{rad})^2 \bar{v}.d\bar{A}}{v_{avg}^2 \int_A \bar{v}.d\bar{A}} + \frac{\int_A (v_{tang})^2 \bar{v}.d\bar{A}}{v_{avg}^2 \int_A \bar{v}.d\bar{A}} \\
&= \alpha_{ax} + \alpha_{rad} + \alpha_{tang}
\end{aligned} \tag{2.59}$$

2.7 Total pressure loss coefficients

The total pressure loss coefficient for purely turbulent flows is defined as the number of dynamic pressure heads lost due to a specific resistance [77DA1, 79MA1]. The equation which represents this definition is:

$$\Delta p_t = K \frac{1}{2} \rho \bar{v}^2 \tag{2.60}$$

This loss coefficient remains constant for the majority of resistances in the ideal flow regime. Ideal flow conditions are characterized by uniform, one-dimensional velocity profiles both upstream and downstream of the resistance. Ideal resistances with characteristics that differ from those for purely turbulent flows have been distinguished [73EC1].

- $\Delta p = A$: pure static resistance
- $\Delta p = A + Bv^2$: static resistance including primary and secondary turbulent frictional resistance
- $\Delta p = Av^n$: polytropic resistance
- $\Delta p = Av$: purely laminar friction

The mechanisms which govern these characteristics can be very complex and extend beyond the scope of this study. The governing relations listed in this section are used to predict some of the phenomena associated with system resistances (refer to section 4.2.3).

2.8 Total pressure loss coefficients (Oblique flow)

The ideal pressure loss coefficient for flow perpendicular to the heat exchangers is determined according to equation (2.60). The difference in pressure loss between normal and oblique flow is that the loss coefficient at the inlet to the heat exchanger increases due to the angular approach to the bundle. The increase in inlet loss coefficient can be determined from a set of empirical equations available from the literature.

The compound loss coefficient for normal turbulent flow through a heat exchanger consists of the contraction losses at the inlet, the frictional losses through the heat exchanger and the expansion losses at the outlet [50KA1].

$$K_{he} = K_c + K_f + K_e \tag{2.61}$$

The contraction losses are available through

$$K_c = \left(\frac{1}{\sigma_{21}}\right)^2 \left(1 - \frac{1}{\sigma_c}\right)^2 \tag{2.62}$$

where σ_{21} is the solidity ratio of the heat exchanger (A_2/A_1) and σ_c the jet contraction area ratio. The jet contraction area ratio is determined from the proposals of Rouse [46RO1]. Figure 2.2 contains his data and is used to determine σ_c.

Once determined, the value for K_c is substituted into the equation for inlet loss coefficient $(K_{i\theta})$ due to oblique flow [79MO2, 84MO1].

$$K_{i\theta} = \left(K_c^2 + \frac{1}{\sin\,\theta_m} - 1\right)^2 \tag{2.63}$$

where θ_m is the corrected incidence angle for A-frames. Bellstedt [85BE1] used data presented by Mohandes [79MO2] to relate θ_m to the semi apex angle.

$$\theta_m = 0{,}0019\,\theta^2 + 0{,}9133\,\theta - 3{,}1558 \tag{2.64}$$

Figure 2.2: Jet contraction ratio for round tubes and parallel plates [46RO1]

The ideal loss coefficient for oblique flow is determined from

$$\begin{aligned} K_{he\theta} &= K_{i\theta} + K_f + K_e \\ &= K_{he} + (K_{i\theta} - K_c) \\ &= K_{he} + \left(\frac{1}{\sin\ \theta_m} - 1\right)\left(2\sqrt{K_c} + \frac{1}{\sin\ \theta_m} - 1\right) \end{aligned} \tag{2.65}$$

Equation (2.65) is utilized to predict the tube bundle loss coefficient for oblique flow from the experimentally determined loss coefficient for normal flow.

2.9 Outlet pressure loss coefficients

The outlet loss coefficients are those losses which occur due to the addition of a windwall. These losses are divided into two components, namely

- the losses attributed to the increase in outlet velocity due to the reduction in outlet area. The increase in dynamic head at the outlet from the cooling unit are dissipated in the atmosphere, causing a decrease in effective pressure work available from the fan.
- the losses occurring between the outlet from the heat exchanger surface and the outlet from the cooling unit. The energy required to change the flow angle, as well as the viscous forces present in this region are responsible for these losses.

Additional pressure losses occur if steam pipes and/or walkways between the A-frames are present. The steam pipes are normally attached to the apex of the A-frame, resulting in a flow distortion. The walkways between the A-frames are distinguished from those inside. They are used for visual inspection of the outer surfaces of the heat exchangers. The resulting region of zero flow has an adverse effect on the pressure loss coefficient [90VA1].

In summary, the outlet pressure loss coefficients are presented by [90VA1]

$$K_d = K_{dj} + K_o \tag{2.66}$$

where K_d - overall outlet loss coefficient.

K_{dj} - jetting losses as described in the previous paragraph.

K_o - outlet energy losses due to increase in dynamic head and the change in kinetic energy flux coefficient (α).

No steam pipes are present for experiments involving the scale model facility. The correlation for the reference tests on a bare A-frame, presented by van Aarde [90VA1] is

$$\begin{aligned}(K_{d0})_{HX} &= K_{dj} + K_o \\ &= \left(4{,}44 - \frac{348\,447}{Ry_{HX}}\right) + 9{,}057\end{aligned} \tag{2.67}$$

This pressure loss coefficient is based on the average velocity through the heat exchanger. The pressure loss coefficients presented in this study are all based on the average velocity through the fan shroud. The above correlation is referenced to the average velocity through the fan for ease of comparison with other data. The derivation of the scaled version of the same correlation is attached in section B.4.5. The result is equation (B.103).

$$(K_{d0})_{fan} = 1{,}182 - \frac{103\,106}{Ry_{fan}} \tag{2.68}$$

The effect of the space between the base of the heat exchangers and the windwalls is accounted for by extrapolating the data by van Aarde. The application of the extrapolating process also resides in section B.4.5. The exponential correlation, found by linear regression, representing this phenomenon is:

$$\frac{K_d}{K_{d0}} = e^{-6{,}8476\frac{L_w}{L_b}}$$

$$= \quad 0,438 \text{ for } \frac{L_w}{L_b} = 0,1205 \tag{2.69}$$

The ratio of 0,1205 is representative of the opening at heat exchanger base for the scale model.

The velocity profile at inlet to the A-frame model tested by van Aarde, is uniform and one-dimensional. This is in contrast to a distorted inlet profile with the fan installed. It is conceivable that a different velocity profile at inlet to the heat exchangers results in a difference in pressure loss across them.

Chapter 3 - Experiments

3.1 Experimental equipment

The experimental data used in this report are obtained from tests performed on two separate facilities. Tests to ascertain the influence of individual parameters on the overall performance of an air cooled heat exchanger system are conducted on a scaled model facility of a unit having a fan casing diameter of 9 216 mm. The performance of the scale model is then compared to results obtained from the full scale unit. A review of specific tests is contained in section 3.2.

3.1.1 Full scale facility

Test unit

The full scale air cooled condenser studied is serving a power generation plant having six turbo generator units. The rated maximum output from each unit is 660 MWe. The air cooled condenser of each unit consists of 48 fans installed in an array of 8 rows each containing 5 condenser units and one dephlegmator unit (figure F.1.1).

The fan casing diameter of the condenser unit is 9 216 mm. The fans are all mounted on vertical shafts. The system is designed to operate in a forced draft mode which means that air first passes through the fan before flowing through the heat exchanger bundles (figure F.1.2). The power consumption of each fan motor is approximately 275 kW. The motors are attached to the fan rotors through reduction gearboxes to ensure fan rotational speeds of 125 rpm. The motor, gearbox and fan rotor are suspended from two 457 x 191 I-beams mounted 2 000 mm apart. These beams also support a walkway of 44 x 40 x 8 mm "recta grid" to ensure easy access for maintenance to gearboxes and motors.

The profile of the fan casings is of elliptical design and include safety grids which are attached to the bottom of the inlet bell. These grids are used during construction and ensure access to the fan blades once the plant has been commissioned. Access to the blades is necessary to adjust and set blade angles and to inspect the fan rotor.

The heat exchanger bundles are mounted in an A-frame configuration with an apex angle of 56°. The cross sectional design of the heat exchanger tubes is elliptical. Each condenser bundle array is 9 660 mm long (effective tube length) with shorter dephlegmator bundles of 8 110 mm. The bundle arrays consist of two rows of finned tubes operating under parallel down flow conditions. The first tube row has a fin pitch of 4,0 mm compared to 2,5 mm for the second row.

Instrumentation

A number of velocity distributions is measured in the full scale unit. The instrumentation for this is located at the following positions:

- directly downstream of the fan inlet safety grid
- directly downstream of the fan rotor
- at the outlet of the A-frame array (between the adjacent steam pipes)
- at a location approximately 1 *km* away from the unit in a north westerly direction where ambient conditions are monitored

A rotating beam fitted with ten individual 220 *mm* diameter vane anemometers is installed downstream of the safety grid at the inlet to each fan under investigation (figure F.4.1). The beam is rotated using a driving wheel which is powered by a stepper motor. The angle through which the beam rotates is selectable using a portable personal computer. The same personal computer is also fitted with an analogue to digital interface card, and is used as data acquisition system. Once the system is operational, the beam rotates through a number of preselected angles until one revolution has been completed, reverses direction and then backtracks at the same angular intervals. Voltage outputs from each vane anemometer are directly transformed to velocity using the predetermined calibration constants.

Velocity distributions immediately downstream of the fan rotor are determined using a staggered beam which is mounted perpendicular to the walkway. This beam is traversed manually from one position to the next. The anemometer readings are once again directly converted into velocities. The resulting grid of measuring points is attached as figure F.5.1. Velocities are measured at a basic height of 800 *mm* above the fan centerline. In the region immediately downstream of the walkway, velocity readings were taken at a height of 1 325 *mm* above the fan centerline.

In addition to all the velocities monitored at the above locations, air temperature is also measured at the inlet to the unit and on the staggered beam directly downstream of the fan rotor.

The static pressure difference between fan inlet an outlet is monitored using a system of calibrated spherical probes. The design and calibration of these probes are described in detail by D.J. van Aarde [90VA1]. Three such probes are attached to the rotating beam at the fan inlet, and another three to the staggered beam at the fan outlet.

Ambient conditions are monitored utilizing a 100 *m* weathermast located at a position approximately 700 *m* away from the northern side of the cooling unit in a north westerly

direction (figure F.1.3). Three dimensional velocity components are measured at 10 m, 20 m, 40 m, 65 m and 96 m above ground level. Air temperatures are measured at 1,2 m, 2,5 m, 5 m, 10 m, 20 m, 40 m, 65 m and 96 m above ground level. Ambient pressure and relative humidity are also measured, but only at a height of 0,3 m above ground level.

Plant instrumentation is also available to measure additional operating parameters such as the electrical power consumption of individual fans.

3.1.2 Scale model facility

Test unit

The full scale condenser unit described in the previous section is so large that it is impractical to investigate the influence of changing the arrangement of flow distorting components on its overall performance. A scale model representing a single condenser unit was designed and erected at the University of Stellenbosch. The advantages of a smaller facility are mainly twofold.

- It is easier to rearrange individual components on a small scale unit. This implies that the influence of individual parameters on the overall fan performance can be investigated.
- A fan close to the windwall (eastern) side of the unit is subjected to a larger cross flow component at the inlet than a fan nearer to the turbine house. Ambient conditions such as wind speed and direction influence the magnitude of this effect. The scale model makes it possible to isolate the effect of cross winds by ensuring axisymmetrical flow at the fan inlet.

The scale factor applied to the model is based upon fan casing diameter of 1 542 mm. This corresponds to a scale factor of 1:5,98. From the drawings attached in section F.2, it can be concluded that the majority of the model dimensions are scaled values of the actual unit. Exceptions are the clearance between the fan rotor and ground level, the physical dimensions of the "recta grid" from which the walkways are constructed and the blade profiles of the fan impellers. Features of the scale model which are not present in the full scale unit are an option to attach windwalls all around the unit and the ability to add or remove any desired component of the unit. The ground clearance of the unit can also be adjusted.

Two different fan rotors are available to test the effect of fan selection on the overall performance of the system. The different designs are known as V-type and GH-type fans. Details of the dimensions and profiles of the model rotors compared to the those present in the actual unit are attached in section F.6.

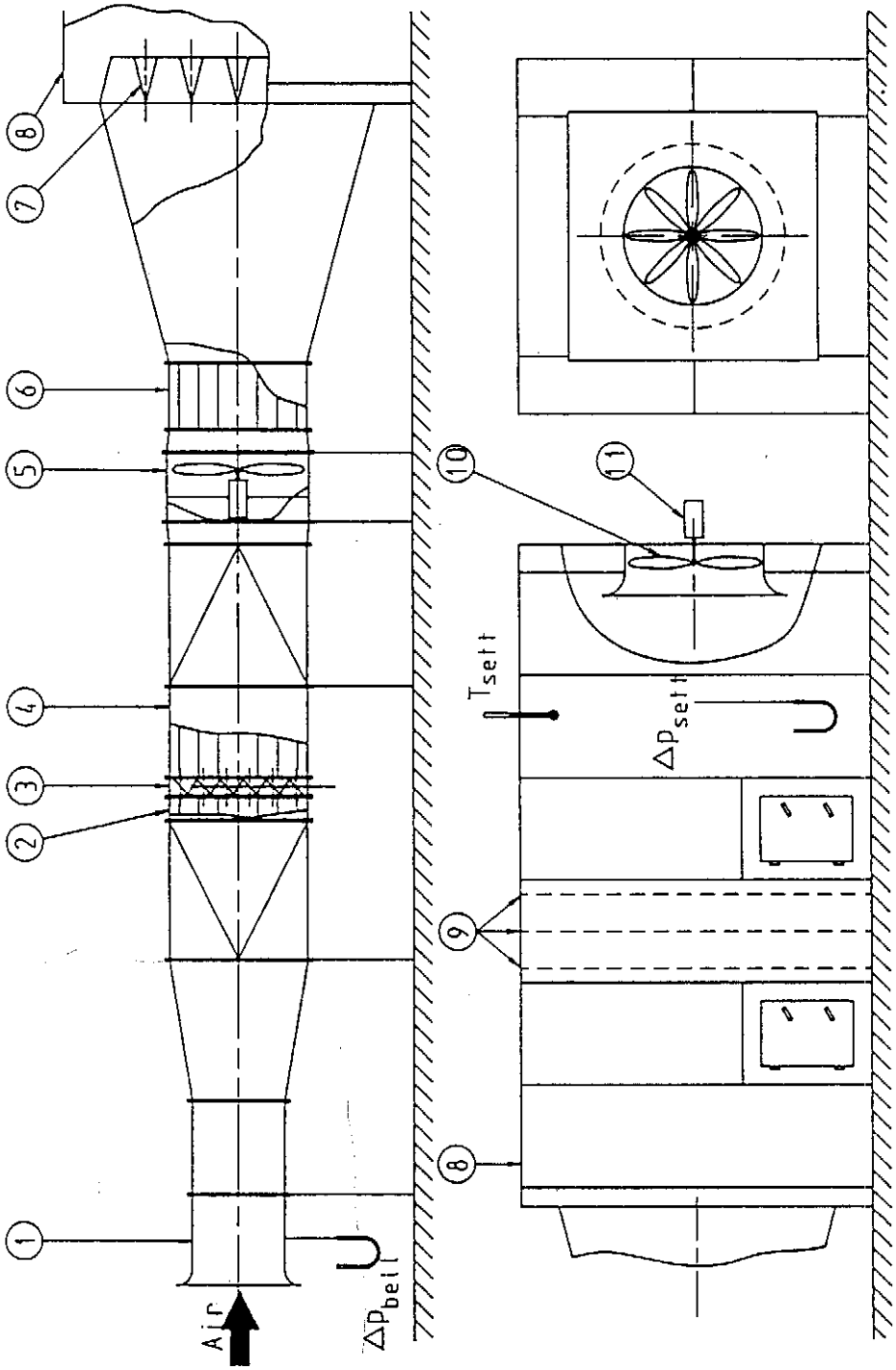

Figure 3.1: Schematic of the standard fan test facility : Type A

The heat exchangers are constructed of identical finned tubes to those used in the full scale unit. This ensures that the pressure loss coefficients of the model approximate those of the full scale unit. An additional option of using a single finned tube array (either 2,5 *mm* or 4,0 *mm* pitch) is also available for the model. Section 3.2 refers to the experimental procedure which is followed and from which it will become apparent that tests relevant to this study are all performed under isothermal conditions. The model is designed, however, to enable future tests with hot water passing through the heat exchangers.

The scale model is attached to a fan test facility designed according to BS 848 [80BS1] (section 3.1.3). Due to this arrangement, the assembly is mounted with the fan shaft horizontally.

Instrumentation

A five hole probe designed and calibrated according to the proposals of A.M. Yocum [78YO1] and T.R. Heidrick [86HE1] is used to measure pressure and velocity distributions at the model test facility (figure F.4.2). The advantage of employing a five hole probe to measure velocity profiles is that the three-dimensionality of the flow can be determined. Both total and static pressure distribution at fan inlet and outlet are available through the pressure coefficients (section D.8).

The probe is automatically traversed in a horizontal direction using a stepper motor driven traversing device with displacement transducer feedback. The height above ground level of the traverse can be adjusted and is used to measure velocity distributions in cases where the flow is not symmetrical with respect to the fan axis.

3.1.3 Code fan test facility

The advantage of using a code test facility to evaluate the performance of an air-cooled condenser model is that parameters such as volumetric flow rate, shaft input power, rotational speed and inlet and outlet pressures can be measured more accurately than in the case of a full scale unit. The diameter of the model fan casing is 1 542 *mm* (section 3.2). With this diameter in mind, it was decided to design and build a standardized fan test facility with the ability to characterize fans with a maximum impeller diameter of 1 600 *mm*. After careful consideration of available fan test standards [46AS1, 66VD1, 74AM1, 75AS1, 80AS1, 80BS1, 85DE1, 85DE2] it was decided to adhere to the specifications of the British Standards Organization. It is worth noting that the modern fan test codes are all closely related [84RO1]. This means that the same facility can normally be used to test fans according to any of these standards.

Test unit

The facility is designed to enable researchers to use it not only for type A tests (free inlet, free outlet), but also for any combination of free or ducted inlet or outlet (types B, C or D tests). As only type A tests are relevant to this study, only features relating to these tests are described.

A calibrated inlet bellmouth is used to determine the volumetric flow rate of air through the system (item 1 in figure 3.1). The average inlet diameter of the section in which the static pressure tappings are installed is 1 008 mm with a maximum deviation of 2,0 mm. (figure F.3.1). The average velocity through the inlet bellmouth is expected to be 1,53 times larger than the average velocity through the 1,5 m diameter duct. A large velocity through the inlet bellmouth is preferable as it ensures higher levels of accuracy in measuring low air flow rates. The bellmouth is calibrated against pitot static tube traverses performed at different volumetric flow rates (section D.1).

An auxiliary fan is installed directly downstream of the throttling device (items 5 and 3 respectively in figure 3.1). This fan is used to overcome pressure losses due to the different components in the flow stream. The fan is powered by an 11 kW electric motor and the rotor is directly attached to the shaft of this motor which is situated in the main air flow stream. The fan rotor has 6 blades and an outer rotor diameter of 1 540 mm. All blade angles are preset at 24^{o}.

Flow straighteners are either of egg-grate or radial blade design according to BS 848 (figures F.3.3 and F.3.8 to F.3.11). Two flow straighteners are mounted on either side of the throttling device, with a third being located directly downstream of the auxiliary fan (items 2, 4 and 6 in figure 3.1). The latter is to eliminate the angular momentum added to the air stream by the auxiliary fan rotation.

A transformation piece is required to connect the calibrated inlet bellmouth to the remainder of the test facility (figure F.3.2). Two transformation pieces convert the round ducts to square and back to round to accommodate the flow throttling device (figure F.3.4). Two transformation pieces are also used to enlarge the channel diameter from 1 500 mm to 1 550 mm and then back to 1 500 mm to accommodate the 1 540 mm diameter auxiliary fan. The last transformation piece is a diffuser ensuring an even distribution of air entering the settling chamber (figure F.3.13). At the exit of this diffuser into the settling chamber, a set of flow guide vanes are installed which distribute the air flow more evenly (item 7 in figure 3.1 and figure F.3.14).

The settling chamber itself is constructed of galvanized sheet metal panels with inside dimensions of 4 000 x 4 000 x 7 000 mm (item 8 of figure 3.1). A set of 3 stainless steel mesh screens (item 9 in figure 3.1) is installed at the locations specified by BS 848 [80BS1]. Access to the inside of the chamber is ensured by including two air tight access

doors, one upstream and one downstream of the wire mesh screens. The outlet of the settling chamber is fitted with a square opening of 2 500 x 2 500 mm through which fan inlets are installed for free inlet fan characteristic tests (figure F.3.13).

As stated in the preceding part of this section, the code fan test facility is designed according to the dimensional requirements of BS 848. It can be appreciated that due to a combination of limited space and the physical size of the facility, some of the dimensions are modified. An investigation of figure F.3.2 reveals that the transformation piece between the inlet bellmouth and the remainder of the facility is only 1 500 mm long as opposed to a length of 3 inlet diameters, or 3 000 mm, required by BS 848. The danger of shortening this diffuser is that the calibration constants as recommended by BS 1042 [81BS1] are no longer valid. Careful calibration of the inlet bellmouth (section D.1) eliminated any of these uncertainties. The calibration is in accordance with BS 1042 [83BS1] which specifies a flow measurement procedure involving pitot tube traverse methods.

Additional calibration of the tunnel included measuring the amount of air leaking into the system (section D.3) and the velocity distribution in plane 3 (section D.4) to ensure a uniform inlet velocity profile. The assumption by BS 848 that the static pressure measured in plane 3 equals the total inlet pressure to the fan is only valid for an average velocity through the chamber of less than 2,5 m/s (corresponding to a dynamic pressure of approximately 3,75 N/m^2). Instead of ignoring the dynamic pressure component in plane 3 as suggested by BS 848, it was decided to account for it when calculating the total pressure at the fan inlet.

The hydraulic power pack used to rotate the model fans has a maximum rated output of 10 kW at 750 rpm. Rotational speed can be varied which means that changes in speed at different flow rates can be compensated for by changing the flow rate of oil to the hydraulic motor.

Instrumentation

The fan test facility is fitted with a number of instruments which are used to measure the various parameters required to compile a set of fan characteristic curves.

Inductive pressure transducers, manufactured by Höttinger (type PD1) are used to measure the pressure. Their range of application is between -1 000 and 1 000 N/m^2. The torque transducer, a Höttinger type T2, has a nominal measuring range of -500 to 500 Nm. The torque transducer is a resistive full bridge instrument. All three of these transducers are connected to a Höttinger KWS 3073 bridge amplifier which amplify the input signals over a range of -10 to +10 V. The calibration of these instruments is discussed in sections D.2 and D.7 respectively.

The instrument used to measure the rotational speed of the fan is a basic magnetic pick up

sensor connected to a frequency counter. The frequency counter has a dual output. The one output is a digital display used to adjust the rotational speed, whilst the other is a linear voltage output measured by the computer. The calibration of this unit is discussed in detail in section D.2.

Output voltages from the bridge amplifier (related to fan inlet pressure, inlet bellmouth pressure and shaft input torque) as well as a voltage related to rotational speed are transmitted to a personal computer (Olivetti M21). Real time voltage inputs are displayed in graphical form to eliminate any transient effects. Once steady state conditions are achieved, 500 voltages are measured at a sampling interval of 20 ms. The average of these data points is calculated and saved to disk to be reduced and presented as fan characteristic curves. The accuracy of the measured data is improved markedly by averaging a large number of voltages instead of using instantaneous values.

Ambient conditions are also monitored continuously. Ambient temperature is measured using a mercury thermometer. The accuracy level of the thermometer is 0,5 $^{\circ}C$. Ambient pressure is measured with a mercury barometer with an accuracy level of 0,05 $mmHg$.

3.2 Experimental procedure

In section 3.1 the different test facilities and instrumentation used to study of the effect of flow distortion on the overall performance of axial flow fans are discussed. The procedure employed to generate experimental data is highlighted in the remainder of the chapter.

3.2.1 Scale model tests

Results generated utilizing the scale model unit are divided into two main sections, namely

- tests pertaining to the influence of individual parameters on the overall performance of the fan, and
- tests aimed at predicting the influence of flow distortions on the velocity profiles in the immediate vicinity of the fan.

The code fan test facility, which is described in section 3.1.3, is used exclusively to perform the parametric study of external influences on overall fan performance. The procedure involves initial base line tests to determine the fan characteristics of the ideal fan. These tests are performed with only the fan rotor installed. It is important to note that the fan blade angle setting is subject to inaccuracies due to the relatively small tip chord of the test fans. Uncertainties ascribed to the inability to accurately set the smaller fan blades

can be eliminated by measuring new fan performance characteristics for each new blade angle setting. All system characteristics are then determined without changing the blade angle and are referred to the fan characteristics relevant to the specific blade angle setting.

The effect of blade angle setting on the individual fan rotors is compared on the basis of fan characteristics. The blade angle of the V-fan is varied between 12^o and 16^o as opposed to a range of 8^o to 10^o for the GH-fan. These blade angles ensure that the power consumption of both fan impellers are approximately the same.

Tip clearance effects are investigated using the V-fan. The possible range of tip clearance settings is between 3,0 and 10,0 mm, with increments at every 1,5 mm. The initial results from fan tip clearance effects revealed that the most efficient operation of the fan is for conditions with as small a tip clearance as possible. This resulted in all remaining tests being performed with the tip clearance set at 3,0 mm. Velocity distributions related to tip clearance effects are not measured because these effects manifest themselves primarily in the vicinity of the casing wall. Wall effects on the calibration of the five hole probe are not considered due to the complexity involved in such a venture.

Preliminary velocity distribution tests revealed an inner core region of reversed flow conditions. A 445 mm diameter solid disc of 3 mm mild steel is attached to the center of the fan. The idea is to reduce the hub to tip ratio of the fan which was considered a possible cause for low fan efficiencies. Velocity profiles at fan inlet and exit are determined for this arrangement.

The remaining tests are concerned with the effect of the walkway, inlet grid and heat exchangers both individually and as combined flow distorting components. The effect of these components on the fan characteristics is determined and represented as deviations from the ideal fan characteristics. Deviations from the ideal velocity distributions at fan inlet and outlet are measured. The flow structures listed at the beginning of this paragraph are all responsible for velocity profiles which are not axisymmetrical. The consequence is that satisfactory results can only be obtained by measuring the complete three dimensional velocity distribution.

3.2.2 Full scale tests

As mentioned before there are certain limitations associated with tests performed in a full scale air cooled heat exchanger unit. The more pronounced of these limitations is that a single fan cannot be isolated and investigated as a single unit. Another disadvantage is that it is impossible to rearrange individual flow distorting components such as the walkway, inlet grid and heat exchangers. Rearranging these components enables the researcher to determine their influence on fan performance.

In spite of the limitations highlighted in the previous paragraph, valuable experimental data were generated using the full scale unit. The experiments are aimed at producing typical velocity profiles for fans at different locations relative to the windwall. The rotating and staggered beams described in section 3.1.3 are used to obtain the velocity profiles at fan inlet and outlet. A row of six fans is used to determine a representative average inlet velocity profile to the fans. The average inlet velocity profile is compared to the typical inlet profiles measured for the scale model. Velocity profiles for selected fans are also determined for different operating conditions to indicate the repeatability of these tests.

Chapter 4 - Results and Discussion

A complete set of fan characteristic curves relates the fan pressure rise, the fan efficiency and the fan power consumption to the volumetric flow rate through a fan (e.g. figures 4.1 to 4.3). In the case of fans with adjustable blade angles, the effect of this adjustment should also be presented on the overall performance maps [66VD1, 74AM1, 75AS1, 80BS1, 85DE1].

Two alternative methods of defining the differential pressure across the fan are recommended by the fan test codes. The different pressure definitions are known as fan static pressure and fan total pressure, with their related fan static and fan total efficiencies [66VD1, 74AM1, 75AS1, 80BS1, 85DE1]. Fan total pressure is defined as the difference between total (or stagnation) pressure at fan inlet and total pressure at fan outlet. Fan static pressure is the fan total pressure minus the fan velocity pressure. Fan velocity pressure is the velocity pressure corresponding to the average velocity at the fan outlet. These definitions are all excerpts from Fans by W. C. Osborne [77OS1] and the differences between them are highlighted in figures 4.4 and 4.5.

Under ideal operating conditions, fan total pressure is directly related to the total amount of energy added to the air stream by the fan impeller (refer to chapter 2). Ideal operating conditions are characterized by steady, uniform and axisymmetric velocity profiles both at fan inlet and outlet. All applications of fans studied in this study are mainly concerned with the influence of distorted flow patterns at fan outlet. These flow distortions are caused by supporting structures and finned tubes in the proximity of the fan impeller. The inlet velocity profiles normally approximate the ideal case (figures A.4.1 to A.4.3). In applications such as these, it is advantageous to consider the fan static pressure as it does not incorporate any assumptions concerning the fan outlet velocity profile. All remaining fan characteristics presented in this report will therefore be based upon fan static pressure and not fan total pressure.

It is important to note that the decision to utilize fan static pressure instead of fan total pressure to present fan characteristics is in agreement with the recommendations of R.A. Wallis [83WA1]. He reasoned that it should be called fan inlet total pressure and should only be used in the case of exhaust units. Note also the discrepancy that exist between the definition of fan total pressure for exhaust units by the Deutsche Normen [85DE1] and the British Standards Organization [80BS1]. This discrepancy arises from the different definitions of fan outlet areas. The British standard assumes the fan outlet area to be the total outlet area inside the fan inlet shroud, while the German standards subtract the effective area blocked by the fan hub and motor from the fan inlet shroud area. This difference between the two standards is eliminated when applying fan static pressure to exhaust units.

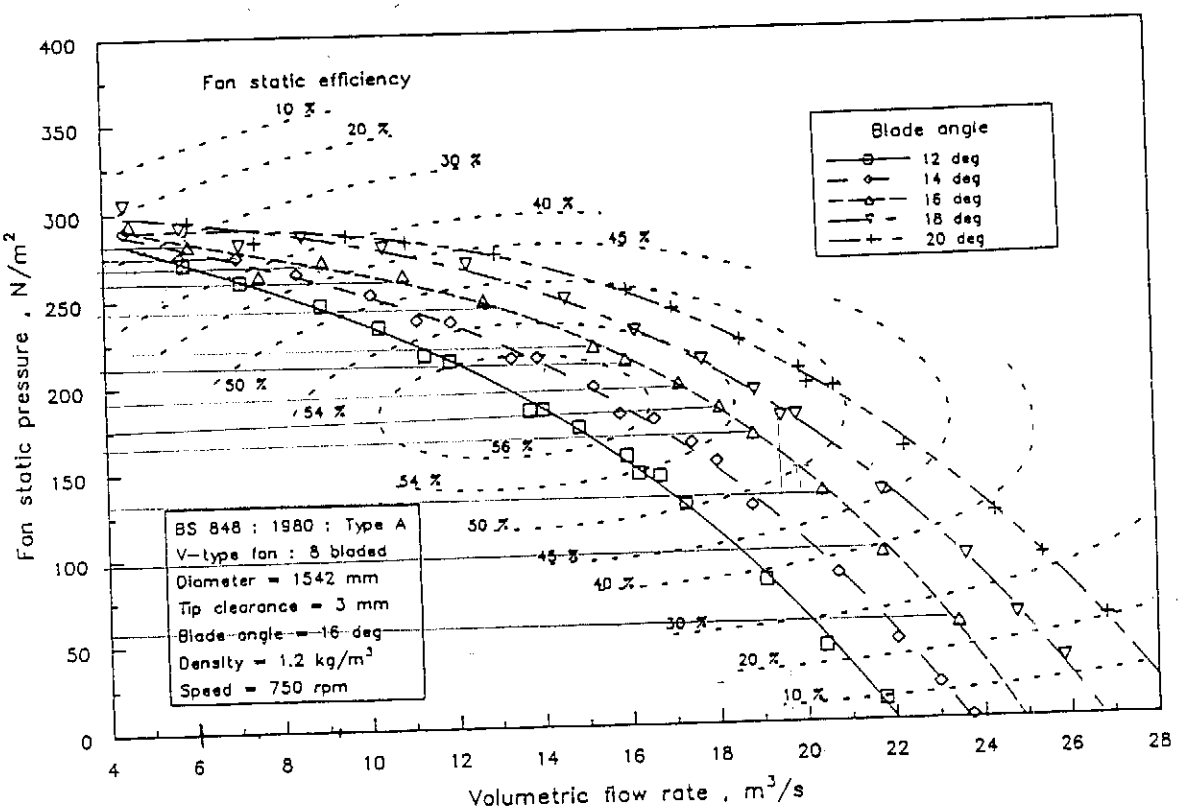

Figure 4.1: Fan static pressure and efficiency curves : V-type fan

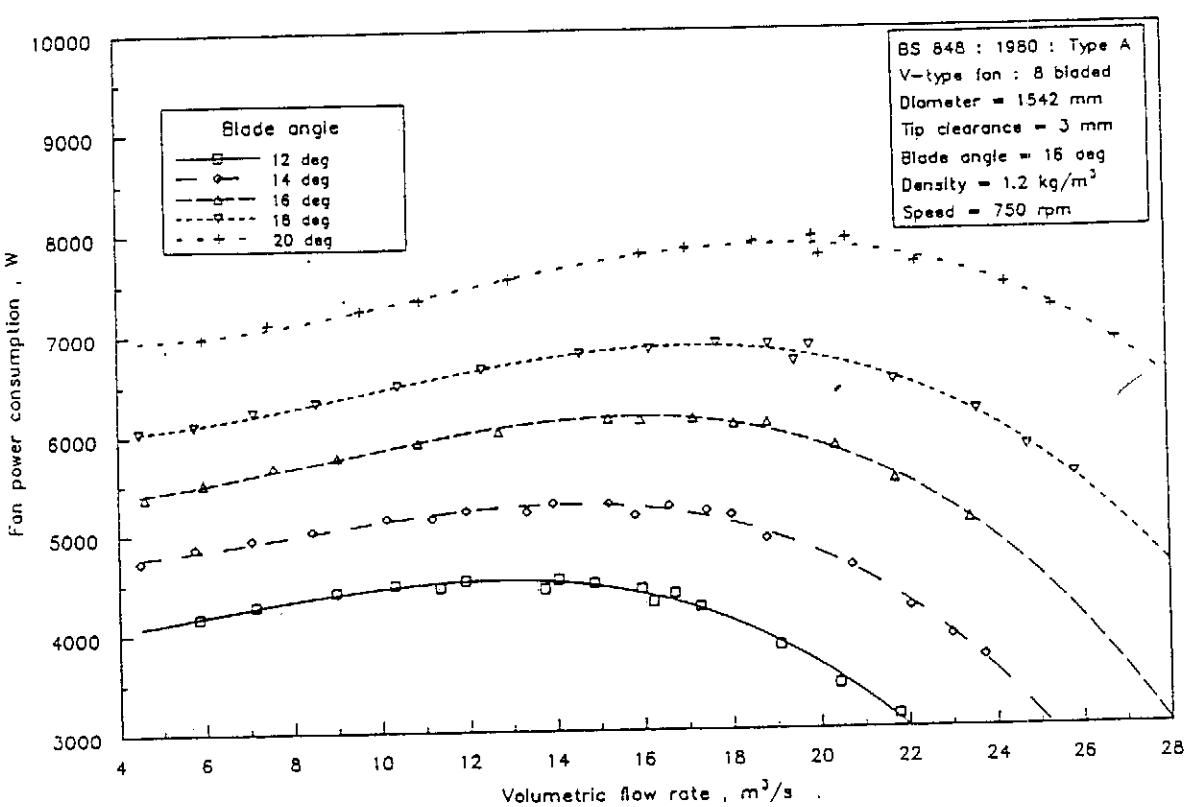

Figure 4.2: Fan power consumption curves : V-type fan

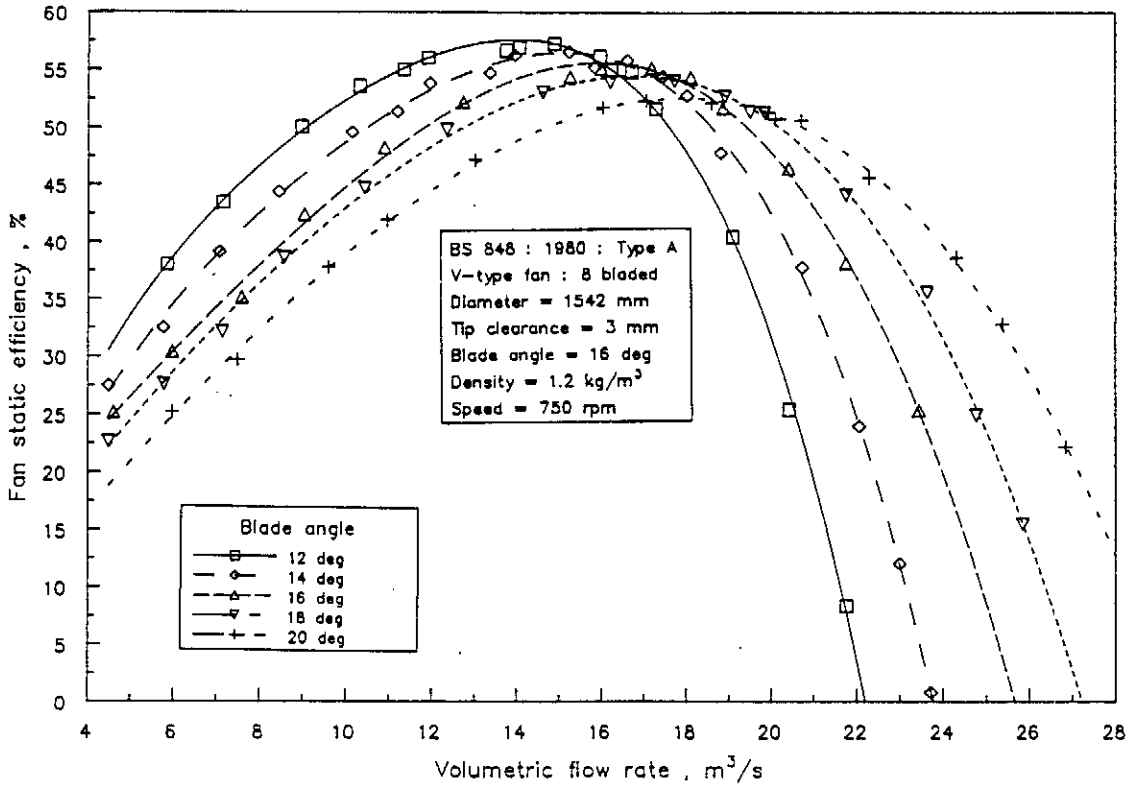

Figure 4.3: Fan static efficiency curves : V-type fan

4.1 Specific fan performance characteristics

The performance curves relevant to the V-type fan are shown as figures 4.1 to 4.3, with the corresponding curves pertaining to the GH-type fan attached as figures A.1.1 to A.1.3. These graphs are all summaries of the fan performances at different blade angle settings, where the fan static efficiencies are presented as contours on the fan static pressure curves.

The differences in performance between the V-type and GH-type fans are highlighted in figures A.1.4 to A.1.6. The fan blade angles are selected to ensure that the power consumption of the two rotors is approximately the same for the practical range of application, namely 16° for the V- type and 9° for the GH-type fan (figure A.1.6). From the graphs it is apparent that fan static pressure and efficiency related to the GH-fan are higher than those of the V-fan for volumetric flow rates below 17 m^3/s. For volumetric flow rates in excess of 17 m^3/s, the fan static pressures and efficiencies associated with the V-type fan are higher than the corresponding parameters for the GH-type fan. The maximum fan static efficiency of the GH-fan is 58% at a volumetric flow rate of 14 m^3/s as opposed to 56% for the V-fan at a volumetric flow rate of 16 m^3/s.

The theoretical operating point of the specific system into which the fan rotor is ultimately installed, corresponds to approximately 16 m^3/s. Although the fan static efficiency for the GH-type fan is 1,5% higher than for the V-type fan operating at 16 m^3/s, this difference

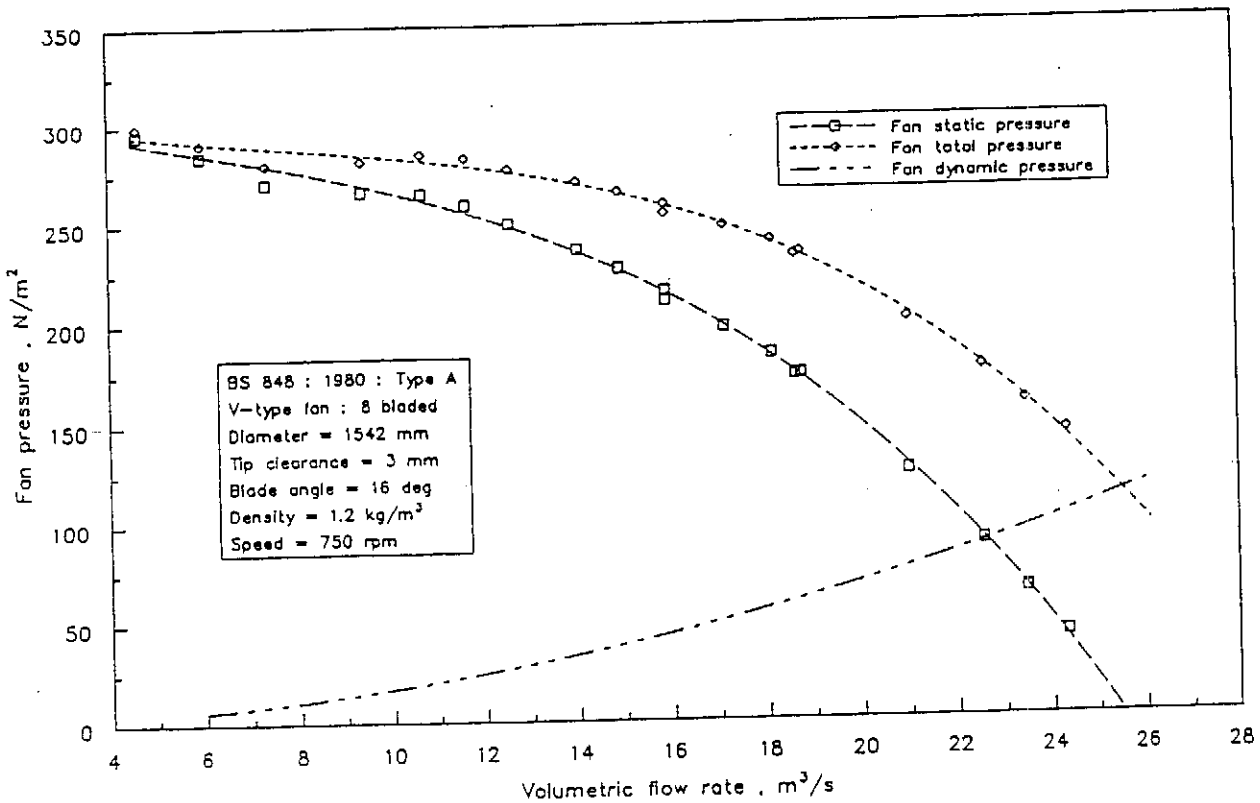

Figure 4.4: Comparison between fan static pressure and fan total pressure

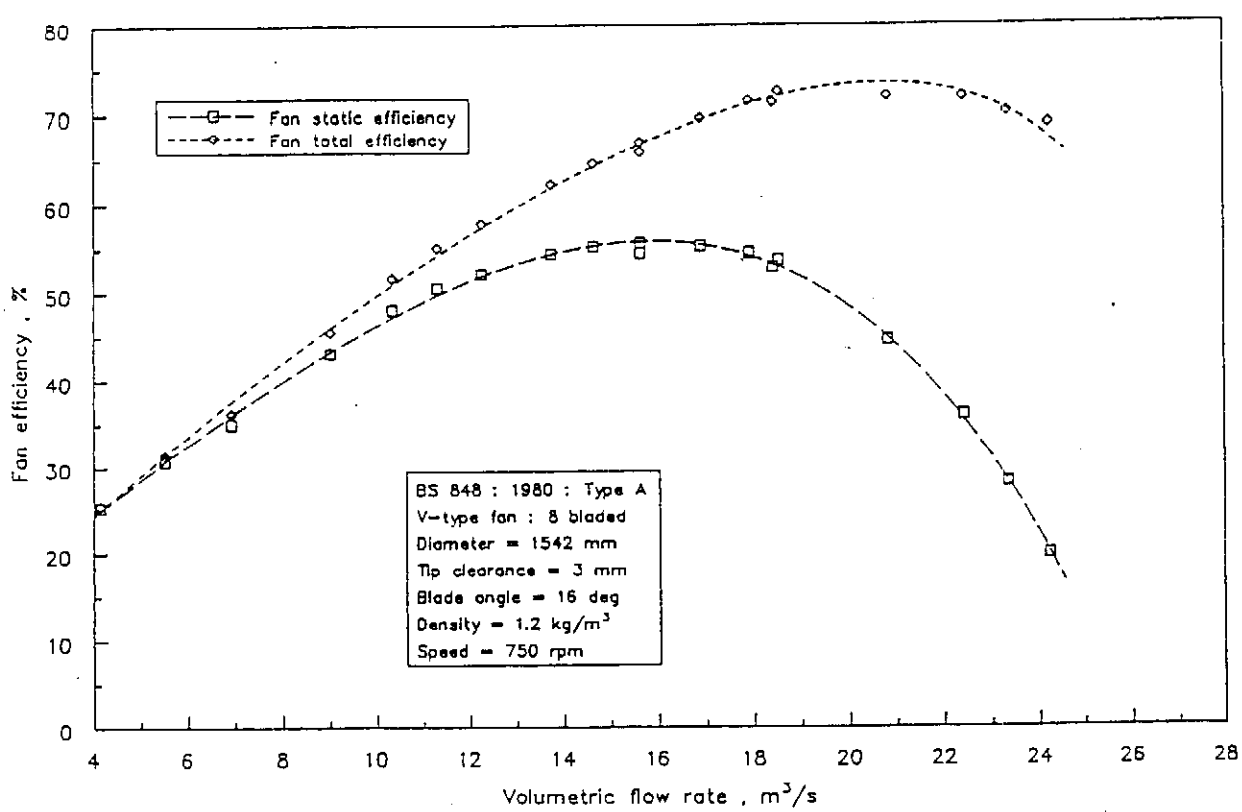

Figure 4.5: Comparison between fan static efficiency and fan total efficiency

is reduced to zero at 17 m^3/s. The V-type fan becomes more efficient at volumetric flow rates in excess of 17 m^3/s. The suggestion to replace the existing V-type impellers with GH-type impellers will therefore not result in any appreciable improvements in the condensers, but might prove valuable for the dephlegmators.

4.2 Effect of flow distortion on fan performance

The effect of different parameters investigated in this study is discussed by referring to the effect of a single flow distorting component, or of a combination of flow distorting components, on system static efficiency. System static efficiency is an indication of the efficiency by which excess air is forced through the system. At the point of zero fan static pressure, the fan static efficiency is also zero (no excess air being displaced). Care should therefore be taken when using system efficiencies as basis to compare two systems. As the rate at which system static efficiency approaches zero is high in the proximity of zero system static pressure.

The importance of system static efficiency is apparent when considering that the rotational speed of an industrial fan installation normally remains constant. The constant rotational speed is associated with a constant frequency input to the alternating current electric motors used for industrial applications. A study of the effect of flow distortion on system static pressure is not necessarily representative of its effect on the overall system performance.

The influence of different disturbances in the flow on fan performance is discussed in the remainder of this section. Section A.2 is dedicated to the results obtained from tests pertaining to the effect of the different arrangements.

4.2.1 Fan tip clearance

A number of authors have reported on the effect of tip clearance on the performance of axial flow turbomachines. The effect of tip clearance on the performance of axial flow fans, compressors and pumps is reviewed Lakshminarayana [70LA1] and Peacock [82PE1, 83PE1]. It is not feasible to match their data to the axial flow fans of interest to this thesis. One reason is that the tip clearance is non-dimensionalized by dividing it through the blade height. The blade height is not well defined for the fans relevant to this thesis as they do not have profiled hubs which fix the distance between hub and tip. Furthermore, these authors express the change in performance of the turbomachines in terms of a deviation from their theoretically predicted total pressure characteristics. The aim of the work done in this thesis is to investigate the deviation of the fan performance from its ideal characteristic curve. This implies that the change in fan performance due to tip clear-

ance effects is expressed in terms of a deviation from the experimentally determined fan static characteristic curves for ideal flow conditions. A number of other publications are concerned with shrouded axial flow fans incorporating flow enhancement devices such as preswirlers and multiple stages [73EC1, 81BA1, 83WA1] which are also not present in fans relevant to this thesis. The publications most applicable to the type of fan investigated in this study are those by Monroe [79MO1], Marcinowski [58MA1] and Stork [73ST1].

Monroe presented his data as a percentage loss in fan total pressure and fan total efficiency plotted as functions of the actual tip clearance. The results obtained in this study are presented as ratios of reduced fan static pressure and fan static efficiency to the ideal of the above mentioned respectively. The preference of fan static pressure over fan total pressure has been stated in the introduction to this chapter. The tip clearance is divided by fan inlet shroud diameter to present it as a dimensionless parameter. This is notably different from the ratio between tip clearance and blade span used by Wallis [83WA1]. The blade span for the axial flow fans under investigation in this work is not as well defined as those having multiple stages. Also the velocity profiles at fan outlet exhibit some reverse flow regimes in the vicinity of the hub. These factors combine to highlight that the tip clearance ratio should be referred to the shroud outlet diameter for fans exhausting directly into the free atmosphere. This is in accordance with other authors [58MA1, 73ST1] who also prefer to present the influence of tip clearance in terms of the ratio between the clearance and the fan shroud diameter.

Section A.2 summarizes the results pertaining to tip clearance effects with all the relevant derivations attached as section B.2. The final graphs representing the effect of tip clearance on fan static pressure and volumetric flow rate (figure 4.6) are applicable to a range of loss coefficients (k) of between 0,17 and 2,32. This corresponds to the normal operating range of the V-fan. The loss coefficients (k) are defined in section B.2. The effect of tip clearance on both fan static pressure and volumetric flow rate is linearly related to the clearance itself, provided that the system losses can be represented by $\Delta p = k\, V^2$.

Unfortunately the fan static efficiency is not only related to the fan static pressure and volumetric flow rate through the system, but also to the amount of power input to the fan. This makes it intractable to use a single graph to present the effect of tip clearance for a range of systems having different loss coefficients. The effect of tip clearance on fan static efficiency is referred to a tip clearance of 3 mm for a range of volumetric flow rates. Figure 4.7 highlights the fact that tip clearance effects on fan efficiencies can not be presented as a single graph pertinent to a specific fan. The effect is dependent upon the required differential pressure of a specific fan application (or system resistance).

The pressure and volumetric flow rate data correspond remarkably well with the data by Monroe [79MO1] considering that he determined the data by measuring the effect of tip clearance at a constant volumetric flow rate (figures 4.6 and 4.7). This is not representative

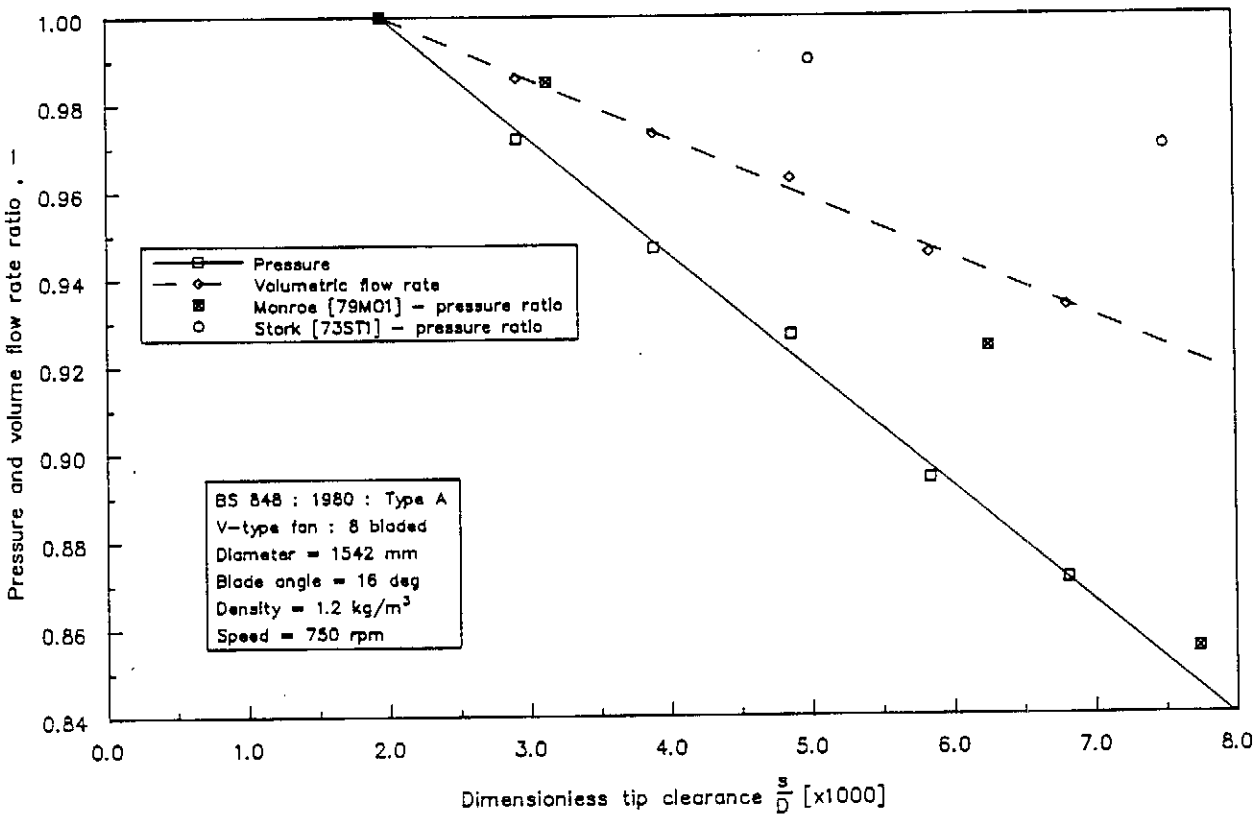

Figure 4.6: The effect of tip clearance on fan static pressure and volume flow

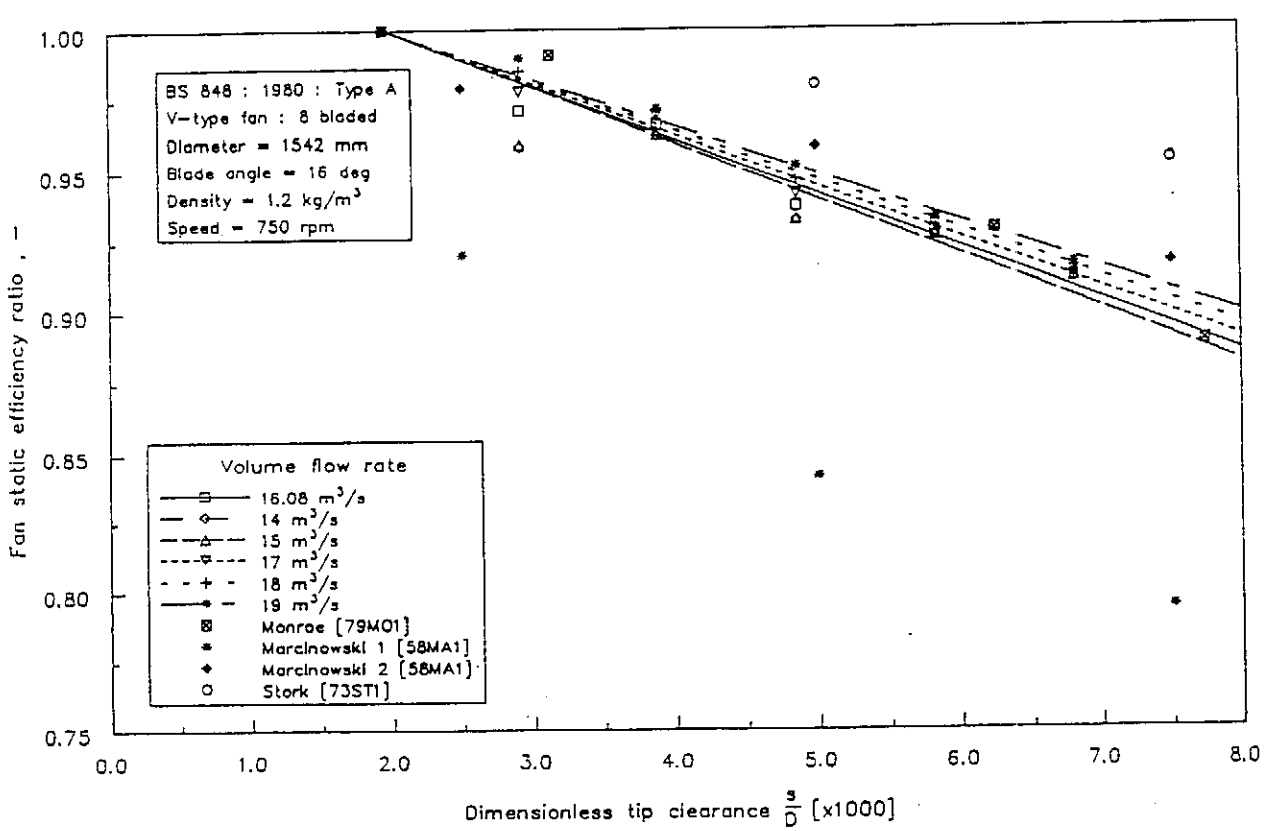

Figure 4.7: The effect of tip clearance on fan static efficiency

of an axial flow fan installed in a system in which only the tip clearance is adjusted. A complete derivation of the method employed to eliminate the inherent shortcomings of Monroe's work is attached as section B.2.1. Stork [73ST1] presented their data in tabular form. Data for the worst possible cases are selected from their tables (maximum values for drop in fan static pressure and efficiency). These are presented as data points on figures 4.6 and 4.7. Their recommendations appears to underestimate the tip clearance effect for both pressure and efficiency effects. Marcinowski [58MA1] investigated the influence of tip clearance on two different fans for which two markedly different results are obtained (figures 4.7). He only stated the influence of tip clearance on fan efficiency. Results from his second set of data (for profiled and twisted blades) correlate well with the findings of this study, but a changed tip clearance resulted in much reduced values for his first set of data (for untwisted steel blades). This accentuates the sensitivity of tip clearance effects on the type of fan model under investigation.

4.2.2 Solid disc

Preliminary tests concerned with the velocity profiles downstream from the fan impeller suggested severe reversed flow conditions at the fan hub. The magnitude of this phenomenon increases progressively with an increase in the fan static pressure, associated with a decrease in fan static efficiency (figures A.4.4 to A.4.6).

In an attempt to replace the region of reversed flow with a region of zero flow, a 445 mm diameter by 2 mm thick mild steel solid disc is attached either upstream or downstream of the fan impeller of a V-type fan. The change in fan performance achieved by the installation of the solid disc is presented as ratios of reduced to reference fan performance values. A performance ratio in excess of 1 is therefore indicative of an improved fan performance where fan static pressure and efficiency are concerned, and of a reduction in fan performance for fan power consumption.

Figures A.2.5 and A.2.6 reveals that there is a fan static pressure advantage in installing an upstream disc for volumetric flow rates below 11,2 m^3/s. Note that the reference curves refer to the fan charateristic curves determined for ideal operating conditions, while the reduced curves are the characteristics once changes have been made to the system. The corresponding fan static efficiency ratio in figure A.2.8 approaches a value of 1 at a volumetric flow rate of 12,2 m^3/s. Both these volumetric flow rates are well below the point of maximum fan static efficiency for the ideal fan of approximately 16 m^3/s. A fan is normally selected to operate in the vicinity of the point of maximum fan static efficiency to reduce the power input for the same operating conditions. The implications of these observations are that the installation of a solid disc upstream of the rotor does not result in any marked improvements in fan performance. If it is suspected that the system is operating near the stall region, it could be advisable to install an upstream disc which

becomes effective under these conditions.

The same disc is installed downstream of the fan rotor with much improved results. The fan static pressure ratio equals 1 at 20 m^3/s which correspond to the point where the fan static efficiency approximates 1. At a volumetric flow rate of 16 m^3/s the improvement in fan static pressure is 8,2 N/m^2 and in fan static efficiency 1,66%. The fan performance improves exponentially from this point downwards for lower volumetric flow rates. The implication is that the fan performance of a V-type fan is improved by attaching a solid disc to the rotor downstream of the fan.

4.2.3 Inlet grid

The inlet grid used to simulate the safety grid in the full scale unit, is a scaled version of the actual safety grid (figure F.2.7). The only difference is that the mesh itself is not included as the effect of the mesh can be calculated from existing data (see section B.4.2). These calculations should be representative of the losses experienced by the fan in the cooling system as the mesh itself does not contribute to deviations from a uniform one-dimensional velocity profile approaching the fan. The same can not be assumed for the effect of the mesh supporting structures. Figure F.2.7 indicates that the positioning of the supporting beams result in an asymmetric velocity profile.

The data pertaining to tests performed with the inlet grid in position are presented as figures A.2.11 to A.2.14. The most relevant of these figures is figure A.2.12 which indicates the dependency of the total pressure loss coefficient on volumetric flow rate through the fan. From these coefficients it is apparent that the effect of the inlet grid cannot be predicted accurately by measuring the pressure loss under ideal conditions (with no fan installed). An explanation for the downward trend observed in the loss coefficient is attached as section B.3.4. The loss coefficients predicted theoretically employing the bulk method (section B.4.1), underestimates the actual effect of the inlet grid on the fan performance. The summation method (section B.4.1) approaches the measured inlet grid effects at higher volumetric flow rates (in excess of 20 m^3/s, but also underestimates these effects in the practical range of fan application (typically in the vicinity of 16 m^3/s for this case).

An inherent assumption associated with both methods of theoretical prediction of the total pressure loss across the inlet grid, is that the loss coefficient (K) is independent of Reynolds number. From figure A.2.12 and the fact that the Reynolds number is directly related to the volumetric flow rate in this case, this is clearly not true. The effective total pressure loss coefficient can much better be described by assuming a polytropic resistance ($K = Av^n$) or by an inverse power law ($K = A + \frac{B}{v}$). The reader is referred to section 2.7 for a detailed description of these phenomena.

4.2.4 Walkway and support beams

The walkway and the structure supporting the fan and walkway (figures F.2.8 to F.2.10) is installed directly downstream of the fan rotor. The flow field immediately downstream of the fan rotor is highly distorted. The effect of the presence of the walkway and supporting beams in this region is investigated by adjusting the distance between them and the fan rotor. The walkway is removed to isolate its effect from the effect of the beams.

The theoretical total pressure loss coefficients are predicted according to the proposals of Stork fan company [85ST1] (section B.4.3). The summation method is used as alternative to predict pressure loss coefficient. This method is described in section B.4.3.

Results from tests pertaining to the effect of various distances between the fan rotor and the supporting beams (including the walkway), are presented as figures A.2.15 to A.2.18. From these it can be concluded that their presence results in an additional loss in system static pressure of up to 70% of the dynamic pressure component based on the fan inlet shroud diameter. As in the case of the inlet grid (section 4.2.3), it is found that the proposed method of measuring the ideal resistance of the structure is not advisable. This method results in an ideal pressure loss coefficient well below the effective measured pressure loss coefficients. The same tendency of an exponential increase in effective loss coefficient is noted. An attempt to correlate these loss coefficients according to either a polytropic resistance or an inverse power law failed.

The theoretical predictions made by employing the bulk method are compared to the experimental results with the following conclusions:

- Theory underestimates the effect of the supporting structure and walkway if they are located relatively far from the fan rotor (292 mm between the centerline of the rotor and the nearest point of the I-beams).
- Theory realistically approximates the experimental results if the support structure is located at 142 mm and 125 mm downstream of the fan rotor. This statement is true for volumetric flow rates in excess of that for maximum fan static efficiency (approximately 16 m^3/s). If the volumetric flow rate is below this point, the measured effective loss coefficient exceeds the predicted values.
- Theory overestimates the effect if the support structure (including the walkway) is located 57 mm downstream of the fan rotor.

The summation method results in a combined pressure loss coefficient of 0,19. This value is only representative of the effective pressure loss coefficient for a downstream distance between rotor and supporting beams of 292 mm.

The system power requirements do not change appreciably with a change in the downstream location of the support structure. The result is that the change in system static efficiency is directly related to the change in system static pressure (figures A.2.17 and A.2.18). Care should therefore be taken when referring to system static efficiency (section 4.2).

Figures A.2.19 to A.2.21 represent results from tests where only the support beams, excluding the walkway, are installed. Measurements are made with the beams installed in two different locations. The distances between the rotor centerline and the I-beams nearest to the rotor are 125 *mm* and 292 *mm* respectively.

The same method of data reduction as for the case combining the influence of the walkway is utilized. The results are not compared to ideally measured total pressure loss coefficients as these are found to be inapplicable if the fan is present. Figure A.2.20 compares the measured effective loss coefficients to the values predicted using the bulk method suggested by Stork [85ST1].

It is apparent that the theory underestimates the effect of the support beams by a bigger margin than for the support beams and the walkway combined. The bulk method prediction results in reasonable values for the combined case with the structure installed 125 *mm* behind the fan rotor. It underestimates the influence of only the support beams. The summation method predicts a pressure loss coefficient of only 0,09. This corresponds to the bulk method prediction related to a downstream distance between fan rotor and support beams of between 142 *mm* and 292 *mm*.

Referring to figures A.2.16 and A.2.20, it can be seen that the overall reduction in system pressure due to the supporting beams exceed the same for the case combining the effect of the walkway. This contradicts the expected phenomenon, namely that additional resistances will necessarily result in an increase in pressure loss. It can only be related to the irregular nature of the flow immediately downstream of the fan rotor. The result is probably related to a larger kinetic energy flux coefficient (α) at system outlet for the bare supporting beams than for the combined case. When the increase in kinetic energy loss exceeds that due to resistance, the above mentioned effect is achieved.

The system power consumption for the two locations behind the rotor remains approximately the same. The previous observation that the change in system static efficiency is directly related to the change in system static pressure is again valid. The reduction in maximum system efficiency is of the same magnitude as for the combined case. It is concluded that very little, if any, energy savings is achieved by removing the walkway from the support beams, or by moving the complete structure to a position further downstream from the rotor.

4.2.5 Heat exchangers

The energy supplied by the fan to air stream is primarily used to overcome the pressure drop associated with the heat exchangers. This pressure drop constitutes the largest single energy consuming component in the system, implying that it is vital to predict its effect accurately. The heat exchangers used in the scale model are presented in figures F.2.3 and F.2.4.

The results pertaining to the effect of heat exchangers installed in an A-frame are attached as figures A.2.23 to A.2.26. The contents of this section focuses on the inlet loss effects, meaning that no windwalls are installed for the range of tests relevant to this section. The basis of comparison used is the pressure loss coefficients referred to the average velocity through the fan inlet shroud. The loss coefficients presented in figure A.2.24 are determined according to the method described in sections B.3.5 and B.3.6.

The theoretical predictions of the oblique flow pressure differential across the heat exchangers are based on experimental data for normal flow pressure loss coefficients. The loss coefficients for normal flow are related to the specific design and orientation of the finned tubes, and are difficult to predict accurately. The effect of the obliquity of the flow is accounted for by utilizing the Mohandes [79MO2] proposals. A detailed description of his proposals is given in section 2.8.

The experimental data for ideal flow conditions (refer to figure A.2.24) is generated by measuring the difference between inlet total pressure (inside the settling chamber) and atmospheric pressure. The components installed for these tests are either a single or double heat exchanger and the fan inlet shroud. The measured pressure loss coefficient includes the kinetic energy dissipated in the free atmosphere at the outlet from the heat exchanger. The kinetic energy flux coefficient (α) is assumed to equal 1 for both the single and double heat exchanger arrangements.

The energy losses at a volumetric flow rate of 16 m^3/s through the system (corresponding to an average velocity of 2,54 m/s through the finned tubes) are 66,00 W and 61,70 W for the single and double heat exchangers respectively. The minimum kinetic energy dissipated in the atmosphere once the fan is installed, has the same values. Any deviations from the previous energy losses are attributed to a kinetic energy flux coefficient in excess of one. This is as a result of flow distortions inside the A-frame caused by the plenum and is included as integral part of the pressure loss coefficient (refer to section B.3.5).

The effective pressure loss coefficients, determined from the change in fan characteristic curves (section B.3.6), for single and double heat exchanger arrangements are presented in figure A.2.24. The total pressure inside the fan plenum is assumed equal to the static pressure at the fan outlet operating under ideal conditions (reference operating conditions).

This correlates with common fan design practice (refer to section B.3.6). The kinetic energy flux coefficients at the outlet from the finned tubes are $\alpha_{HX_o} = 1{,}15$ and $\alpha_{HX_o} = 1{,}04$ respectively for the single and double heat exchangers. The actual measured velocity distributions for these two cases are presented as figures A.4.7 and A.4.8. The velocity profiles presented in these figures relate to an atmospheric fan inlet total pressure. It corresponds to volumetric flow rates of 23,0 m^3/s and 19,2 m^3/s respectively for the single and the double heat exchanger arrangements. Deviations from the ideal is attributed to the distorted flow conditions caused by the fan and the A-frame plenum at the inlet to the heat exchangers. As expected, the higher pressure differential across the double heat exchangers results in a more uniformly distributed velocity profile at heat exchanger outlet than for the lower pressure differential associated with the single heat exchangers.

In comparison, it can be deduced that all three theoretical and effective pressure loss coefficients exhibit a good correspondence with each other. The difference between the effective and the ideal pressure loss coefficients for the single heat exchanger installation increases at lower volume flows. The same does not occur for the double heat exchanger arrangement. Referring again to figure A.2.24, this means that the additional energy losses due to flow distortion at the outlet from the heat exchanger, progressively increases with a decrease in volumetric flow rate. At a volumetric flow rate of 16 m^3/s the difference between the theoretical and the effective energy losses are 218,45 W and 133,89 W respectively. The fan power consumption at 16 m^3/s is 5 850 W and 5 950 W respectively for the single and the double heat exchanger installations. This constitutes a 3,70% and 2,25% energy loss as a percentage of the input power.

Unlike the inlet safety grid, support beams and walkways, the pressure loss coefficients determined under ideal conditions compare favorably with the theory. At lower volume flow rates, the theoretically determined pressure loss coefficients underestimate the ideally determined experimental values. This phenomenon is associated with the decrease in pressure differential across the heat exchangers at lower entrance velocities. It means that the kinetic energy flux coefficient (α) increases with a decrease in volumetric flow rate. The energy loss coefficient for the theoretical values remains one, even for low volumetric flow rates [90VA1]. The difference is that the facility used to generate the ideal data incorporates the fan inlet shroud, causing an air jet to enter the plenum. The theoretical model assumes an uniform one-dimensional velocity profile approaching the A-frame arrangement.

4.2.6 Windwalls (Downstream losses)

The reason for adding the windwalls (figures F.2.1) to the test facility is to simulate the line of symmetry present between two adjacent A-frames in the full scale heat exchanger array. Van Aarde [90VA1] reports on the effect of the outlet velocity profile from the

cooling unit.

The downstream losses (losses associated with the windwalls) consist of the two components discussed in section 2.9. These are the jetting losses (K_{dj}) and the losses the kinetic energy in the outlet from the unit (K_o).

The eventual energy leaving an industrial cooling unit, which is dissipated in the free atmosphere, is the kinetic energy exiting the cooling unit at the apex between two adjacent A-frame modules. This loss is combined with the other downstream losses and not excluded from the effective loss coefficient (section B.3.7). The velocity profile at the outlet plane from the unit (figures A.4.9 and A.4.10) is integrated according to equation (2.58) to obtain the kinetic energy flux coefficient. The calculated value for α, based on the free outlet area from the unit, is 1,61. It compares favorably with values in the vicinity of 1,5 reported by Van Aarde [90VA1]. The corresponding value for α, based on the fan inlet shroud diameter, is 0,16 for an atmospheric total pressure inside the settling chamber. This is less than unity due to the area ratio between the fan inlet shroud and the exit area from the heat exchangers. It is important to specify the operating conditions at which the velocity profile is determined as they influence the velocity profiles at the various measuring planes (refer to figures A.4.9 to A.4.10). The difference between α at unit exit and the curve for the effective loss coefficient presented in figure A.3.6 is attributed to the jetting losses. Jetting losses occur due to the flow turning and the viscous forces acting on the flow in the region between two adjacent A-frame modules.

The overall downstream loss coefficient for the scale model with windwalls installed is lower than the value predicted by Van Aarde (refer to figure A.3.6). The extrapolation process employed to make these predictions (section B.4.5) is a probable cause of error. Also the flow distortion inside the plenum is not present in the test facility used by Van Aarde to generate his experimental data.

The power consumption of the system does not change appreciably between installations where the windwalls are included or removed (refer to figure A.3.9). This means that the variation in system static efficiency noted in figure A.3.8 is almost exclusively due to the change in system pressure (figure A.3.5).

4.3 Combined effects

The ultimate goal of this project is to ensure a better understanding of the governing mechanisms present when flow distorting components are installed in close proximity of an axial flow fan. In the preceding part of the report, the effect of individual components on the system performance are investigated. The results of these lead to the expectation that the various components influence each other if installed simultaneously in a system.

The combined effect of different components is investigated and reported on in this section.

4.3.1 Inlet grid, walkway and support beams

The effect of combinations of the inlet safety grid and support beams with walkway installed is investigated. Two different reference installation types are employed to measure these effects. They are

Type A The reference curve is determined from the facility with only the fan rotor and inlet shroud installed. The walkway and support beams are added to this configuration to determine their respective influences.

Type B The reference curve for the second method is determined with not only the fan rotor and inlet shroud installed, but also a double set of heat exchangers and the windwalls. This is an approximation of an actual industrial unit.

The results from these test methods are presented as figures A.3.2 and A.3.7 respectively.

Figure A.3.2 reveals that for a type A installation the theoretically predicted pressure loss coefficient for the inlet safety grid is less than the effective loss coefficient for the same determined according to section B.3.3. Comparing the corresponding loss coefficients determined with type B the installation (figure A.3.7) the results exhibit the opposite tendency. The characteristics of the pressure loss coefficient for volumetric flow rates between 8 m^3/s and 20 m^3/s also changes. The coefficient increases exponentially as the volume flow rate (which is directly proportional to the Reynolds number) decreases in the type A installation. The type B installation produces a pressure loss coefficient which remains almost constant with a change in volume flow rates of between 8 m^3/s and 20 m^3/s.

The pressure loss coefficient associated with the walkway and supporting beams has a maximum of approximately 0,55 at a volumetric flow rate of 13 m^3/s for a type A installation. The same coefficient measured in a type B installation, has a local minimum of 0,18 at 10 m^3/s and a maximum of 0,31 at 15,5 m^3/s (refer to figure A.3.7). The theoretically predicted value for the loss coefficient of 0,32 underestimates the effective loss coefficient determined with the type A installation for the complete range of volumetric flow rates of between 8 m^3/s and 20 m^3/s. It overestimates the pressure coefficient for the same volumetric flow rate range if data is generated utilizing the type B installation.

The data for the combined effect of the inlet safety grid and the walkway attached to the supporting beams is compared to the results of the individual components numerically

added together. Figure A.3.2, representative of a type A installation, reveals that the combination of these components results in a slight increase in effective pressure loss coefficient from the tests pertaining to only the walkway and support beams (figure A.3.2). This means that the pressure loss coefficient determined by adding isolated effects of the inlet grid and the walkway attached to the support beams, is substantially larger than the actual measured value (0,85 as opposed to a measured loss coefficient of 0,60). In contrast, the maximum deviation in pressure loss coefficient between results from the type B installation and their numerically added counterparts is 0,025 (figure A.3.7).

The system power consumption for different configurations in both types of tests remains approximately constant (figures A.3.4 and A.3.9). This implies that the variations in system efficiencies between different configurations, presented in figures A.3.3 and A.3.8, are directly related to the change in excess system static pressure (figures A.3.1 and A.3.6).

The discussion of results in the preceding part of this section serves to accentuate the difference in character between flow distorting components installed in a fan system which exhaust directly to the free atmosphere, as opposed to a system which is connected to an A-frame plenum and windwalls. It highlights the danger of applying total pressure loss coefficients, determined for ideal flow conditions, to a fan installation where the system effect is evident.

4.4 Overall analysis

The overall analysis is performed to compare the theoretically predicted pressure losses to the actual measured values for the complete system. The complete system comprises the following

- fan rotor
- fan inlet shroud
- walkway
- support beams at 125 *mm* behind the rotor
- double heat exchangers
- windwalls

The tip clearance is not changed from the ideal (reference) fan tests to the system characterization.

The pressure loss coefficients based on empirical correlations for the individual components, are presented as figures 4.8 and 4.9. Note that the loss coefficient of the inlet

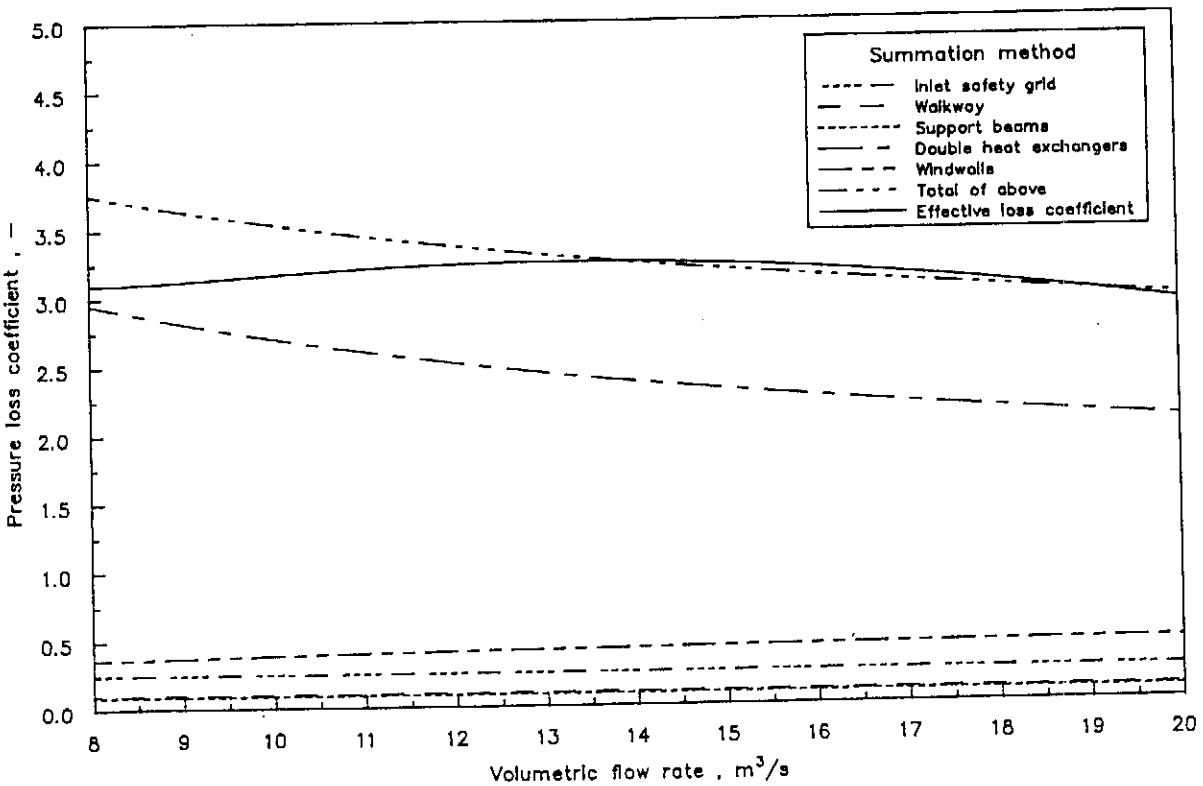

Figure 4.8: Theorectical vs. experimental pressure loss coefficients : Summation method

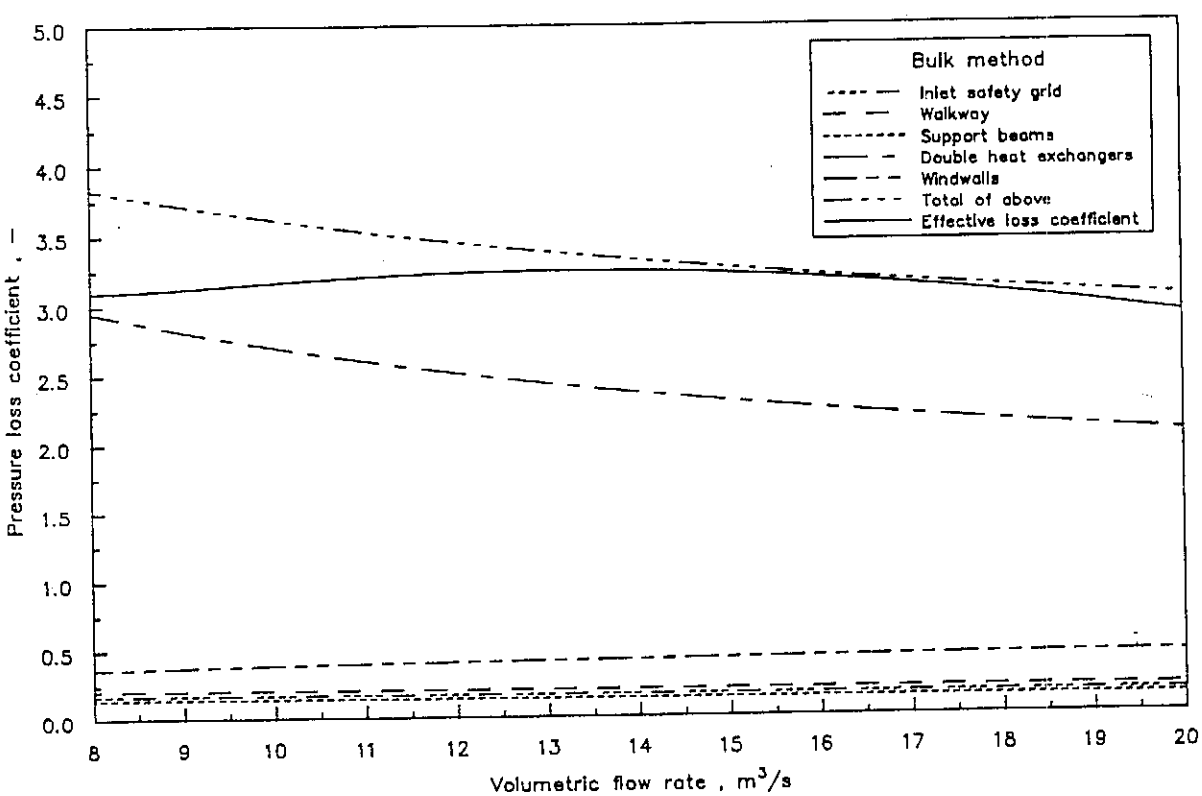

Figure 4.9: Theorectical vs. experimental pressure loss coefficients : Bulk method

shroud is incorporated into both the ideal fan and the system characteristics. It is incorrect to add it to the other resistances constituting the overall system resistance.

The results presented in figures 4.8 and 4.9 relate to the summation and the bulk methods respectively, applied as theory to predict effects attributed to the inlet grid, the walkway and the support beams (refer to section B.4.1).

The heat exchanger losses are accounted for according to the assumptions listed in section B.3.6 where the total system resistance curve is matched to the fan static pressure. An important implication of this practice is that the kinetic energy exiting the fan operated under ideal conditions is discarded. Alternatively it can be envisaged that the static pressure at the fan outlet for ideal operating conditions (reference tests) is assumed to be the effective total pressure available inside the fan plenum. It corresponds to common design practice. The downstream losses, determined according to the method described in section B.4.5, include the kinetic energy at the exit from the cooling unit (between the apexes of two adjoining A-frame arrays).

The summation and bulk method theoretical predictions for overall pressure loss coefficient correspond well with each other. The maximum difference between the two methods is 2,75% over the complete practical volume flow range of 8 m^3/s to 20 m^3/s. Analogously, the theoretical values equal the effective pressure loss coefficients at a volumetric flow rate of 16 m^3/s (corresponding to the maximum efficiency of the fan)

No margin for additional pressure losses present in the full scale cooling unit remains. These losses include inlet losses of air approaching the complete unit, as well as the effect of cross-flow patterns at the inlet to the fan shroud. Both these effects result in an increase in the kinetic energy flux coefficient (α_{F_o}). Equation (B.75) represents the effect of a change in α_{F_o} on the overall system performance. The increased kinetic flux coefficient relates to less available energy to overcome the pressure differential associated with the remainder of the system. This means volume flow rate and system efficiency decrease to accommodate increased power requirements. A change in kinetic energy at fan outlet also influences the assumption that the ideal static pressure at fan outlet equals the actual total pressure inside the fan plenum.

Chapter 5 - Conclusions and recommendations

5.1 Conclusions

A parametric study is performed in appendix E to illustrate the application of fan characteristic curves to off-design operation. The effect of a change in the system resistance is investigated by using typical system resistance curves for a dephlegmator and condenser application of a full scale condensing unit. The loss coefficients of the resistances for these two units are tabulated in table E.3. The effect of tip clearance, a solid disc and of different numbers of fan blades are investigated by assuming the input power to the fan shaft to remain constant at its reference value.

The minimum adjustment for tip clearance ratio $\left(\frac{s}{D}\right)$ of the scale model is 0,19%. This ratio is found to result in the best fan performance characteristics (figures 4.6 and 4.7). The assumption by Stork [85ST1] that the fan performance is not affected by a variation in tip clearance ratio smaller than 0,5% or that the tip clearance ratio should not be smaller than 0,33% (type of installation not specified) is found not to be valid for the present installation. The improvements in delivered fan pressures are 4,66% and 4,32% for the dephlegmator and the condenser respectively (refer to table E.10). The corresponding improvements in volume flow are 2,6% and 2,4% respectively. These results are achieved by decreasing the tip clearance ratio from 0,45% to 0,19%. The corresponding improvements in fan static efficiency are 7,4% and 6,8% respectively. The method used to compare the different results is presented in section E.3. It is based on an assumption that the shaft power input to the fan remains constant for the different fan configurations under investigation e.g. for different fan tip clearance settings.

The 445 mm diameter solid disc (corresponding to a diameter ratio of 0,289) is installed both upstream and downstream of the fan rotor. In the normal operating range (between 14 m^3/s and 20 m^3/s), it is found that the disc does not exhibit significant improvements in fan performance if installed upstream of the fan rotor (figures A.2.6 to A.2.10). The same disc, attached to the downstream side of the rotor, results in considerable improvements in the fan static pressure and efficiency. The method of section E.3 is again employed to determine the effect of the upstream rotor. Improvements of 2,31% and 1,85% in fan static pressure and of 1,31% and 0,85% in volume flow rate for the dephlegmator and condenser units respectively are achieved (table E.12). The corresponding improvements in fan static efficiency are 3,65% and 2,17% respectively.

The effect of different numbers of fan blades is investigated by applying the method of constant shaft power to the characteristic curves of S-type fans. These characteristics are supplied by the manufacturer. It is obvious that should the number of blades be reduced, the fan performance also reduces (refer to table E.16). An increase in number of blades

from 8 to 9, results in a marginally better fan performance with improvements in any single parameter (volumetric flow rate, fan static pressure or fan static efficiency) of less than 1%.

The system effect on flow resistances is illustrated by comparing the theoretically predicted pressure loss coefficients to actual measured values. A distinction is made between distortive flow resistances (e.g. inlet grids and walkways) and system resistances (e.g. heat exchangers and windwalls).

The classical approach of predicting pressure loss coefficients (assuming $\Delta p = K \frac{1}{2}\rho v^2$) underestimates the influence of auxiliary flow resistances both upstream and downstream of the fan rotor. These flow resistances comprise an inlet grid upstream from and a walkway and support beams downstream from the fan rotor. The inaccuracies in theoretical and experimental predictions of pressure loss coefficients (refer to figures A.2.16, A.2.20 and A.2.24) highlight the fact that the fan performance in a specific installation should ideally be determined experimentally on a scale model of the complete full scale unit. The common practice of testing only the fan rotor and inlet is unacceptable.

The characteristics of the pressure loss coefficient of a specific flow resisting component depend upon the presence or absence of other such components. Section 4.3.1 relates to the effect of changes in the characteristics of the pressure loss coefficients associated with the inlet grid, the walkway and the support beams installed either separately or simultaneously (see also figures A.3.2). The effect of adding the heat exchangers and windwalls to the previous configurations, is also evaluated in section 4.3.1 (figures A.3.6 and A.3.7). The final conclusion is that the characteristics of the pressure loss coefficient for each configuration is different. The conclusion made in the previous paragraph, that a scale model of the complete proposed unit needs to be investigated, is once again accentuated.

The pressure loss coefficients associated with the finned tube bundles are approximated by both theoretical and experimental predictions for oblique flow. The assumption incorporated to obtain the data presented in figure A.2.24 is that static pressure at the fan outlet measured for the ideal reference test equals the total pressure generated inside the fan plenum (section 4.2.5). The ideal reference test is performed with only the fan rotor and inlet shroud installed. It is obvious that, although a relatively good approximation is achieved for the fan installation investigated in this study, this assumption depends upon the specific fan application. The assumption is influenced by changes in the velocity distributions both at the fan inlet and outlet.

The results pertaining to the overall system (figures A.3.5 to A.3.9) reveal that, for the same assumption as stated in the previous paragraph, the predicted and measured losses almost coincide at optimum fan static efficiency. Additional losses not accounted for in the prevailing tests of this thesis, but present in an actual mechanical draft air cooled heat exchanger, include inlet pressure losses due to air approaching the unit, cross-flow at the

fan inlet and smaller heat exchanger outlet areas in the dephlegmator units. All these losses are related to a change in velocity distribution inside the fan plenum, resulting in possible deviations from the assumption that the total pressure inside the plenum equals the static pressure at outlet from the ideal reference test for the fan rotor.

5.2 Recommendations

Based on the conclusions of the previous section, the following topics are recommended for future research

- Investigations into the effect of solid discs of different diameters installed for a range of different types of axial flow fan rotors.
- Research to determine the effect of changes in plenum dimensions and configuration on the assumption that the total pressure inside the fan plenum equals the static pressure at fan outlet when tested under ideal operating conditions.
- Predictions of the influence of the maldistribution of air flow, resulting from the system effect, on the performance of the heat transfer process for non-isothermal operation of the unit.

Results from the suggested research topics will complete a data base which can be used in the design of future mechanical draft heat exchanger units.

The results from this research project highlights the fact that a reduction in the tip clearance of the fan results in a noticable improvement in the overall performance of the full scale cooling unit. It is also found that the performance of the system can be improved by installing a solid disc to the downstream side of the rotor. An increase in the number of fan blades from 8 to 9 leads to a marginally better system performance. All these conclusions are based on the assumption that the current electric motors and gearboxes are used, i.e. that the available power input to the fan remains the same. Another method of improving the system is to either remove certain flow resisting components, or to rearrange their relative positions within the cooling unit. These involve structural changes to the exixting unit and are expensive.

References

37KE1 Keller, C., adapted by Marks, L.S., The theory and performance of axial flow fans, First edition, McGraw-Hill, May 1937.

46AS1 American Society of Mechanical Engineers, Test code for fans, PTC II, 1946.

46RO1 Rouse, H., Elementary mechanics of fluids, John Wiley and Sons, New York, USA, 1946.

50KA1 Kays, W.M., Loss coefficients for abrupt changes in flow cross section with low Reynolds number flow in single and multiple-tube systems, Trans. of the ASME, Vol. 72, pp. 1067-1074, Nov. 1950.

58MA1 Marcinowski, H., The influence of impeller gap in free discharging axial-flow fans without guide wheel, Voith-Forschung u. Konstruktion, No. 3, 1958, (referenced by [73EC1] and [83GE1]).

61JO1 Jorgensen, R.(ed.), Fan engineering, Buffalo Forge Company, Sixth edition, New York, USA, 1961.

66VD1 Verein Deutscher Ingenieure, VDI-Richtlinien - Abnahme- und Leistungsversuche an Ventilatoren, VDI 2044, Berlin und Köln, 1966.

70LA1 Lakshminarayana, B., Methods of predicting the tip clearance effects in axial flow turbomachinery, Trans. of the ASME, Journal of basic engineering, Vol. 107, pp. 354-364, Sep. 1970.

72AS1 American Society of Heating, Refrigerating and Air-Conditioning Engineers, Inc., Handbook of fundamentals, Atlanta, USA, 1972.

72BA1 Bass, R.M., The design of a low weight high performance centrifugal fan for a tracked hovercraft, Comments by F.O.J. Otway, Conference on fan technology and practice, Organized by the Institution of Mechanical Engineers, pp. 7-14, London, 18-19 April 1972.

72CO1 Cohen, H., Rogers, G.F.C. and Saravanamuttoo, H.I.H., Gas turbine theory, SI Units, Second edition, Longman, 1972.

72ES1 Engineering Sciences Data Unit, Pressure drop in ducts across round-wire gauzes normal to the flow, Item no. 72009, London, June 1972.

72GU1 Gunter, A.Y. and Shipes, K.V., Hot air recirculation by air coolers, Chemical engineering progress, Vol. 68, No. 2, pp. 49-58, February 1972.

72HA1 Hay, N. and Taylor, S.R.G., The effects of vehicle cooling system geometry on fan performance, Conference on fan technology and practice, Organized by the Institution of Mechanical Engineers, pp. 176-192, London, 18-19 April 1972.

72LA1 Lambert, P.C., Cowan, G.H. and Bott, T.R., Flow characteristics in a box-shaped plenum chamber associated with an air-cooled heat exchanger, United Kingdom Atomic Energy Authority, Research Group, Harwell, Berkshire, UK, 1972.

73EC1 Eck, B., Fans - design and operation of centrifugal, axial-flow and cross-flow fans, Pergamon Press, Germany, 1973.

73FO1 Fox, R.W. and McDonald, A.T., Introduction to fluid mechanics, John Wiley and Sons, USA, 1973.

73ST1 Ventilatoren Stork Hengelo, General applications for E-type fans, V.691181, 73-08, 1973.

73ST2 Stone, R.D. and Wen, S.H., Airflow characteristics of built-up fan plenums and performance of airflow correction devices, ASHRAE Semi-annual Meeting, Chicago IL., 28 January - 1 February 1973.

74AM1 Air Moving and Conditioning Association, Laboratory methods of testing fans for rating purposes, AMCA Standard 210-74, 1974.

75AS1 American Society of Heating, Refrigerating and Air-Conditioning Engineers, Laboratory methods of testing fans for rating purposes, ASHRAE Standard 51-75, 1975.

72ES1 Engineering Sciences Data Unit, Fluid forces on lattice structures, Item no. 75011, London, August 1975.

76ZU1 Zucrow, M.J. and Hoffman, J.D., Gas dynamics, Volume 1, John Wiley and Sons, USA, 1976.

77OS1 Osborne, W.C., Fans, International series on heating, ventilation and refrigeration, Volume 1, Pergamon Press Ltd., 1977.

77DA1 Daugherty, L.D. and Franzini, J.B, Fluid mechanics with engineering applications, Seventh edition, McGraw-Hill, Tokyo, Japan, 1977.

78DA1 Daly, B.B., Woods practical guide to fan engineering, Woods of Colchester Ltd., Third edition, 1978.

78DI1 Dixon, S.L., Fluid mechanics - thermodynamics of turbomachinery, Metric units, Third edition, William Clowes (Beccles) Ltd., Great Britain, 1978.

78EA1 Eastop, T.D. and McConkey, A., Applied thermodynamics for engineering technologists, S.I. Units, Longman, 1978.

78RU1 Russell, C.M.B. and Berryman, R.J., The calculation of pressure losses in air-cooled heat exchanger air inlets and plenum chambers, American Society of Mechanical Engineers, Heat transfer division, HTD vol. 96, publ. by ASME, New York, USA, pp. 429-434, 1978.

78VA1 Van Wylen, G.J. and Sonntag, R.E., Fundamentals of classical thermodynamics, SI Version, John Wiley and Sons, 1978.

78YO1 Yocum, A.M., The effects of design and operating variables on the response of an axial flow fan to inlet flow distortions, Pennsylvania State University, Institute for Science and Engineering, Applied Research Laboratory, 1978.

79HU1 Hudson Products Corporation, Air cooled heat exchangers - a proven means for cooling in the process industry, Houston, Texas, USA, 1979.

79MA1 Massey, B.S., Mechanics of fluids, 4th edition, Van Nostrand Reinhold Co., London, 1979.

79MO1 Monroe, R.C., Improving cooling tower fan system efficiencies, Combustion, May 1979.

79MO2 Mohandes, M.A., The flow through heat exchanger banks, PhD thesis, Oxford University, 1979.

79NO1 Nowakowski, J.K., Pressure losses in the inlet and outlet channels of high-pressure single- and two-stage axial-flow fans, Proceedings of the sixth conference on fluid machinery, Hungary, pp. 760-769, 1979.

80AS1 American Society of Mechanical Engineers, Performance test codes - General instructions, PTC 1, 1980.

80AS2 American Society of Heating, Refrigerating and Air-Conditioning Engineers, Inc., Handbook and product directory, Systems, Atlanta, USA, 1980.

80BE1 Benedict, P.B., Fundamentals of pipe flow, John Wiley and Sons, USA, 1980.

80BE2 Beard, R.A., Truck radiator technology, Part II, Product application technology, Heat Transfer Division, Covrad Ltd., Coventry, England, 1980.

80BS1 British Standards Institution, Fans for general purposes, Part 1, Methods of testing performance, BS 848, 1980.

81BA1 Balje, O.E., Turbomachines - a guide to design, selection and theory, Wiley and Sons, New York, USA, 1981.

81BS1 British Standards Institution, Measurement of fluid flow in closed conduits, Section 1.1, Specification for square-edged orifice plates, nozzles and venturi tubes inserted in circular cross section conduits running full, BS 1042, 1981.

81GR1 Graham, J.B., Fan selection and application considerations, Symposium proceedings on power plant fans - state of the art, Indianapolis, USA, 14-16 Oct. 1981.

82CO1 Cory, W.T.W., Fan performance testing and the effects of the system, International conference on fan design and applications, Guildford, England, Sponsored by BHRA Fluid Engineering, 7-9 September 1982.

82IS1 International Organization for Standardization, Measurement of fluid flow in closed conduits, Section 2.1, Method using pitot static tubes, ISO 3966-1977, 1982.

82PE1 Peacock, R.E., A review of turbomachinery tip gap effects, Part 1 : Cascades, Int. journal of heat and fluid flow, Vol. 3, No. 4, pp. 185-193, Dec. 1982.

83BS1 British Standards Institution, Measurement of fluid flow in closed conduits, Section 2.1, Method using pitot static tubes, BS 1042, 1983.

83BS2 British Standards Institution, Measurement of fluid flow in closed conduits, Section 2.2, Method of measurement of velocity at one point of a conduit of circular cross section, BS 1042, 1983.

83BS3 British Standards Institution, Measurement of fluid flow in closed conduits, Section 2.3, Methods of measurement in swirling or asymmetric flow conditions in circular ducts by means of current-meters or Pitot static tubes, BS 1042, 1983.

83CO1 Coward, C.W., A summary of pressure loss values for various fan inlet and outlet duct fittings, ASHRAE Transactions, Vol. 89, Part 1, 1983.

83GE1 General Electric, Fans - axial flow, Fluid flow division, section 409.3, April 1983.

83OC1 O'Connor, J.F., The system effect and how it changes fan performance, ASHRAE Transactions, Vol. 89, Part 1, 1983.

83PE1 Peacock, R.E., A review of turbomachinery tip gap effects, Part 1 : Rotating Machinery, Int. journal of heat and fluid flow, Vol. 4, No. 1, pp. 3-16, Mar. 1982.

83WA1 Wallis, R.A., Axial flow fans and ducts, John Wiley and Sons, New York, USA, 1983.

84BS1 British Standards Organization, Measurement of fluid flow in closed conduits, Section 1.2, Specification for square-edged orifice plates and nozzles (with drain holes, in pipes below 50 mm diameter, as inlet and outlet devices) and other orifice plates and Borda inlets, BS 1042, 1984.

84BS2 British Standards Organization, Measurement of fluid flow in closed conduits, Section 1.4, Guide to use of devices specified in Sections 1.1 and 1.2, BS 1042, 1984.

84DA1 Daly, B.B., Interaction between fan and the system, Installation effects in ducted fan systems ,Institution of Mechanical Engineers, Conference publications, No. C110/84, pp. 1-7, 1984.

84DE1 Deeprose, W.M. and Smith, T.W., The usefulness of BS 848 Part 1:1980 in establishing the installed performance of a fan, Institution of Mechanical Engineers, Conference publications, No. C115/84, pp. 9-20, 1984.

84MO1 Mohandes, M.A., Jones, T.V. and Russell, C.M.B., Pressure loss mechanisms in resistances inclined to an air flow with application to fin tubes, Paper presented at the First National Heat Transfer Conference, Leeds, 1984.

84RO1 Roslyng, O., Installation effect on axial flow fan caused by swirl and non-uniform velocity distribution, Installation effects in ducted fan systems ,Institution of Mechanical Engineers, Conference publications, No. C114/84, pp. 21-28, 1984.

85BE1 Bellstedt, M.O., Performance prediction of air cooling towers, MSc thesis, Department of Mechanical Engineering, University of Stellenbosch, Republic of South Africa, November 1985.

85DE1 Deutsche Norm, Ventilatoren; Leistungsmessung, Normkennlinien, Deutsches Institut für Normung, Berlin, DIN 24 163, Teil 1, 1985.

85DE2 Deutsche Norm, Ventilatoren; Leistungsmessung, Normkennlinien, Deutsches Institut für Normung, Berlin, DIN 24 163, Teil 2, 1985.

85ST1 Ventilatoren Stork Hengelo, General instructions for E-type fans, V.960874, 1985.

86HE1 Heidrick, T.R., Pressure and velocity measurements, in Advanced experimental techniques in turbomachinery, ed. David Japikse, Principal Lecture Series No. 1, Concepts ETI, Inc., Norwich, Vermont, USA, 1986.

87BE1 Berryman, R.J. and Russell, C.M.B., Airflow in Air-cooled heat exchangers, Heat transfer engineering, Vol. 8, No. 4, pp. 40-44, 1987.

90VA1 Van Aarde, D.J., The flow losses through an A-frame finned tube heat exchanger installation (in Afrikaans), MSc thesis, Department of Mechanical Engineering, University of Stellenbosch, Republic of South Africa, November 1990.

Appendix A - Experimental results

The graphs included in this appendix all represent experimental data obtained from the experimental installations described in Chapter 3. The results are divided into a number of subsections to enhance cross referencing from the main text. The raw data has been transformed to more meaningful data by using the theoretical manipulations described in Chapter 2. Sample calculations for these transformations are attached as Appendix B.

A.1 Fan characteristics

The results presented in this section are typical fan characteristics of the available fans that are tested. The characteristics for the V-type fan are considered to be the basis of reference for the majority of the scale model tests (refer to section A.2). The graphs for these results are therefore included in the main body of the text (chapter 4). Figures A.1.3 to A.1.5 are included to enhance the comparison between the two scale model fans being investigated.

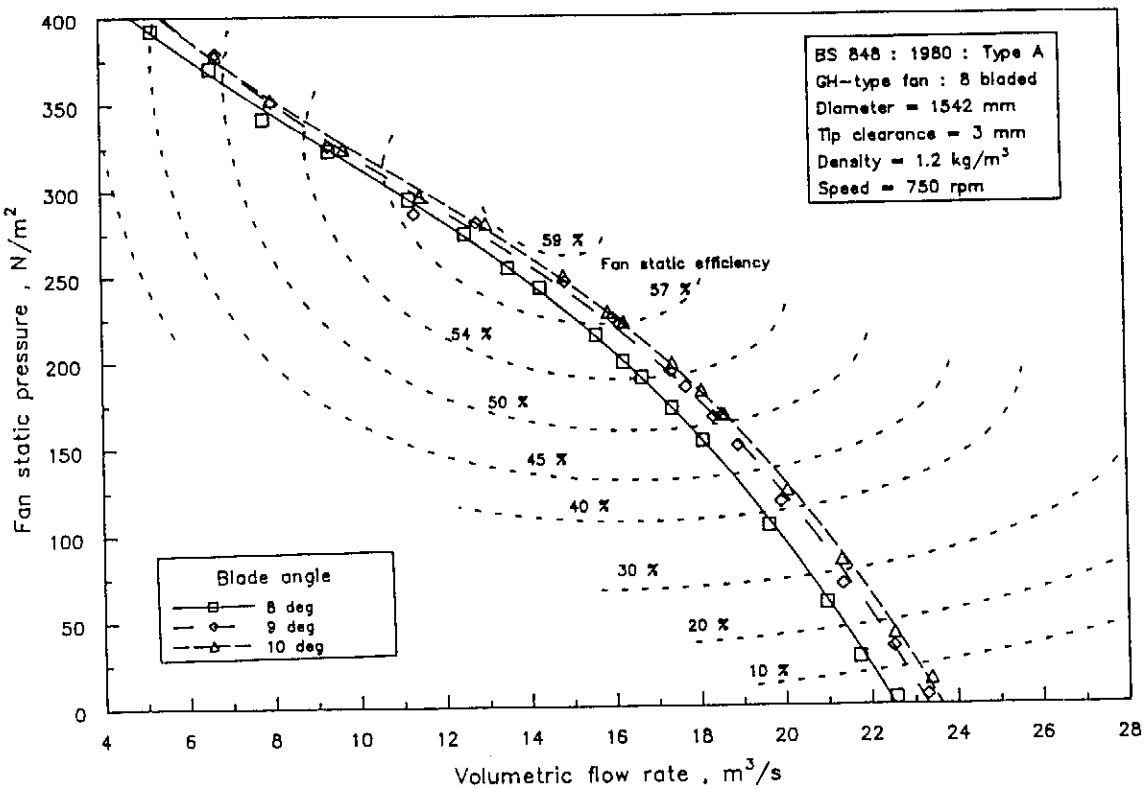

Figure A.1.1: Fan static pressure : GH–fan

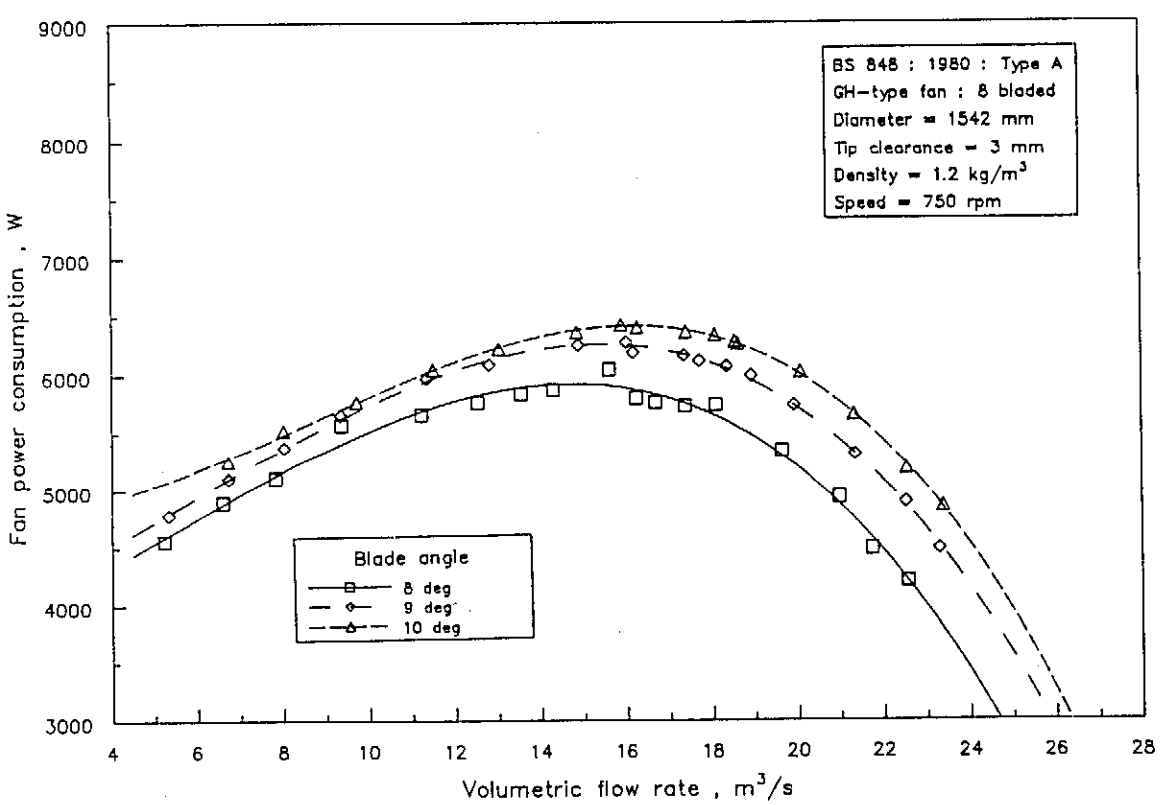

Figure A.1.2: Fan power consumption : GH–fan

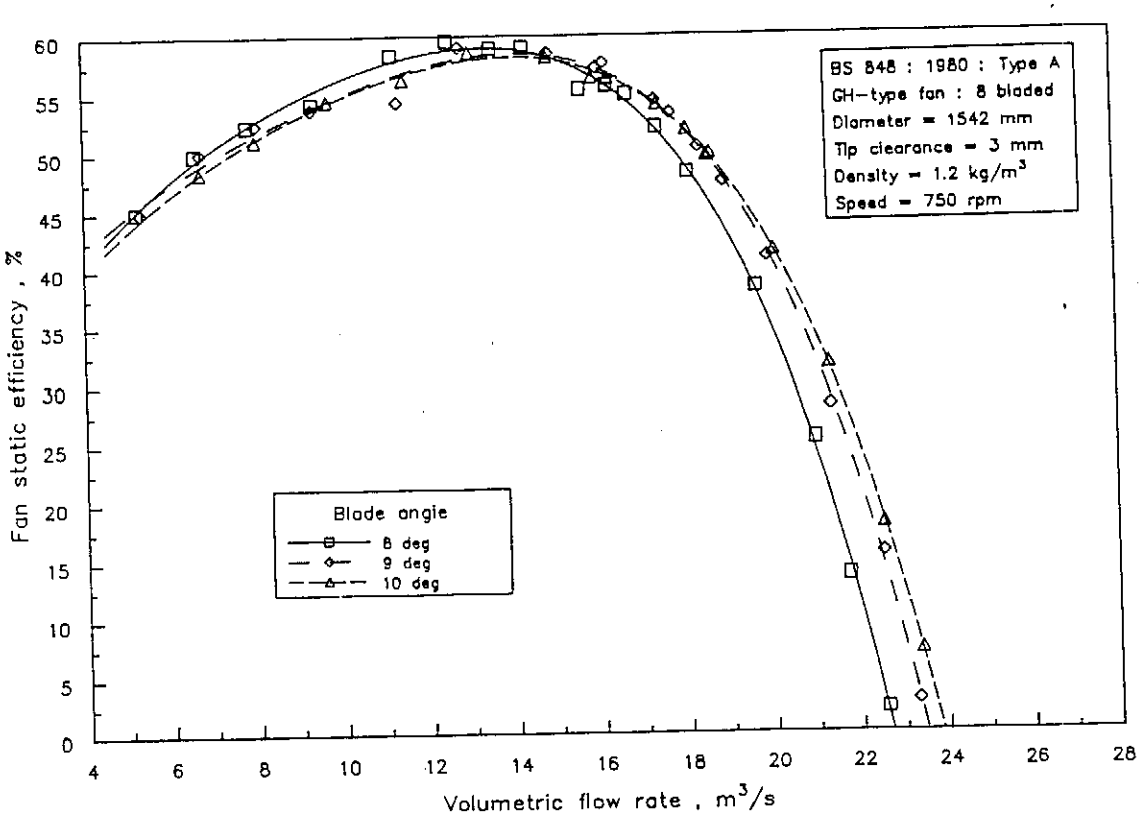

Figure A.1.3: Fan static efficiency : GH–fan

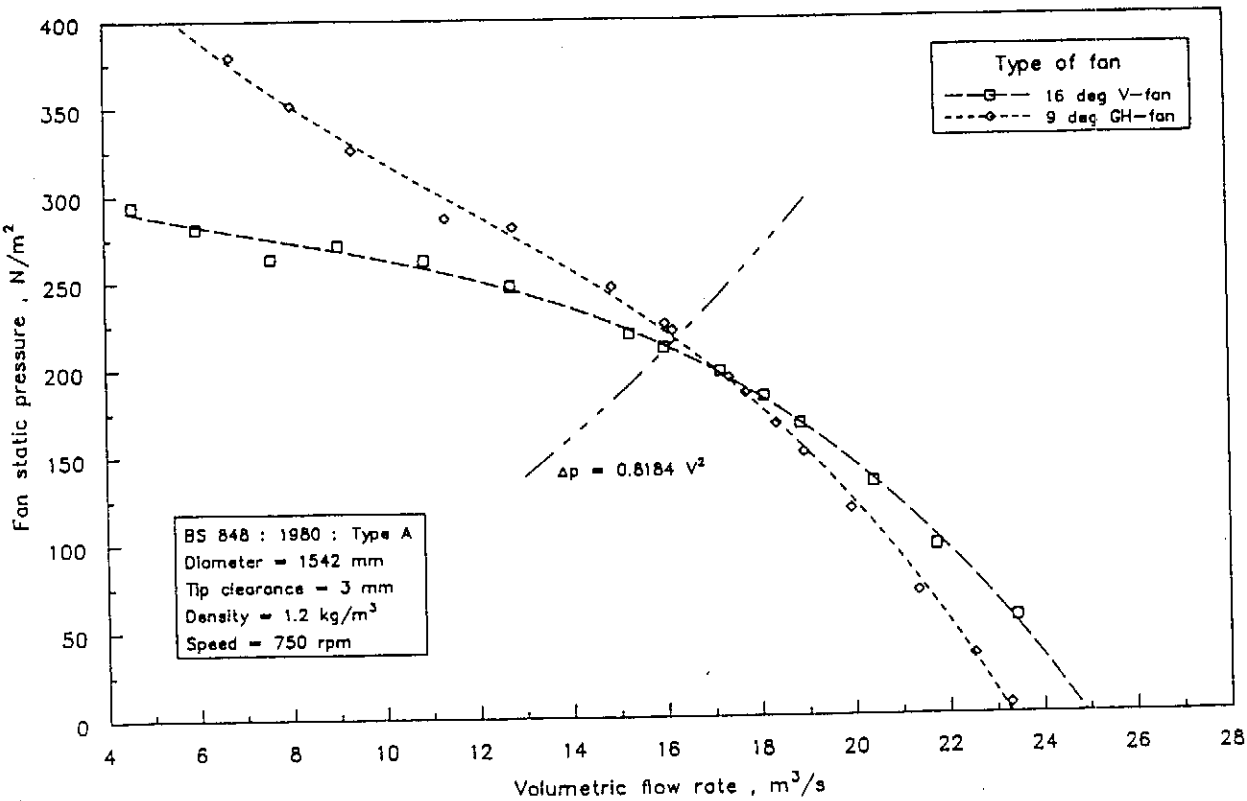

Figure A.1.4: Fan static pressure : V-fan vs. GH-fan

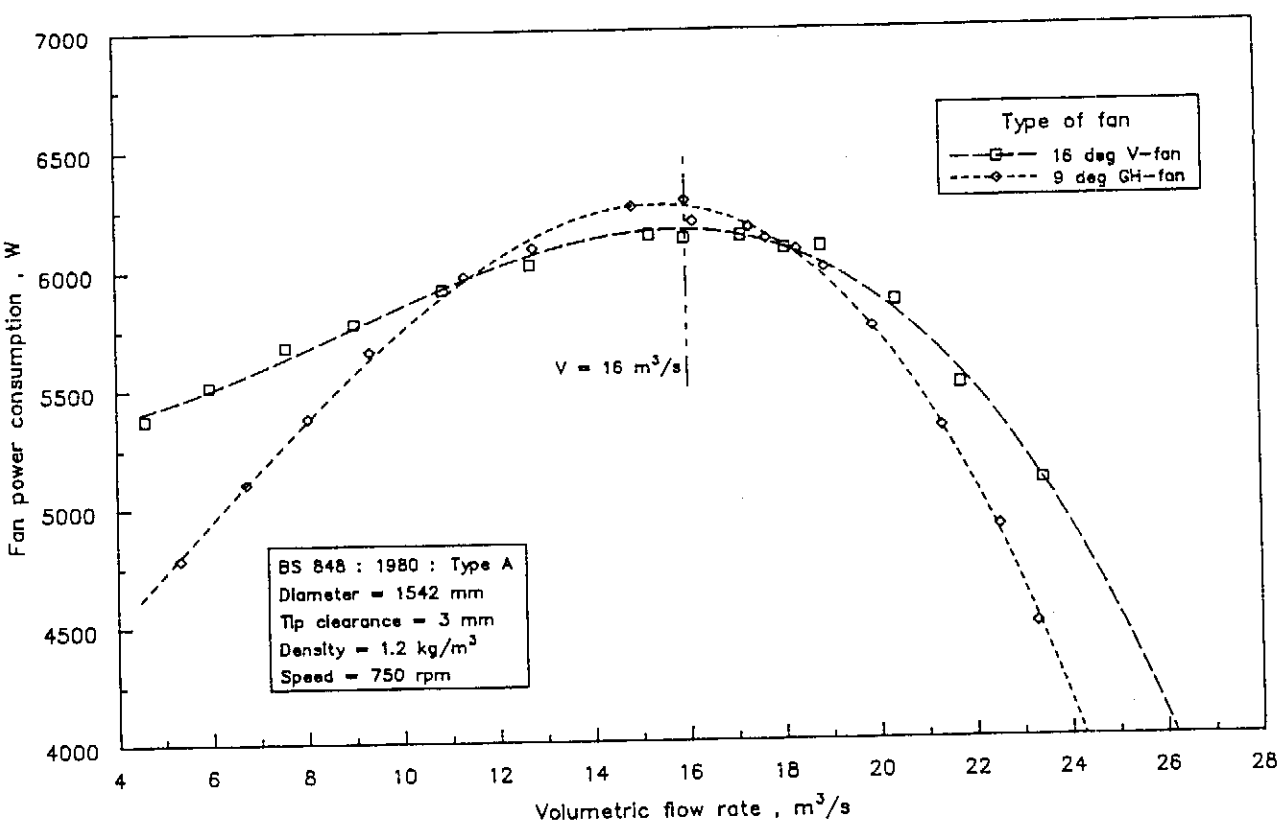

Figure A.1.5: Fan power consumption : V-fan vs. GH-fan

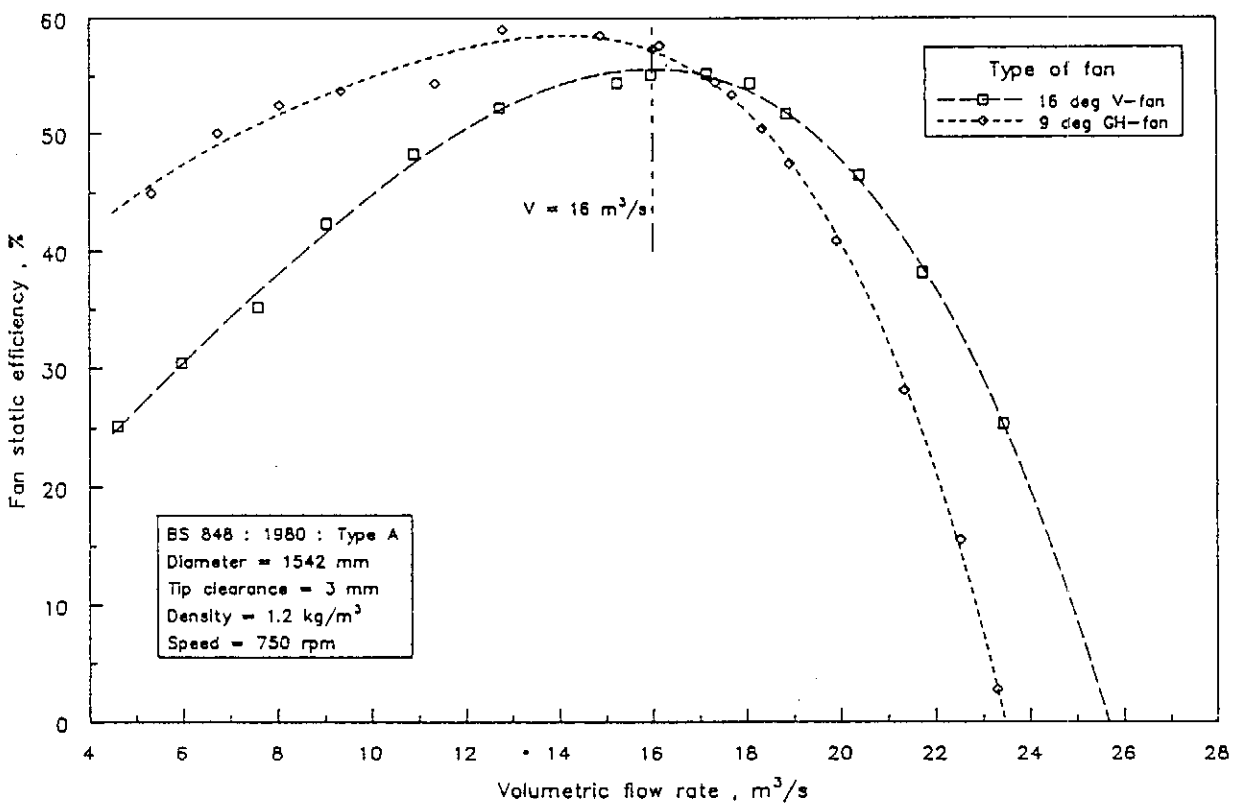

Figure A.1.6: Fan static efficiency : V-fan vs. GH-fan

A.2 Individual flow distorting components

The individual flow distorting components refer to the effect of fan installation and different ancillaries on the overall fan performance. These include the effect of tip clearance, a solid disc, an inlet grid, a walkway, support beams and the heat exchangers. Different configurations of the ancillary equipment are investigated and the results are presented in this section.

Figures A.2.1 to A.2.4 refer to tip clearance effects. The effect of the presence of a solid disc is presented as figures A.2.5 to A.2.10. The inlet grid is installed to obtain the experimental results presented in figures A.2.11 to A.2.14. The effect of the walkway and supporting beams at fan outlet can be derived from figures A.2.15 to A.2.22. Figures A.2.23 to A.2.24 relate to the pressure losses associated with the heat exchangers.

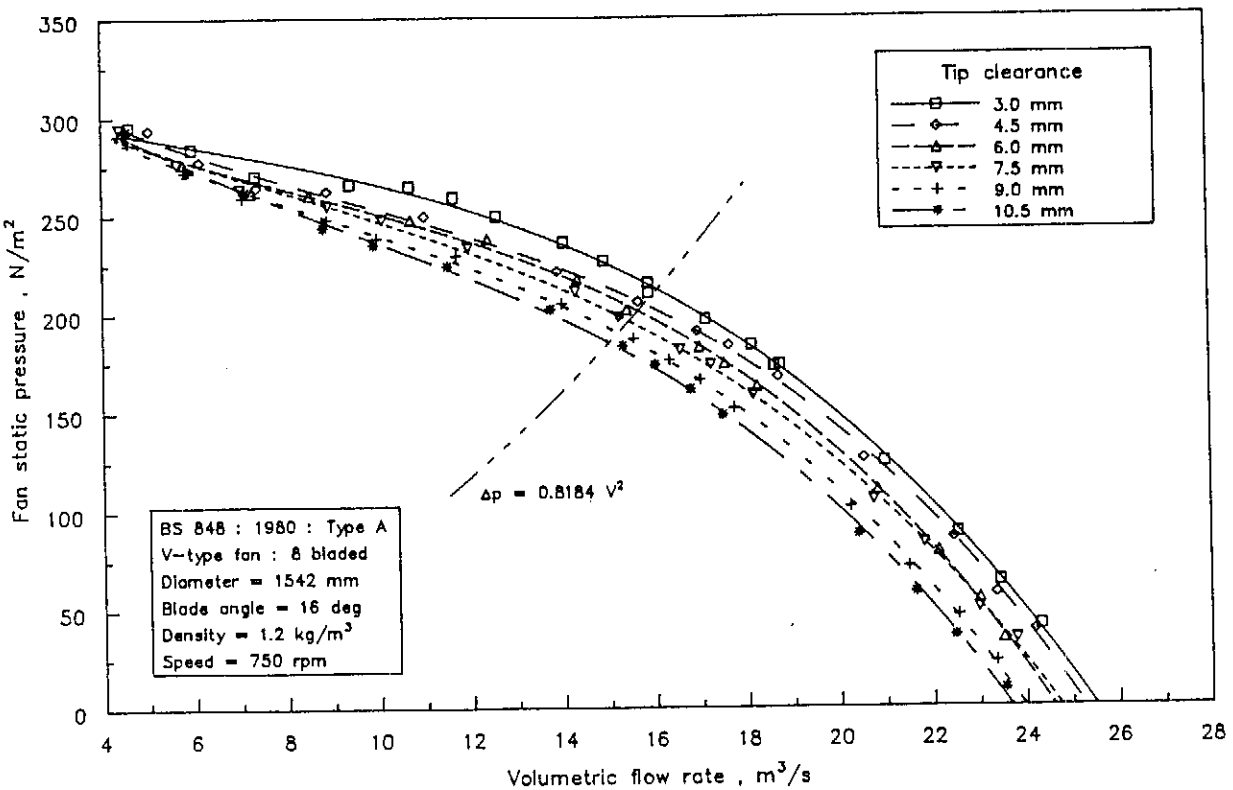

Figure A.2.1: Tip clearance effects : Δp_{sF} vs. V

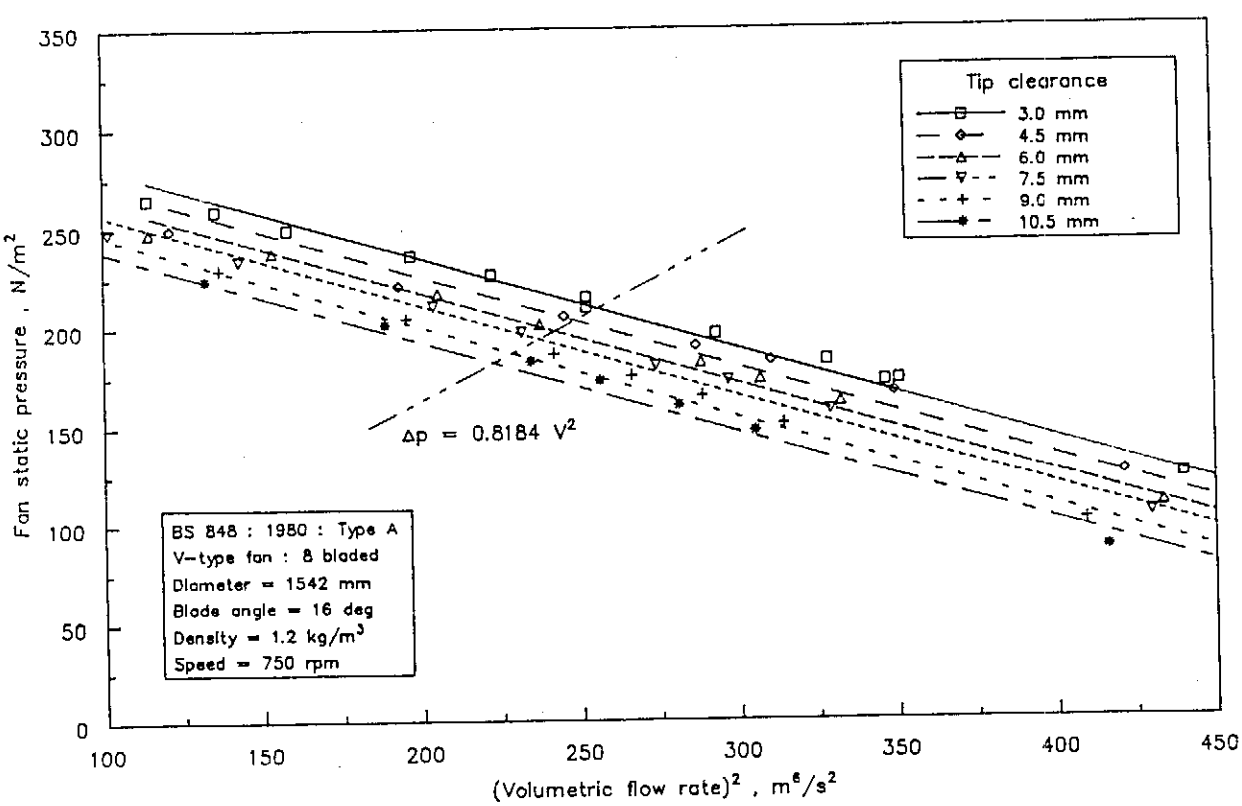

Figure A.2.2: Tip clearance effects : Δp_{sF} vs. V^2

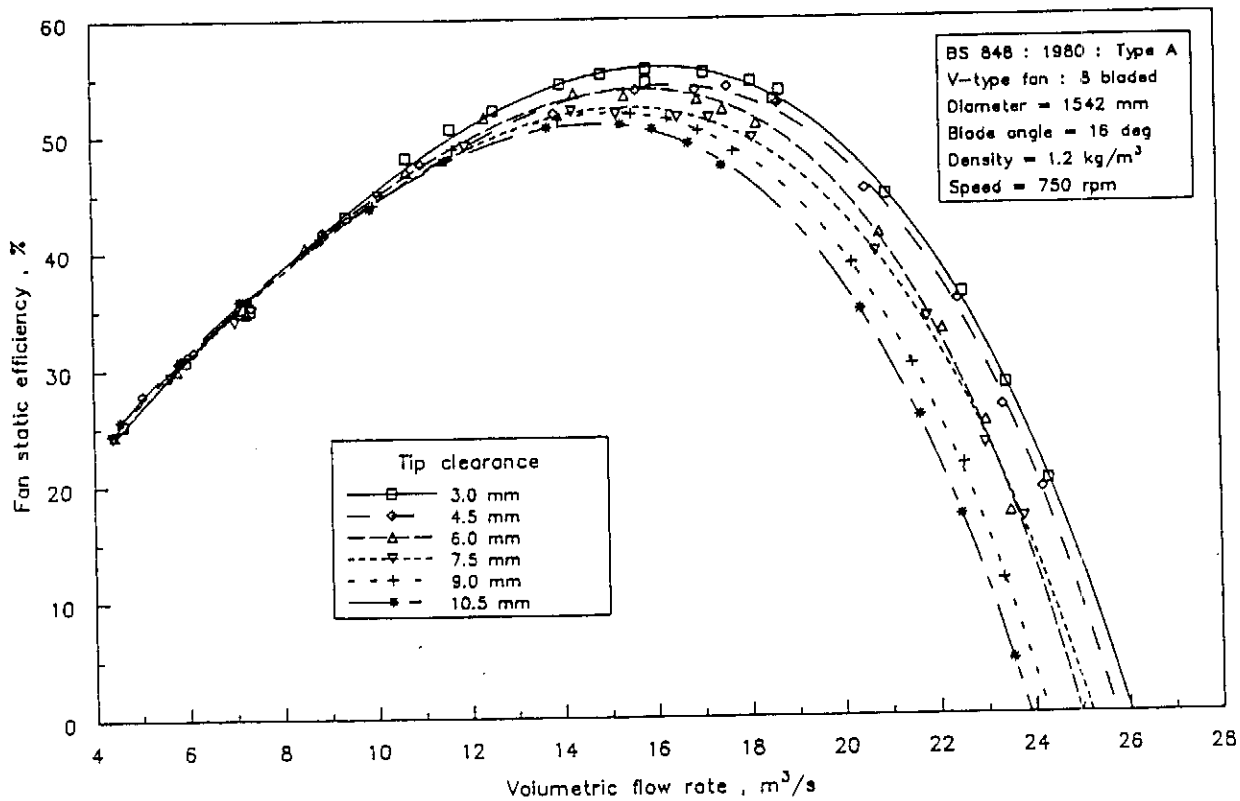

Figure A.2.3: Tip clearance effects : Fan static efficiency

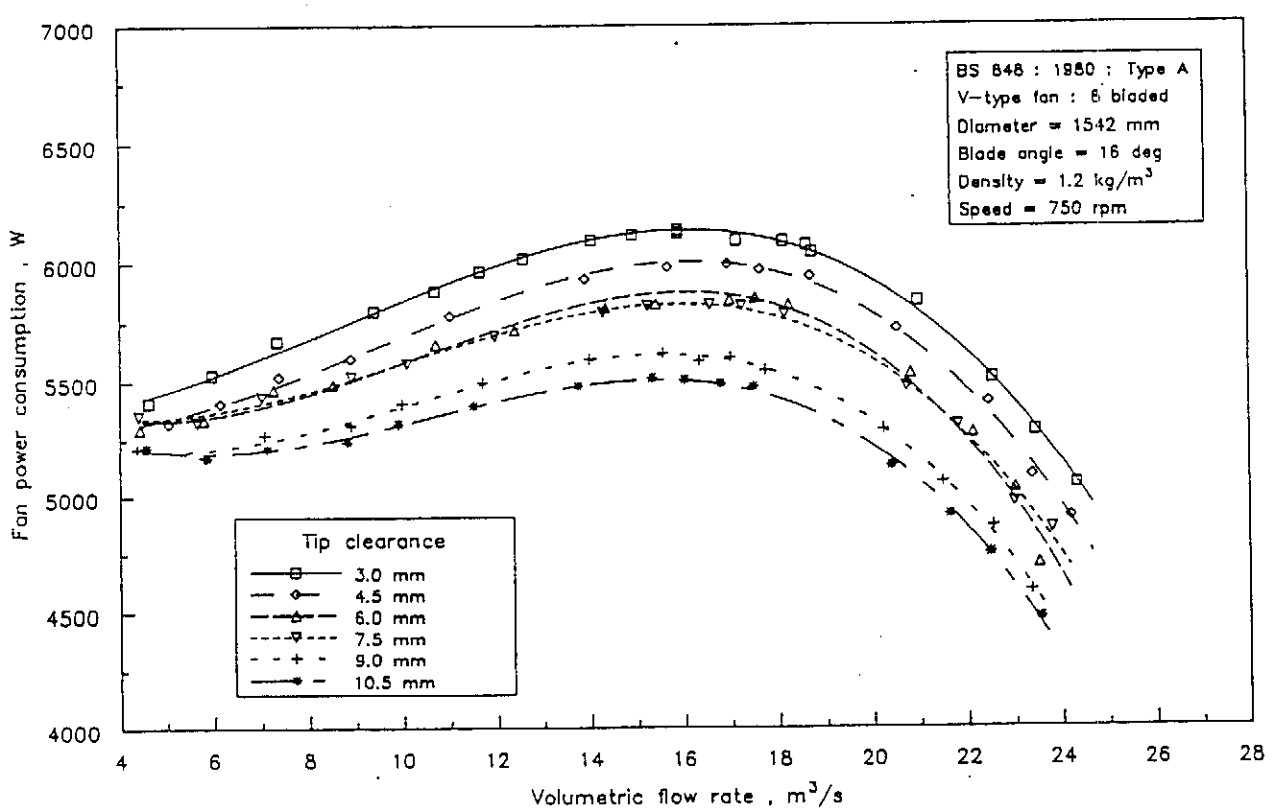

Figure A.2.4: Tip clearance effects : Fan power consumption

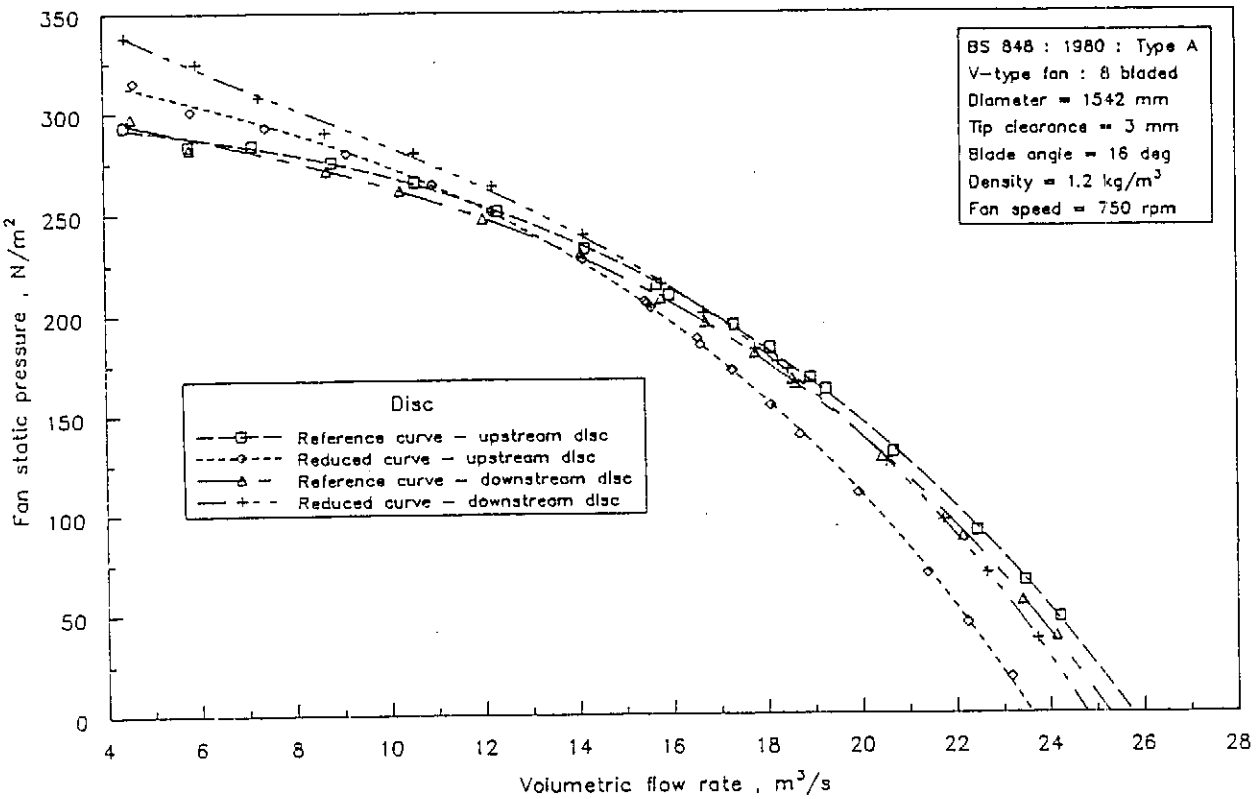

Figure A.2.5: Solid disc effects : Fan static pressure

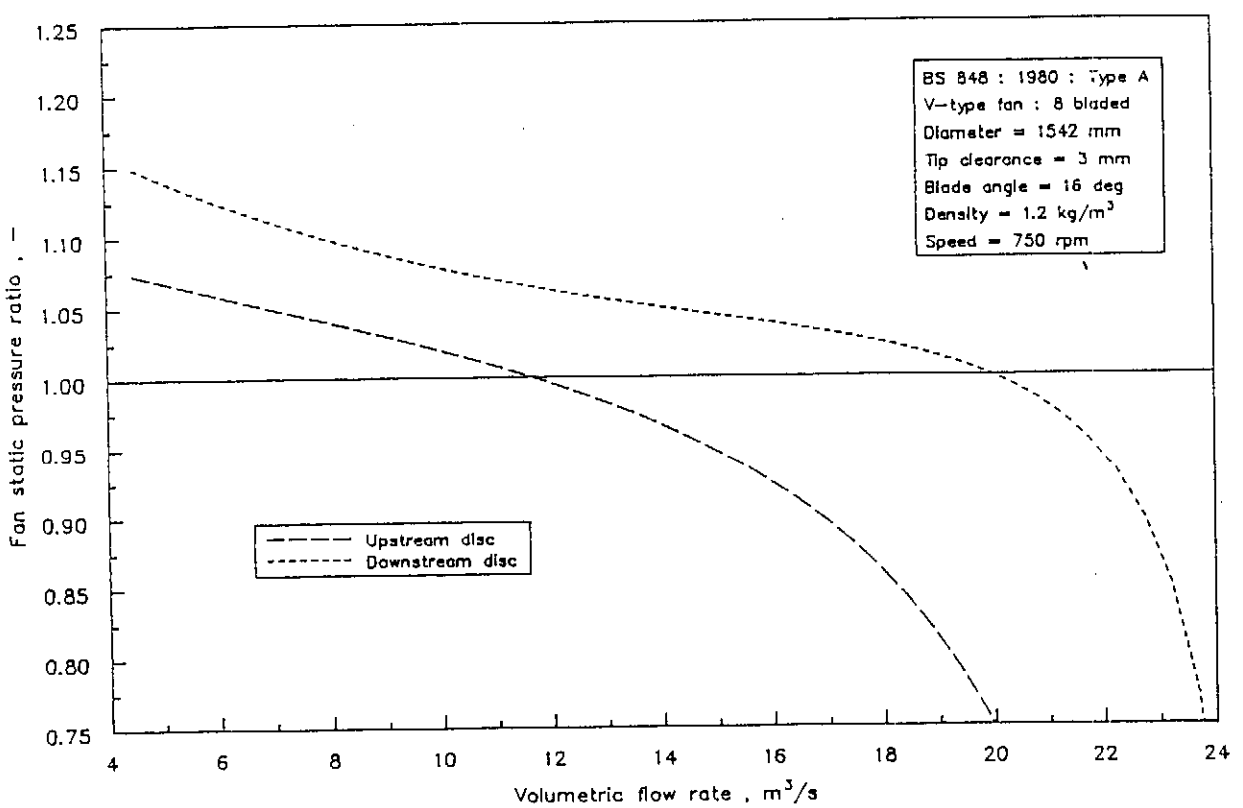

Figure A.2.6: Solid disc effects : Fan static pressure ratio

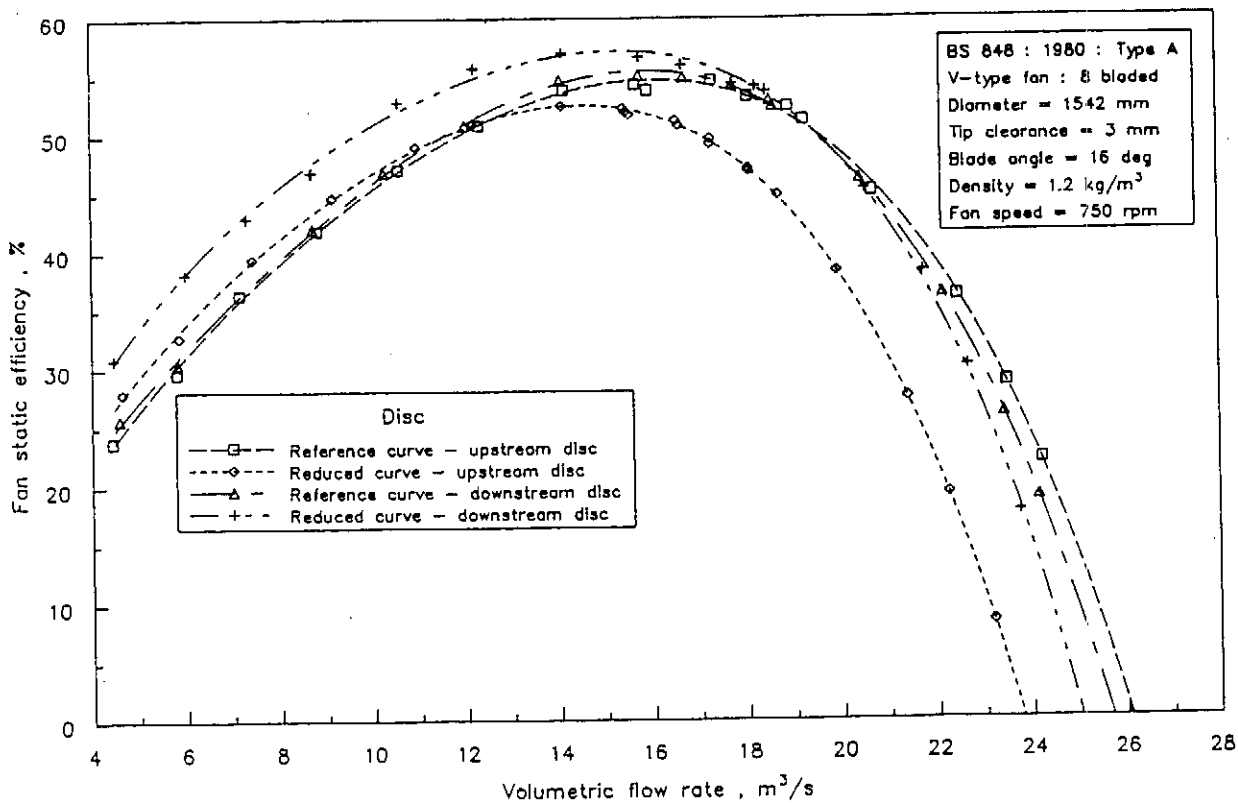

Figure A.2.7: Solid disc effects : Fan static efficiency

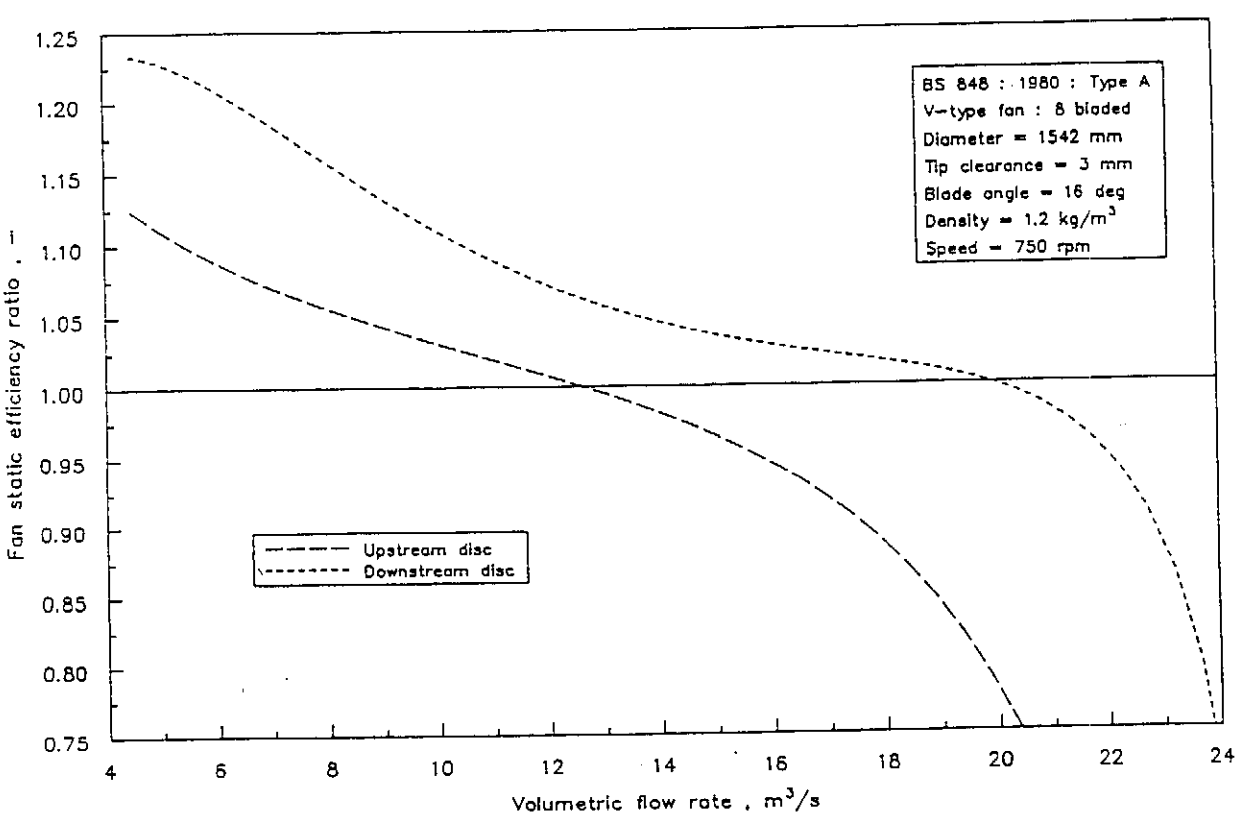

Figure A.2.8: Solid disc effects : Fan static efficiency ratio

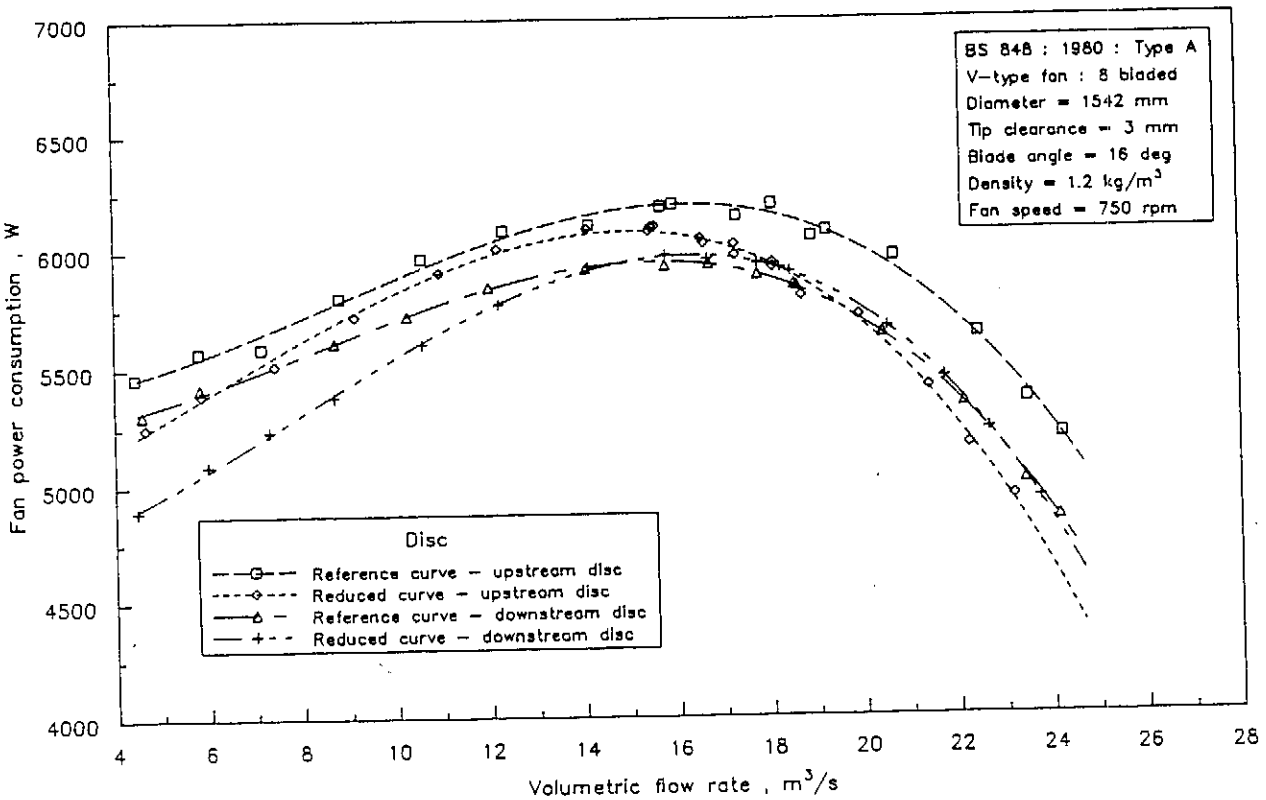

Figure A.2.9: Solid disc effects : Fan power consumption

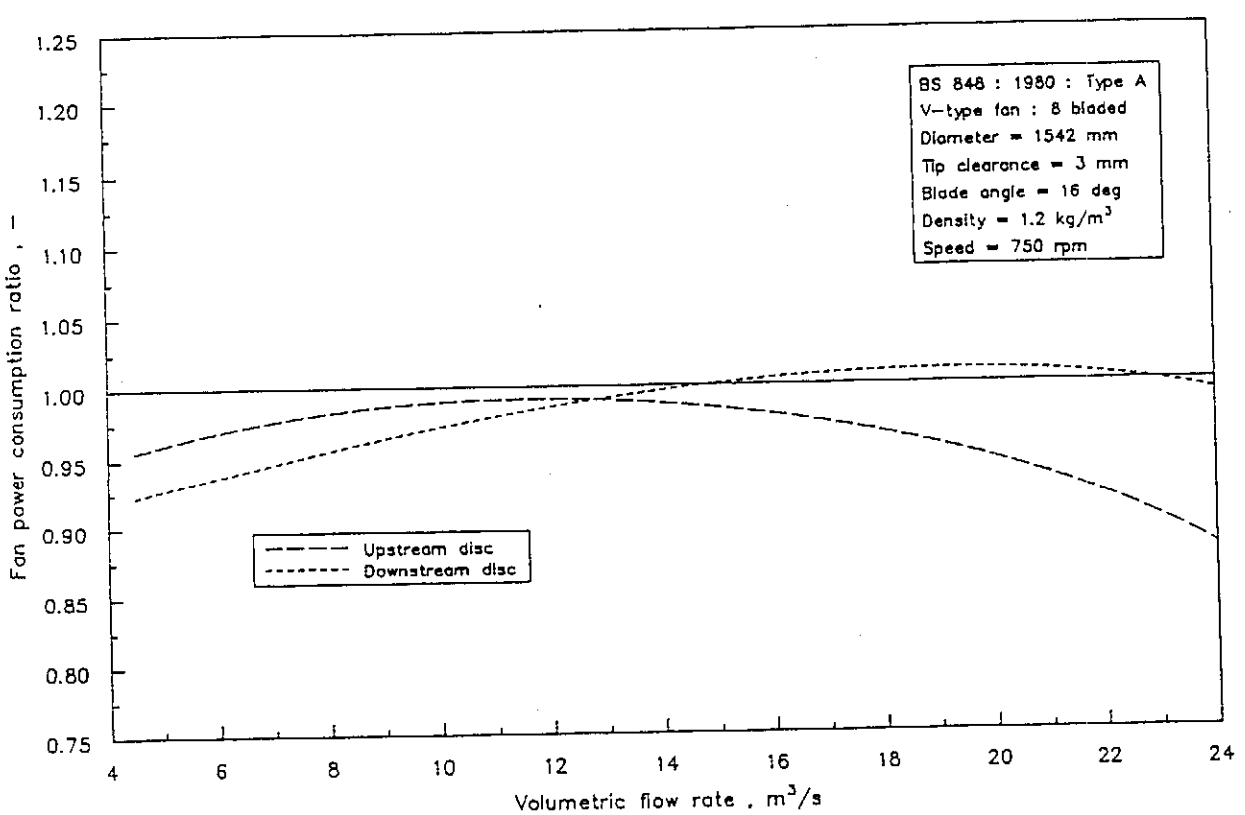

Figure A.2.10: Solid disc effects : Fan power consumption ratio

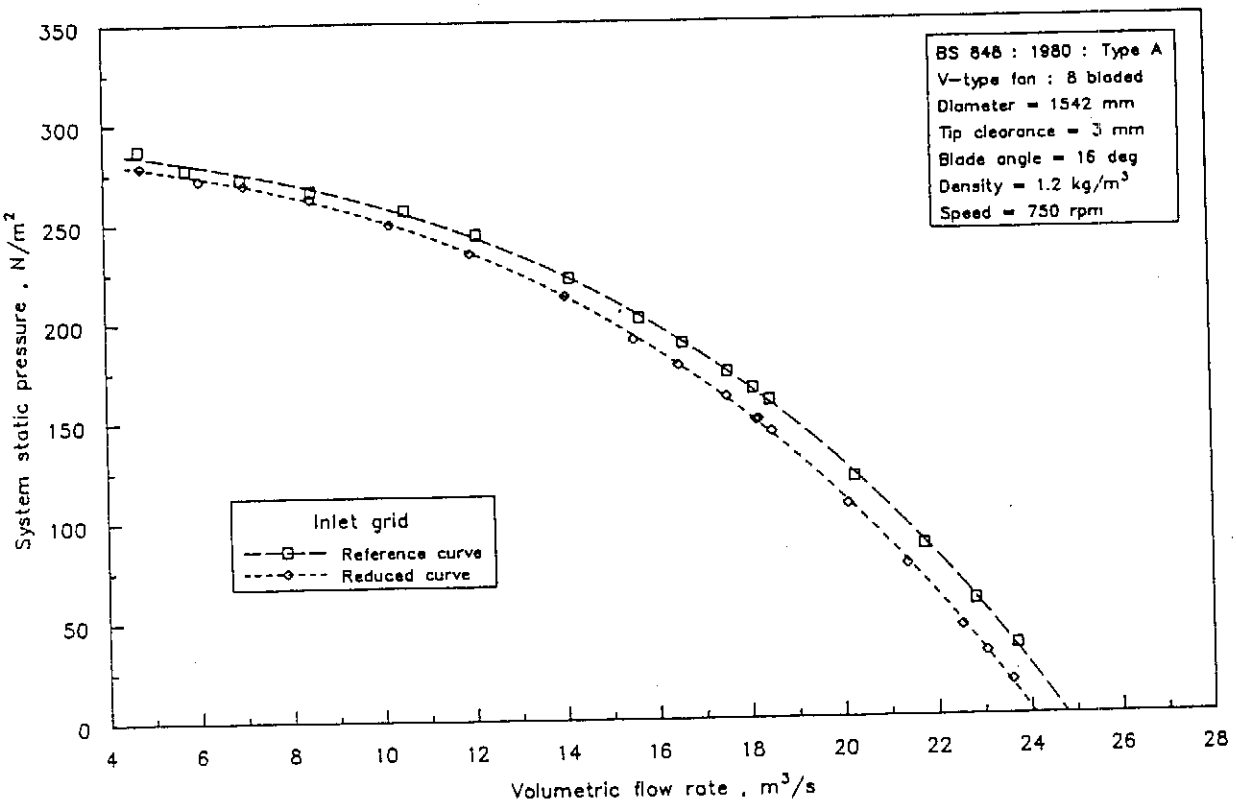

Figure A.2.11: Inlet grid effects : System static pressure

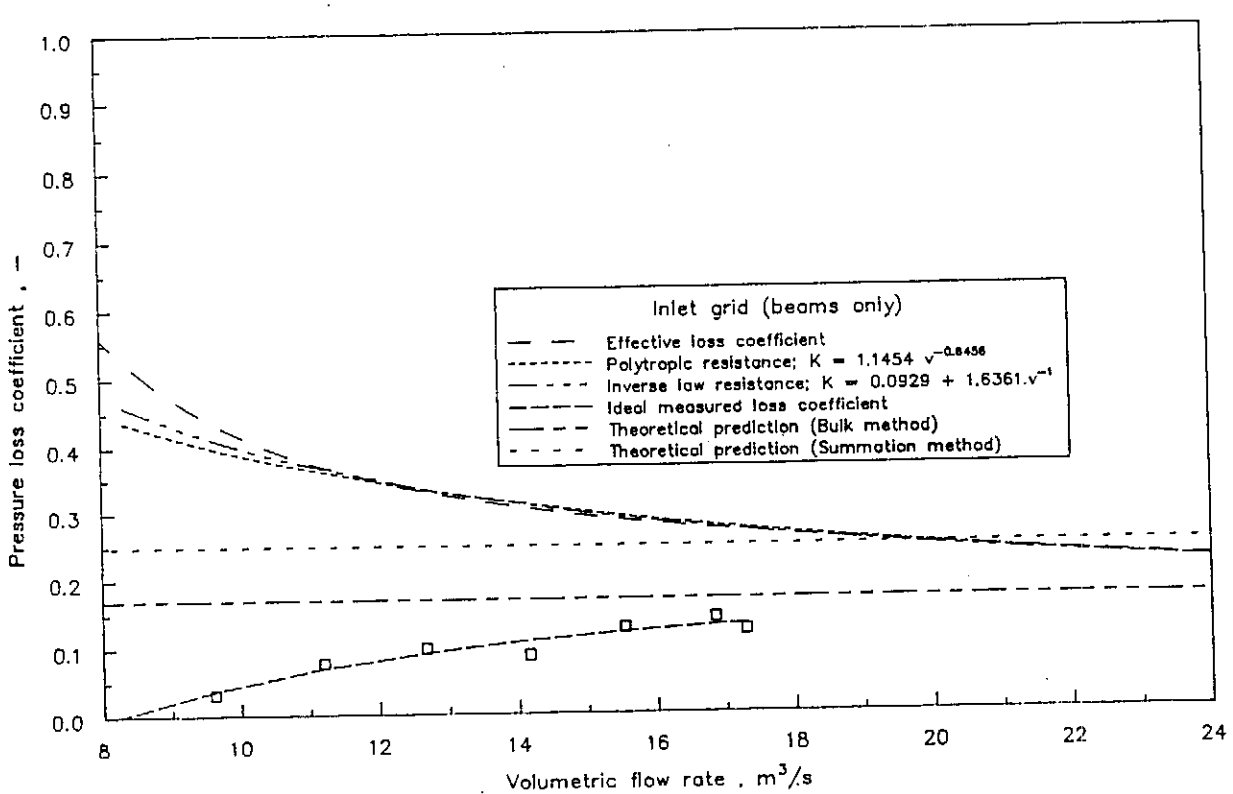

Figure A.2.12: Inlet grid effects : Pressure loss coefficient

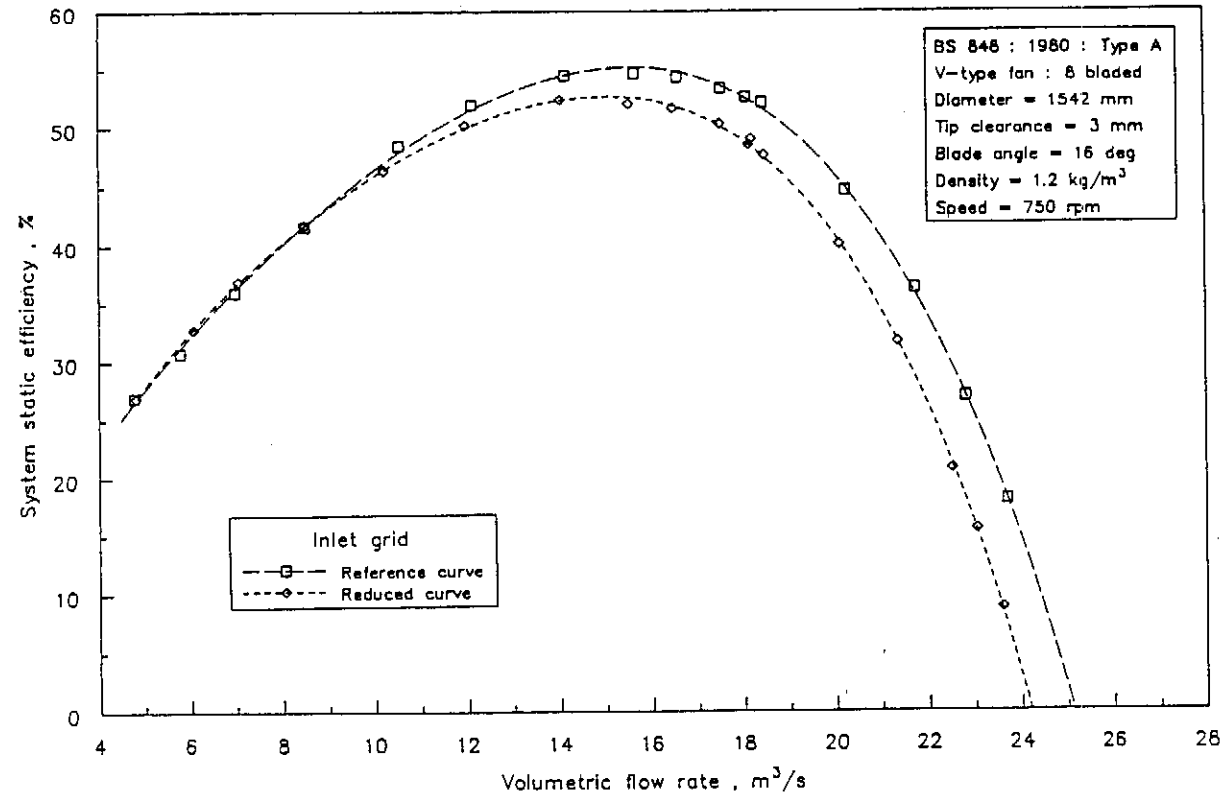

Figure A.2.13: Inlet grid effects : System static efficiency

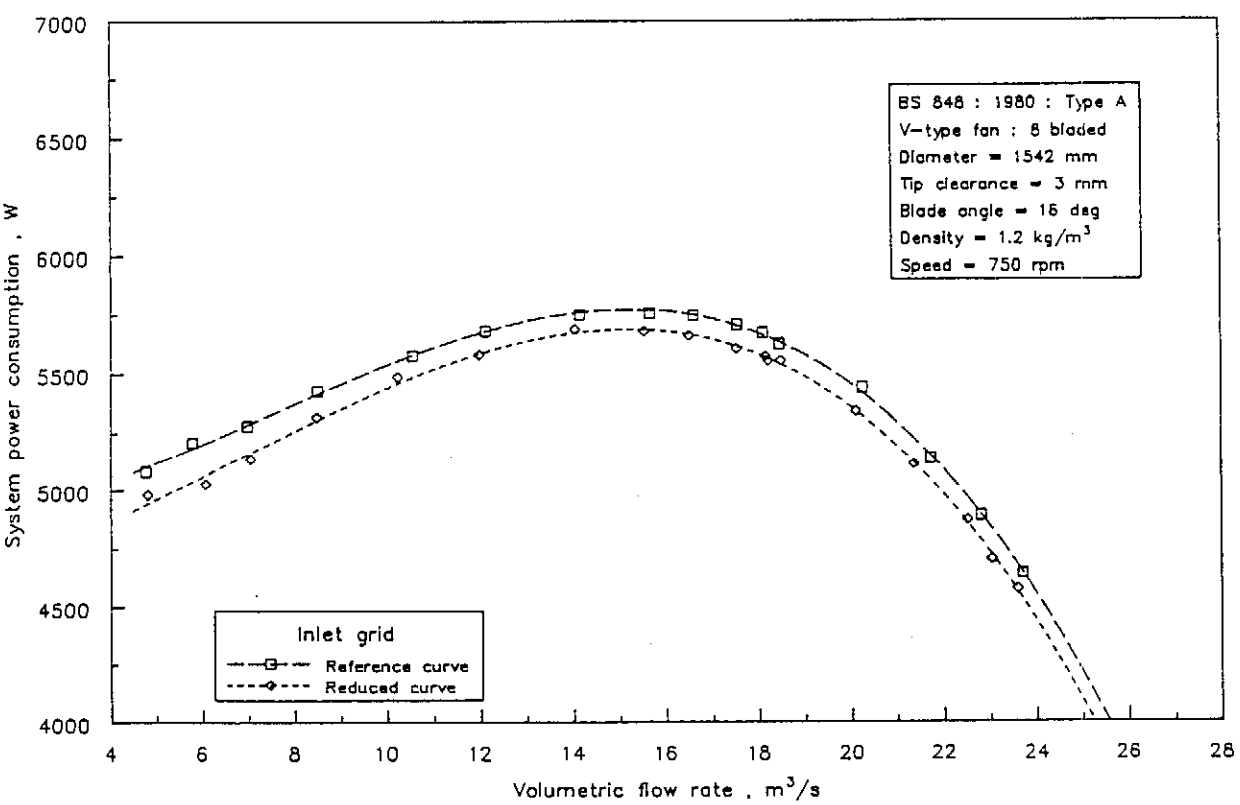

Figure A.2.14: Inlet grid effects : System power consumption

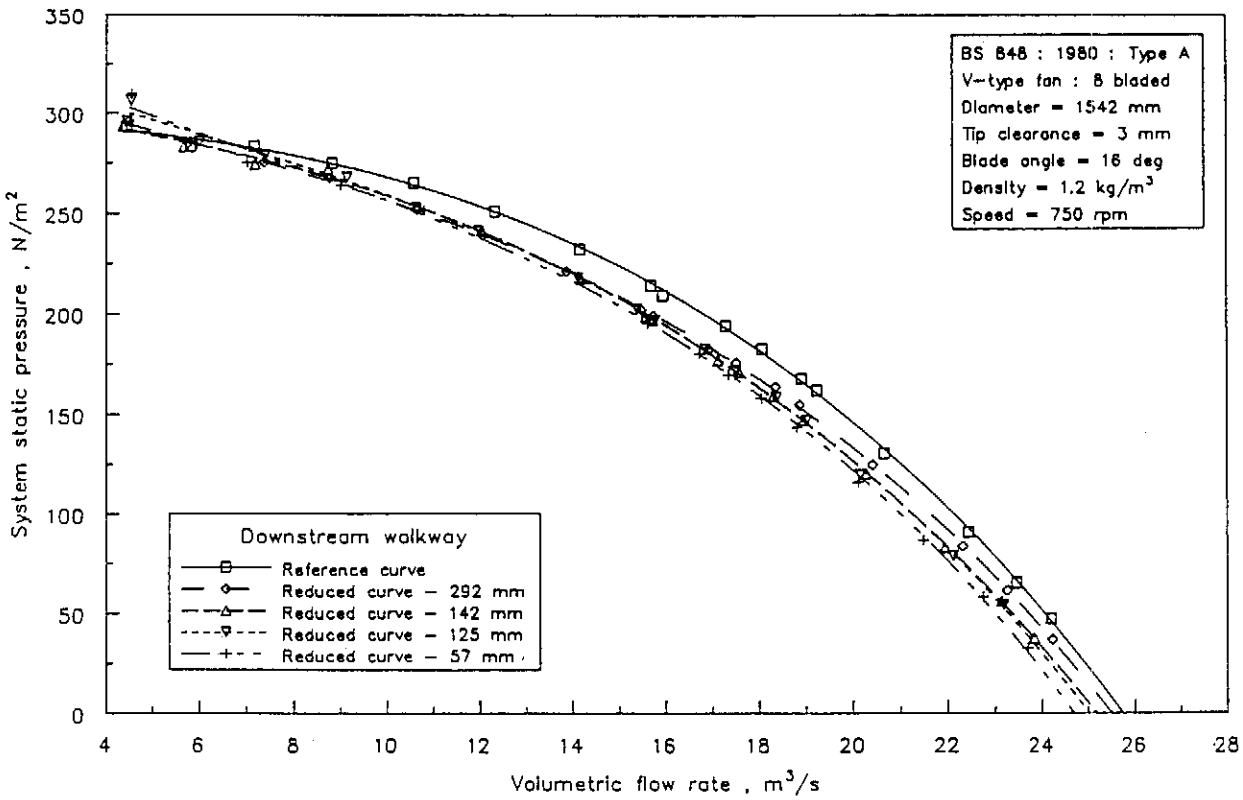

Figure A.2.15: Walkway effects : System static pressure

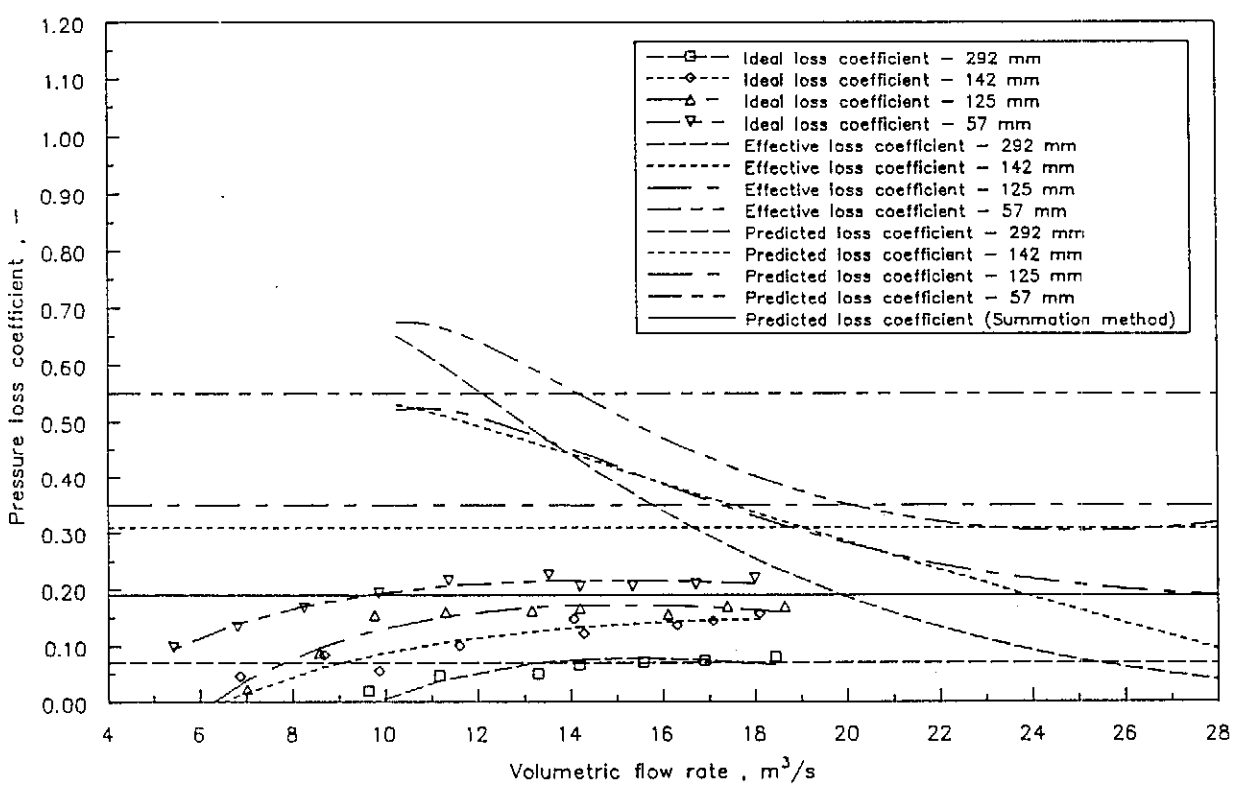

Figure A.2.16: Walkway effects : Pressure loss coefficient

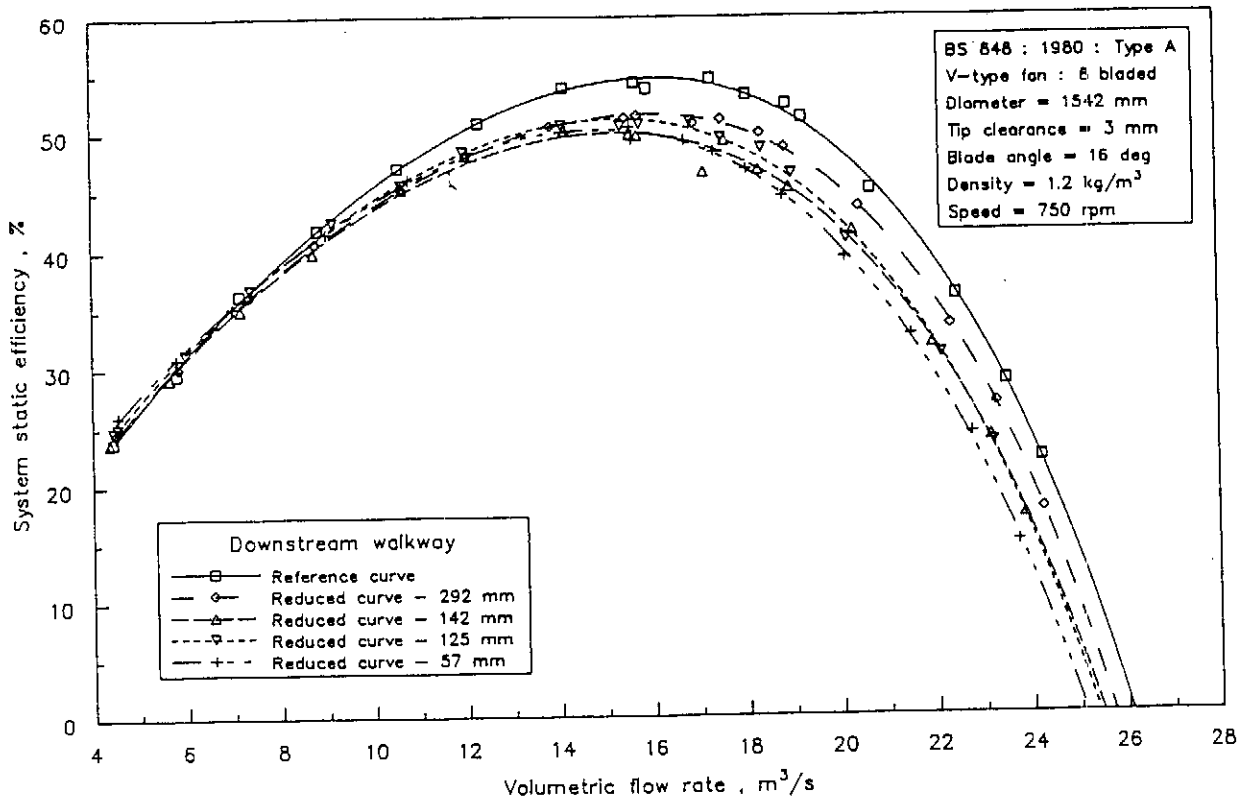

Figure A.2.17: Walkway effects : System static efficiency

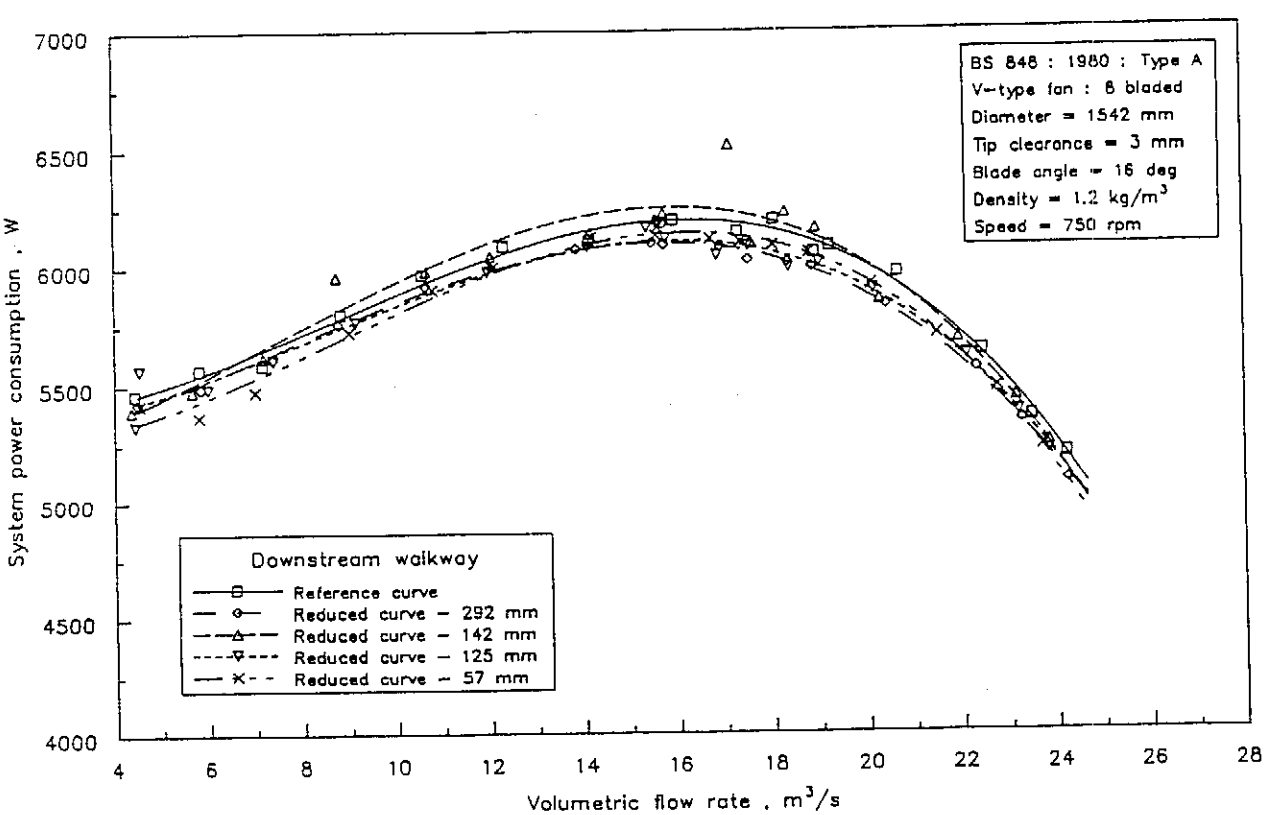

Figure A.2.18: Walkway effects : System power consumption

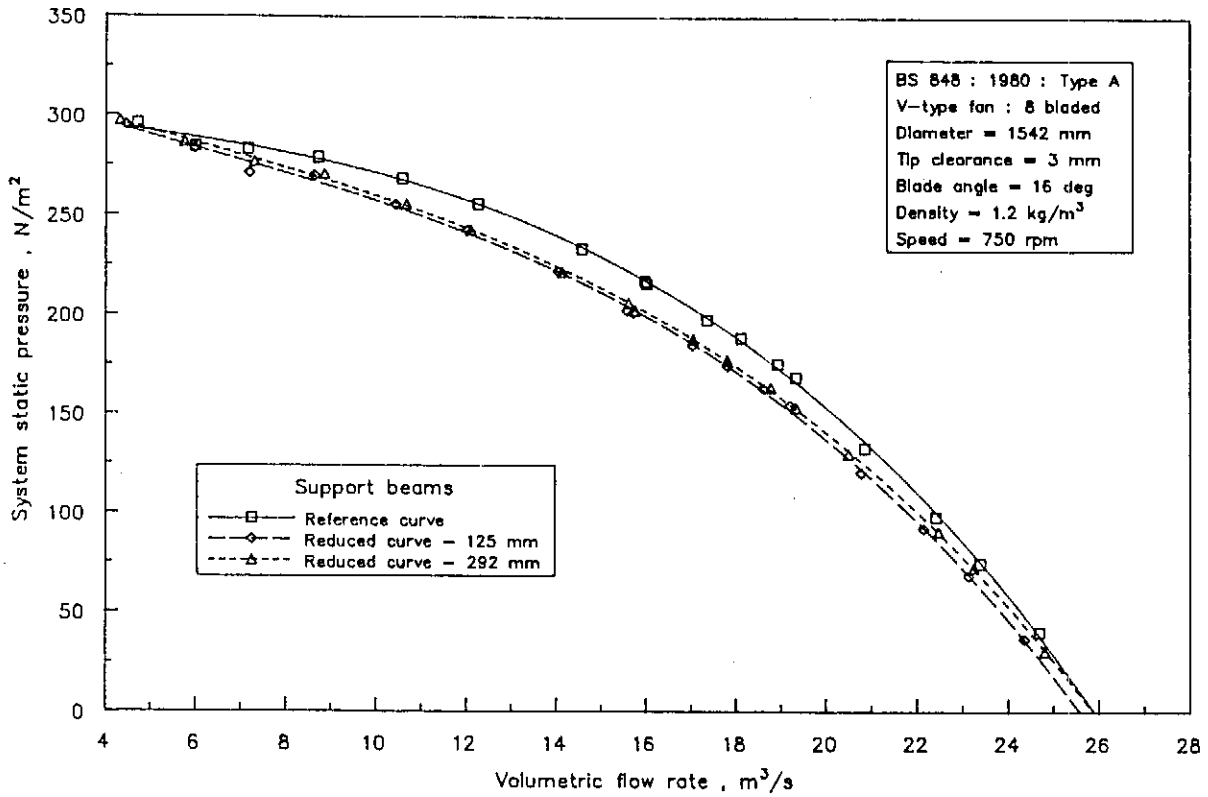

Figure A.2.19: Supporting beams effects : System static pressure

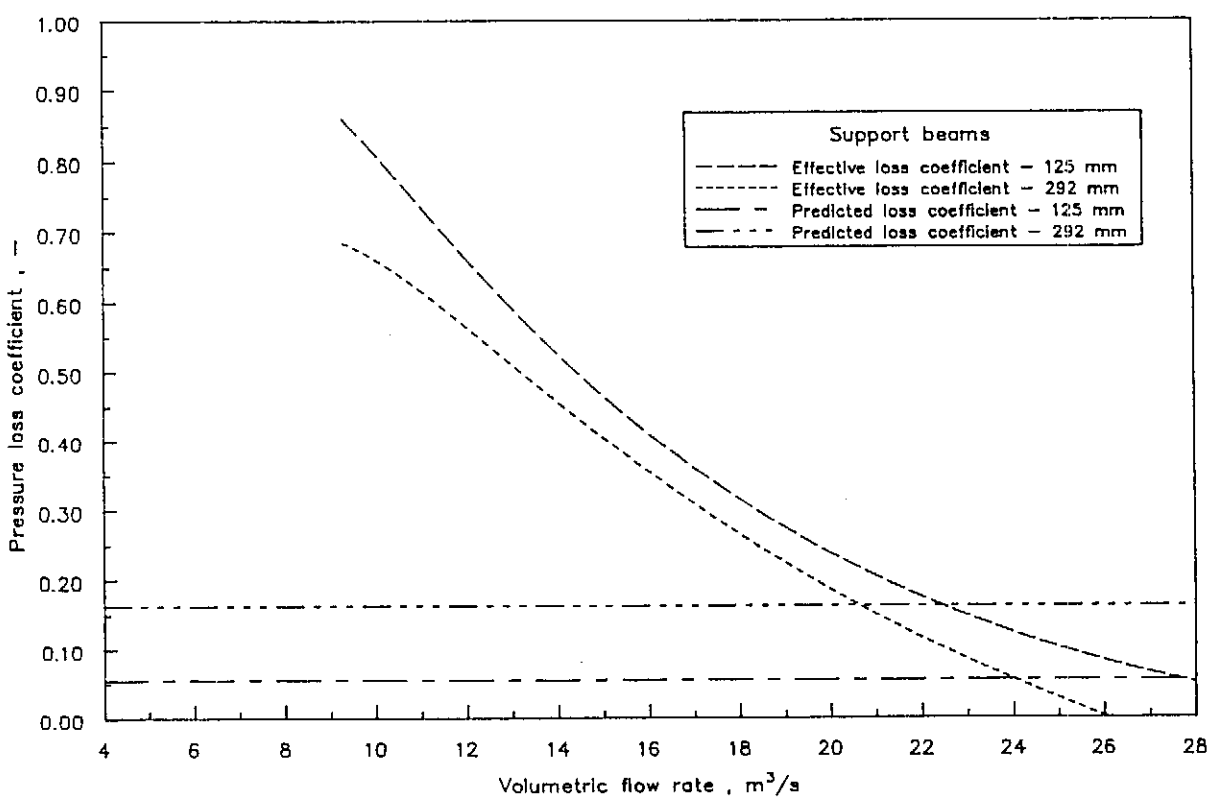

Figure A.2.20: Supporting beams effects : Pressure loss coefficient

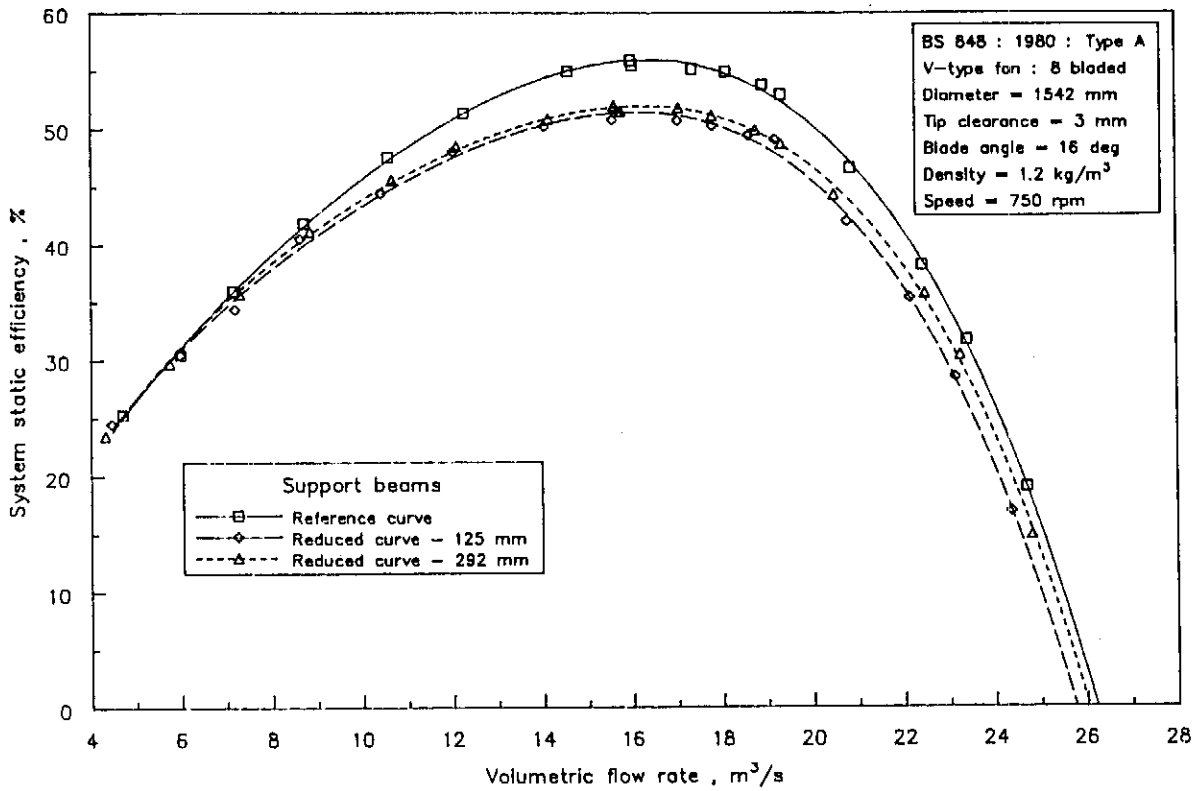

Figure A.2.21: Supporting beams effects : System static efficiency

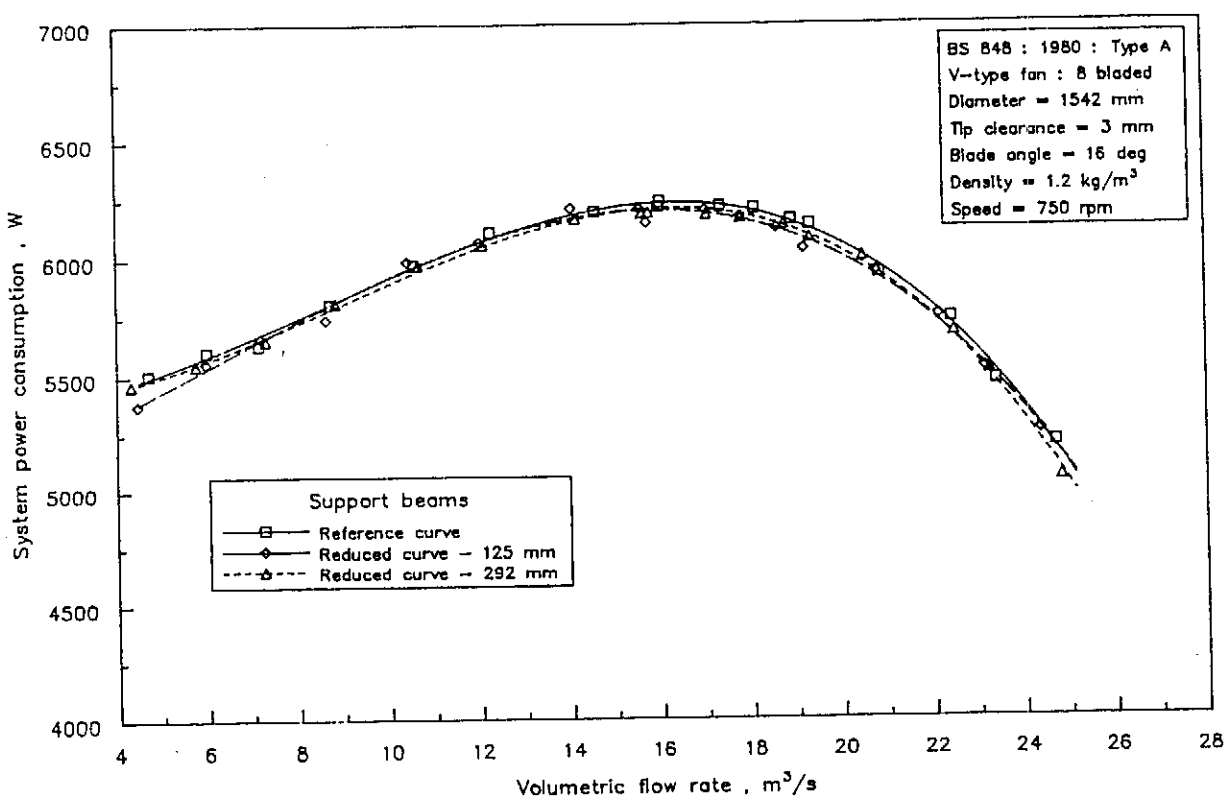

Figure A.2.22: Supporting beams effects : System power consumption

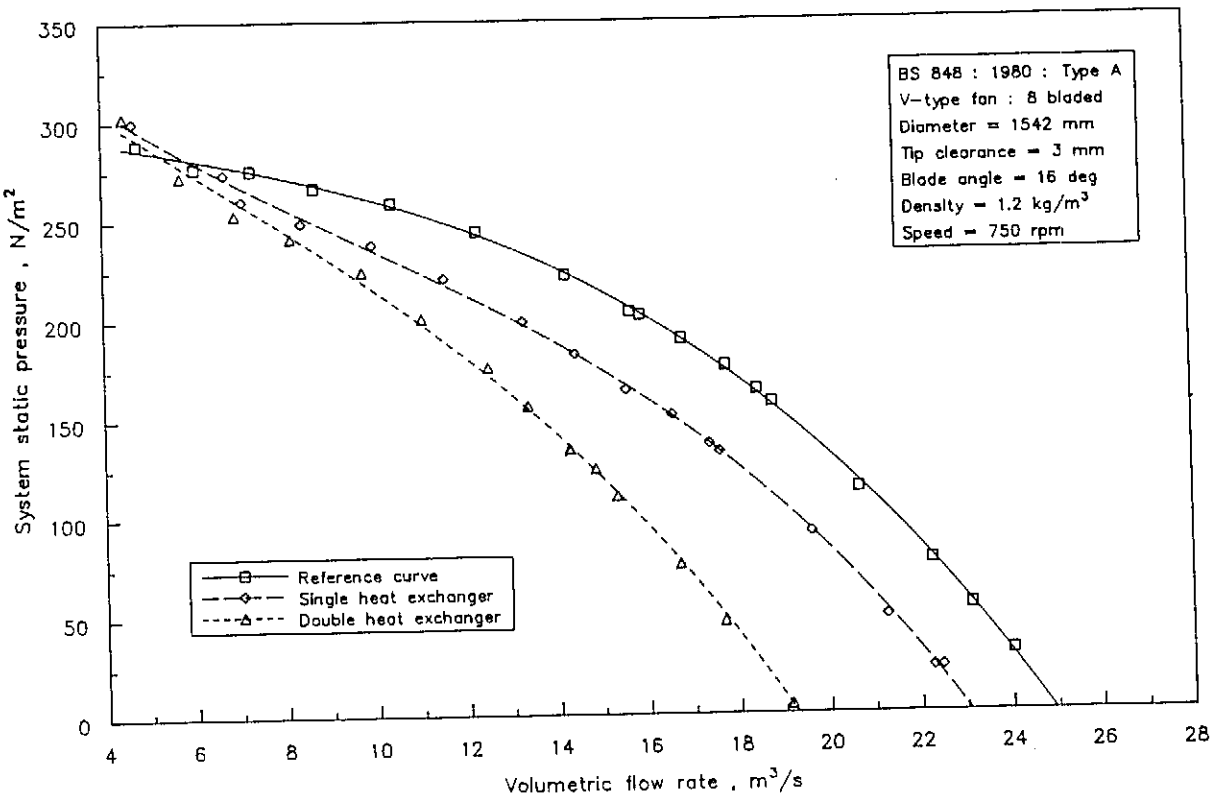

Figure A.2.23: Heat exchanger effects : System static pressure

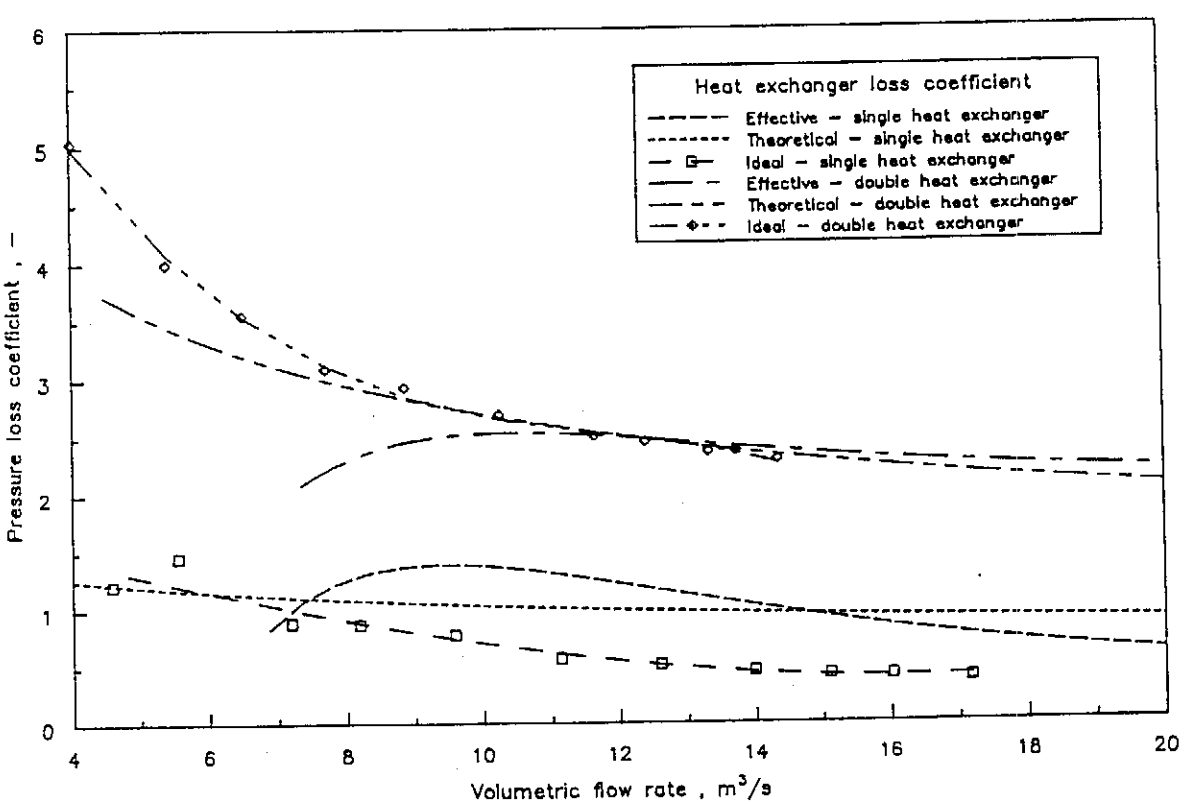

Figure A.2.24: Heat exchanger effects : Pressure loss coefficient

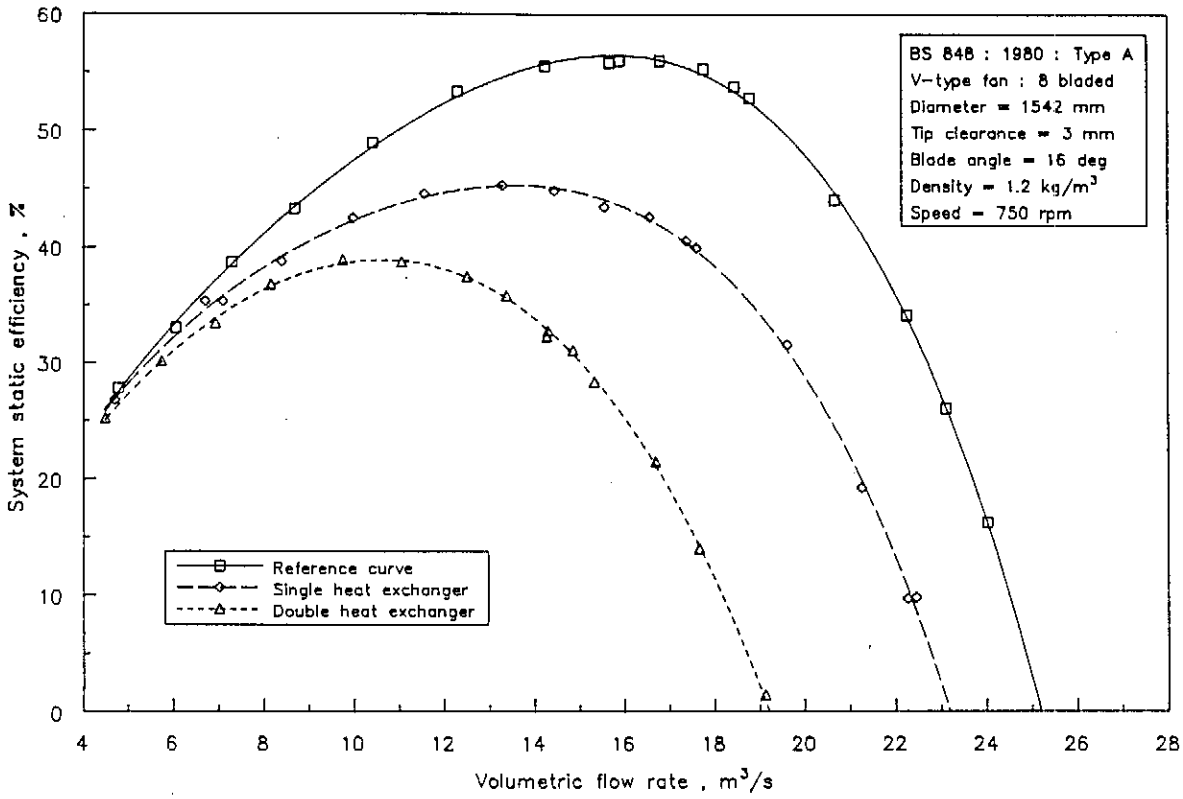

Figure A.2.25: Heat exchanger effects : System static efficiency

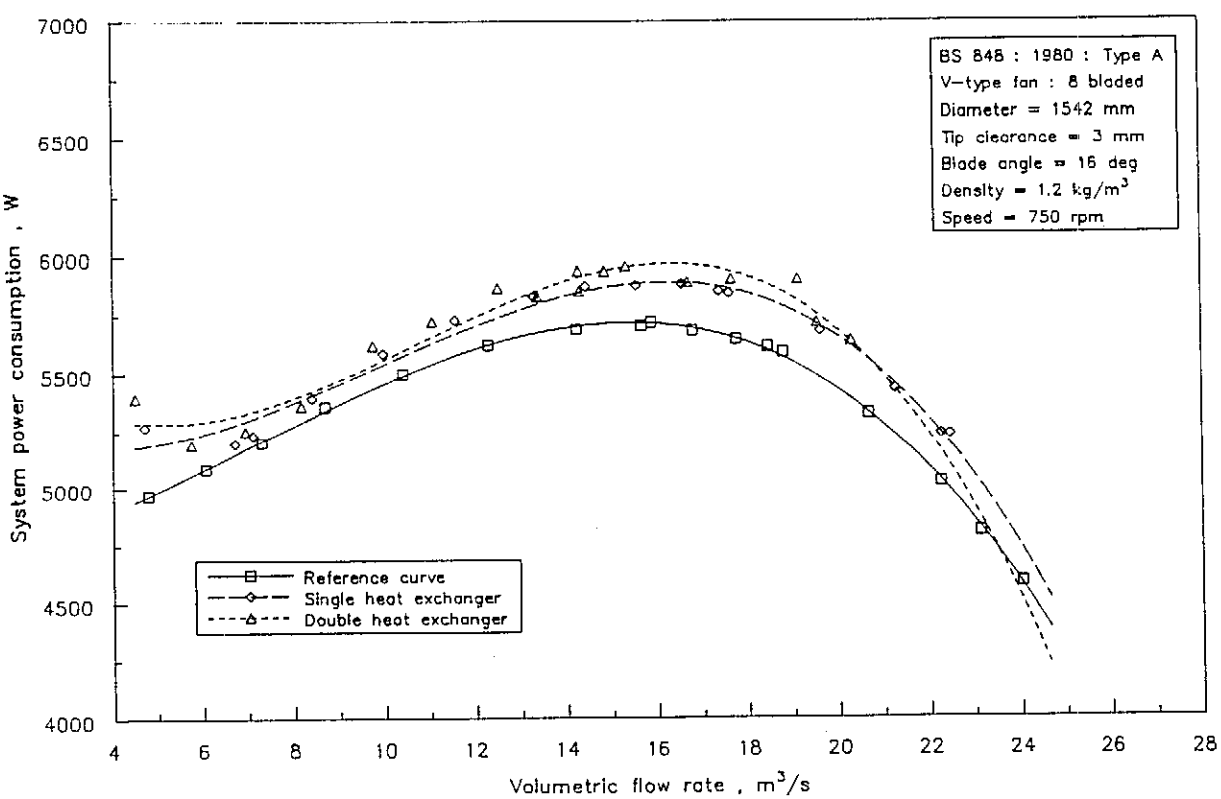

Figure A.2.26: Heat exchanger effects : System power consumption

A.3 Combined flow distorting components

The different ancillaries used to investigate the combined effects consist of the inlet safety grid, the walkway and support beams and the double heat exchangers.

Figures A.3.1 to A.3.4 refer to the combined effect of the walkway and support structure in an ideal system (excluding the heat exchangers). Figure A.3.5 to A.3.9 represent the effect of different combinations on a system including double heat exchangers. The downstream losses are presented in figure A.3.6.

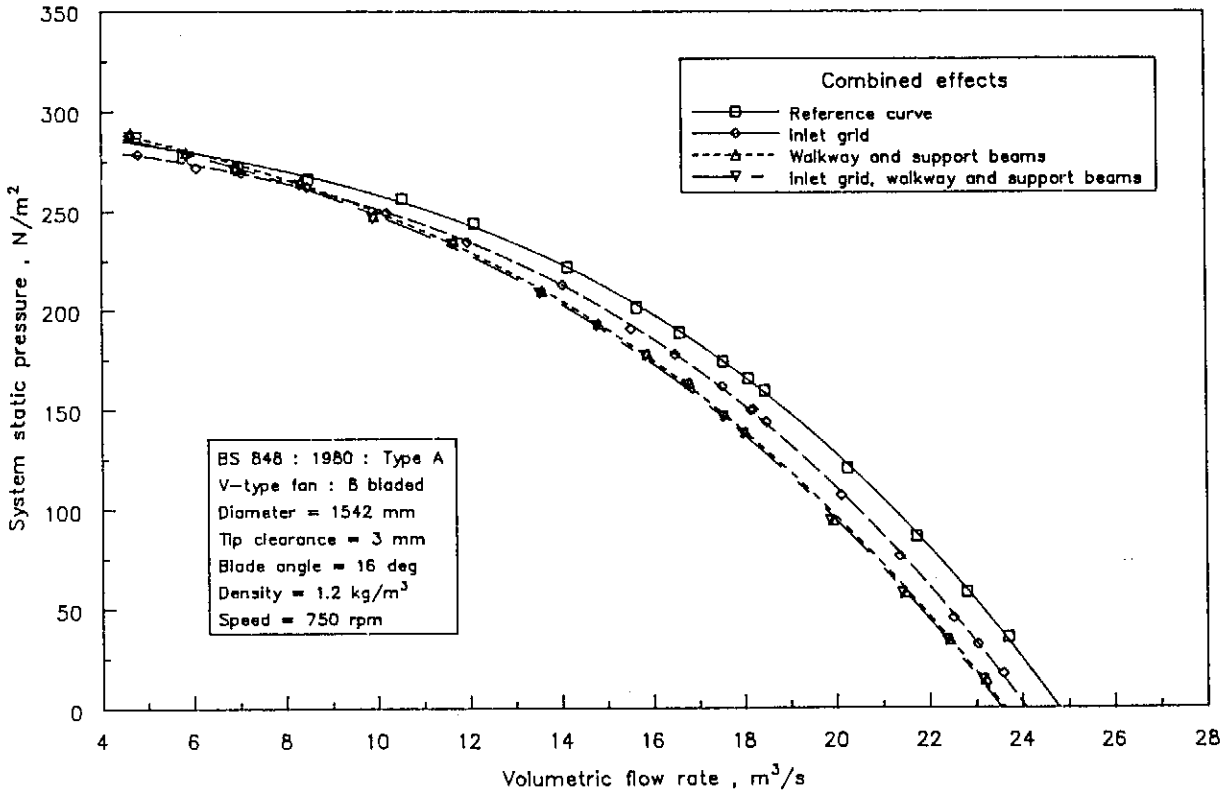

Figure A.3.1: Combined system static pressure effects : Excluding heat exchangers

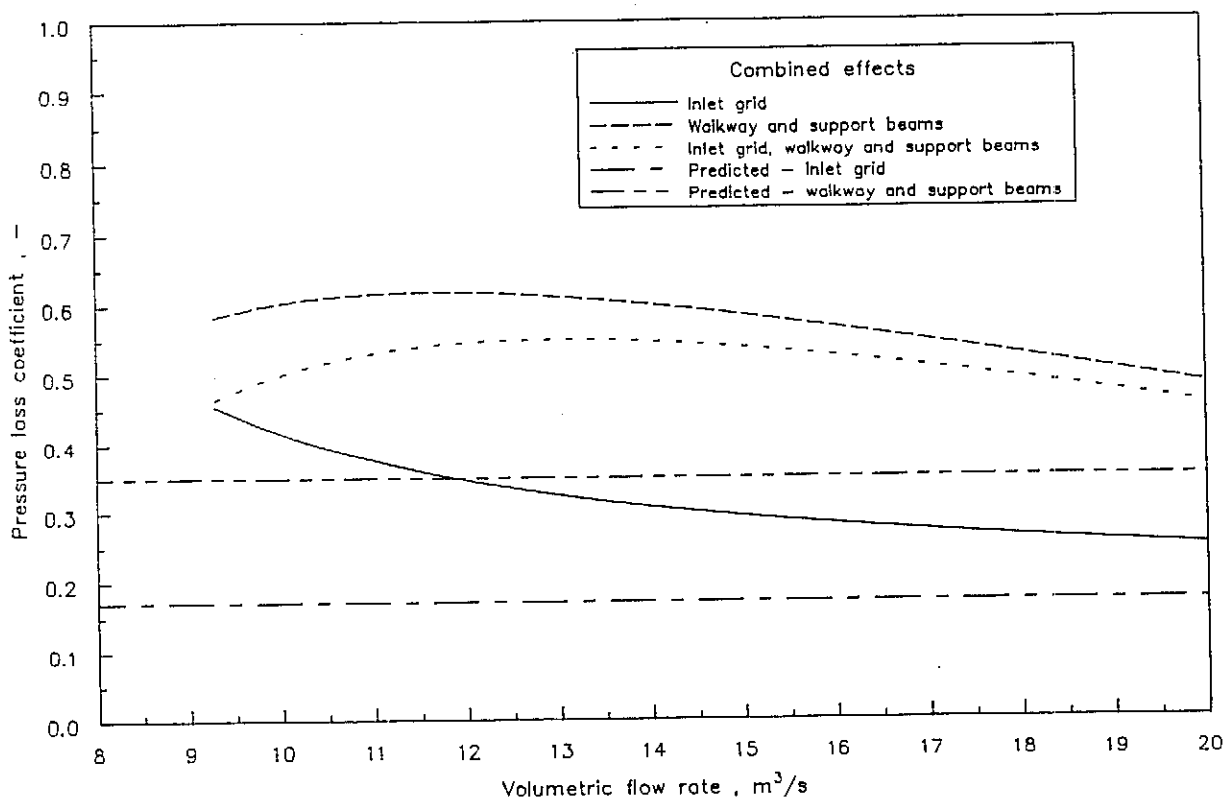

Figure A.3.2: Combined pressure loss coefficient effects : Excluding heat exchangers

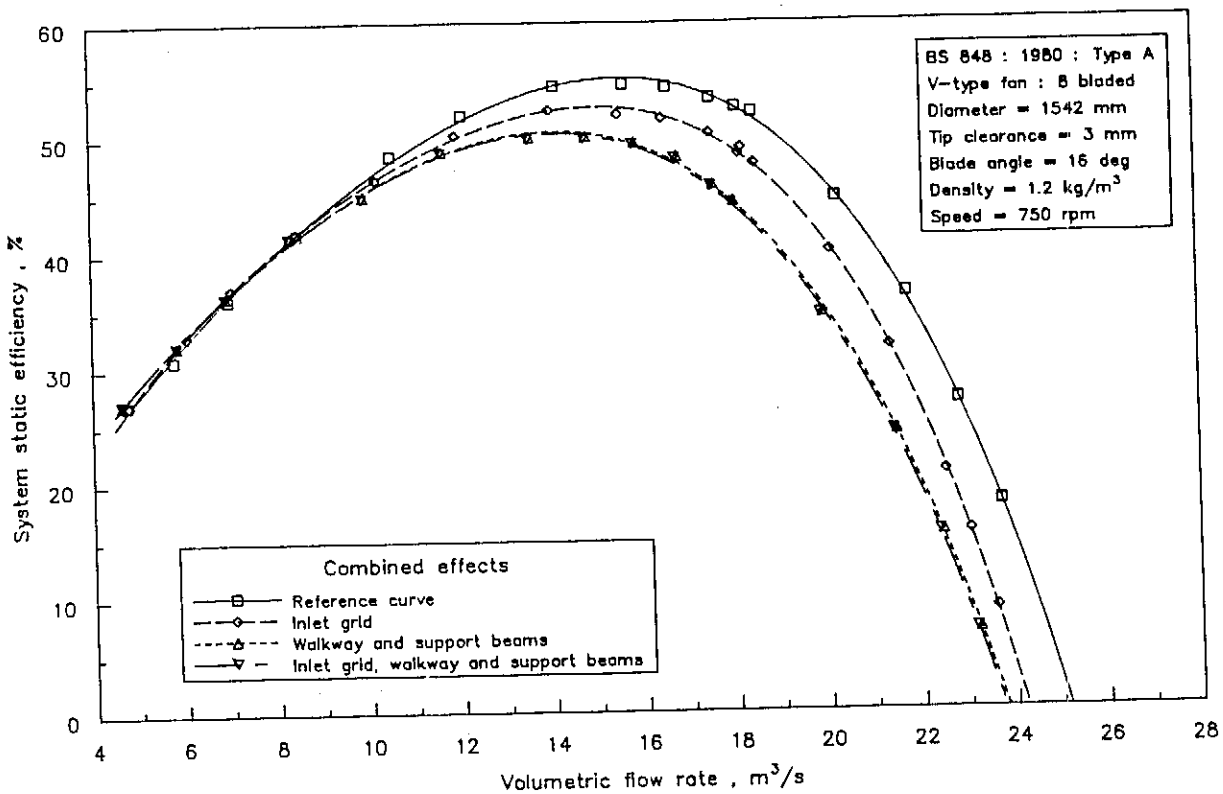

Figure A.3.3: Combined system static efficiency effects : Excluding heat exchangers

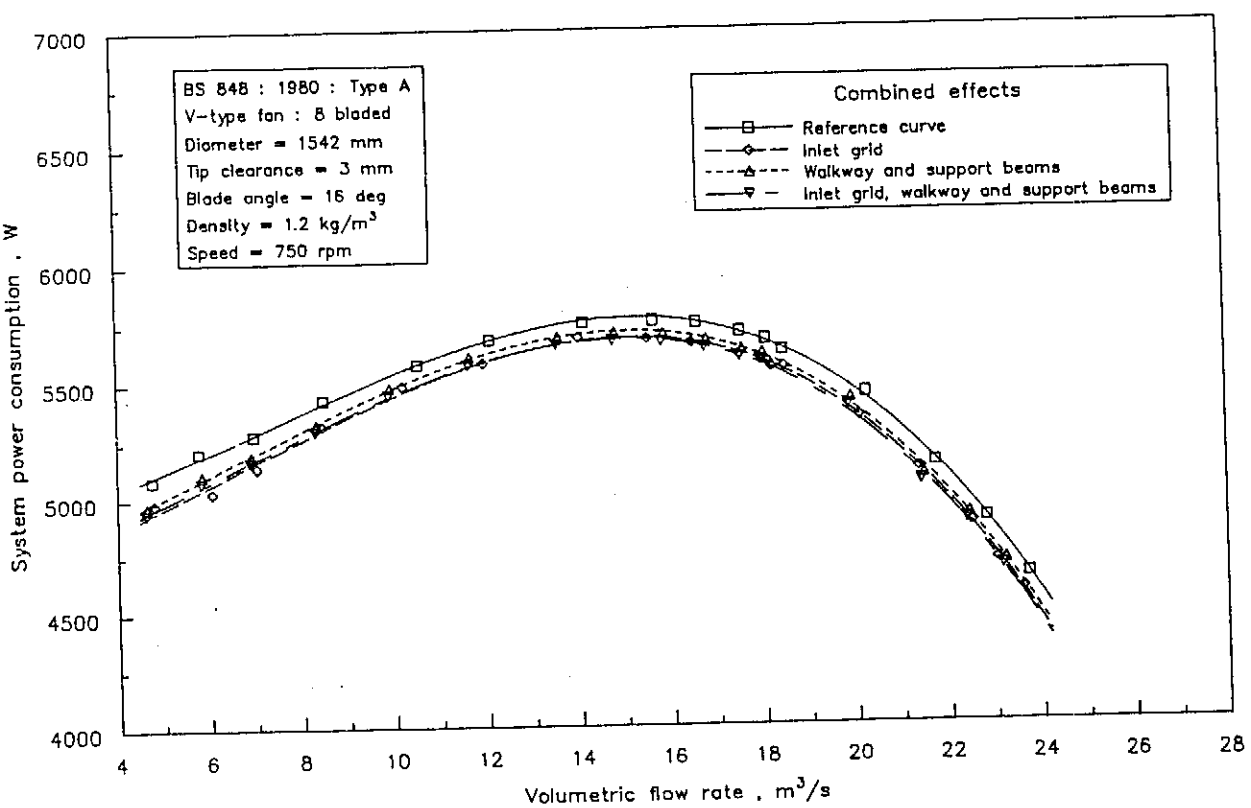

Figure A.3.4: Combined system power consumption effects : Excluding heat exchangers

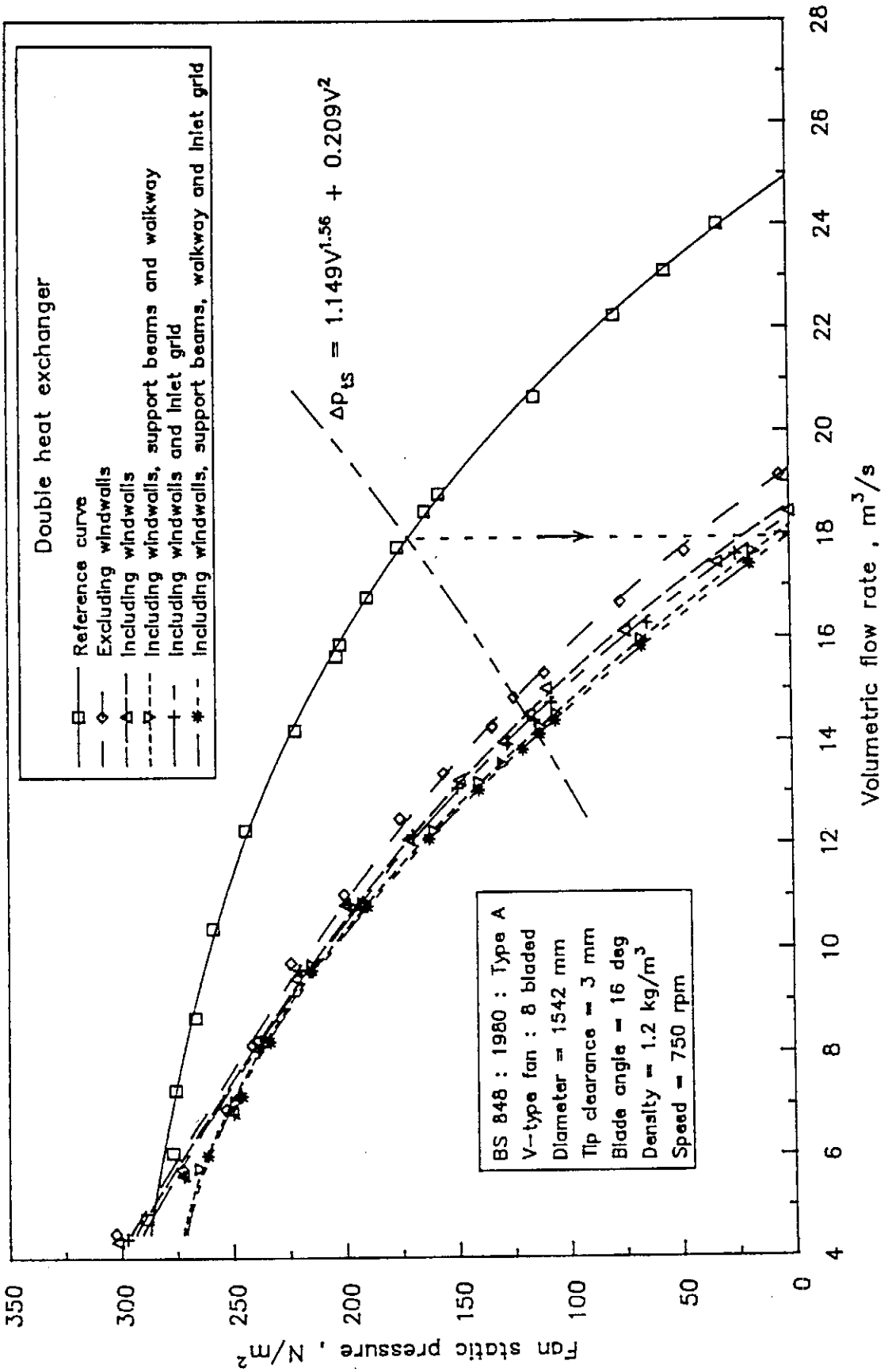

Figure A.3.5: Combined system static pressure effects : Including heat exchangers

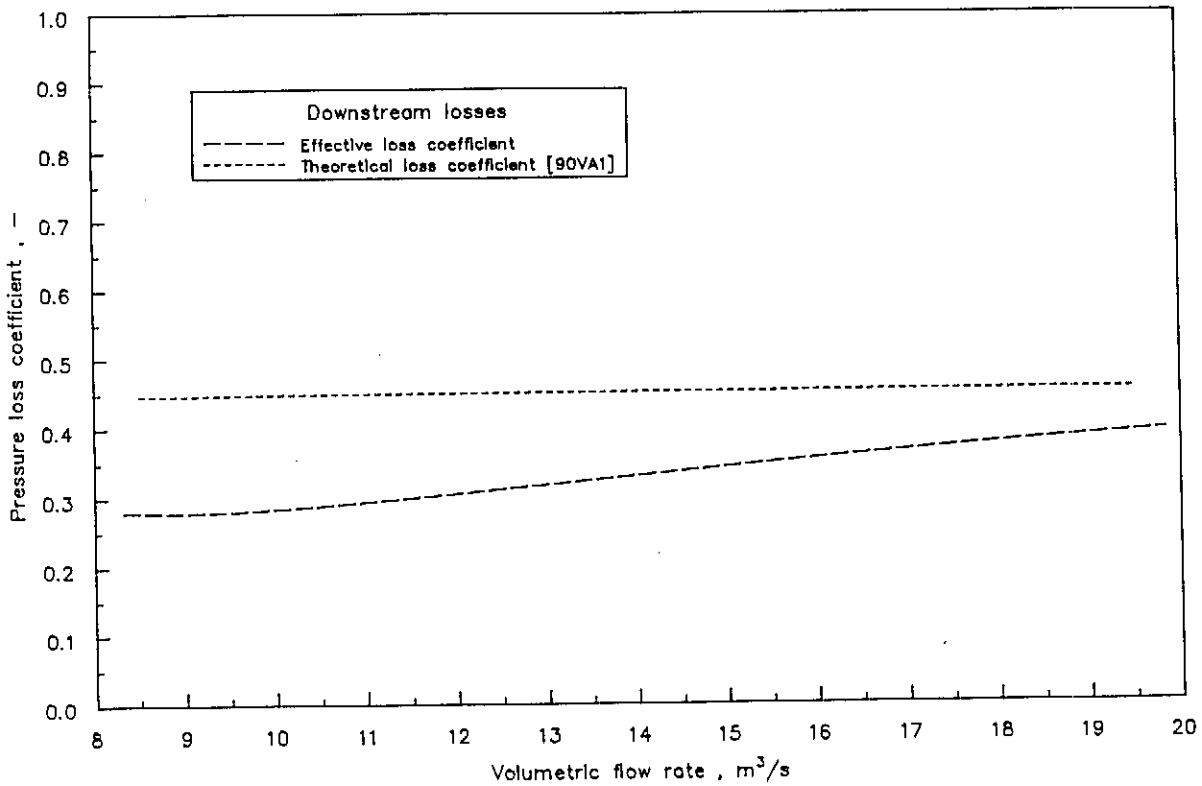

Figure A.3.6: Downstream pressure loss coefficient effects : Including heat exchangers

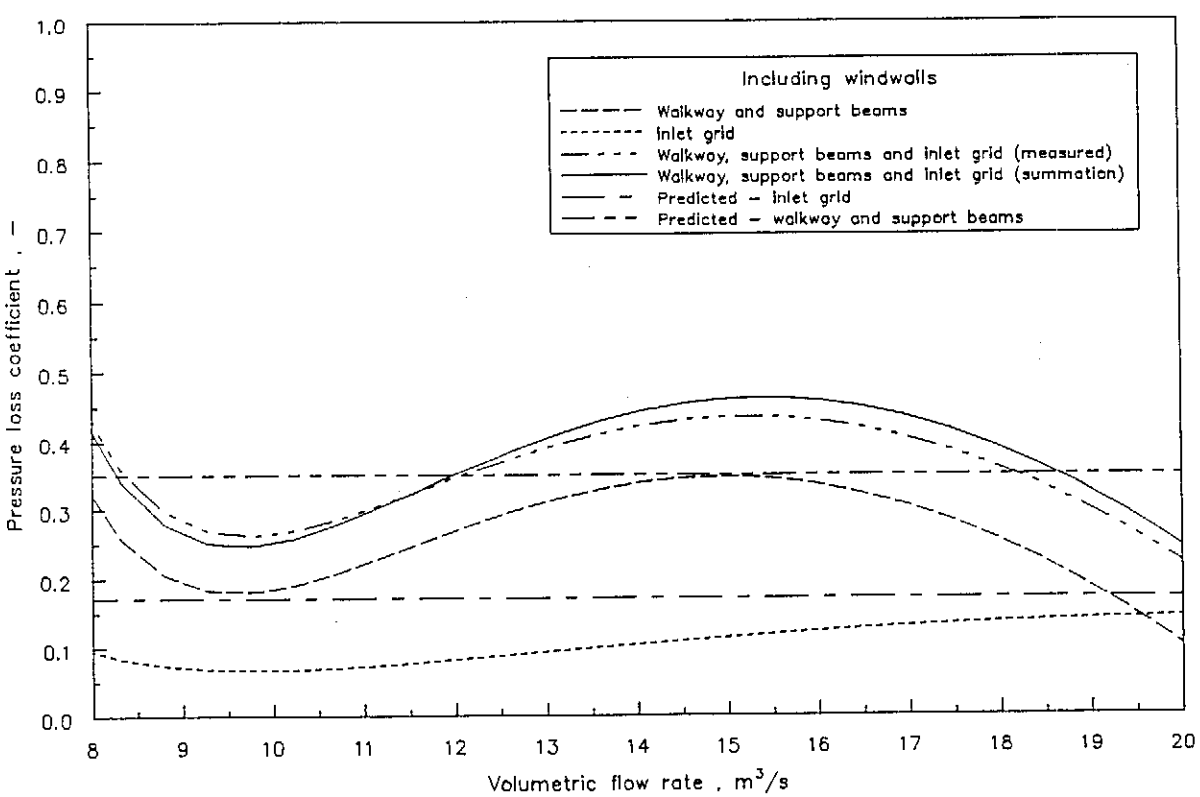

Figure A.3.7: Combined pressure loss coefficient effects : Including heat exchangers

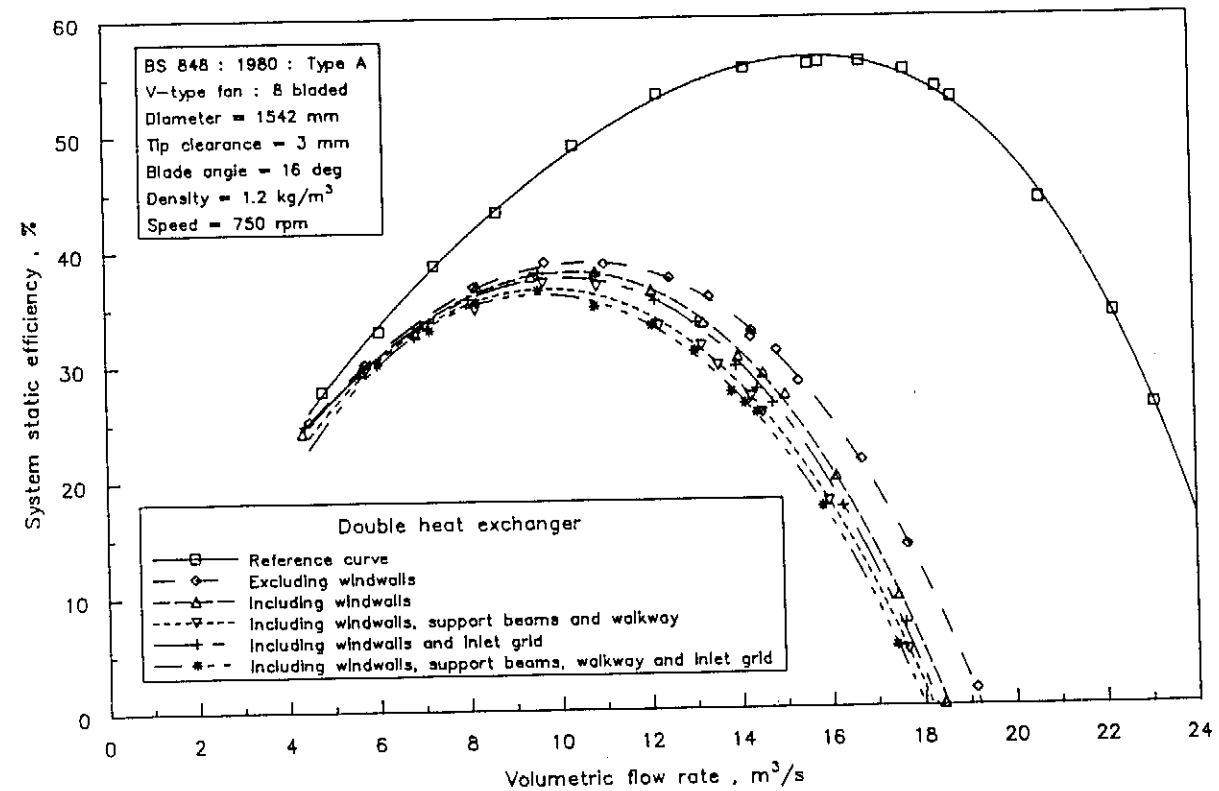

Figure A.3.8: Combined system static efficiency effects : Including heat exchangers

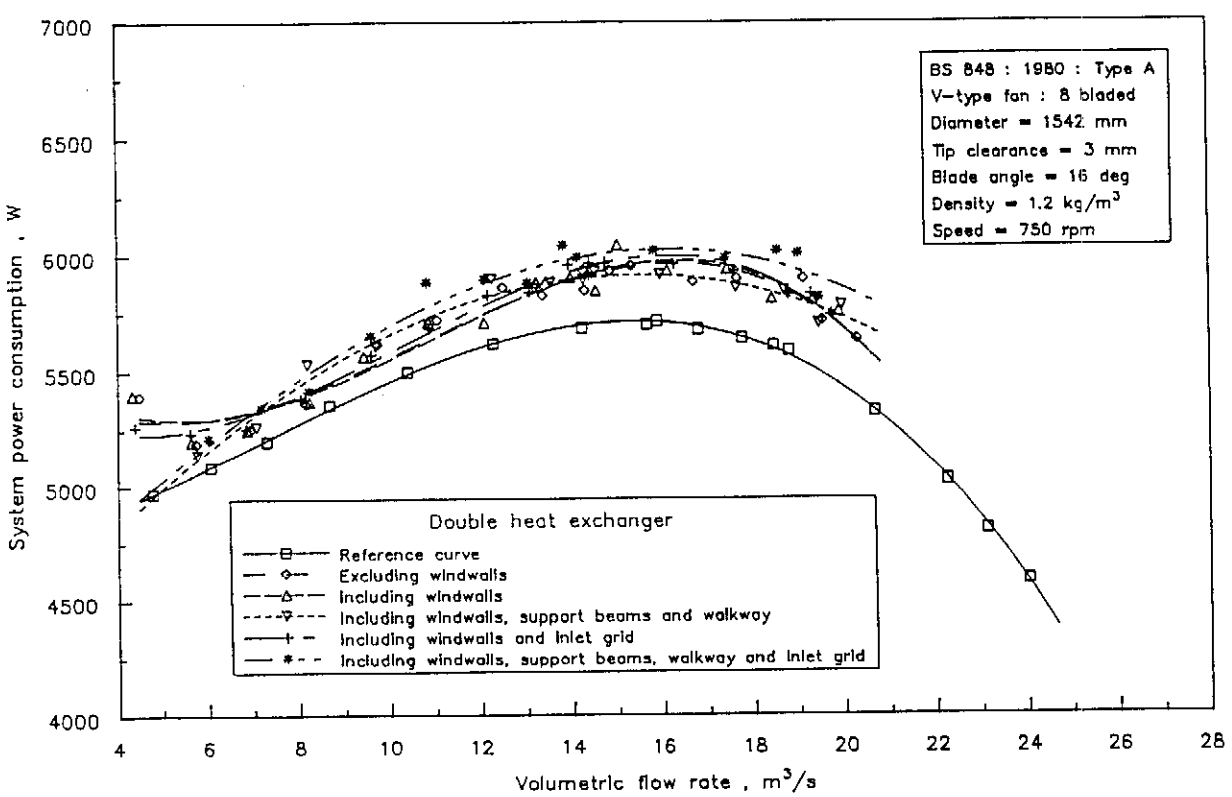

Figure A.3.9: Combined system power consumption effects : Including heat exchangers

A.4 Velocity distributions

The velocity distributions for different fan installations are presented in this section.

Figures A.4.1 to A.4.3 refer to the three velocity components at fan inlet in a spherical coordinate system. The velocity distributions for the same components at outlet from the fan are presented as figures A.4.4 to A.4.6. The velocity profiles in all these figures are determined with the five hole probe described in appendix C. The fan system includes only the fan inlet shroud and the fan rotor. Three different volume flow rates are used to indicate the influence of volume flow rate on the velocity distributions. Also important is to note that an absolute flow angle of beyond 30° is beyond the range of applicability of the probe. This explains the smaller amount of relevant data with an increase in kinetic energy flux coefficient (α).

The three dimensional velocity distributions presented in figures A.4.7 and A.4.8 are determined with a $\phi 225\ mm$ vane anemometer traversed 25 mm downstream from the finned tube bundles. The fan inlet total pressure for both the single (figure A.4.7) and the double (figure A.4.8) heat exchangers is atmospheric pressure. This corresponds to volumetric flow rates of 23 m^3/s and 19,2 m^3/s installations incorporating single and double heat exchangers respectively.

The velocity profiles at the outlet from the unit (between two adjacent apexes of the A-frames) are measured using the same $\phi 225\ mm$ vane anemometer at 7 different planes. These profiles are independent of the location of the measuring plane which dictates the decision to present the unit outlet velocity distribution as the average of all eight measured profiles (refer to figure A.4.10).

Figure A.4.11 compares the velocity distribution parallel to the bundle surface for tests pertaining to a system excluding and including windwalls.

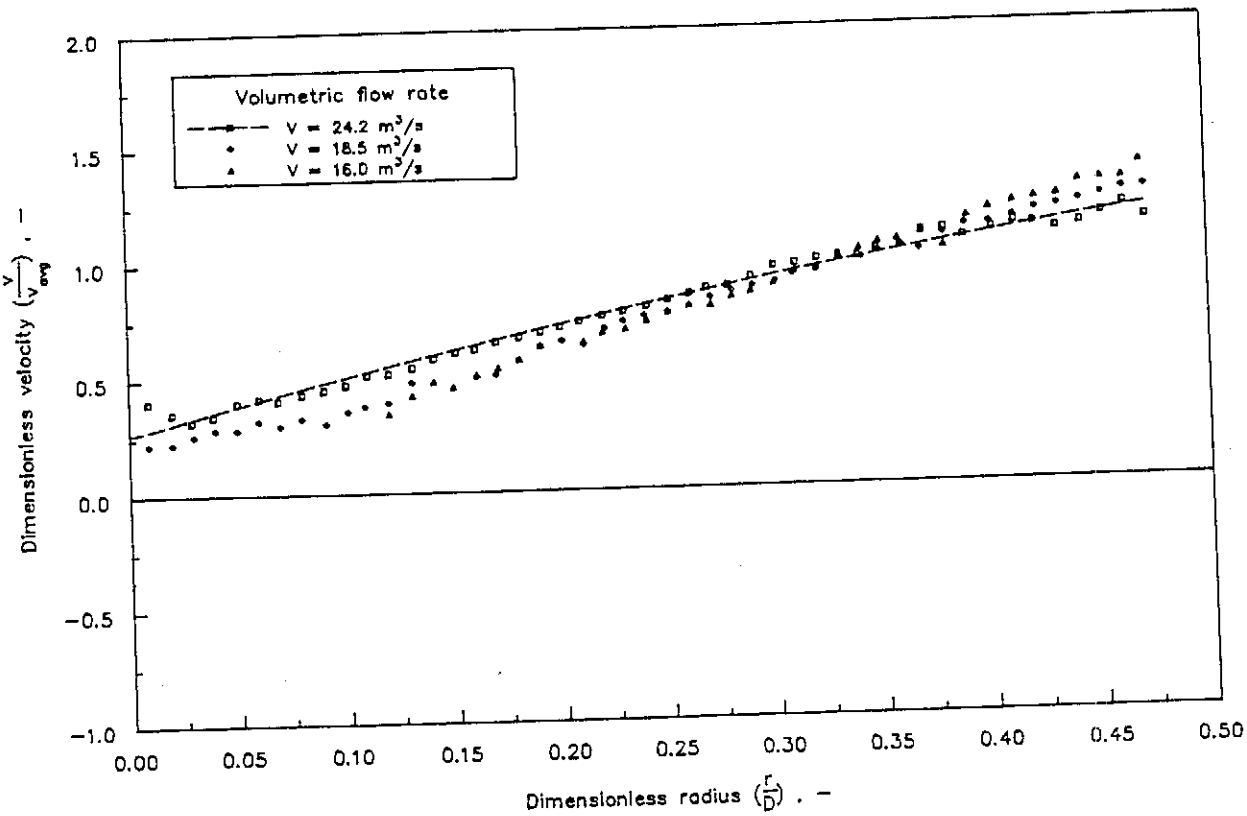

Figure A.4.1: Fan inlet velocity distribution : Axial component

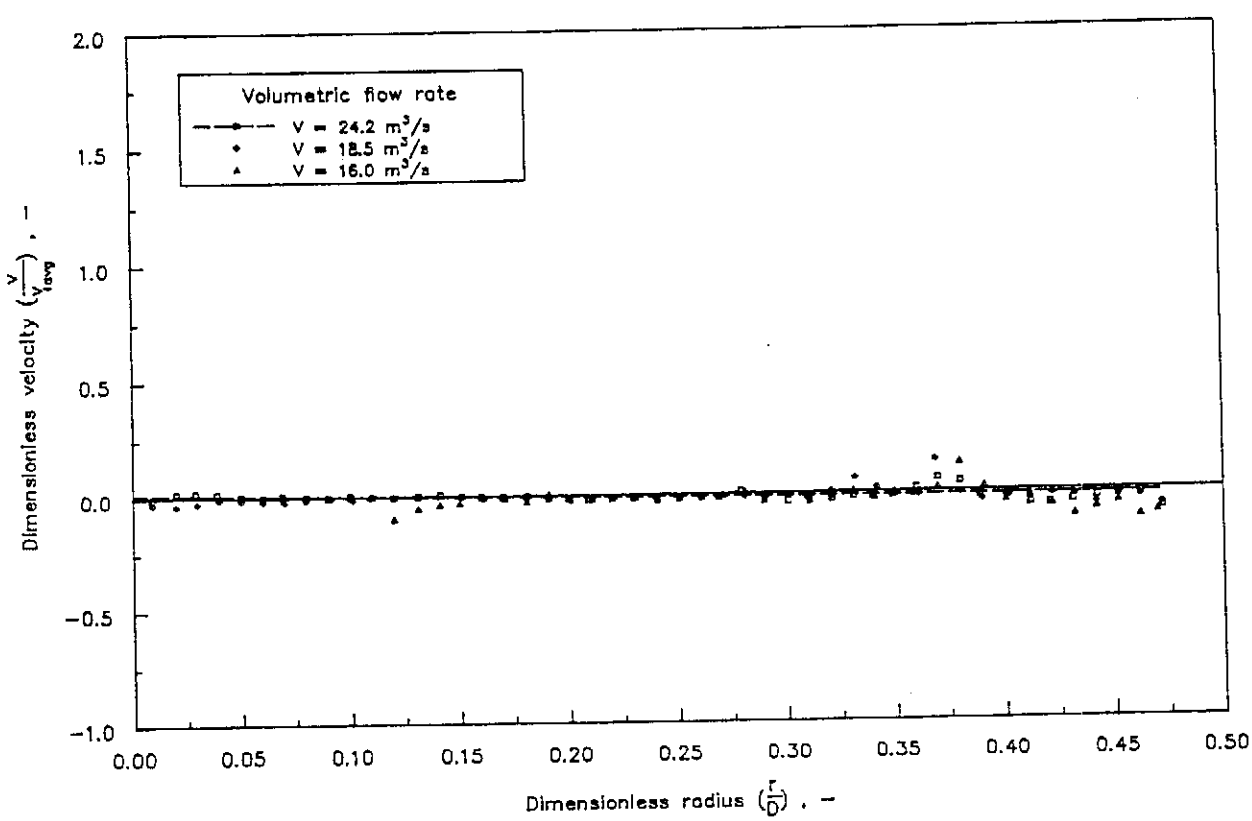

Figure A.4.2: Fan inlet velocity distribution : Radial component

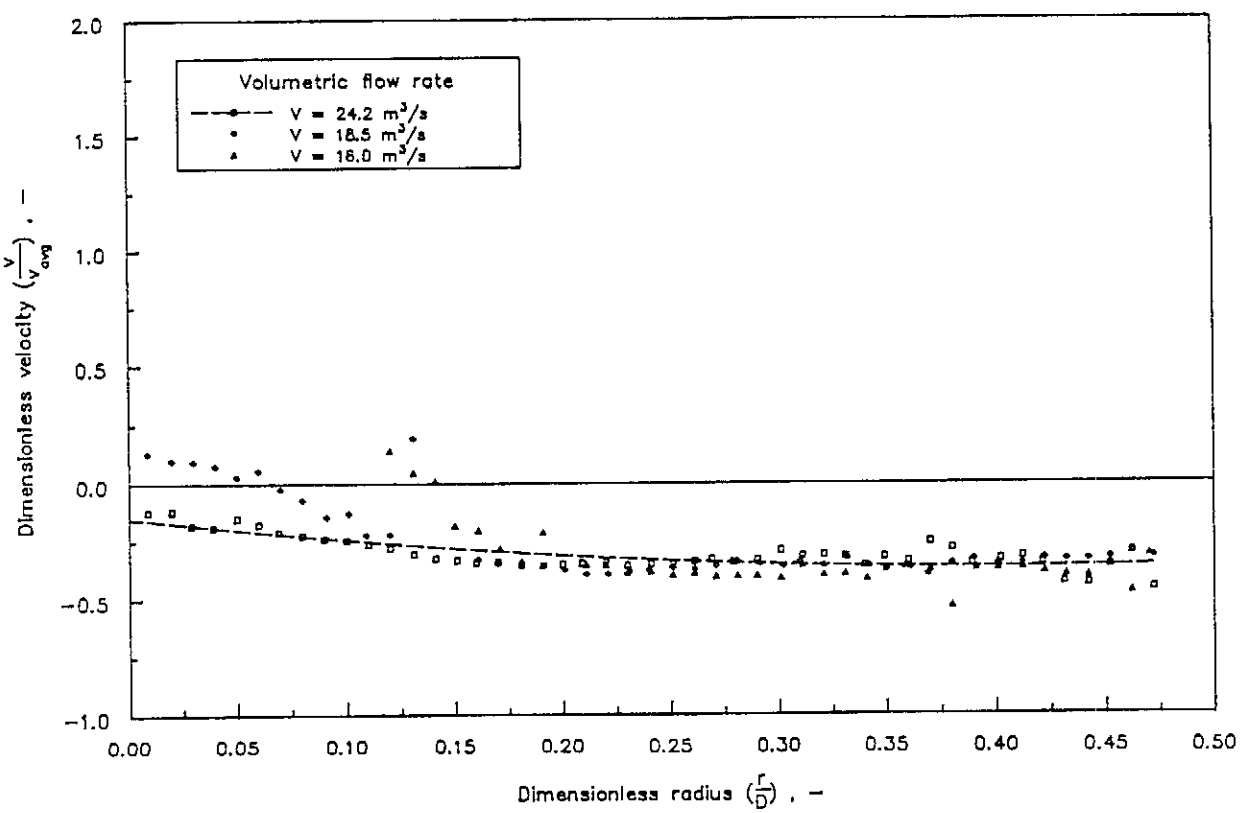

Figure A.4.3: Fan inlet velocity distribution : Tangential component

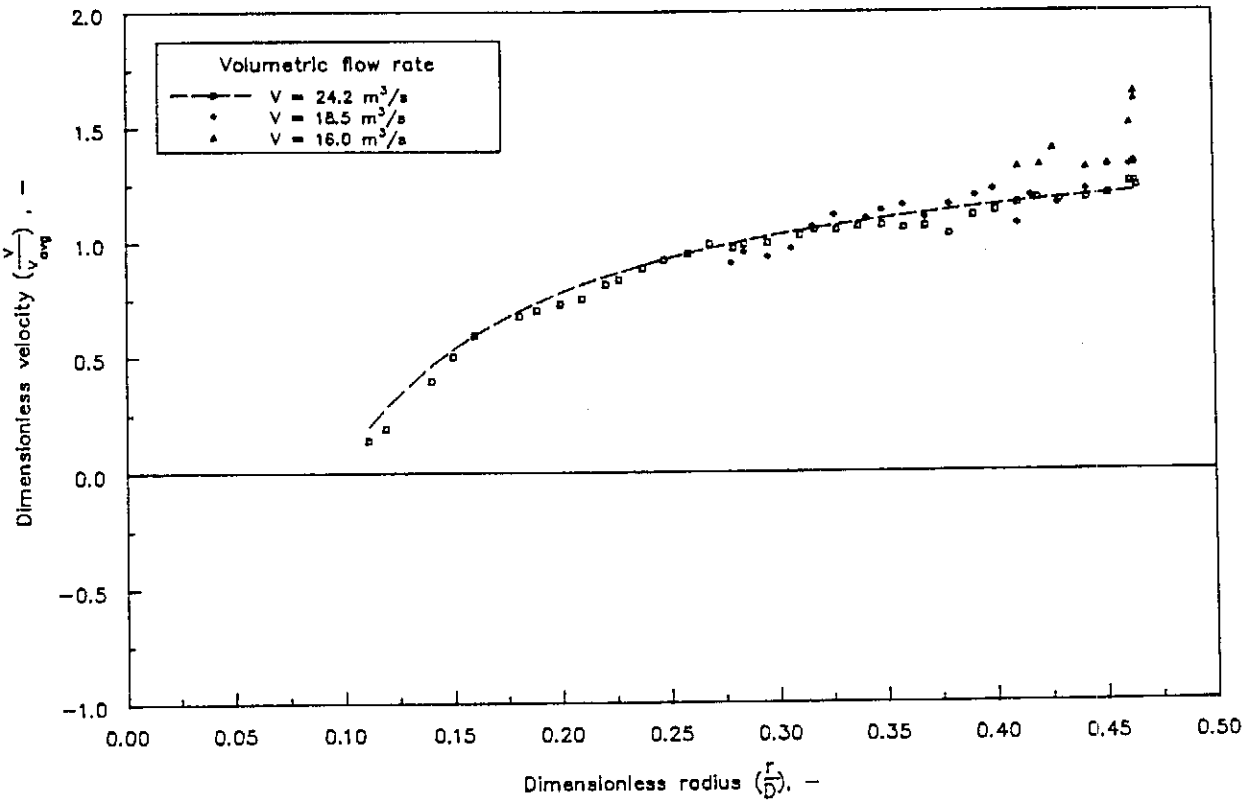

Figure A.4.4: Fan outlet velocity distribution : Axial component

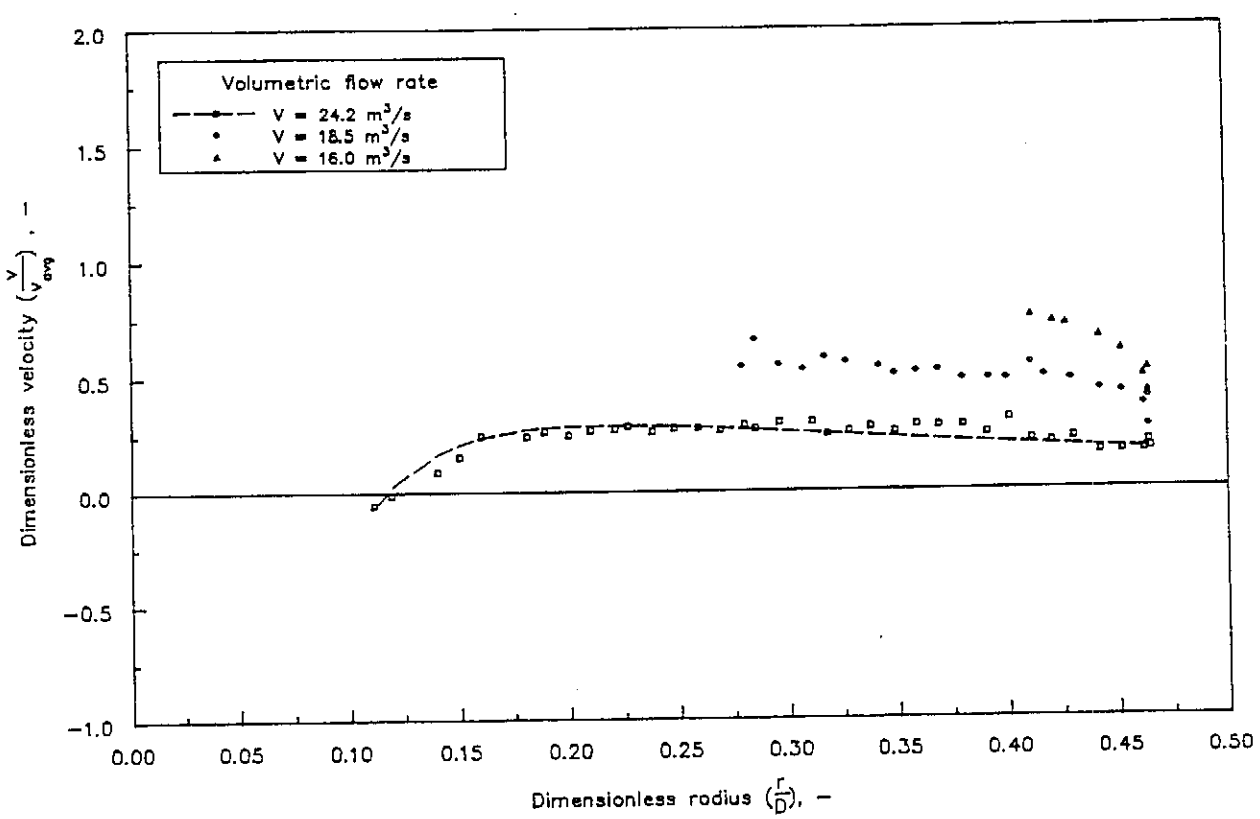

Figure A.4.5: Fan outlet velocity distribution : Radial component

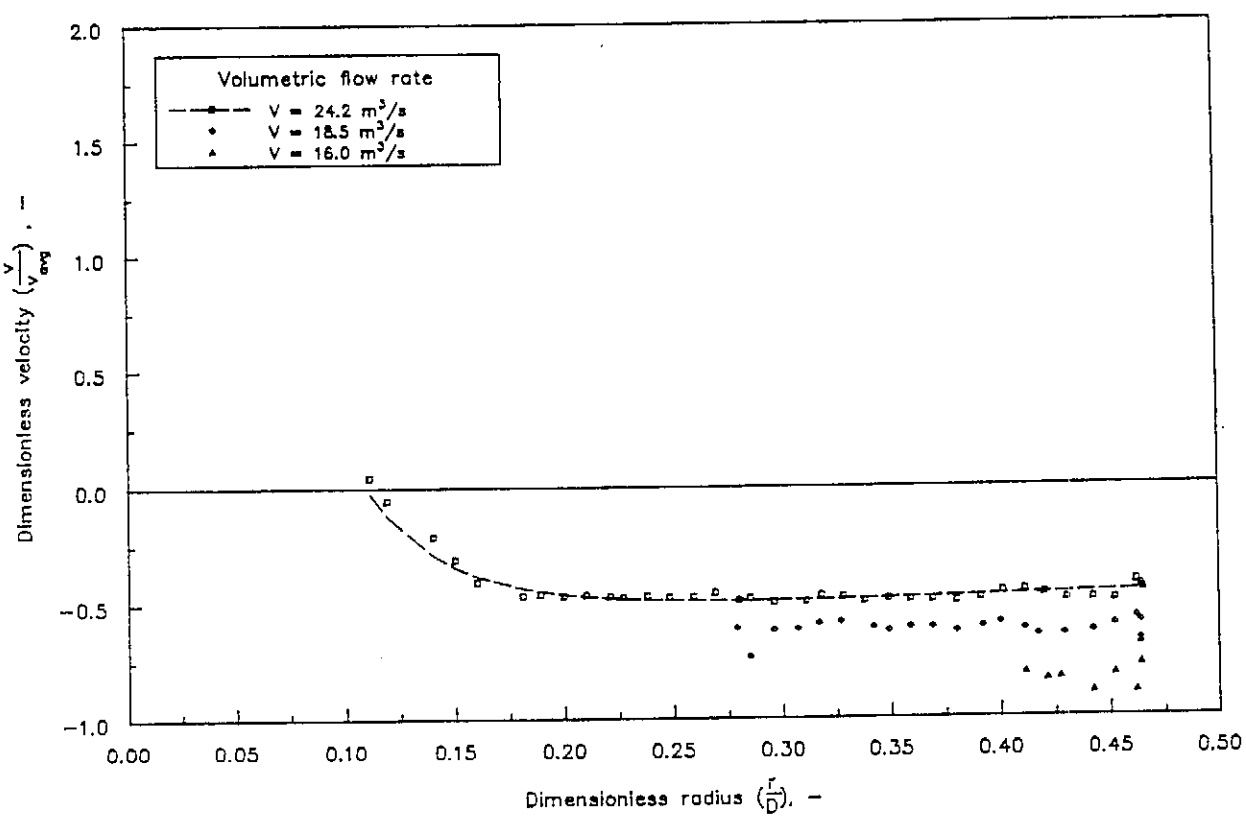

Figure A.4.6: Fan outlet velocity distribution : Tangential component

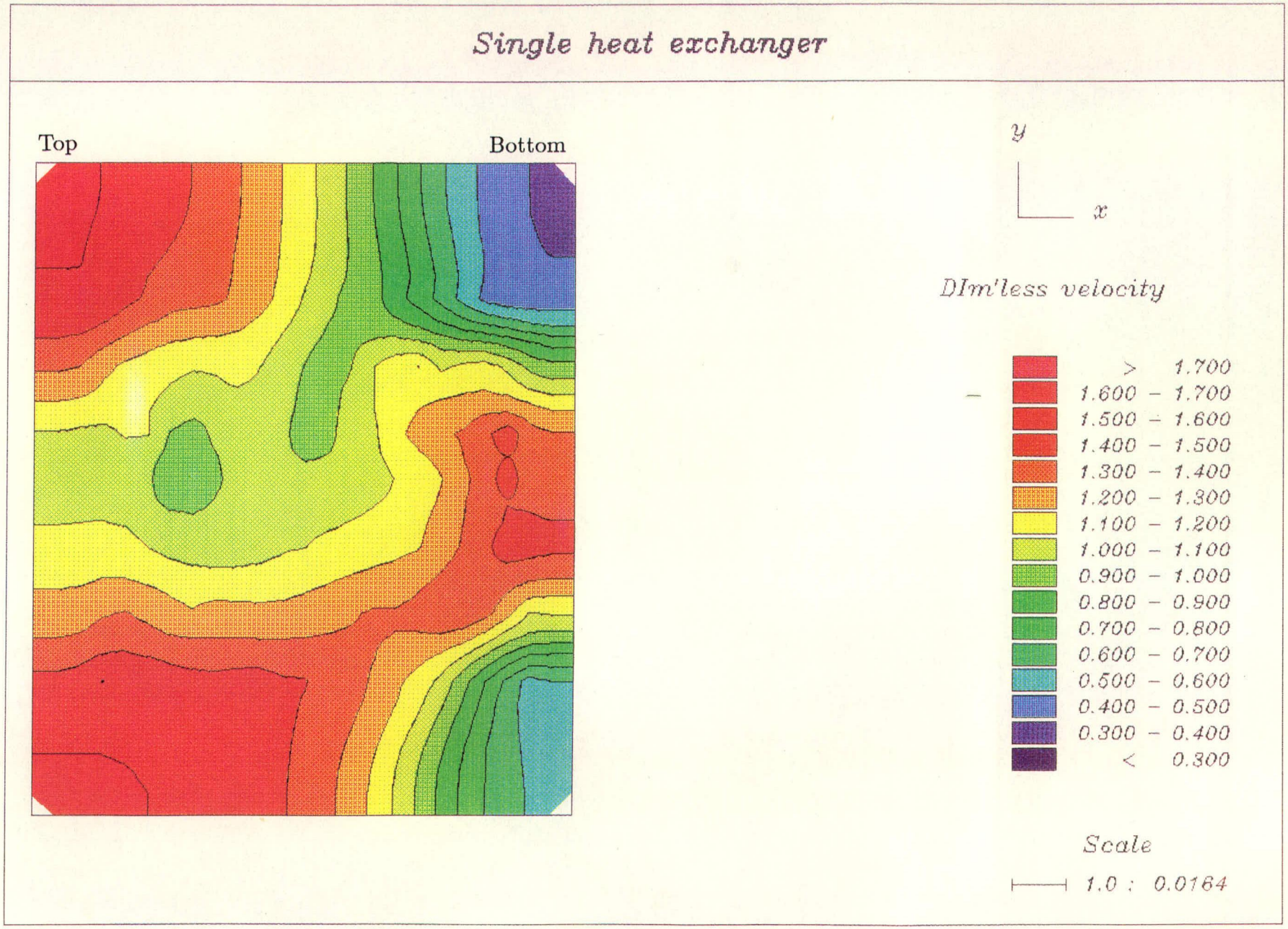

Figure A.4.7: Bundle outlet velocity distribution : Single heat exchanger without windwalls

Figure A.4.8: Bundle outlet velocity distribution : Double heat exchanger without wind-walls

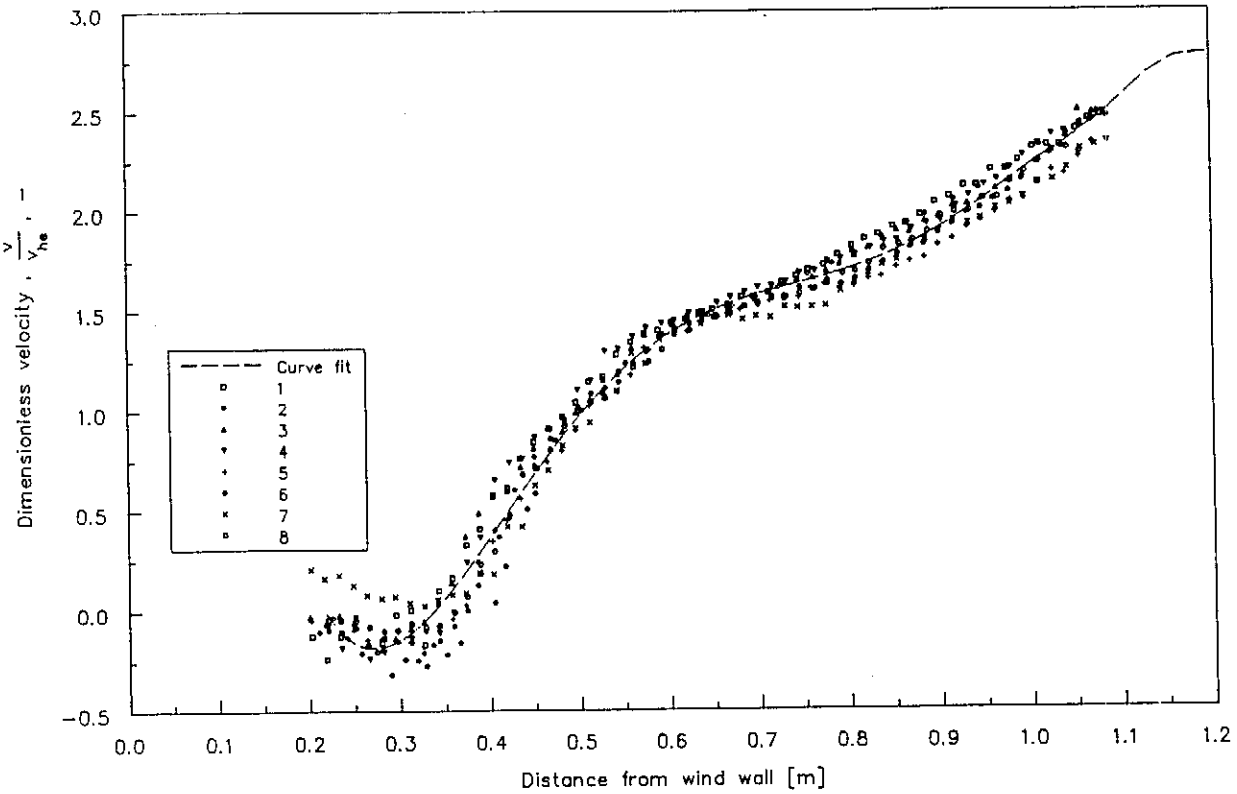

Figure A.4.9: Unit outlet velocity distribution : Data points

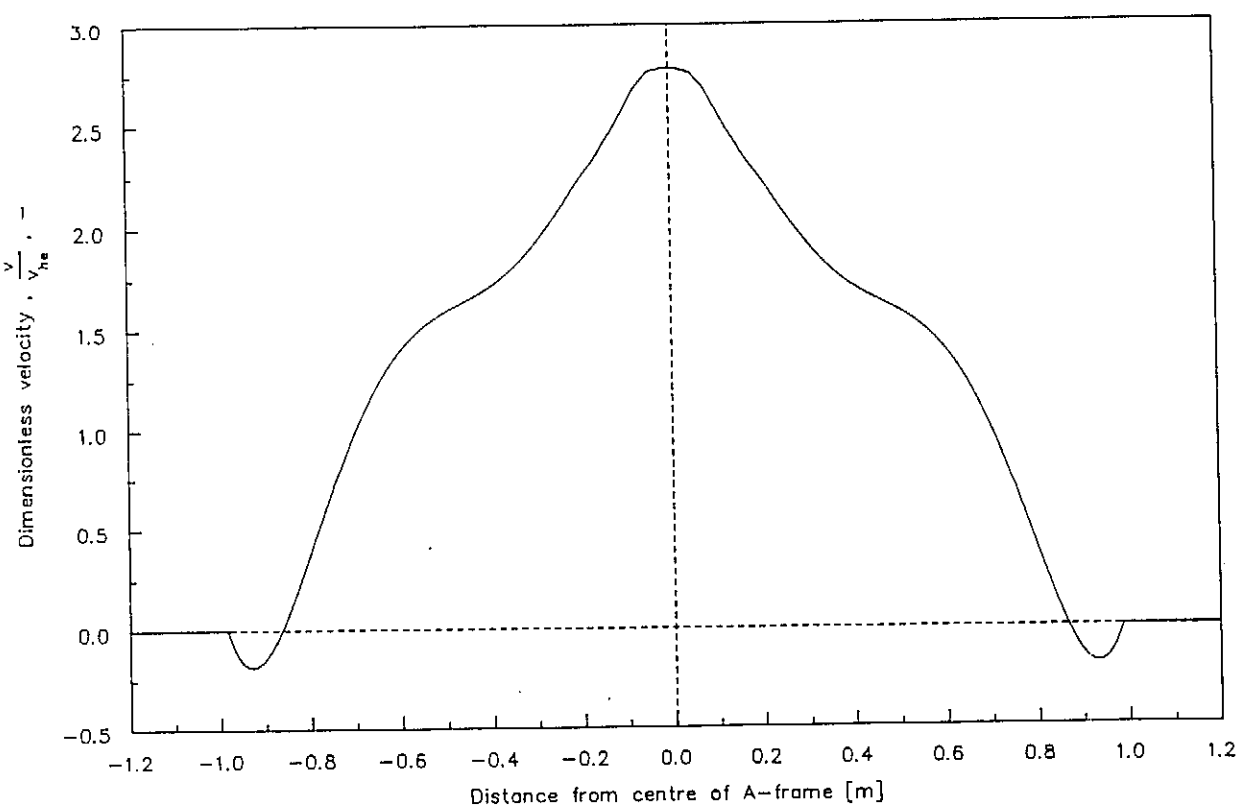

Figure A.4.10: Unit outlet velocity distribution : Average profile

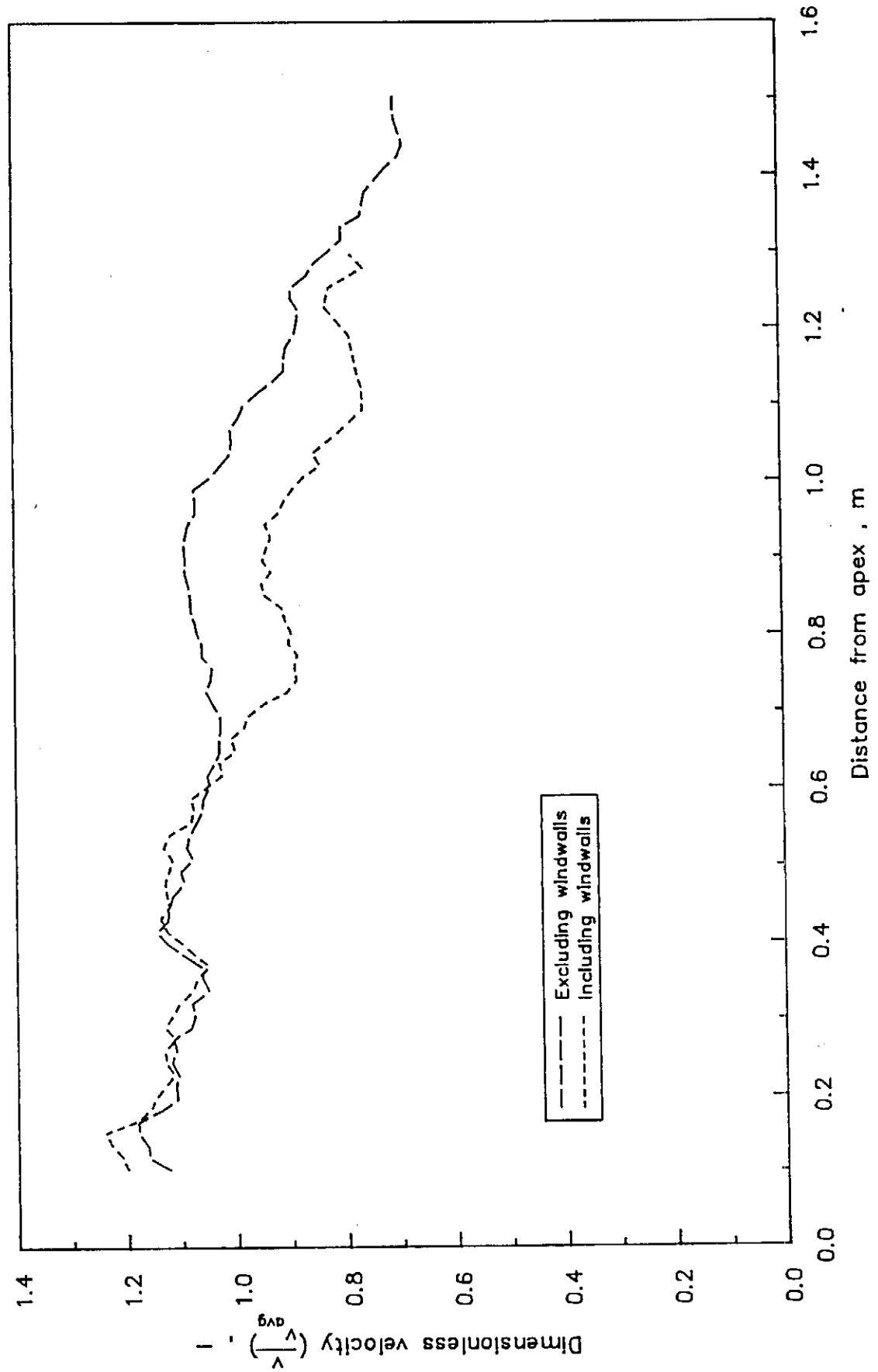

Figure A.4.11: Bundle outlet velocity distribution : Windwall effects

Appendix B - Sample calculations and theoretical derivations

B.1 Fan characteristic calculations

The data point with the following parameters is used as an example:

Blade angle = $16\ ^{o}$

Tip clearance = $3\ mm$

Rotational speed $(N) = 749\ rpm$

Input torque $(T) = 77{,}41\ N.m$

Inlet bellmouth pressure $(\Delta p_{bell}) = 244{,}43\ N/m^2$

Settling chamber pressure $(\Delta p_{sett}) = -213{,}68\ N/m^2$

Ambient temperature $(T_{amb}) = 20\ ^{o}C$

Ambient pressure $(p_{amb}) = 757{,}6\ mmHg$

Local gravitational acceleration = $9{,}796\ m/s^2$

The ambient pressure may be expressed as

$$\begin{aligned} p_{amb} &= 757{,}6 \times 13{,}55 \times 9{,}796 \\ &= 100\,560{,}64\ N/m^2 \end{aligned}$$

The corresponding ambient air density follows from the universal gas law

$$\begin{aligned} \rho_{amb} &= \frac{p_{amb}}{RT_{amb}} \\ &= \frac{100\,560{,}64}{(287{,}08)(273{,}15+20)} \\ &= 1{,}1942\ kg/m^3 \end{aligned} \qquad \text{(B.1)}$$

The density of air in the settling chamber follows from equation (2.45)

$$\rho_{sett} = \rho_{amb}\frac{(p_{amb} + \Delta p_{sett})}{p_{amb}} \tag{B.2}$$

$$= 1,1941\frac{(100\,499,05 - 213,68)}{100499,05}$$

$$= 1,1916\,kg/m^3$$

The air mass flow rate through the fan follows from the calibration of the inlet bellmouth (refer to section D.1)

$$\dot{m} = \alpha\epsilon\,\frac{\pi d_{bell}^2}{4}\,\sqrt{2\rho_{amb}\Delta p_{bell}} \tag{B.3}$$

$$= 0,9803\,\frac{\pi(1,008)^2}{4}\,\sqrt{2(1,1942)(244,43)}$$

$$= 18,8989\,kg/s$$

In the settling chamber, the dynamic pressure is presented by equation (2.47)

$$p_{dsett} = \frac{\dot{m}^2}{2\rho_{sett}A_{sett}^2} \tag{B.4}$$

$$= \frac{(18,8989)^2}{2(1,1916)(4\times 4)^2}$$

$$= 0,59\,N/m^2$$

The total pressure drop across the fan is determined from equation (2.46)

$$\Delta p_{t_{sett}} = \Delta p_{s_{sett}} + p_{d_{sett}} \tag{B.5}$$

$$= -213,68 + 0,59$$

$$= -213,09\,N/m^2$$

The fan static pressure follows from equation (2.48)

$$\Delta p_{sF} = -\Delta p_{t_{sett}} \tag{B.6}$$

$$= 213,09\ N/m^2$$

The power input to the fan shaft is related to the measured rotational speed and input torque through equation (2.50)

$$P_R = \frac{2\pi N}{60} T \tag{B.7}$$

$$= \frac{2\pi(749)}{60}(77,41)$$

$$= 6\,071,66W$$

From equation (2.50), the volumetric flow rate of air through the system is

$$V = \frac{\dot{m}}{\rho_{sett}} \tag{B.8}$$

$$= \frac{18,8989}{1,1916}$$

$$= 15,8606\ m^3/s$$

The fan static efficiency follows from equation (2.51)

$$\eta_{sF} = \frac{\Delta p_{sF} V}{P_R} \times 100 \tag{B.9}$$

$$= \frac{(213,09)(15,8606)}{6\,071,66} \times 100$$

$$= 55,67\,\%$$

The final step is to scale the results to be representative of data generated at $\rho' = 1,2\ kg/m^3$ and $N' = 750\ rpm$ using equations (2.53) to (2.56). The diameter ratio equals 1 because the scaling is performed for the same fan at different values for density and rotational speed.

$$V' = V\left(\frac{N'}{N}\right) \tag{B.10}$$

$$= 15,8606\left(\frac{750}{749}\right)$$

$$= 15,882\, m^3/s$$

$$\Delta p'_{sF} = \Delta p_{sF}\left(\frac{N'}{N}\right)^2\left(\frac{\rho'}{\rho_{sett}}\right) \tag{B.11}$$

$$= 213,09\left(\frac{750}{749}\right)^2\left(\frac{1,200}{1,1916}\right)$$

$$= 215,18\, N/m^2$$

$$P'_R = P_R\left(\frac{N'}{N}\right)^3\left(\frac{\rho'}{\rho_{sett}}\right) \tag{B.12}$$

$$= 6\,071,66\left(\frac{750}{749}\right)^3\left(\frac{1,200}{1,1916}\right)$$

$$= 6\,139,21\, W$$

$$\eta'_{sF} = \eta_{sF} = 55,67\,\% \tag{B.13}$$

B.2 Fan tip clearance

The method used to predict the losses in fan static pressure and volumetric flow rate, associated with an increase in fan tip clearance, is discussed in this section. The basic assumption incorporated into this method is that the fan static pressure curves for different tip clearances can be approximated by $\Delta p_{sF} = mV^2 + c$. Figure A.2.1 illustrates the reasoning behind such an approximation. A distinction is made between parallel and non-parallel fan static pressure curves presented on graphs similar to figure A.2.2. Parallel curves will all have the same gradient (m) whilst non-parallel curves each has a unique gradient.

It is also argued that the drop in performance of the fan should be related to the losses in a specific system. Monroe [79MO1], for instance, investigated the drop in pressure and efficiency at constant volumetric flow rates. This method is not representative of the reduction in fan performance if the same fan is installed in the same system with different tip

clearances. An arbitrary system resistance line (through the point of maximum efficiency) is used to illustrate the argument (refer to figure A.2.1).

Classically, the system losses are assumed to be directly proportional to the square of the velocity, or volume flow rate, through the system (see section 2.7). The definition of pressure loss coefficients states that

$$\begin{aligned} \Delta p &= K \frac{1}{2}\rho \bar{v}^2 \\ &= kV^2 \end{aligned} \tag{B.14}$$

$$\text{where } k = \frac{K\rho}{2A^2}$$

$$\text{and } V = \bar{v}A$$

The reduction in fan performance is indicated by fan static pressure and volumetric flow rate ratios. These ratios are defined as:

$$\text{Fan static pressure ratio} = \frac{(\Delta p_{sF})_{red}}{(\Delta p_{sF})_{id}} \tag{B.15}$$

$$\text{Volumetric flow rate ratio} = \frac{V_{red}}{V_{id}} \tag{B.16}$$

In the application of fan characteristic curves to specific systems, the operating point is determined by obtaining the intercept between the increase in pressure due to the fan (fan static pressure) and the resistance of the system. This means that the following relationship between volumetric flow rate and fan static pressure at the operating point can be deduced.

$$\begin{aligned} (\Delta p_{sF})_{id} &= \Delta p_{id} \\ &= kV_{id}^2 \end{aligned} \tag{B.17}$$

Similarly $(\Delta p_{sF})_{red} = kV_{red}^2$

$$\text{thus } \frac{V_{id}}{V_{red}} = \sqrt{\frac{(\Delta p_{sF})_{red}}{(\Delta p_{sF})_{id}}} \tag{B.18}$$

The direct relationship between fan static pressure and volumetric flow rate loss ratios for the same system reduces the number of calculations required to predict the effect of tip clearance on the fan performance. A more general definition of the loss ratios can be formulated by determining an average value valid for systems having pressure loss coefficients in the practical range of application of the fan (say k ranges between k_1 and k_2). The average fan static pressure ratio for this range is equated as

$$\left(\frac{(\Delta p_{sF})_{red}}{(\Delta p_{sF})_{id}}\right)_{avg} = \frac{\int_{k_1}^{k_2} \frac{(\Delta p_{sF})_{red}}{(\Delta p_{sF})_{id}} dk}{\int_{k_1}^{k_2} dk} \tag{B.19}$$

B.2.1 Determination of flow and pressure ratios (Parallel curves)

A case study is performed to determine the pressure and volumetric flow rate ratios for a reduction in fan performance due to a specific tip clearance. Assume that the fan static pressure curve for the ideal case is given by

$$(\Delta p_{sF})_{id} = mV_{id}^2 + c_{id} \tag{B.20}$$

and that the reduced fan static pressure curve for the specific tip clearance is

$$(\Delta p_{sF})_{red} = mV_{red}^2 + c_{red} \tag{B.21}$$

Note that the gradient for these two cases is the same value m which follows from the assumption that the curves are parallel to each other. Also from the previously defined pressure drop due to losses in the system the following two equations can be derived for the operating points of each system

$$\Delta p_{id} = kV_{id}^2 \tag{B.22}$$

$$\Delta p_{red} = kV_{red}^2 \tag{B.23}$$

The operating point for the ideal situation is the point at which the fan static pressure and the system pressure loss are equal. These two pressures are eliminated by substitution, resulting in

$$kV_{id}^2 = mV_{id}^2 + c_{id}$$

$$\text{thus } V_{id}^2 = \frac{c_{id}}{k-m} \tag{B.24}$$

The same method can be used to derive the relationship for the reduced fan static pressure

$$V_{red}^2 = \frac{c_{red}}{k-m} \tag{B.25}$$

The fan static pressure ratio is therefore

$$\begin{aligned}
\frac{(\Delta p_{sF})_{red}}{(\Delta p_{sF})_{id}} &= \frac{mV^2 + c_{red}}{mV^2 + c_{id}} \\
&= \frac{\frac{mc_{red}}{k-m} + c_{red}}{\frac{mc_{id}}{k-m} + c_{id}} \\
&= \frac{\frac{kc_{red}}{k-m}}{\frac{kc_{id}}{k-m}} \\
&= \frac{c_{red}}{c_{id}} \qquad \text{(B.26)}
\end{aligned}$$

which is independent of the system resistance in which the fan is installed. The average ratios are

$$\text{Average fan static pressure ratio} = \frac{c_{red}}{c_{id}} \tag{B.27}$$

$$\text{Average volumetric flow rate ratio} = \sqrt{\frac{c_{red}}{c_{id}}} \tag{B.28}$$

To determine the values for these ratios is elementary once the values of m, c_{id} and c_{red} have been determined using a straight line least squares curve fit for each set of data relating to different tip clearances.

B.2.2 Determination of loss ratios (Non-parallel curves)

If the fan static pressure lines plotted against V^2 are not parallel, the derivation for the ratios is similar to the one stated in the previous section. The result is, however, somewhat more complex.

The fan static pressure curve for the ideal case is given by

$$(\Delta p_{sF})_{id} = m_{id} V_{id}^2 + c_{id} \tag{B.29}$$

and for the reduced fan static pressure curve for the specific tip clearance by

$$(\Delta p_{sF})_{red} = m_{red} V_{red}^2 + c_{red} \tag{B.30}$$

Note that the gradients for these two cases have unique values m_{id} and m_{red}.

Again from the previously defined pressure drop due to losses in the system the following two equations can be derived for the operating points of each system

$$\Delta p_{id} = k V_{id}^2 \tag{B.31}$$

$$\Delta p_{red} = k V_{red}^2 \tag{B.32}$$

These two pressures are eliminated by substitution, resulting in

$$k V_{id}^2 = m_{id} V_{id}^2 + c_{id}$$

$$\text{thus } V_{id}^2 = \frac{c_{id}}{k - m_{id}} \tag{B.33}$$

The same method can be used to derive the relationship for the reduced fan static pressure

$$V_{red} = \frac{c_{red}}{k - m_{red}} \tag{B.34}$$

The fan static pressure ratio is therefore

$$\frac{(\Delta p_{sF})_{red}}{(\Delta p_{sF})_{id}} = \frac{m_{red} V^2 + c_{red}}{m_{id} V^2 + c_{id}}$$

$$= \frac{\frac{m_{red} c_{red}}{k - m_{red}} + c_{red}}{\frac{m_{id} c_{id}}{k - m_{id}} + c_{id}}$$

$$= \frac{\frac{kc_{red}}{k - m_{red}}}{\frac{kc_{id}}{k - m_{id}}}$$

$$= \frac{c_{red}}{c_{id}} \left(\frac{k - m_{id}}{k - m_{red}} \right) \tag{B.35}$$

The average fan static pressure ratio is

$$\left(\frac{(\Delta p_{sF})_{red}}{(\Delta p_{sF})_{red}} \right)_{avg} = \frac{\int_{k_1}^{k_2} \frac{(\Delta p_{sF})_{red}}{(\Delta p_{sF})_{id}} dk}{\int_{k_1}^{k_2} dk}$$

$$\text{where } \int_{k_1}^{k_2} \frac{(\Delta p_{sF})_{red}}{(\Delta p_{sF})_{id}} dk = \int_{k_1}^{k_2} \frac{c_{red}}{c_{id}} \left(\frac{k - m_{id}}{k - m_{red}} \right) dk$$

$$= \frac{c_{red}}{c_{id}} \left[(k_2 - k_1) + (m_{red} - m_{id}) \ln \left(\frac{k_2 - m_{red}}{k_1 - m_{red}} \right) \right] \tag{B.36}$$

B.3 Experimental predictions of pressure loss coefficients

Flow losses in a fan application system due to support structures and/or inlet screens are commonly expressed as

$$\Delta p_{tot} = K \frac{1}{2} \rho \bar{v}^2 \tag{B.37}$$

where $\bar{v}$ represents the average velocity through the channel (section 2.7).

The assumption of a constant value for the loss coefficient (K) is only valid for purely turbulent flow at higher Reynolds numbers. As an illustration it was found that the total pressure loss coefficient remains constant for normal flow across round-wire gauzes having Reynolds numbers (based on wire diameter) in excess of 2 000 [72ES1]. If the Reynolds number drops below 2 000, the pressure loss coefficient K exhibits a marked increase with decrease in Reynolds number. This characteristic of round-wire gauzes is attributed to the dominance of viscous fluid forces over inertia fluid forces at low Reynolds numbers. The effect can be extrapolated to other related devices such as perforated plates and heat exchangers.

B.3.1 Fan inlet shroud

The total pressure loss coefficient for the fan inlet shroud is determined separately. This is achieved by relating the measured velocity through the fan inlet shroud to the total pressure drop across the inlet shroud. The total pressure at the outlet from the shroud is calculated by assuming the flow to be one-dimensional (axial) and uniform (α=1) at the fan shroud outlet. The static pressure at the shroud outlet is assumed to be atmospheric ($\Delta p_{s_{ISo}} = 0$).

The total pressure differential across the fan inlet shroud is presented by

$$\begin{aligned}
\Delta p_{t_{IS}} &= \Delta p_{t_{ISi}} - \Delta p_{t_{ISo}} \\
&= \Delta p_{t_{sett}} - \Delta p_{t_{ISo}} \\
&= \left(\Delta p_{s_{sett}} + \frac{1}{2}\rho \bar{v}_{sett}^2\right) - \left(\Delta p_{s_{ISo}} + \frac{1}{2}\rho \bar{v}_{IS}^2\right)
\end{aligned} \tag{B.38}$$

Continuity states that

$$\bar{v}_{IS} A_{IS} = \bar{v}_{sett} A_{sett} \tag{B.39}$$

Substitute for $\Delta p_{s_{ISo}} = 0$ and equation (B.39) into equation (B.38) to obtain

$$\begin{aligned}
\Delta p_{t_{IS}} &= \Delta p_{s_{sett}} + \frac{1}{2}\rho \left(\frac{A_{IS}}{A_{sett}}\right)^2 \bar{v}_{IS}^2 - \frac{1}{2}\rho \bar{v}_{IS}^2 \\
&= \Delta p_{s_{sett}} + \frac{1}{2}\rho \bar{v}_{IS}^2 \left[\left(\frac{A_{IS}}{A_{sett}}\right)^2 - 1\right]
\end{aligned} \tag{B.40}$$

The total pressure loss coefficient follows from its definition (equation B.37).

$$\begin{aligned}
K_{IS} &= \frac{\Delta p_{t_{IS}}}{\frac{1}{2}\rho \bar{v}_{IS}^2} \\
&= \frac{\Delta p_{s_{sett}}}{\frac{1}{2}\rho \bar{v}_{IS}^2} + \left[\left(\frac{A_{IS}}{A_{sett}}\right)^2 - 1\right]
\end{aligned} \tag{B.41}$$

A typical set of measured input parameters to determine the total pressure loss coefficient for the fan inlet shroud are

Inlet bellmouth pressure (Δp_{bell}) = 250,97 N/m^2

Settling chamber pressure (Δp_{sett}) = 50,93 N/m^2

The mass flow rate of air through the inlet bellmouth is determined from equation (2.44)

$$\dot{m} = \alpha\epsilon \frac{\pi d_{bell}^2}{4} \sqrt{2\rho_{amb}\Delta p_{bell}} \tag{B.42}$$

The dynamic pressure in the inlet bellmouth follows from equation (B.42) and continuity.

$$\begin{aligned} \frac{1}{2}\rho\bar{v}_{bell}^2 &= (\alpha\epsilon)^2 \Delta p_{bell} \\ &= (0,9802)^2(250,97) \\ &= 241,13\ N/m^2 \end{aligned} \tag{B.43}$$

From continuity $\bar{v}_{IS}A_{IS} = \bar{v}_{bell}A_{bell}$

$$\begin{aligned} \text{thus } \bar{v}_{IS} &= \bar{v}_{bell}\frac{A_{bell}}{A_{IS}} \\ &= \bar{v}_{bell}\left(\frac{d_{bell}}{d_{IS}}\right)^2 \end{aligned} \tag{B.44}$$

From equation (B.44) it follows that the dynamic pressure at the shroud outlet is

$$\begin{aligned} \frac{1}{2}\rho v_{IS}^2 &= \frac{1}{2}\rho v_{bell}^2\left(\frac{d_{bell}}{d_{IS}}\right)^4 \\ &= 241,13\left(\frac{1,008}{1,542}\right)^4 \\ &= 44,03\ N/m^2 \end{aligned} \tag{B.45}$$

The total pressure loss coefficient across the inlet shroud follows from equation (B.41)

$$K_{IS} = \frac{\Delta p_{s_{sett}}}{\frac{1}{2}\rho \bar{v}_{IS}^2} + \left[\left(\frac{A_{IS}}{A_{sett}}\right)^2 - 1\right] \quad \text{(B.46)}$$

$$= \frac{50,93}{44,03} + \left[\left(\frac{1,8675}{4 \times 4}\right)^2 - 1\right]$$

$$= 0,17$$

The same calculations are performed for a range of volumetric flow rates through the inlet shroud. The average total pressure loss coefficient through the fan inlet shroud is 0,168.

An important observation can be made at this stage by comparing the compound calibration constant ($\alpha\epsilon$) to the total pressure loss coefficient of any inlet.

From equation (B.41) the compound calibration constant is related to pressure by

$$(\alpha\epsilon)^2 = \frac{\frac{1}{2}\rho \bar{v}^2}{(\Delta p_{t_{ISi}} - \Delta p_{s_{ISo}})} \quad \text{(B.47)}$$

The total pressure loss coefficient is

$$K = \frac{(\Delta p_{t_{ISi}} - \Delta p_{t_{ISo}})}{\frac{1}{2}\rho \bar{v}^2} \quad \text{(B.48)}$$

$$= \frac{1}{(\alpha\epsilon)^2} - 1$$

Equation (B.48) can be rewritten as

$$\alpha\epsilon = \sqrt{\frac{1}{K+1}} \quad \text{(B.49)}$$

$$= \sqrt{\frac{1}{1,168}}$$

$$= 0,9253$$

B.3.2 Ancillaries (Ideal loss coefficient)

The ideal total pressure loss coefficient for any of the structural flow distorting components (e.g. the walkway, supporting beams or inlet safety grid) is determined by installing the particular component with the fan inlet shroud in place. The total pressure drop across the combination of this component and the inlet shroud is measured in a similar fashion to that described in section B.3.1. The pressure at the outlet from the combined installation is assumed to be atmospheric ($\Delta p_{t_{Co}} = 0$).

A typical set of measured input parameters to determine the total pressure loss coefficient for the fan inlet safety grid are

Inlet bellmouth pressure (Δp_{bell}) = 272,72 N/m^2

Settling chamber pressure ($\Delta p_{s_{sett}}$) = 61,93 N/m^2

The dynamic pressure in the inlet bellmouth follows from equation (B.42).

$$\begin{aligned} \frac{1}{2}\rho\bar{v}_{bell}^2 &= (\alpha\epsilon)^2\,\Delta p_{bell} \\ &= (0,9802)^2(272,72) \\ &= 262,03\ N/m^2 \end{aligned} \tag{B.50}$$

From continuity $\bar{v}_C A_C = \bar{v}_{bell} A_{bell}$ where the subscript C refer to the combined effect of both the inlet safety grid and the fan inlet shroud.

$$\begin{aligned} \text{thus } \bar{v}_C &= \bar{v}_{bell}\frac{A_{bell}}{A_C} \\ &= \bar{v}_{bell}\left(\frac{d_{bell}}{d_C}\right)^2 \end{aligned} \tag{B.51}$$

From equation (B.51) it follows that the dynamic pressure at the shroud outlet is

$$\begin{aligned} \frac{1}{2}\rho\bar{v}_C^2 &= \frac{1}{2}\rho\bar{v}_{bell}^2\left(\frac{d_{bell}}{d_C}\right)^4 \\ &= 262,03\left(\frac{1,008}{1,542}\right)^4 \end{aligned} \tag{B.52}$$

$$= 47,85\, N/m^2$$

The total pressure loss coefficient across the combination of the inlet shroud and the inlet grid follows similar to equation (B.41).

$$K_C = \frac{\Delta p_{s_{sett}}}{\frac{1}{2}\rho \bar{v}_C^2} + \left[\left(\frac{A_{IS}}{A_{sett}}\right)^2 - 1\right] \tag{B.53}$$

$$= \frac{61,93}{47,85} + \left[\left(\frac{1,8675}{4 \times 4}\right)^2 - 1\right]$$

$$= 0,308$$

The average pressure loss coefficient for the fan inlet shroud, determined according to equation (B.46) is subtracted from the combined total pressure loss coefficient. The result is a pressure loss coefficient which accounts for the added effect of the inlet safety grid. This effect is experienced as an increase in total pressure loss due to the resistance of the ancillary, as well as the pressure loss due to the maldistribution of air flow at the outlet from the fan shroud.

$$K_{SG} = K_C - K_{IS} \tag{B.54}$$

$$= 0,308 - 0,168$$

$$= 0,140$$

The pressure loss coefficient described by equation (B.54) is only an example of the method used to determine the pressure loss coefficients for the complete range of volumetric flow rates used for the test (see section A.2). The same method is used to calculate the effective loss coefficients when required e.g. for the walkway and support beams. The typical decrease in ideal loss coefficient with decreasing Reynolds number is reported upon in section B.3.6.

B.3.3 Ancillaries (Effective loss coefficient)

The effective loss coefficient is determined from the pressure losses experienced by the fan with a specific ancillary installed in close proximity of the fan rotor.

The method to determine these loss coefficients involve the measurement of a set of system static characteristics, which are subtracted from the reference set of ideal fan static pressure characteristics. The static pressure differential is divided by the corresponding fan dynamic pressure to obtain the effective pressure loss coefficient. A feasible method to achieve this is to fit third order polynomial curves through both sets of data to ensure a continuous line of pressure loss coefficients (e.g. figures A.2.12, A.2.16 and A.2.20).

The method employed to determine the effective pressure loss coefficient for an added ancillary is illustrated by applying it to the case where the inlet safety grid is installed. The combined effect of the fan inlet shroud and the fan rotor is included in the reference fan characteristic curve. By definition,

$$\Delta p_{sF} = \Delta p_{s_{Fo}} - \Delta p_{t_{Fi}} \tag{B.55}$$

The system static pressure curve incorporates the effect of the rotor, inlet shroud and the inlet safety grid. A similar definition to equation (B.55) is used to define system static pressure.

$$\Delta p_{sS} = \Delta p_{s_{So}} - \Delta p_{t_{Si}} \tag{B.56}$$

It is assumed that the fan inlet and the system inlet velocity distributions are the same for a specific volumetric flow rate. This means that $\Delta p_{t_{Fi}} = \Delta p_{t_{Si}}$

The total pressure loss coefficient across the fan inlet safety grid is presented by

$$\begin{aligned}
\Delta p_{t_{SG}} &= \Delta p_{t_{SGi}} - \Delta p_{t_{SGo}} \\
&= \Delta p_{t_{Fo}} - \Delta p_{tSo} \\
&= \left(\Delta p_{s_{Fo}} + \alpha_{Fo}\,\frac{1}{2}\rho\bar{v}^2\right) - \left(\Delta p_{s_{So}} + \alpha_{So}\,\frac{1}{2}\rho\bar{v}^2\right) \\
&= (\Delta p_{sF} - \Delta p_{sS}) + (\alpha_{Fo} - \alpha_{So})\,\frac{1}{2}\rho\bar{v}^2
\end{aligned} \tag{B.57}$$

The total pressure loss coefficient follows from its definition in equation (B.37).

$$K_{t_{SG}} = \frac{\Delta p_{sF} - \Delta p_{sS}}{\frac{1}{2}\rho\bar{v}^2} + (\alpha_{Fo} - \alpha_{So}) \tag{B.58}$$

The velocity distribution at the outlet from the system (including the safety grid) can be vastly different from the outlet velocity profile associated with the reference curve. This variation in velocity distribution constitutes an additional energy loss attributable to the added effect of the safety grid. This additional energy loss can be integrated with the effective pressure loss coefficient (K_{SG}) by rewriting equation (B.58).

$$\begin{aligned} K_{SG} &= K_{t_{SG}} + (\alpha_{So} - \alpha_{Fo}) \\ &= \frac{\Delta p_{sF} - \Delta p_{sS}}{\frac{1}{2}\rho \bar{v}^2} \end{aligned} \tag{B.59}$$

The effective pressure loss coefficients determined according to these suggestions include the effect of the change in velocity distribution at fan outlet. This means that, for instance, the change in kinetic energy at fan outlet due to a change in velocity profile is included in the effective loss coefficient. The deviations between the effective loss coefficients and the published values for specific components can be attributed to these deviations. It is important to remember that a change in outlet area e.g. from fan shroud outlet to the heat exchanger outlet results in a change in kinetic energy lost to the atmosphere.

B.3.4 Partially blocked passageways

An experimental investigation into the effect of a channel outlet covered only partially by a screen is performed in an attempt to validate the controversial results for the ideal total pressure loss coefficients (section B.3.2). A perforated plate with 10 mm diameter holes and a solidity ratio of 0,56 is used in these experiments. The pressure loss coefficients for cases of 100 % and 32 % blockage area at the channel outlet are determined and presented as figure B.1. The velocity distribution approaching the perforated plate and at channel outlet is assumed uniform and one-dimensional, resulting in kinetic energy flux coefficients (α) of 1 in both cases.

The investigation reveals that the dependency of the pressure loss coefficient (K) on Reynolds number (or Ry number as used in figure B.1) differ for the two cases. The pressure loss coefficient for 100 % blockage increases as the Reynolds number decreases, while the same coefficient decreases with a decrease in Reynolds number in the case of 32 % blockage. This trend can be accounted for by considering the velocity distribution at the channel outlet. The distribution is not uniform and is dependent upon the Ry number.

The influence of the non-uniform velocity profile is referred to the basic definition of K (equation B.37).

$$K = \frac{\Delta p_{tot}}{\frac{1}{2}\rho\bar{v}^2} \tag{B.60}$$

$$\text{where } \Delta p_{tot} = \left(\Delta p_{s_{up}} + \alpha_{up}\frac{1}{2}\rho\bar{v}^2\right) - \left(\Delta p_{s_{dn}} + \alpha_{dn}\frac{1}{2}\rho\bar{v}^2\right) \tag{B.61}$$

In applications where the inlet velocity profile is uniform ($\alpha_{up} = 1$) and the resistance screen is mounted at the channel exhaust to atmosphere ($\Delta p_{s_{dn}} = 0$) the equation simplifies to

$$\begin{aligned} \Delta p_t &= \Delta p_{s_{up}} + \frac{1}{2}\rho\bar{v}^2 - \alpha_{s_{dn}}\frac{1}{2}\rho\bar{v}^2 \\ &= \Delta p_{s_{up}} + \frac{1}{2}\bar{v}^2(1 - \alpha_{dn}) \end{aligned} \tag{B.62}$$

Substitution equation (B.62) into equation (B.60) results in

$$K = \frac{\Delta p_{s_{up}}}{\frac{1}{2}\rho\bar{v}^2} + (1 - \alpha_{dn}) \tag{B.63}$$

From the above, it is obvious that an increase in outlet energy flux coefficient (α_{dn}) results in a decrease in pressure loss coefficient (K). It is found that α_{dn} increases with a decrease in Ry number. The increase in energy flux coefficient is attributed to the increased pressure loss across the screen at lower Ry numbers. The result being a higher relative velocity in the free flow regions not covered by the screen. The lower relative velocity through the perforated plate also results in a lower total pressure loss due to the resistance being related to velocity through the perforated plate. The inaccurate assumption of a uniform outlet velocity distribution dominates the effect of viscous forces at lower Ry numbers.

The contents of this section is only aimed at providing an insight into the characteristics of the pressure loss curves of individual flow distorting components e.g. inlet grid and walkway. It is important to remember that these curves are still valid indications of the experimentally determined pressure losses for fan static pressure characteristics as supported for the purposes of this thesis. The basis for this statement originates from the definition of fan static pressure which does not consider the dynamic pressure component at the fan outlet.

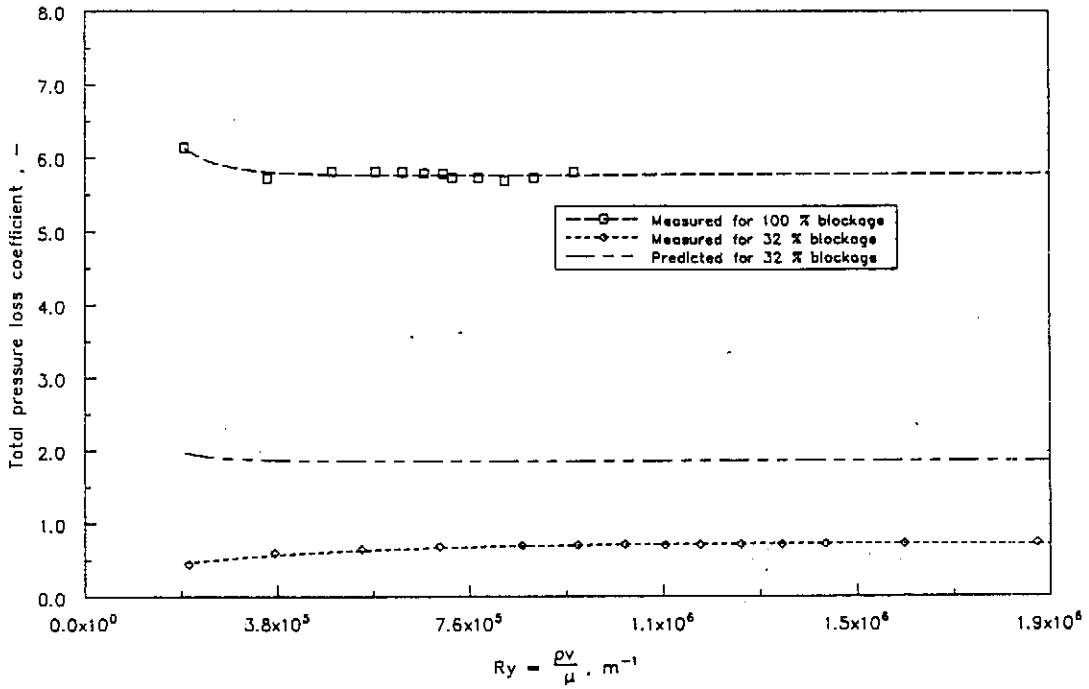

Figure B.1: The effect of partially blocked passageways

B.3.5 Heat exchanger (Ideal loss coefficient)

The pressure loss coefficients across the heat exchangers are based on the same assumption as used in section B.3.3. The assumption is that the velocity distribution at the outlet from the finned tubes is uniform and one-dimensional (i.e. $\alpha = 1$). Any deviations from this assumption is therefore incorporated into the pressure loss coefficient. It means that if the A-frame itself results in a maldistribution of air at heat exchanger outlet, this maldistribution is accounted for by including it in the ideal pressure loss coefficient.

The ideal pressure loss across the heat exchanger is calculated by subtracting the total pressure at heat exchanger outlet from the total pressure inside the plenum.

$$\Delta p_{t_{HX}} = \Delta p_{t_{HXi}} - \Delta p_{t_{HXo}} \tag{B.64}$$

The total pressure inside the plenum follows from the difference between the total pressure loss across the fan inlet shroud and the fan total pressure at fan inlet.

$$\begin{aligned} \Delta p_{t_{HXi}} &= \Delta p_{t_{Fi}} - \Delta p_{t_{IS}} \\ &= \Delta p_{t_{sett}} - K_{IS}\,\frac{1}{2}\rho \bar{v}^2_{fan} \end{aligned} \tag{B.65}$$

$$\text{from continuity } v_{fan}\, A_{fan} = v_{HX}\, A_{HX}$$

$$\text{thus } v_{HX} = v_{fan}\, \frac{A_{fan}}{A_{HX}} \tag{B.66}$$

Substituting equations (B.65) and (B.66) into equation (B.64) results in

$$\begin{aligned} \Delta p_{t_{HX}} &= \Delta p_{t_{sett}} - \left[K_{IS} + \left(\frac{A_{fan}}{A_{HX}}\right)^2\right] \frac{1}{2}\rho \bar{v}_{fan}^2 \\ &= \Delta p_{s_{sett}} + \frac{1}{2}\rho \bar{v}_{sett}^2 - \frac{1}{2}\rho \bar{v}_{fan}^2 \left[K_{IS} + \left(\frac{A_{fan}}{A_{HX}}\right)^2\right] \end{aligned} \tag{B.67}$$

From the definition of the total pressure loss coefficient, it can be deduced that

$$\begin{aligned} K_{HX} &= \frac{\Delta p_{t_{HX}}}{\frac{1}{2}\rho \bar{v}_{fan}^2} \\ &= \frac{\Delta p_{s_{sett}}}{\frac{1}{2}\rho \bar{v}_{fan}^2} - \left[K_{IS} + \left(\frac{A_{fan}}{A_{HX}}\right)^2 - \left(\frac{A_{fan}}{A_{sett}}\right)^2\right] \end{aligned} \tag{B.68}$$

The coefficient K_{HX} is the ideal total pressure loss coefficient and incorporates the downstream effects created by any flow distortion inside the A-frame plenum.

B.3.6 Heat exchanger (Effective loss coefficient)

The effective total pressure loss coefficients across the heat exchangers are determined from the difference between the reference fan static pressure and the actual system static pressure. The inherent assumptions incorporated in common design practice are highlighted. The more important of these are that the kinetic energy inside the A-frame plenum is discarded, and that the kinetic energy flux coefficient at the outlet from the heat exchangers is assumed to be unity. It is illustrated that deviations in the kinetic energy flux coefficients inside the plenum and at the outlet from the finned tubes influence the final value of the total pressure loss coefficient.

The total pressure differential across the heat exchangers used to determine the total pressure loss coefficient is

$$\Delta p_{t_{HX}} = \Delta p_{t_{HXi}} - \Delta p_{t_{HXo}} \tag{B.69}$$

From the definition of fan static pressure (Δp_{sF}) it follows

$$\Delta p_{sF} = \Delta p_{s_{Fo}} - \Delta p_{t_{Fi}} \tag{B.70}$$

The system static pressure is defined similarly. The system in this case includes the fan inlet shroud, fan rotor and the finned tube bundles.

$$\Delta p_{sS} = \Delta p_{s_{So}} - \Delta p_{t_{Si}} \tag{B.71}$$

The following assumptions, valid at a specific volumetric flow rate through the system, are used to combine equations (B.69) to (B.71).

- The velocity profile at fan inlet is independent of the system in which the fan is installed. It is related to the volume flow rate.

$$\Delta p_{t_{Si}} = \Delta p_{t_{Fi}} \tag{B.72}$$

- The total pressure contribution of the fan to the air stream is not influenced by its installation, but is dependent on the volumetric flow rate through the fan. The following is therefore true:

$$\Delta p_{t_{Fo}} = \Delta p_{t_{HXi}} \tag{B.73}$$

- The kinetic energy flux coefficient at the outlet from the heat exchanger equals unity. This means that the velocity at this location is assumed to be uniform and one-dimensional. With this assumption, the kinetic energy at the outlet from the system assumes the same value as the kinetic energy at the outlet from the heat exchangers.

$$\Delta p_{t_{Fo}} = \Delta p_{t_{HXi}} \tag{B.74}$$

Combining equations (B.69) to (B.71) with these assumptions equations (B.72) to (B.74) results in:

$$
\begin{aligned}
\Delta p_{t_{HX}} &= \Delta p_{t_{HXi}} - \Delta p_{t_{HXo}} \\
&= \Delta p_{t_{Fo}} - \Delta p_{t_{So}} \\
&= \left(\Delta p_{s_{Fo}} + \alpha_{Fo}\,\frac{1}{2}\rho\bar{v}^2_{fan}\right) - \left(\Delta p_{s_{So}} + \frac{1}{2}\rho\bar{v}^2_{HX}\right) \\
&= (\Delta p_{sF} - \Delta p_{sS}) + \alpha_{Fo}\,\frac{1}{2}\rho\bar{v}^2_{fan} - \frac{1}{2}\rho\bar{v}^2_{HX} \qquad \text{(B.75)}
\end{aligned}
$$

Equation (B.75) can only be solved once the value of α_{F_o} has been determined. This kinetic energy coefficient is difficult to determine due to its dependence on the type of fan used, the volumetric flow rate through the system, as well as the specific system in which the fan is installed.

In practice, however, the fan is matched to the system by determining the intercept between the fan static pressure curve and the theoretically determined total pressure loss coefficient of the system. In effect this means that the kinetic energy introduced by the fan to the inside of the plenum is assumed to be dissipated in its entirety, and does not contribute to the energy content of the air advancing through the system.

In the final analysis, the designer is interested in the margin of error attributed to the system effect which is not accounted for in conventional design practice. The kinetic energy at fan inlet is therefore excluded from equation (B.75), resulting in.

$$
\begin{aligned}
\Delta p_{t_{HX}} &= (\Delta p_{sF} - \Delta p_{sS}) - \frac{1}{2}\rho\bar{v}^2_{HX} \\
&= (\Delta p_{sF} - \Delta p_{sS}) - \left(\frac{A_{fan}}{A_{HX}}\right)^2 \frac{1}{2}\rho\bar{v}^2_{fan} \qquad \text{(B.76)}
\end{aligned}
$$

The effective pressure loss coefficient presented in appendix A is

$$
K_{HX} = \frac{(\Delta p_{sF} - \Delta p_{sS})}{\frac{1}{2}\rho\bar{v}^2_{fan}} - \left(\frac{A_{fan}}{A_{HX}}\right)^2 \qquad \text{(B.77)}
$$

The effective pressure loss coefficient (defined in this section) and the ideal pressure loss coefficient (defined in the previous section) for the system approximate each other under ideal operating conditions (figures 4.8 and 4.9). It is important to realize that the effective pressure loss is influenced by the kinetic energy at the outlet from the fan as is apparent from equation (B.75). The pressure loss coefficient defined in equation (B.77) should therefore carefully be considered before it is applied to systems with inlet flow distortions.

B.3.7 Outlet (Effective loss coefficient)

The effective downstream loss coefficients are determined by considering the additional effect on the system performance of adding the windwalls. This effect is divided into the jetting losses (K_{dj}) and the kinetic energy at the outlet from the unit dissipated in the free atmosphere (K_o). The combined effect of these two components is determined by considering the total pressure differential between the surface of the finned tubes and the outlet from the unit.

$$\Delta p_{t_d} = \Delta p_{t_{HXo}} - \Delta p_{t_{Uo}} \tag{B.78}$$

Assuming the inlet velocity profiles to remain the same in both cases, $\Delta p_{t_{Shxi}} = \Delta p_{t_{Swwo}}$. Equation (B.78) is rewritten as:

$$\begin{aligned} \Delta p_{t_d} &= \left(\Delta p_{t_{Shxo}} - \Delta p_{t_{Shxi}}\right) + \left(\Delta p_{t_{Shxo}} - \Delta p_{t_{Shxi}}\right) \\ &= \Delta p_{s_{Shx}} - \Delta p_{s_{Sww}} - \alpha_{Swwo}\,\frac{1}{2}\rho\bar{v}^2_{Swwo} \end{aligned} \tag{B.79}$$

Equation (B.79) is substituted in the definition for the total pressure loss coefficient (equation B.37), which results in:

$$\begin{aligned} K_{t_d} &= \frac{\left(\Delta p_{s_{Shx}} - \Delta p_{s_{Sww}}\right)}{\frac{1}{2}\rho\bar{v}^2_{fan}} - \alpha_{Swwo}\left(\frac{A_{fan}}{A_{ww}}\right)^2 \\ &= \frac{\left(\Delta p_{s_{Shx}} - \Delta p_{s_{Sww}}\right)}{\frac{1}{2}\rho\bar{v}^2_{fan}} - \alpha_{Swwo}\left(\frac{1,86749}{1,650 \times 2,414}\right)^2 \\ &= \frac{\left(\Delta p_{s_{Shx}} - \Delta p_{s_{Sww}}\right)}{\frac{1}{2}\rho\bar{v}^2_{fan}} - 0,220\;\alpha_{Swwo} \end{aligned} \tag{B.80}$$

The outlet loss coefficient term in equation (B.80) is combined with the total pressure loss coefficient (K_{t_d}) to obtain the effective loss coefficient (which includes the kinetic energy dissipated in the free atmosphere).

$$K_d = K_{t_d} + 0,220\;\alpha_{Swwo}$$

$$= \frac{\Delta p_{s_{hx}} - \Delta p_{s_{ww}}}{\frac{1}{2}\rho \bar{v}_{fan}^2} \qquad \text{(B.81)}$$

The effective pressure loss coefficient of equation (B.81) is used to generate the effective loss coefficient curve of figure A.3.6.

B.4 Theoretical predictions of loss coefficients

The theoretical predictions of pressure loss coefficients are almost exclusively based on the following assumption

$$\Delta p_{tot} = K \frac{1}{2}\rho \bar{v}^2 \qquad \text{(B.82)}$$

$$\text{where } K = f(Re)$$

Equation (B.82) accounts for the influence of viscous forces at low Reynolds numbers. This effect results in an increase in the loss coefficient K with decrease in Reynolds number [72ES1, 73FO1].

B.4.1 Inlet grid (Support beams only)

The loss coefficient associated with an inlet safety grid is determined according to two independent methods.

The first method is a bulk method which entails the determination of the total blockage area at fan inlet. The blockage area and the distance from the fan rotor is then correlated to a pressure loss coefficient. This method is attributed to the Stork fan company who published the relevant curves needed to utilize this method [85ST1].

The second method concerns the determination of the overall loss coefficient by summation of the loss coefficients of individual components.

(a) Bulk method

The reader is referred to figure F.2.7 which is a drawing of the dimensions of the inlet grid. The first step when employing the bulk method is to determine the total frontal areas of the components exposed to the air stream.

I-beam ($42 \times 24\ mm$)

$l_1 = 1,542\,m$

$A_{F_1} = l_1 w_1 = (1,542)(0,024) = 0,037\,m^2$

I-beam ($27 \times 14\,mm$)

$l_2 = 4(0,465) = 1,861\,m$

$A_{F_2} = l_2 w_2 = (1,861)(0,014) = 0,026\,m^2$

Double L-beam ($15 \times 11\,mm$)

$l_3 = 4\,[(0,736 - 0,014) + 0,603] = 5,300\,m$

$A_{F_3} = l_3 w_3 = (5,300)(0,022) = 0,117\,m^2$

Single circular L-beam ($15 \times 11\,mm$)

$l_4 = \pi(1,542) = 4,844\,m$

$A_{F_4} = l_4 w_4 = (4,844)(0,011) = 0,053\,m^2$

Single L-beam ($10 \times 10\,mm$)

$l_5 = 4\,[0,736 + 0,645 - 4(0,022)] + 2(0,771 - 0,615) = 5,484\,m$

$A_{F_5} = l_5 w_5 = (5,484)(0,010) = 0,055\,m^2$

The total frontal area of the inlet grid is

$$\begin{aligned} A_{F_{beam}} &= A_{F_1} + A_{F_2} + A_{F_3} + A_{F_4} + A_{F_5} \\ &= 0,037 + 0,026 + 0,117 + 0,053 + 0,055 \\ &= 0,288\,m^2 \end{aligned}$$

$$A_{fan} = \frac{\pi d_{fan}^2}{4} = 1,868\, m^2$$

$$\frac{A_{F_{beam}}}{A_{fan}} = 0,154 \tag{B.83}$$

The distance between the inlet beams and the fan rotor (X_{beam}) is 0,224 m.

$$\frac{X_{beam}}{d_{fan}} = 0,145 \tag{B.84}$$

The loss coefficient for the support beams of the inlet grid (K_{beam}) is determined from the figure for resistance factors for obstacles on the suction side of the fan [85ST1] (see figure B.2) resulting in $K_{beam} = 0,17$.

(b) Summation method

The drag forces exerted on the fluid by individual components are

$$F = C_d A_F \frac{\rho v^2}{2} \tag{B.85}$$

and the corresponding pressure losses

$$\Delta p = \frac{F}{A_{tot}} \tag{B.86}$$

Combining equations (B.85) and (B.86) leads to

$$K = C_d \frac{A_F}{A_{tot}} \tag{B.87}$$

Equation (B.87) is used to determine the loss coefficient of the individual components before adding them to obtain the total loss coefficient. The values for the drag coefficients (C_d) of the different components are obtained from the Engineering Sciences Data Unit [75ES1].

I-beam ($42 \times 24\ mm$)

$$C_{d_1} = 1,68$$

$$\frac{A_{F_1}}{A_{fan}} = \frac{0,037}{1,868} = 0,020$$

thus $K_1 = 0,033$

I-beam ($27 \times 14\ mm$)

$C_{d_2} = 1,68$

$$\frac{A_{F_2}}{A_{fan}} = \frac{0,026}{1,868} = 0,014$$

thus $K_2 = 0,023$

Double L-beam ($15 \times 11\ mm$)

$C_{d_3} = 1,38$

$$\frac{A_{F_3}}{A_{fan}} = \frac{0,117}{1,868} = 0,063$$

thus $K_3 = 0,087$

Single circular L-beam ($15 \times 11\ mm$)

$C_{d_4} = 1,82$

$$\frac{A_{F_4}}{A_{fan}} = \frac{0,053}{1,868} = 0,028$$

thus $K_4 = 0,052$

Single L-beam ($10 \times 10\ mm$)

$C_{d_5} = 1,82$

$$\frac{A_{F_5}}{A_{fan}} = \frac{0,055}{1,868} = 0,030$$

thus $K_5 = 0,054$

The total pressure loss coefficient for the support beams of the inlet grid is

$$\begin{aligned} K_{beam} &= K_1 + K_2 + K_3 + K_4 + K_5 \\ &= 0,033 + 0,023 + 0,087 + 0,052 + 0,054 \\ &= 0,249 \end{aligned} \tag{B.88}$$

B.4.2 Inlet safety screen (Full scale unit only)

The safety screen present in the full scale unit, but not in the scale model consist of a $75 \times 75 \times 5\ mm$ mesh with a solidity ratio of 0,129. The screen covers 98,3 % of the total area exposed to the flow.

(a) Bulk method

The area ratio can be determined from

$$\frac{A_{F_{screen}}}{A_{fan}} = (0,983)(0,129) = 0,127 \tag{B.89}$$

The ratio between distance of the inlet grid from the fan rotor and the fan diameter is:

$$\frac{X_{screen}}{d_{fan}} = 0,140 \tag{B.90}$$

The loss coefficient (K_{screen}) is found to be 0,13 from figure B.2.

(b) Summation method

The summation method employed in this case is to assume the screen to consist of a number of 5 mm diameter cylinders for which the drag coefficient is available [72ES1]. The pressure loss coefficient can be determined, using the method suggested previously in this section.

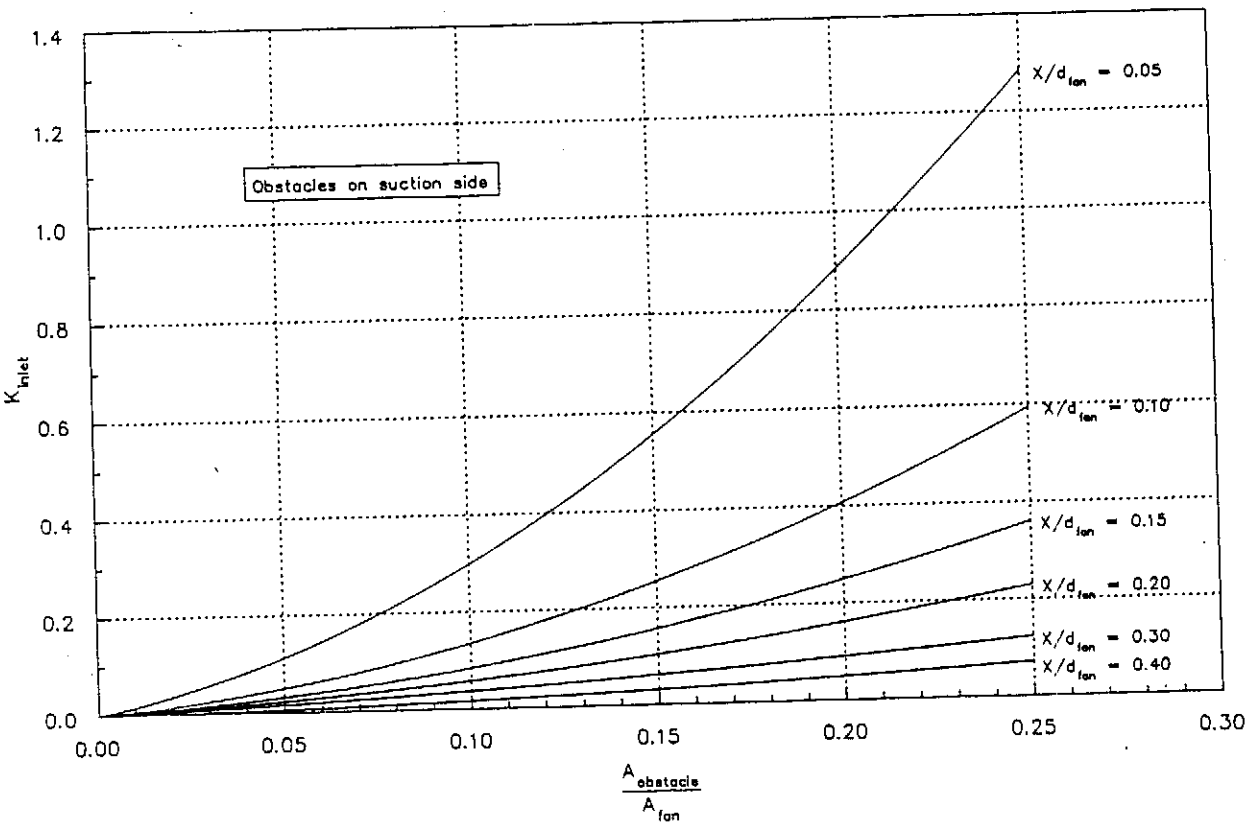

Figure B.2: Resistance factor for obstacles on suction side [85ST1]

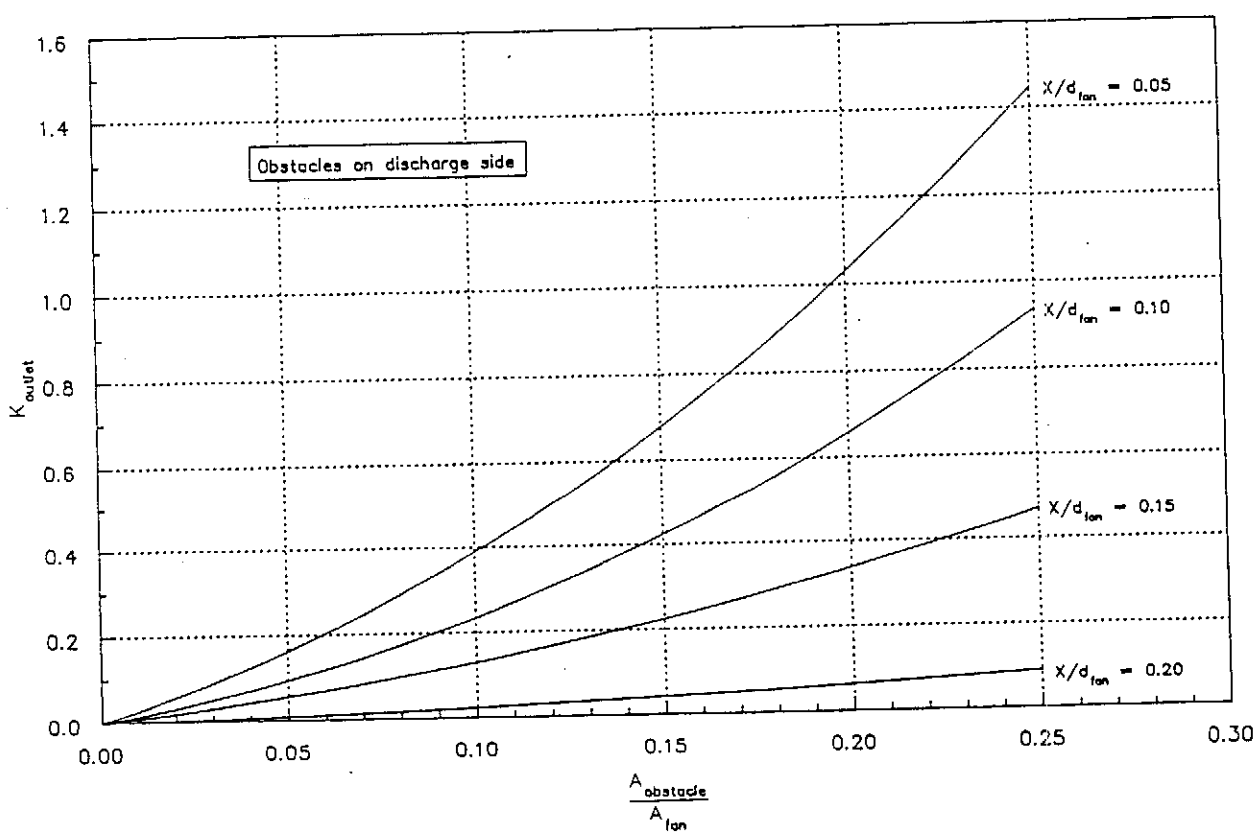

Figure B.3: Resistance factor for obstacles on discharge side [85ST1]

$$C_{d_{screen}} = 1,2$$

$$\frac{A_{F_{screen}}}{A_{fan}} = 0,127 \tag{B.91}$$

$$\text{thus } K_{screen} = (1,2)(0,127) = 0,152 \tag{B.92}$$

An average value of $K_{screen} = 0,14$ is assumed for any calculations involving this parameter in the remainder of this study.

B.4.3 Walkway and support beams

The most relevant method employed to predict the effective loss coefficient of the walkway and its supporting beams in the wake of the fan is the one proposed by Stork [85ST1]. This is the only model which incorporates a downstream effect on overall fan performance (the system effect).

(a) Bulk method

The method is similar to the one used in the previous section for the fan inlet, but the graph relating the pressure loss coefficient to area ratio and distance behind fan blade is different (compare figure B.2 to figure B.3).

The overall length of beams used to support the walkway and fan assembly that is exposed to the air stream is 3,054 m. The dimensions of these I-beams are 32 x 80 mm resulting in an overall exposed area of 0,0977 m^2. The area ratio is determined from

$$\frac{A_{F_{support}}}{A_{fan}} = \frac{0,0977}{1,8675} = 0,0523 \tag{B.93}$$

The 40 x 38 x 8 mm "recta grid" used to construct the walkway has a solidity ratio of 0,368. The total area covered by the walkway is 0,4622 m^2, resulting in a overall blocked area of 0,1703 m^2. The area ratio used to apply figure B.3 is

$$\frac{A_{F_{walk}}}{A_{fan}} = \frac{0,1703}{1,8675} = 0,0912 \tag{B.94}$$

The downstream distance between fan center line and the supporting beams is varied to determine the influence of different walkway positions on the overall fan performance. These

distances, as well as the corresponding dimensionless distances between fan rotor and supporting beams, between fan rotor and walkway grid and the pressure loss coefficients from figure B.3 are listed in table B.1.

(b) Summation method

The summation method stated in section B.4.1 (equations B.85 to B.87) is utilized to determine the pressure loss coefficient for this configuration.

The drag coefficient for an I-beam has already been stated. The total pressure loss coefficient for the support beams is determined from the method described in section B.4.1.

$$C_{d_{support}} = 1,68$$

$$\frac{A_{F_{support}}}{A_{fan}} = 0,0523$$

thus $K_{support} = (0,0523)(1,68) = 0,088$

The same technique, applied to the walkway, results in:

$$C_{d_{walk}} = 1,10 \text{ from [72AS1]}$$

$$\frac{A_{F_{walk}}}{A_{fan}} = 0,0912$$

thus $K_{walk} = (0,0912)(1,10) = 0,100$

The total pressure loss coefficient for the combined effect of the walkway and the support beams is determined by summation of the previous two loss coefficients.

$$\begin{aligned} K_{tot} &= K_{support} + K_{walk} \\ &= 0,088 + 0,100 \\ &= 0,188 \end{aligned}$$

Table B.1

Pressure loss coefficients for walkway and support beams

Distance behind rotor mm	Method	$\frac{X_{walk}}{d_{fan}}$ -	K_{walk} -	X_{supp} -	K_{supp} -	K_{tot} -
57	Stork	0,061	0,32	0,011	0,23	0,55
125	Stork	0,105	0,21	0,055	0,14	0,35
142	Stork	0,116	0,17	0,066	0,13	0,31
292	Stork	0,213	0,02	0,163	0,04	0,07
-	Summation	-	0,10	-	0,09	0,19

B.4.4 Oblique flow losses

Section 2.9 is concerned with the theoretical predictions of the effect of oblique flow on the pressure loss coefficient across the heat exchangers of the A-frame installation. The equations are applied to the specific arrangement investigated in this study.

$$\text{Upstream fin pitch} = 4,0\,mm$$

$$\text{Upstream fin thickness} = 0,5mm$$

$$\text{thus } \sigma_{21} = \frac{A_2}{A_1} = \frac{4 - 0,5}{4} = 0,875 \tag{B.95}$$

The corresponding value of $\sigma_c = 0,78$ is obtained from figure 2.2. Equation (2.62) is used to calculate K_c.

$$\begin{aligned} K_c &= \left(\frac{1}{\sigma_{21}}\right)^2 \left(1 - \frac{1}{\sigma_c}\right)^2 \\ &= \left(\frac{1}{0,875}\right)^2 \left(1 - \frac{1}{0,78}\right)^2 \\ &= 0,104 \end{aligned} \tag{B.96}$$

The actual semi apex angle of the A-frame is 28°. Equation (2.64) gives the semi apex angle, corrected for oblique flow inside the A-frame, as

$$\theta_m = 0,0019\,\theta^2 + 0,9133\,\theta - 3,1558$$

$$= 23,91^o \qquad \text{(B.97)}$$

Equation (2.65) relates the corrected pressure loss coefficient for oblique flow to the loss coefficient for normal flow.

$$K_{he\theta} = K_{he} + \left(\frac{1}{\sin\,\theta_m} - 1\right)\left(2\sqrt{K_c} + \frac{1}{\sin\,\theta_m} - 1\right)$$

$$= K_{he} + 3,038 \qquad \text{(B.98)}$$

The experimental data obtained for the total pressure loss coefficients for normal flow through the heat exchanger is correlated to be:

for the 4,0 mm pitch finned tubes

$$K_{he} = 246,36\;Ry^{-0,2888} \qquad \text{(B.99)}$$

for the combination of the 4,0 mm and the 2,5 mm pitch finned tubes

$$K_{he} = 4\,464,83\;Ry^{-0,439} \qquad \text{(B.100)}$$

Equations (B.99) and (B.100) are substituted into equation (B.98) to obtain the theoretically predicted values for the overall heat exchanger pressure loss coefficients without any windwalls fitted. It is important to remember that the resulting pressure loss coefficients have to be corrected for the difference in area between fan inlet shroud and heat exchanger outlet. All pressure loss coefficients in this report are referred to fan inlet shroud area. The outlet pressure losses are zero if no windwalls are present. Outlet pressure losses are discussed and accounted for in the next section.

B.4.5 Downstream losses

The outlet pressure loss coefficients are determined from the experimental findings of van Aarde [90VA1]. According to him, the overall outlet pressure loss coefficient is related to the Ry number by:

$$(K_{d0})_{hx} = K_{dj} + K_o$$

$$= \left(4,44 - \frac{348\,447}{Ry_{hx}}\right) + 9,057 \qquad \text{(B.101)}$$

where K_{d0} - the downstream pressure loss coefficient relevant if no walkways are located between two consecutive A-frames

K_{dj} - the downstream jetting pressure loss coefficient

K_o - the outlet energy loss coefficient

$(K_{d0})_{hx}$ and Ry_{hx} refer to a pressure loss coefficient and Ry number respectively, based on the average velocity through the heat exchangers. The pressure loss coefficients investigated in this study are all referred to the average velocity through the fan shroud. Equation (B.101) can be transformed to relate to the latter by considering the following:

from continuity $\bar{v}_{HX} A_{HX} = \bar{v}_{fan} A_{fan}$

$$\text{thus } Ry_{hx} = \frac{\rho \bar{v}_{HX}}{\mu}$$

$$= \frac{\rho \bar{v}_{fan}}{\mu}\left(\frac{A_{fan}}{A_{HX}}\right)$$

$$= Ry_{fan}\left(\frac{A_{fan}}{A_{HX}}\right) \qquad \text{(B.102)}$$

$$\text{and } (K_{d0})_{hx} = \frac{\Delta p}{\frac{1}{2}\rho \bar{v}_{HX}^2}$$

$$= \frac{\Delta p}{\frac{1}{2}\rho \bar{v}_{fan}^2}\left(\frac{A_{HX}}{A_{fan}}\right)^2$$

$$= (K_{d0})_{fan}\left(\frac{A_{HX}}{A_{fan}}\right)^2 \qquad \text{(B.103)}$$

$$\text{where } \frac{A_{fan}}{A_{HX}} = \frac{1,8675}{2(1,610)(1,960)}$$

$$= 0,296 \qquad \text{(B.104)}$$

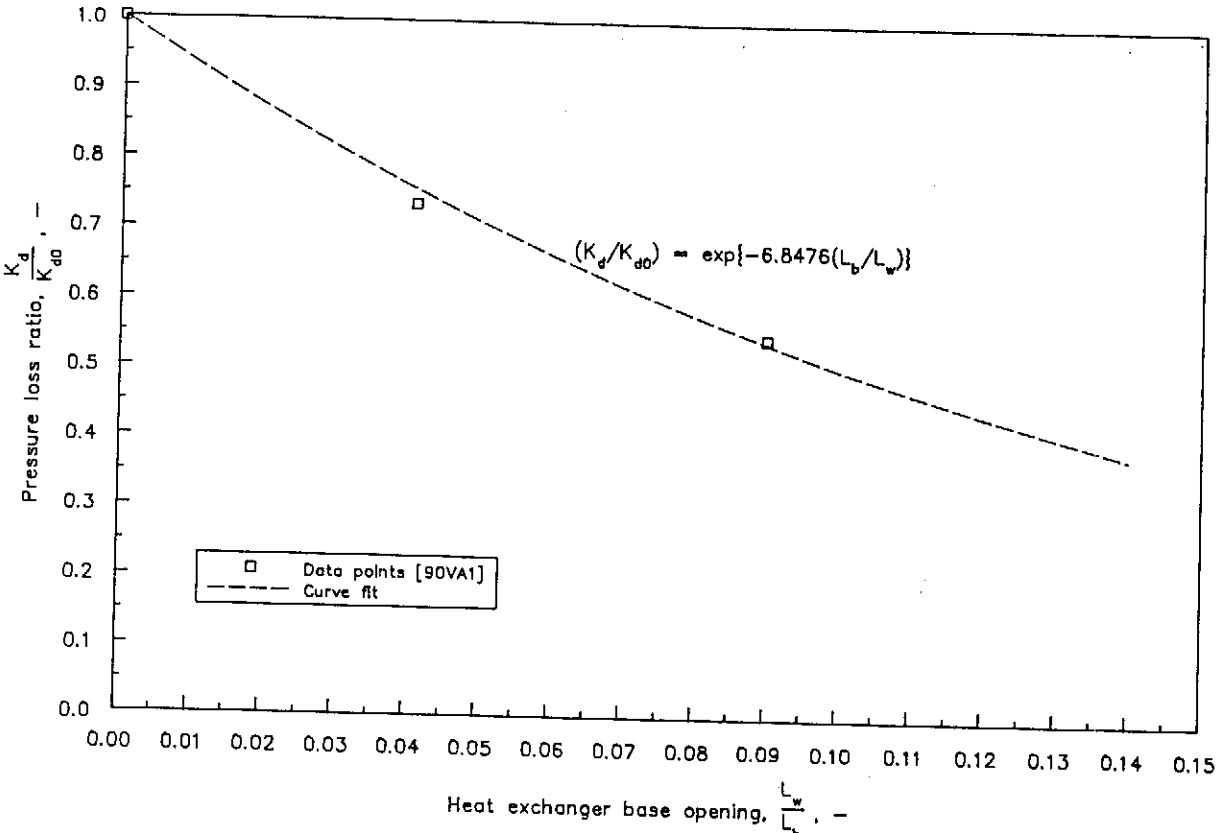

Figure B.4: The effect of an opening between two consecutive A-frames [90VA1]

Equations (B.102) to (B.104) are substituted into equation (B.101) to obtain the correlation in terms of average velocity through the fan shroud.

$$(K_{d0})_{fan} = 1,182 - \frac{103\,106}{Ry_{fan}} \tag{B.105}$$

Equation (B.105) is valid for an A-frame arrangement with no steam pipes or open spaces between two consecutive A-frames. The influence of an opening between the A-frames (e.g. a walkway for access to the heat exchangers in the full scale unit) is also investigated by van Aarde. Figure B.4 represents his findings, with the exponential curve fitted through the data points being:

$$\frac{K_d}{K_{d0}} = e^{-6,8476\frac{L_w}{L_b}} \tag{B.106}$$

The ratio $\frac{L_w}{L_b}$ for the experimental facility utilized in this study is 0,1205 corresponding to an outlet pressure loss coefficient ratio of

$$\frac{K_d}{K_{d0}} = 0,438 \tag{B.107}$$

K_{d0}, determined from equation (B.105), is substituted into equation (B.107) to determine K_d which is the theoretical curve displayed on figure A.3.6.

Appendix C - Five hole probe

An important parameter which can be used to indicate the extent of flow distortion is the velocity profile in the vicinity of the fan rotor. After careful consideration it was decided to use a five hole probe to measure the three-dimensional velocity components as well as the static and total pressure distributions in this region.

The design of the five hole probe is based on design suggestions by Yocum [78YO01] and Heidrick [86HE01]. A modification to their design which improves the probe sensitivity to pitch angle is made. This modification entails a change in the angles between the surfaces into which the pitch angle holes (numbers 4 and 5 in figure C.1) are machined and the probe axis. This angle is changed from being perpendicular to an angle of 45^{o} relative to the probe axis. The manufacturing process is also simplified by incorporating this modification.

C.1 Probe calibration

The authors referenced in the previous section [78YO01 and 86HE01] both define the following dimensionless pressure coefficients which are supposedly independent of Reynolds number.

$$p_{avg} = \frac{(p_2 + p_3 + p_4 + p_5)}{4} \tag{C.1}$$

$$C_{yaw} = \frac{(p_2 - p_3)}{(p_1 - p_{avg})} \tag{C.2}$$

$$C_{pitch} = \frac{(p_5 - p_4)}{(p_1 - p_{avg})} \tag{C.3}$$

$$C_{tot} = \frac{(p_1 - p_{tot})}{(p_1 - p_{avg})} \tag{C.4}$$

$$C_{stat} = \frac{(p_{avg} - p_{stat})}{(p_1 - p_{avg})} \tag{C.5}$$

where C_{yaw} - yaw pressure coefficient

C_{pitch} - pitch pressure coefficient

C_{tot} - total pressure coefficient

C_{stat} - static pressure coefficient

p_1 to p_5 - measured probe pressures corresponding to figure C.1 in $[N/m^2]$

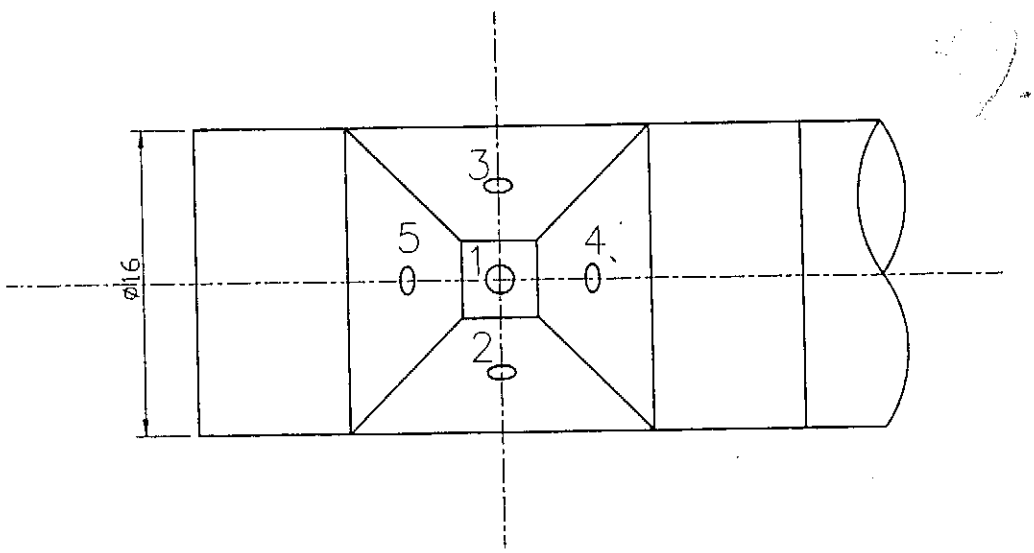

Figure C.1: Numbering of holes for the five hole probe

A set of calibration curves is determined and presented as figures C.2 to C.6. From these curves the effect that yaw angle, pitch angle and Reynolds number have on the pressure coefficients, as defined in equations C.1 to C.5 can be deduced. The axes of the calibration curves are selected to enable the user to determine yaw and pitch angles utilizing the calculated values for yaw and pitch pressure coefficients. Once the angles have been determined, total and static pressures are determined from the calibrated values for the static and total pressure coefficients. The regression curves are determined by fitting a Fourier series expansion through the measured data points. Note that the phase angles are adjusted to ensure that only a single cycle of the Fourier series occur for the complete range of the independent variable. The Reynolds number referred to in these graphs is defined as

$$Re_{pd} = \frac{\rho v d_{probe}}{\mu}$$

where v - the resultant velocity at the measuring point in $[m/s]$

d_{probe} - probe diameter which is 0,016 m

ρ - local density of air in $[kg/m^3]$

μ - local dynamic viscosity of air in $[kg/m.s]$

C.2 Application of the probe

Once the calibration of the probe has been completed, it is necessary to automate the calculation of velocity components and pressure distributions. Flow charts representing the calculation techniques employed to determine yaw angle, pitch angle, total pressure and static pressure from the probe pressure readings are attached as figures C.7.1 to C.7.3. The absolute magnitude of the velocity vector is related to total and static pressure by

$$v = \frac{2\sqrt{p_{tot} - p_{stat}}}{\rho} \tag{C.6}$$

The velocity components in the cartesian coordinate system are determined as follows

$$v_z = v \cos\lambda \cos\alpha \tag{C.7}$$

$$\begin{aligned} v_x &= v_z \tan\lambda \\ &= v \sin\lambda \cos\alpha \end{aligned} \tag{C.8}$$

$$\begin{aligned} v_y &= v_z \tan\alpha \\ &= v \cos\lambda \sin\alpha \end{aligned} \tag{C.9}$$

where α - yaw angle

λ - pitch angle

v_z - velocity component in the axial direction

v_x - velocity component in the x-direction

v_y - velocity component int the y-direction

The cartesian velocity components are transformed to cylindrical coordinates using the following relations

$$v_z = v_z \tag{C.10}$$

$$v_r = v_x \cos\theta + v_y \sin\theta \tag{C.11}$$

$$v_\theta = v_x \sin\theta + v_y \cos\theta \tag{C.12}$$

where $\tan\theta = \frac{y}{x}$

and $r = \sqrt{x^2 + y^2}$

The symbols in these equations present the following

- v_z - velocity component in the axial direction (positive in the flow direction)
- v_r - velocity component in the radial direction (positive outwards)
- v_θ - velocity component in the tangential direction (according to the right hand rule)

In the final application of the program, the pressure readings and the distance from the fan centerline in the x-direction are automatically read from the data file. The user only supplies the file name containing the measured data, ambient pressure and temperature and the distance above fan axis. All pressures are automatically compensated for changes in atmospheric conditions before the required distributions are saved on disc.

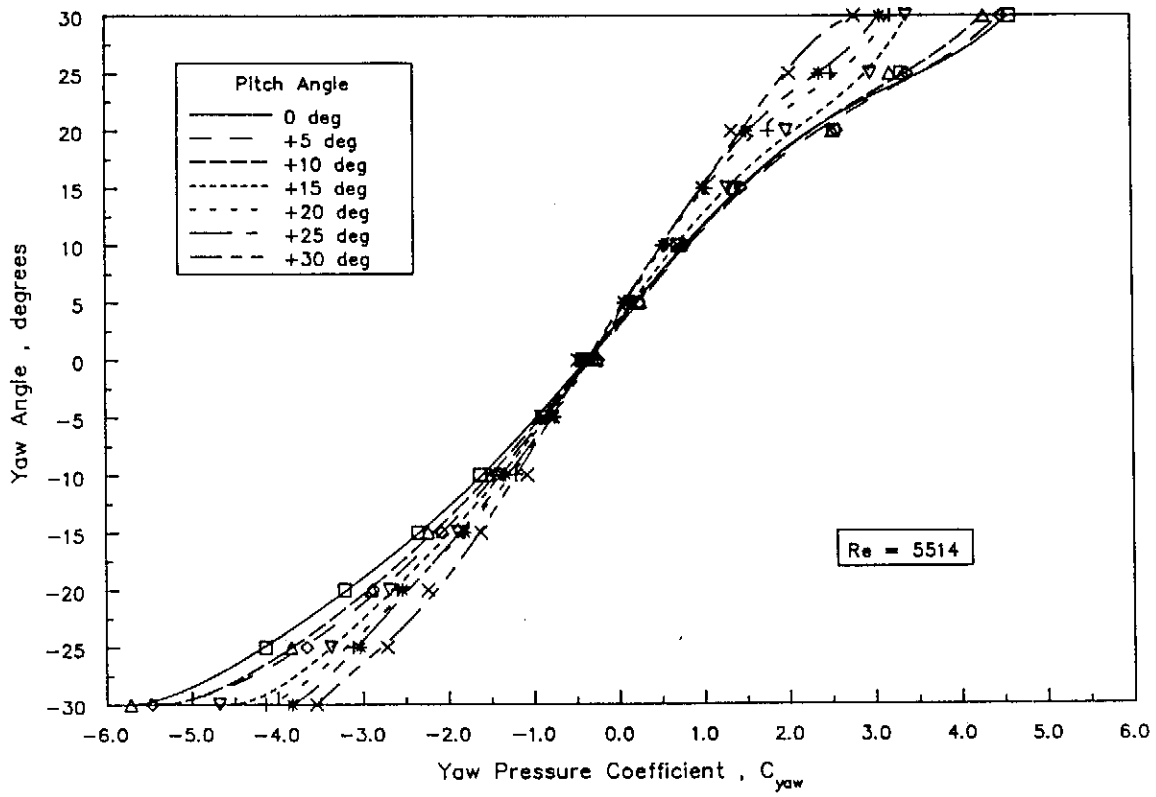

Figure C.2.1.1: Yaw angle for positive pitch angles (Re = 5514)

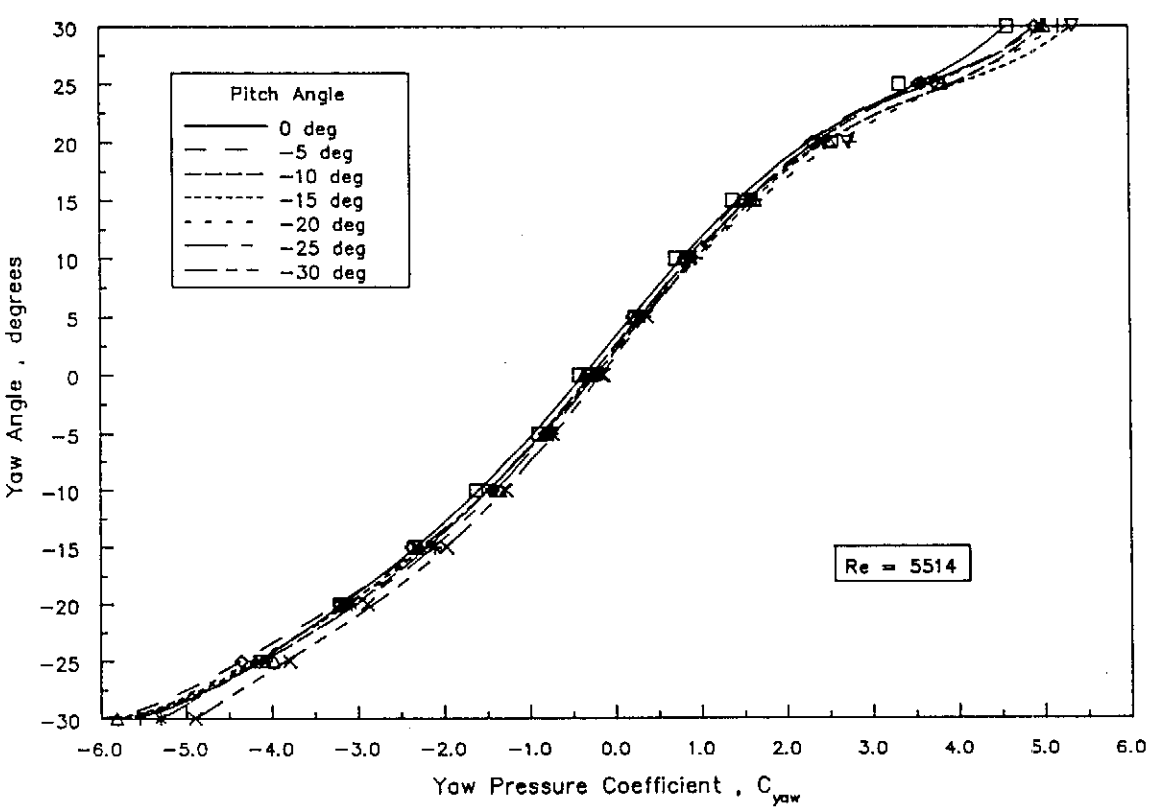

Figure C.2.1.2: Yaw angle for negative pitch angles (Re = 5514)

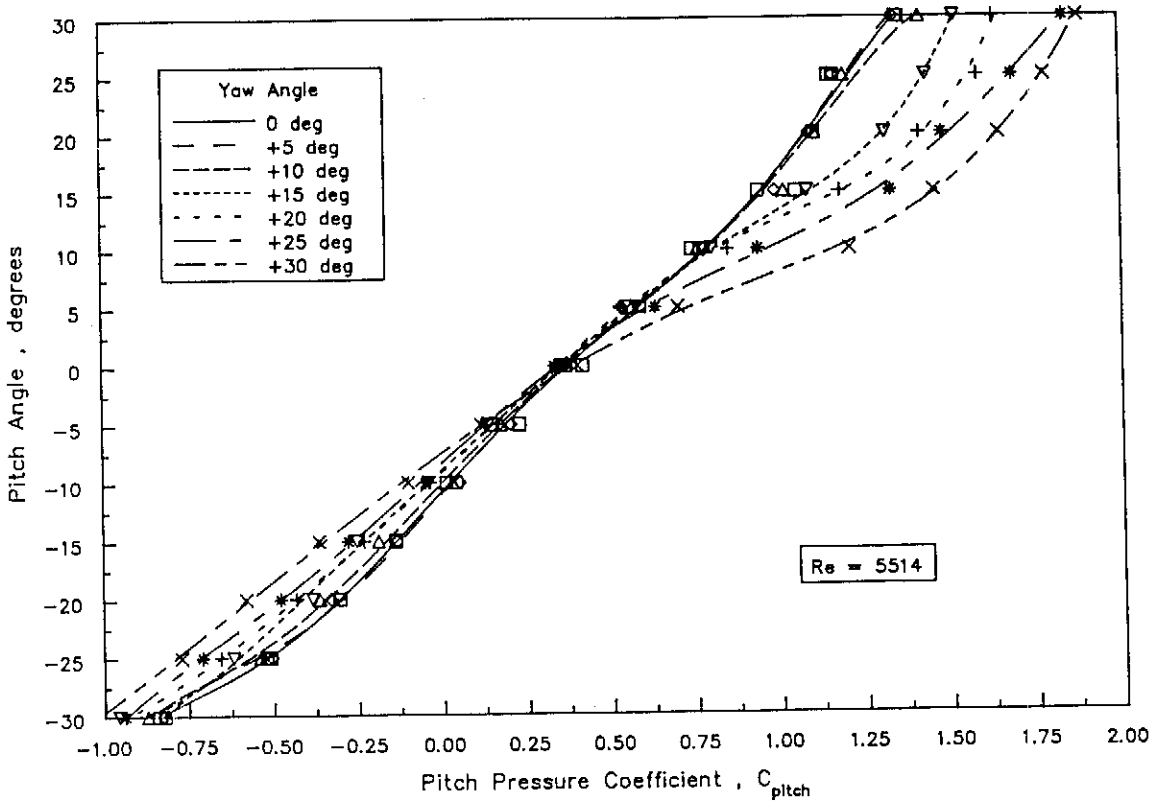

Figure C.2.2.1: Pitch angle for positive yaw angles ($Re = 5514$)

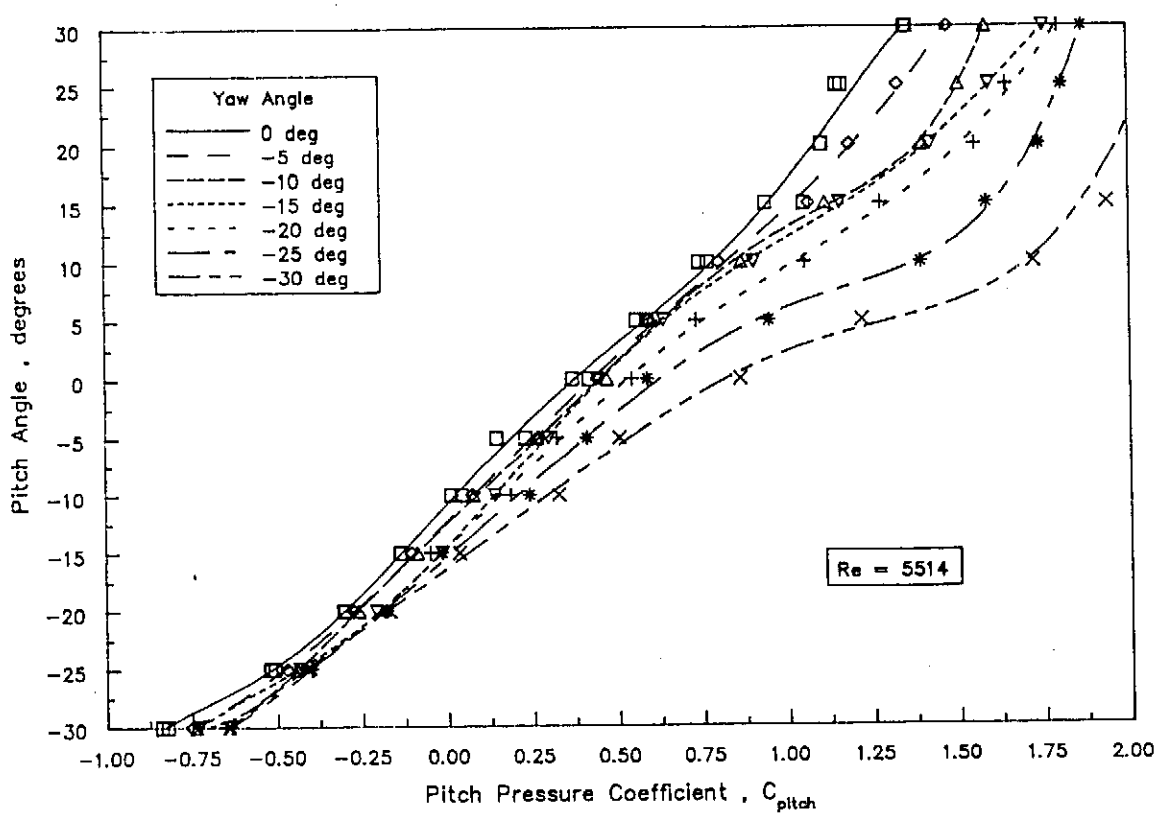

Figure C.2.2.2: Pitch angle for negative yaw angles ($Re = 5514$)

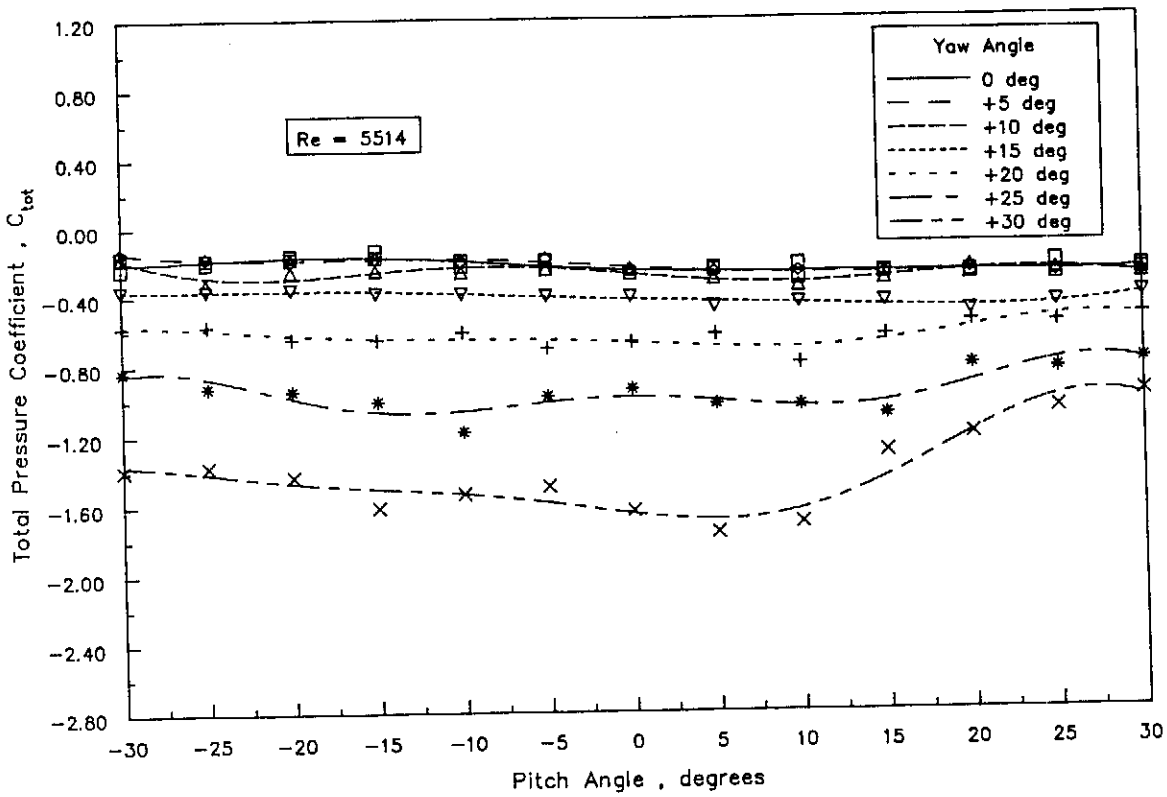

Figure C.2.3.1: C_{tot} for positive yaw angles (Re = 5514)

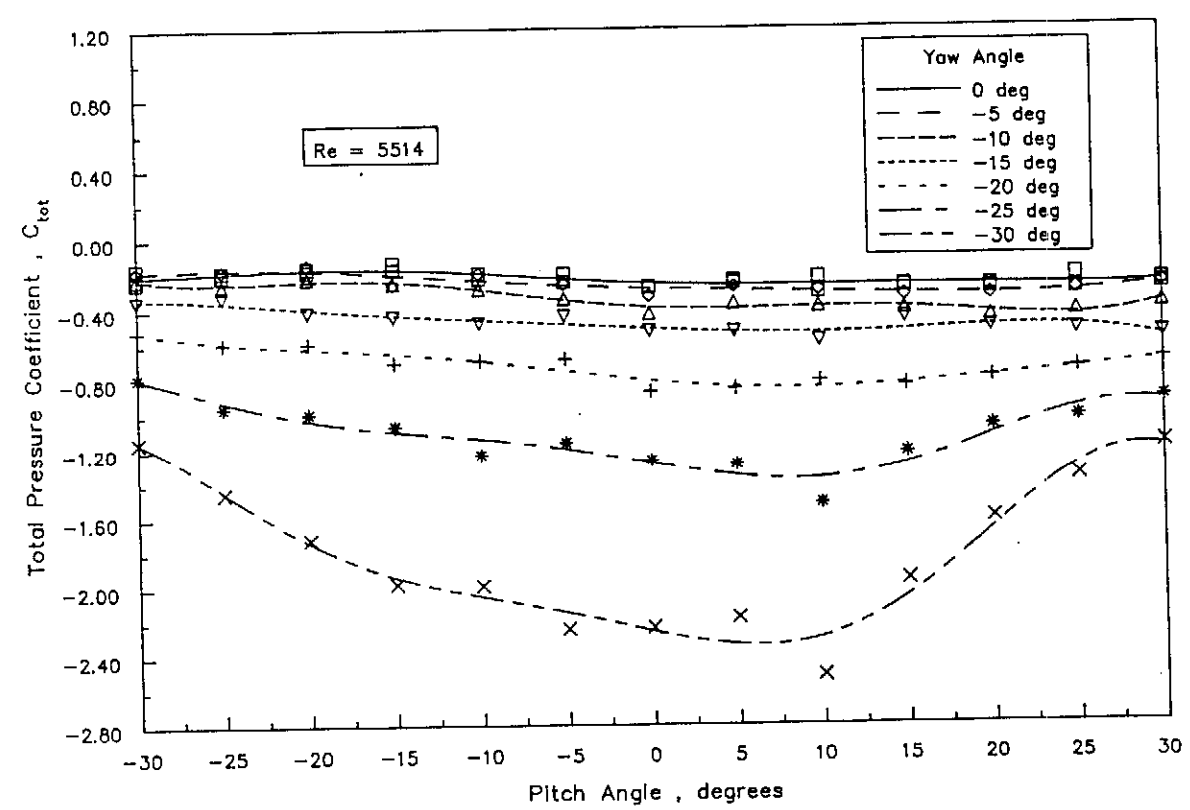

Figure C.2.3.2: C_{tot} for negative yaw angles (Re = 5514)

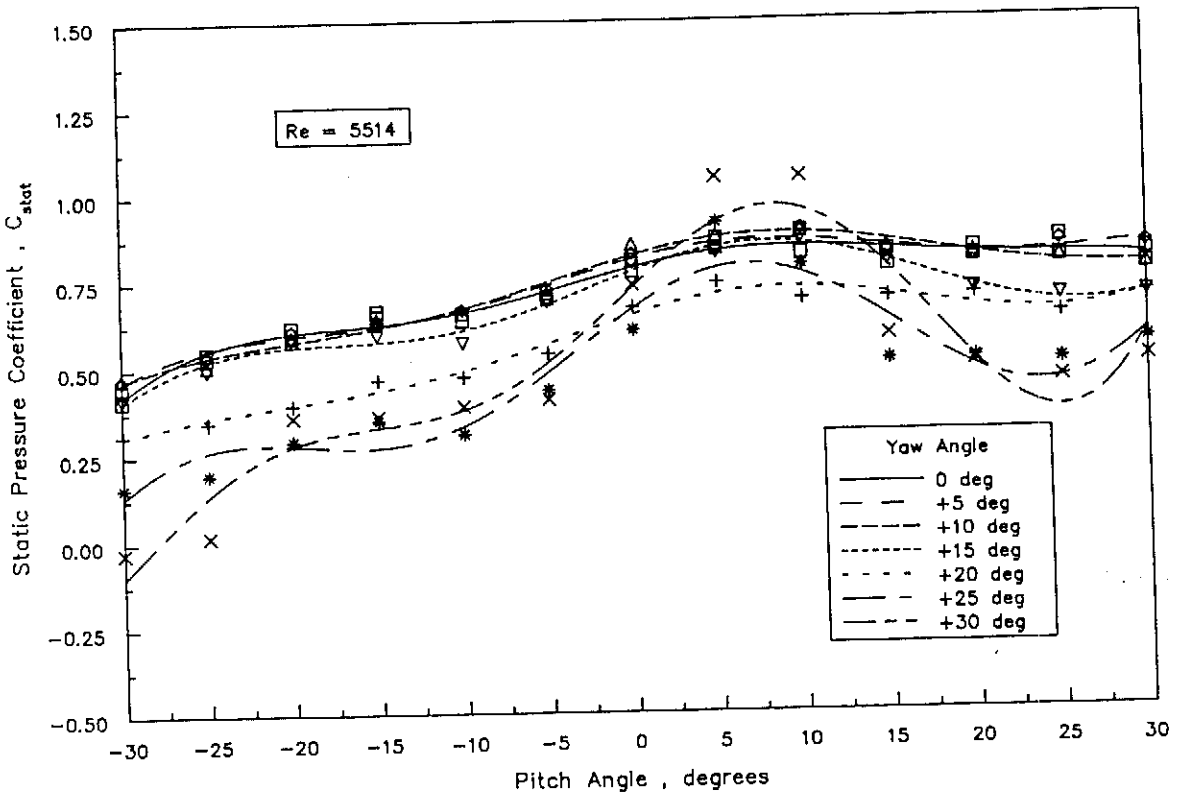

Figure C.2.4.1: C_{stat} for positive yaw angles (Re = 5514)

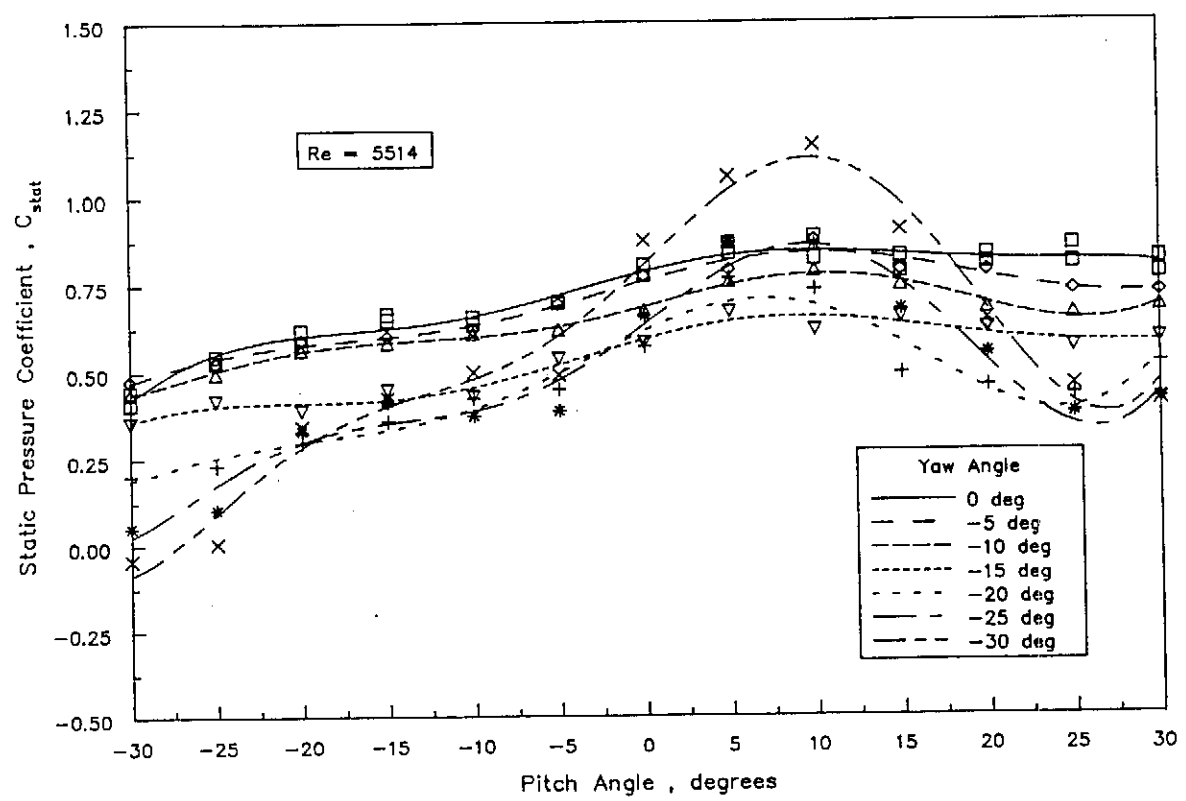

Figure C.2.4.2: C_{stat} for negative yaw angles (Re = 5514)

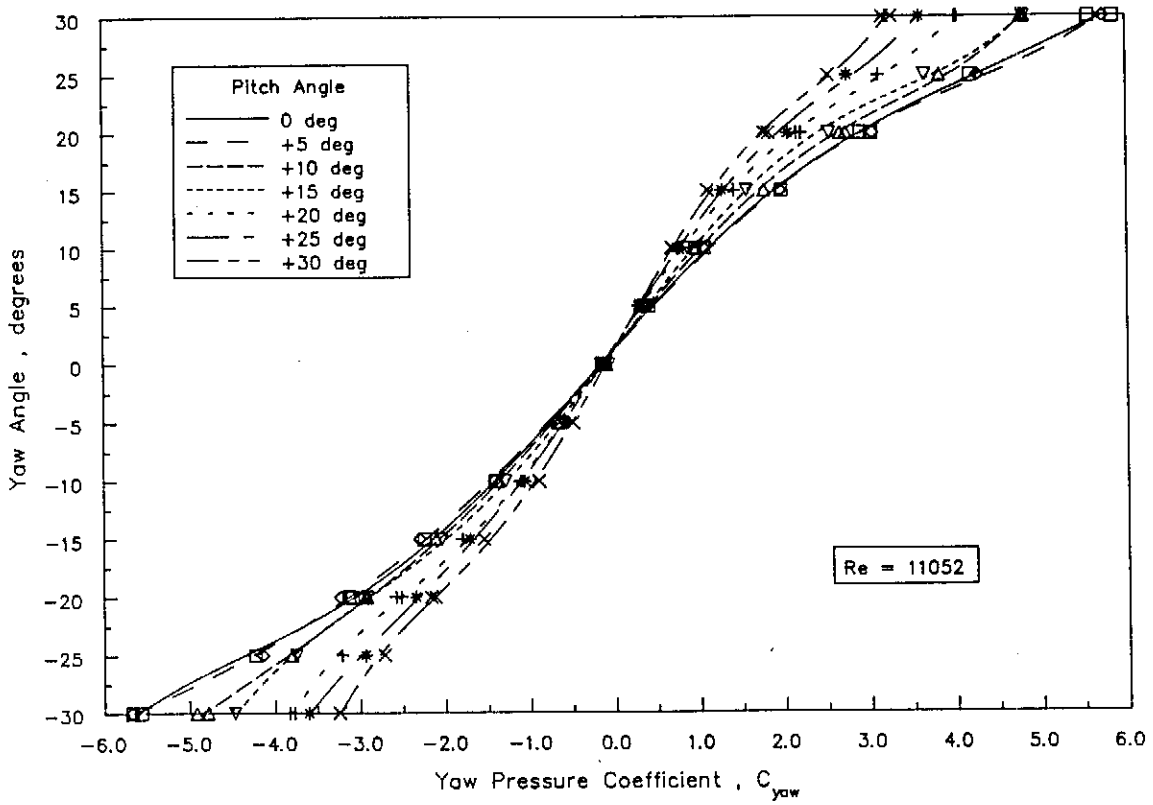

Figure C.3.1.1: Yaw angle for positive pitch angles (Re = 11052)

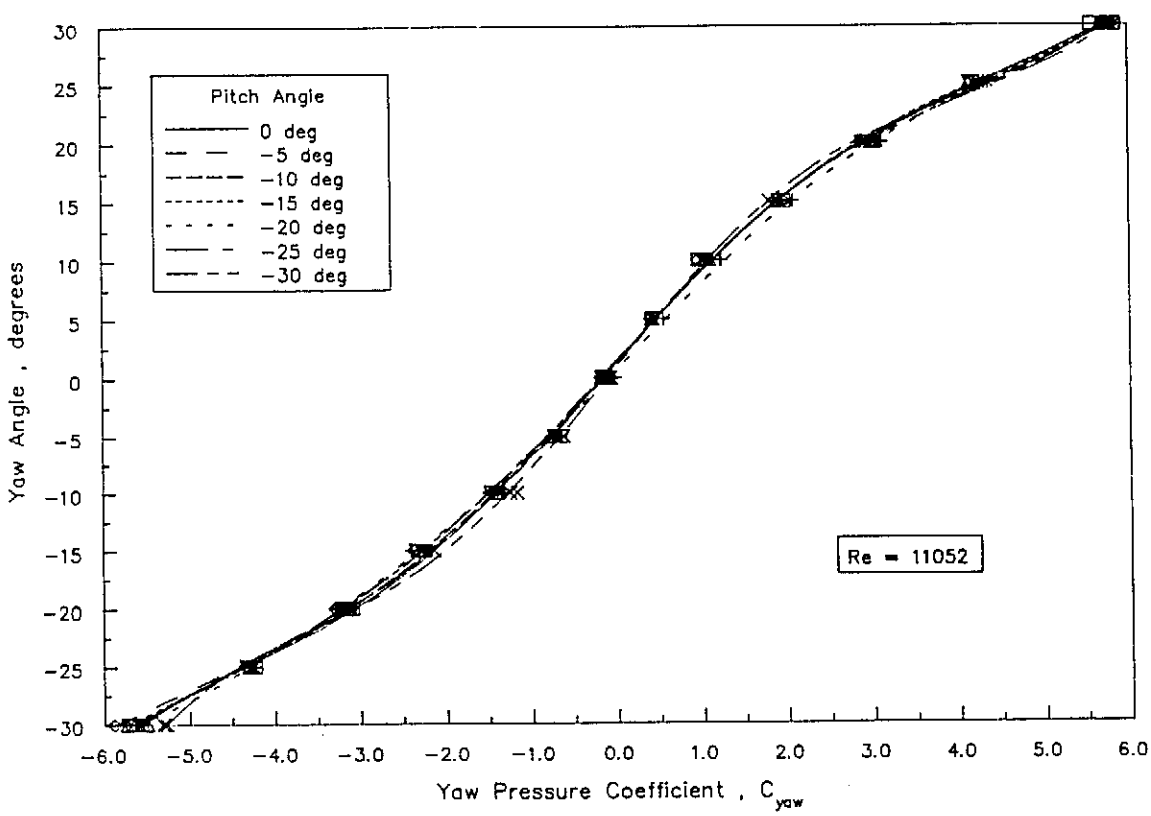

Figure C.3.1.2: Yaw angle for negative pitch angles (Re = 11052)

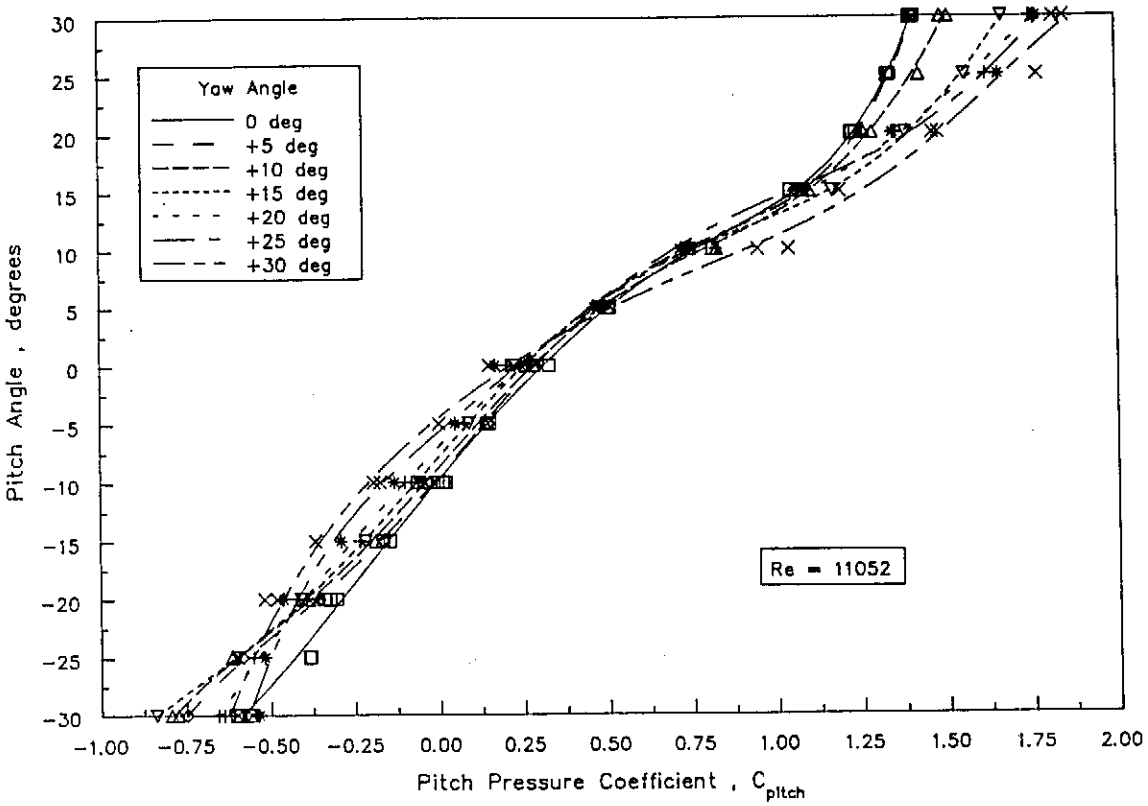

Figure C.3.2.1: Pitch angle for positive yaw angles (Re = 11052)

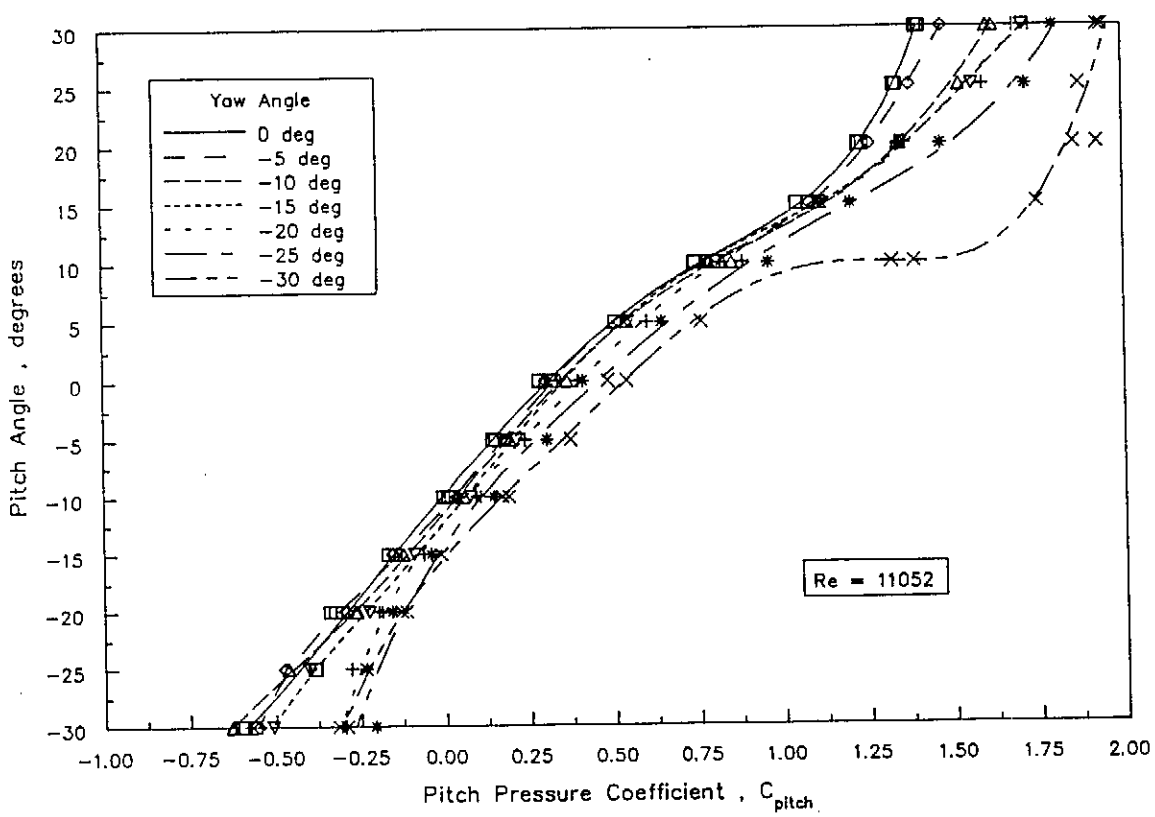

Figure C.3.2.2: Pitch angle for negative yaw angles (Re = 11052)

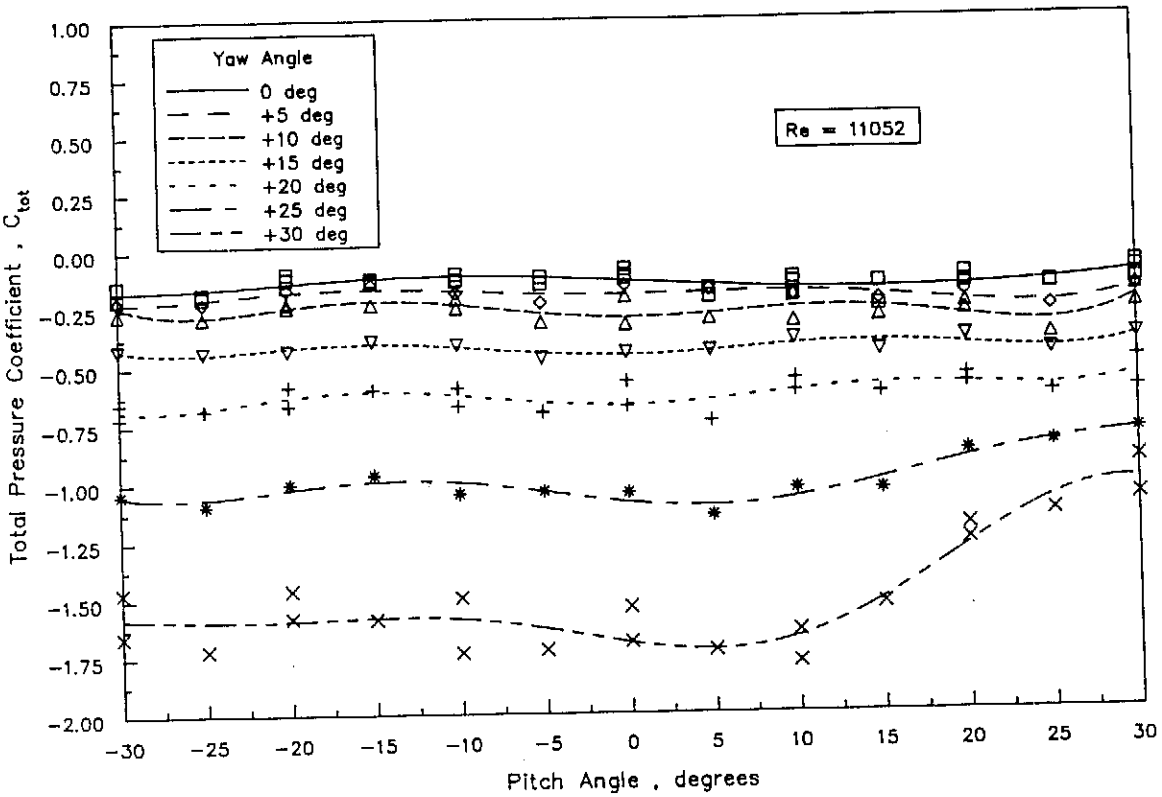

Figure C.3.3.1: C_{tot} for positive yaw angles (Re = 11052)

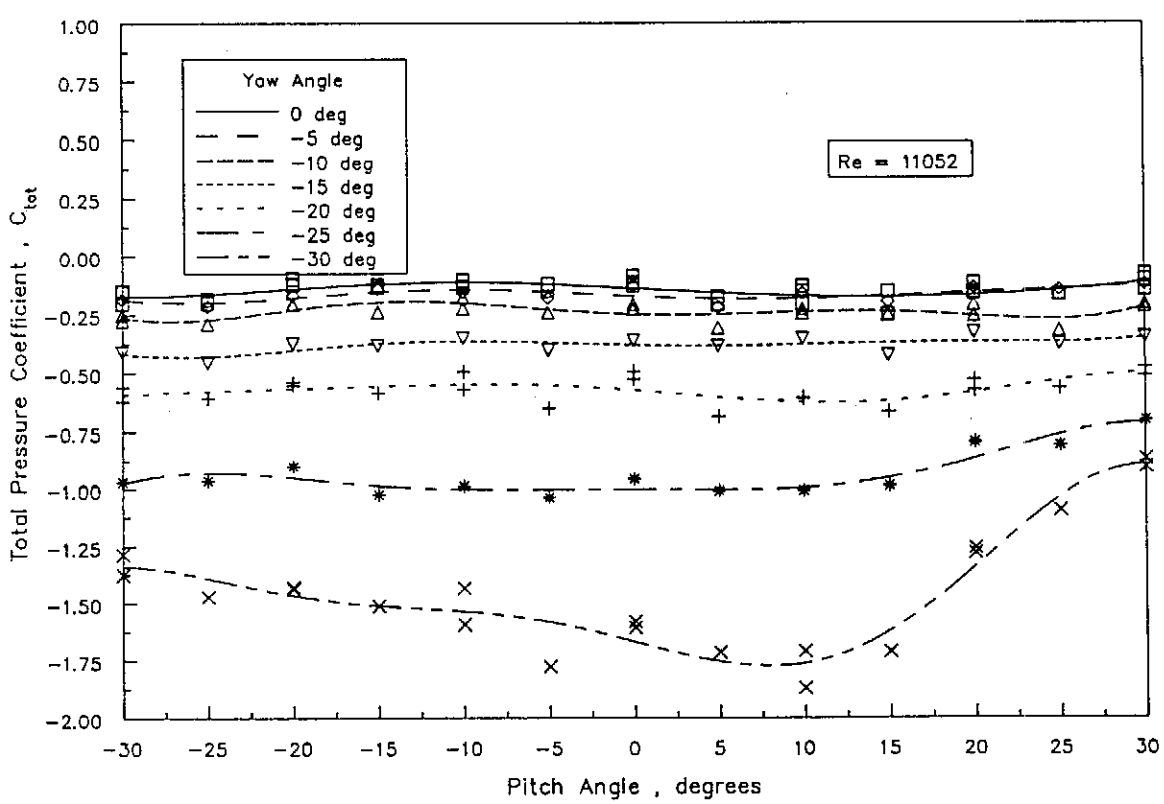

Figure C.3.3.2: C_{tot} for negative yaw angles (Re = 11052)

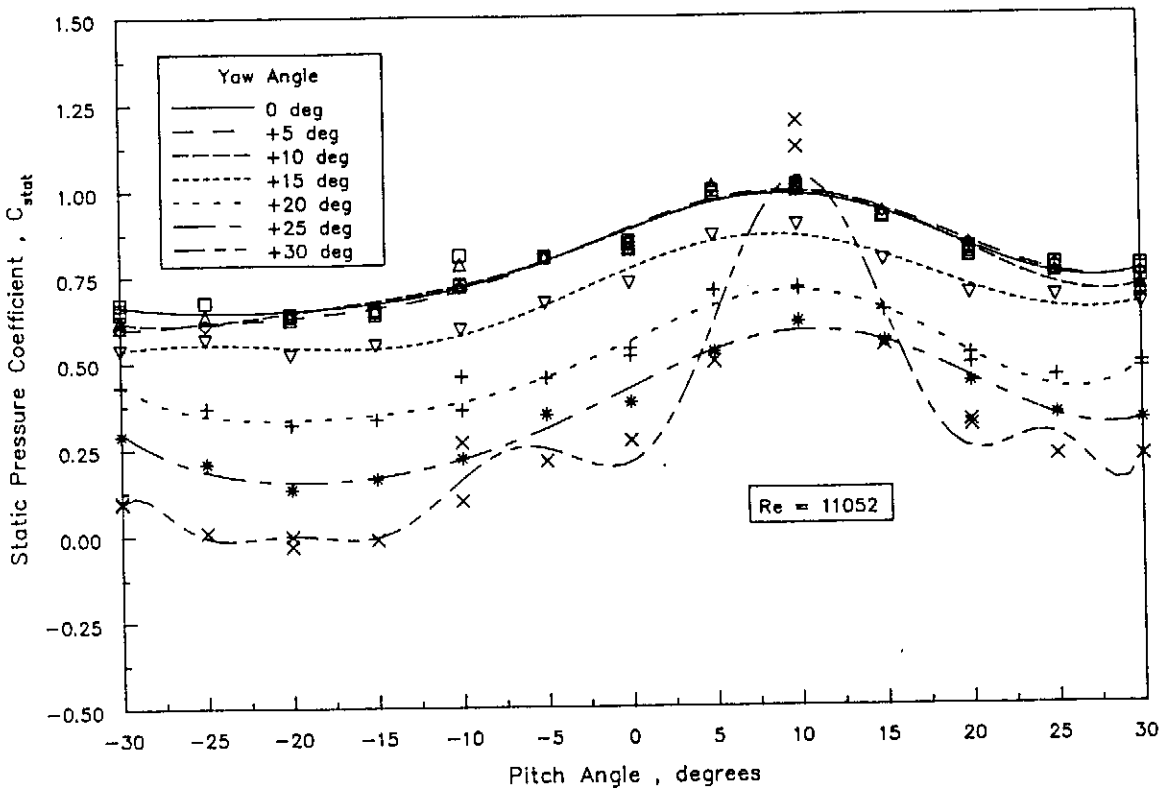

Figure C.3.4.1: C_{stat} for positive yaw angles (Re = 11052)

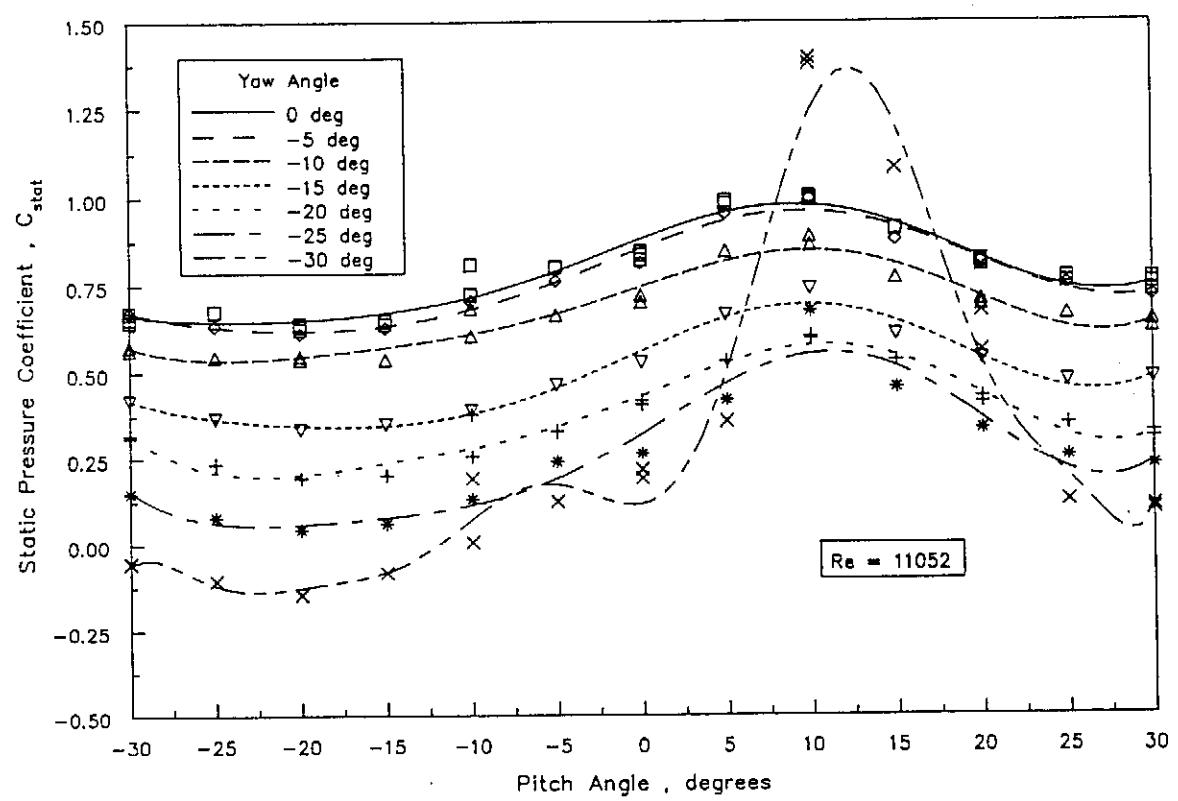

Figure C.3.4.2: C_{stat} for negative yaw angles (Re = 11052)

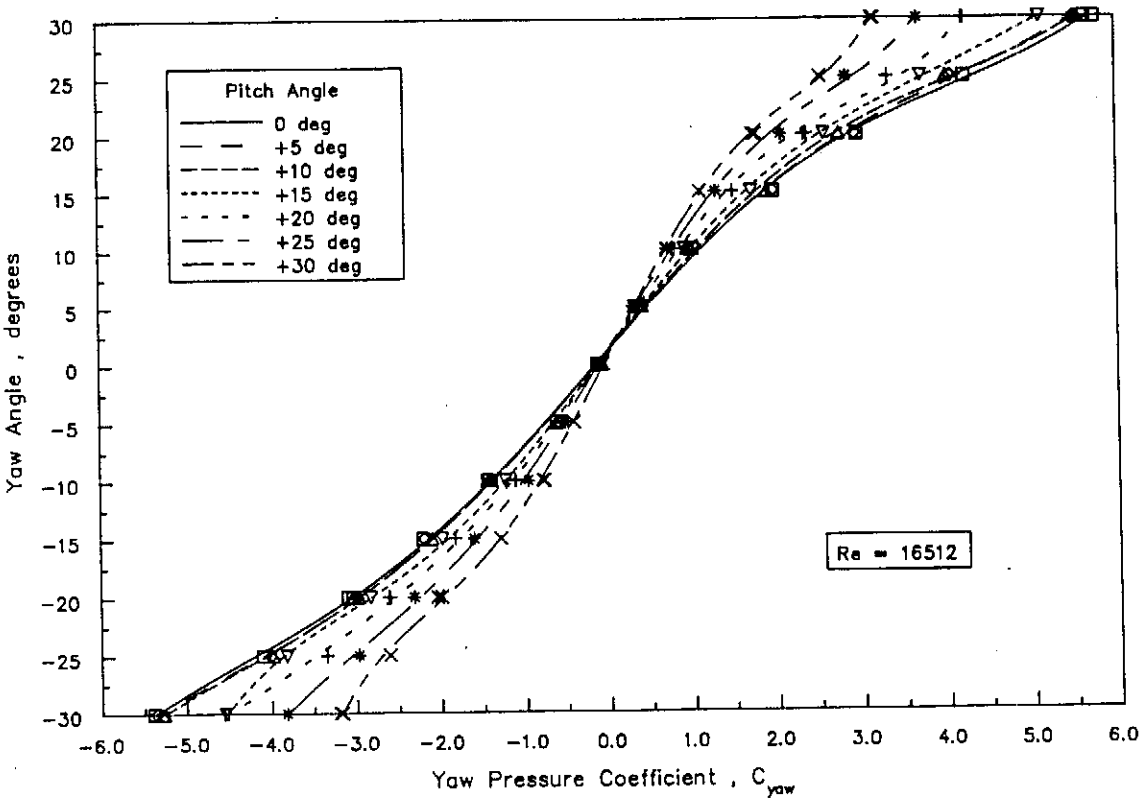

Figure C.4.1.1: Yaw angle for positive pitch angles (Re = 16512)

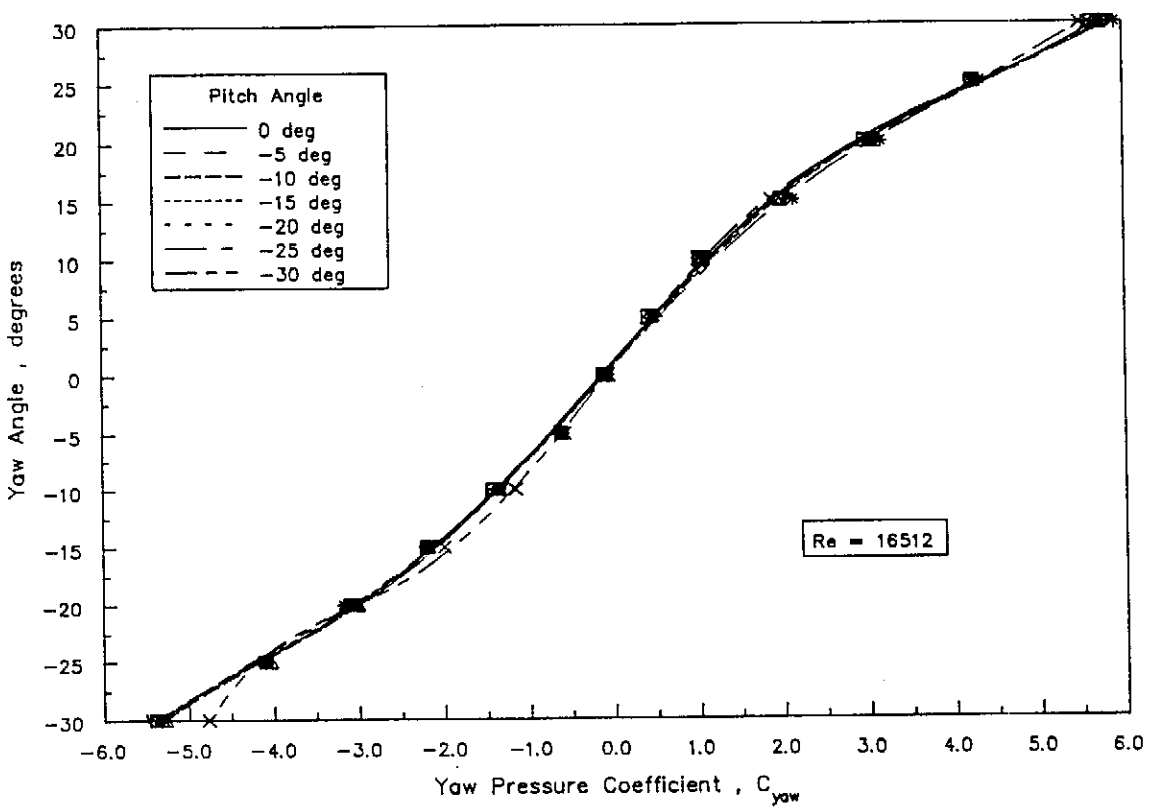

Figure C.4.1.2: Yaw angle for negative pitch angles (Re = 16512)

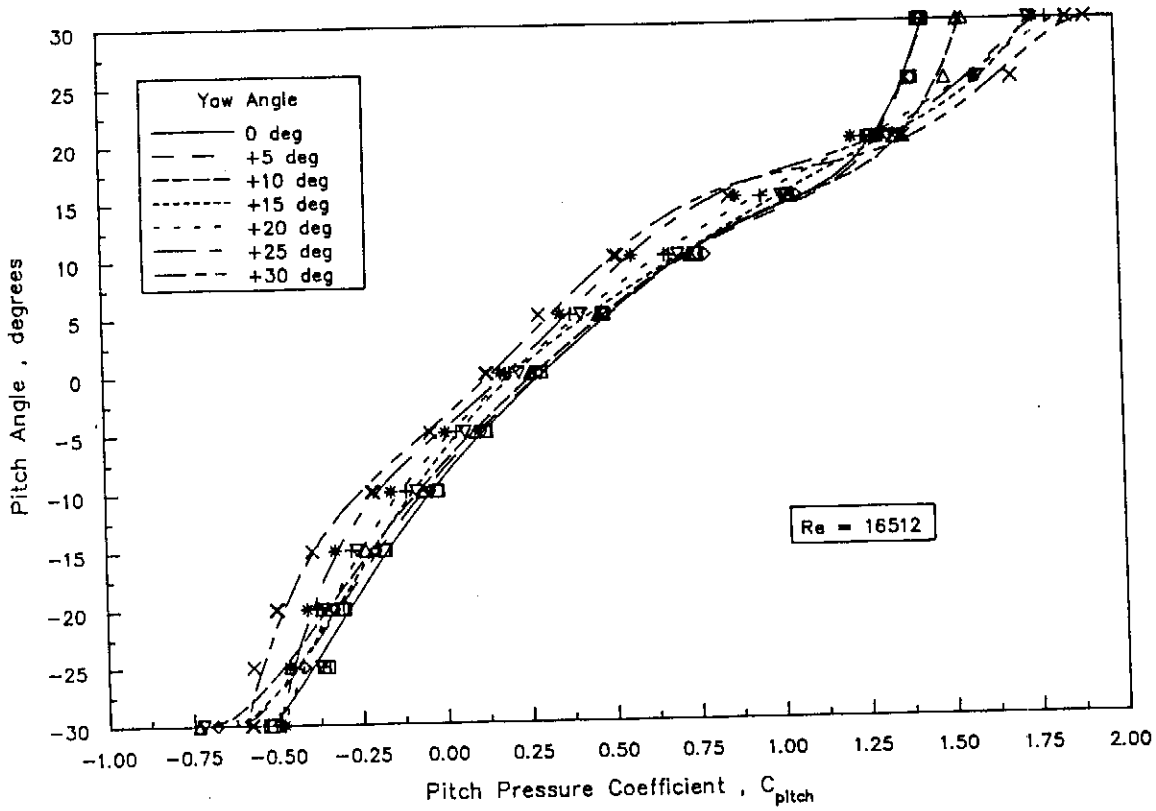

Figure C.4.2.1: Pitch angle for positive yaw angles ($Re = 16512$)

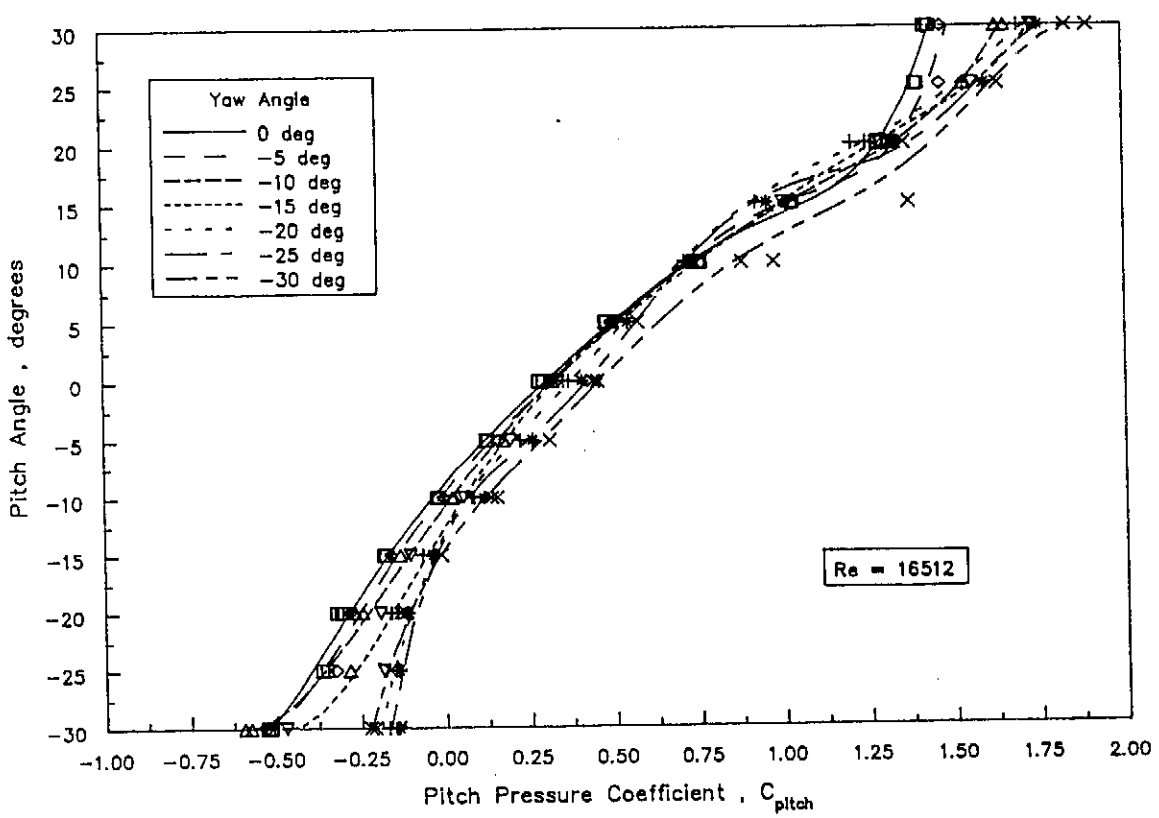

Figure C.4.2.2: Pitch angle for negative yaw angles ($Re = 16512$)

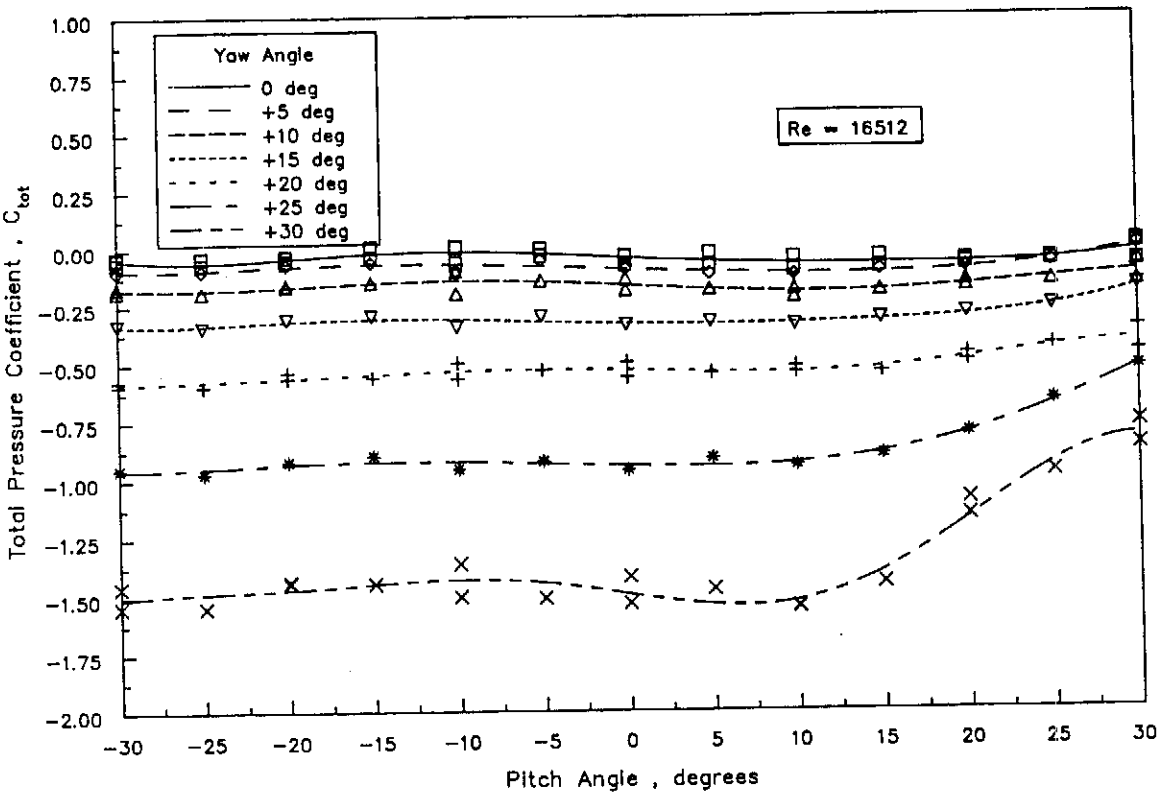

Figure C.4.3.1: C_{tot} for positive yaw angles (Re = 16512)

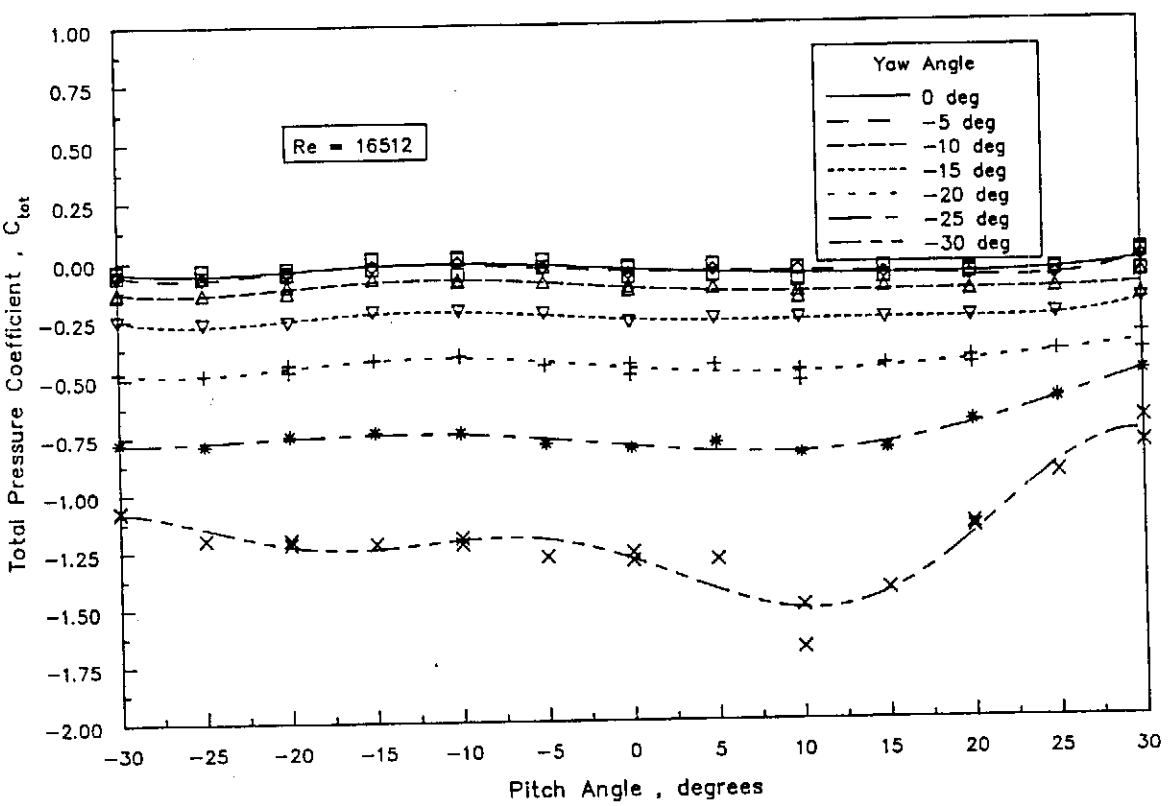

Figure C.4.3.2: C_{tot} for negative yaw angles (Re = 16512)

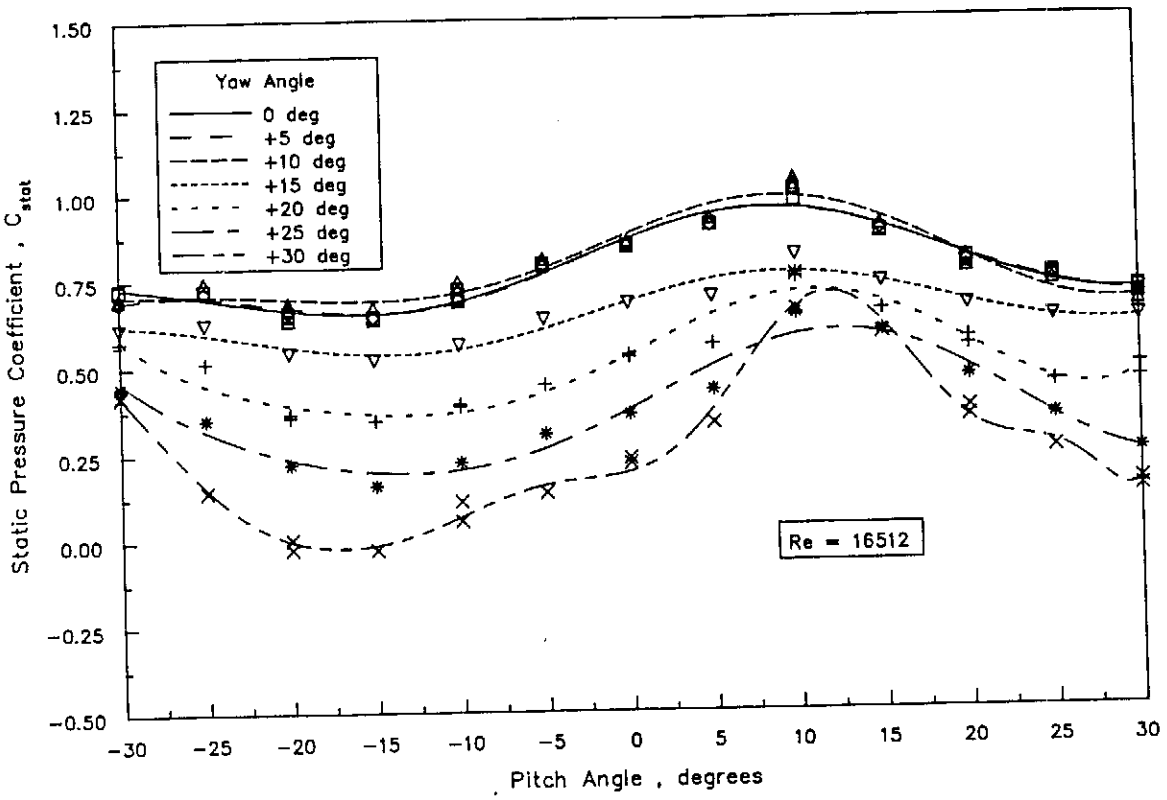

Figure C.4.4.1: C_{stat} for positive yaw angles (Re = 16512)

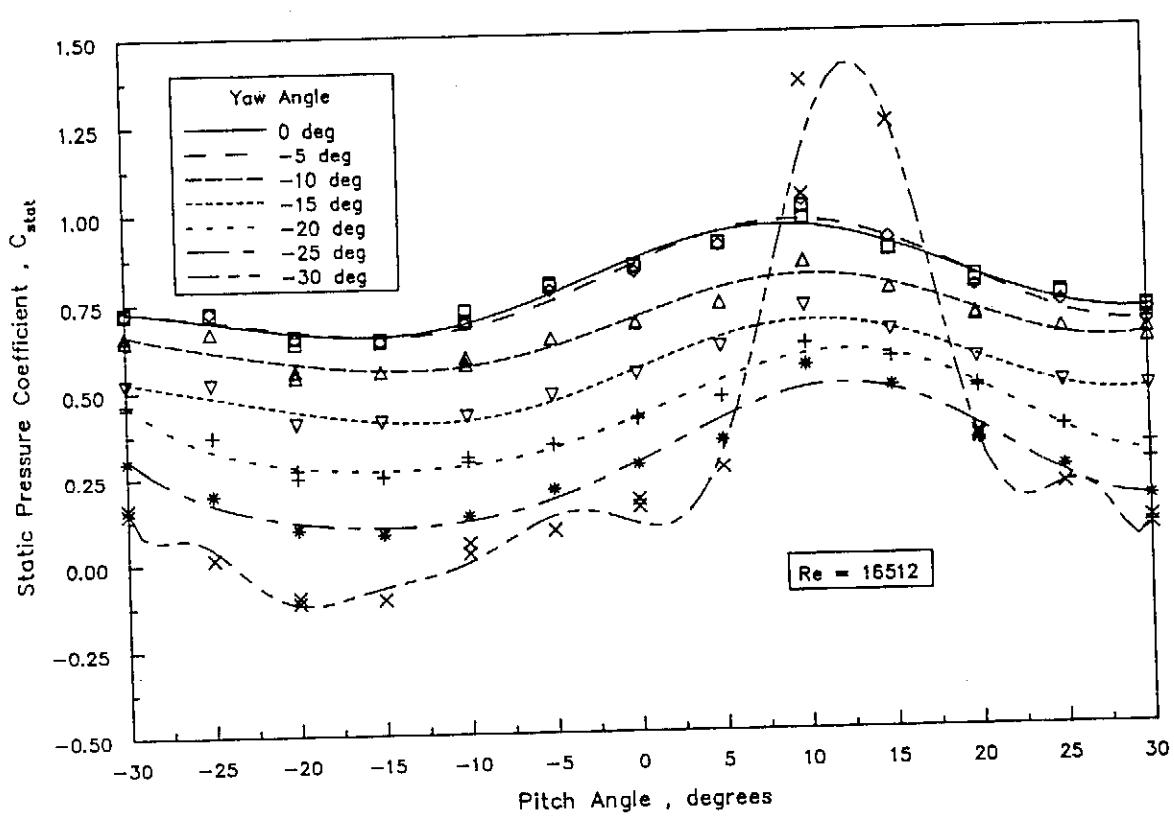

Figure C.4.4.2: C_{stat} for negative yaw angles (Re = 16512)

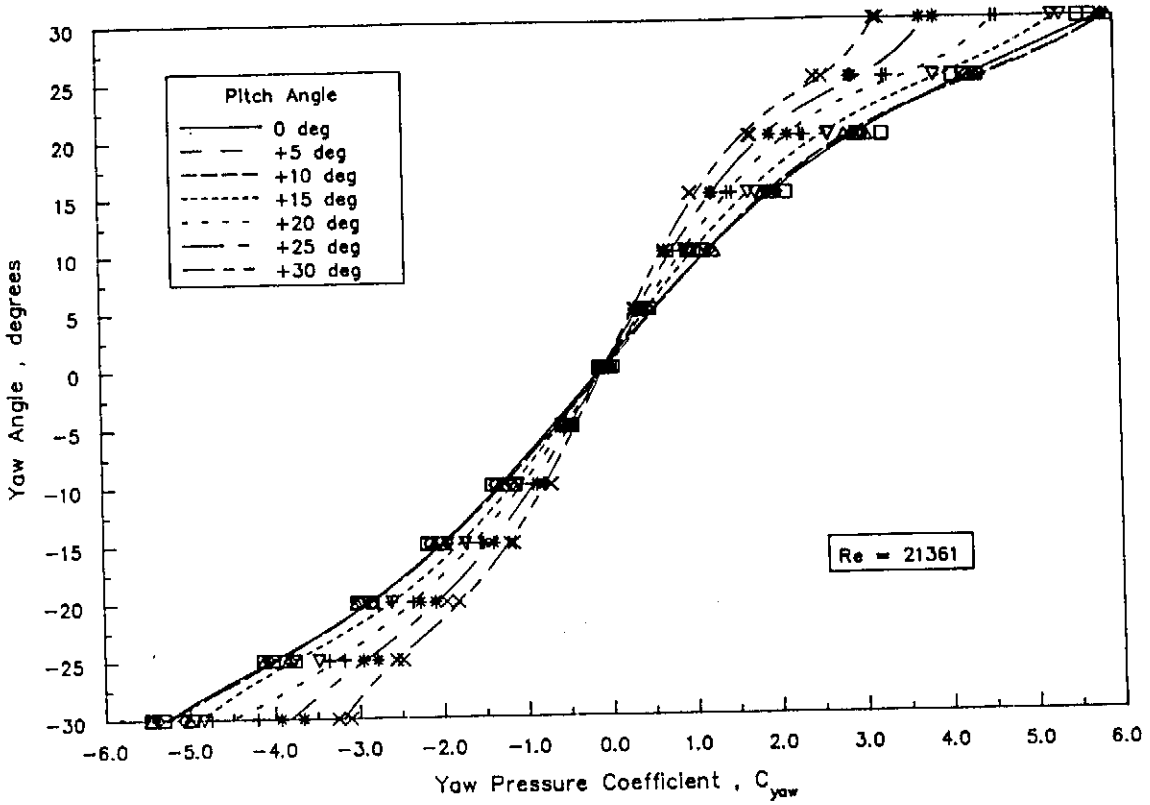

Figure C.5.1.1: Yaw angle for positive pitch angles (Re = 21361)

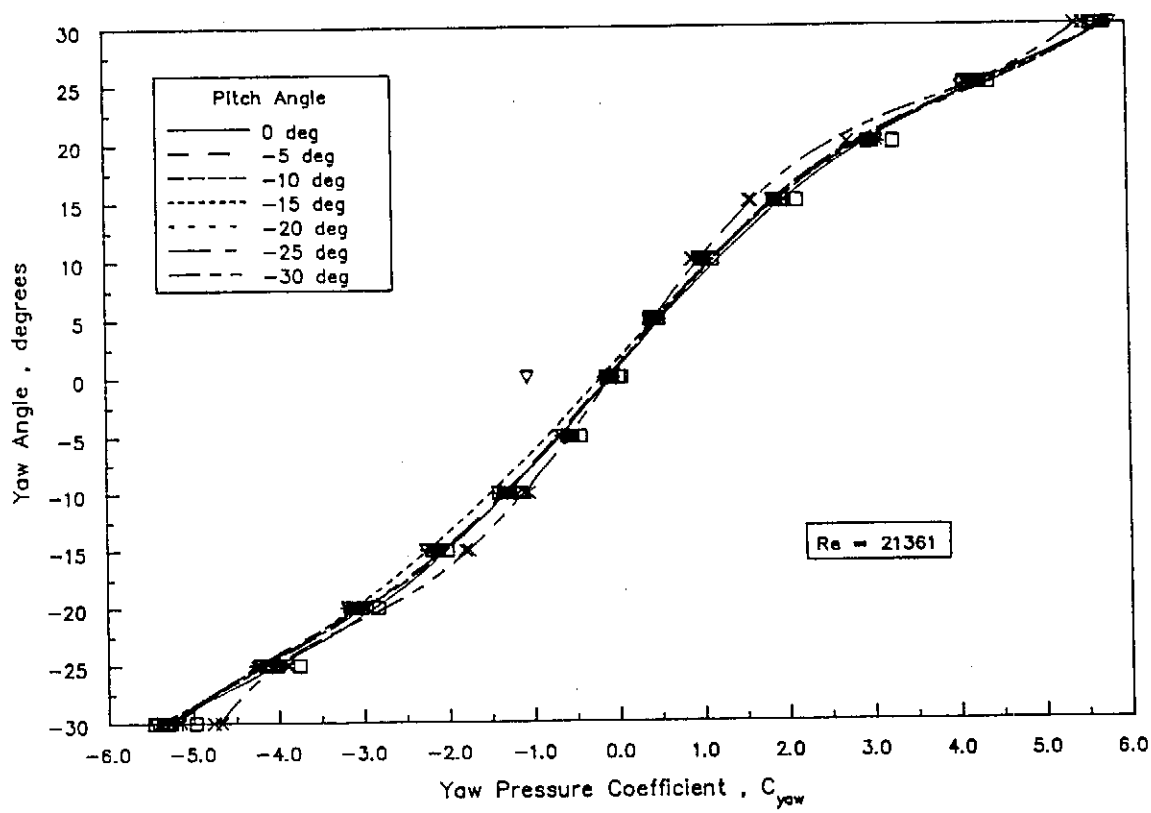

Figure C.5.1.2: Yaw angle for negative pitch angles (Re = 21361)

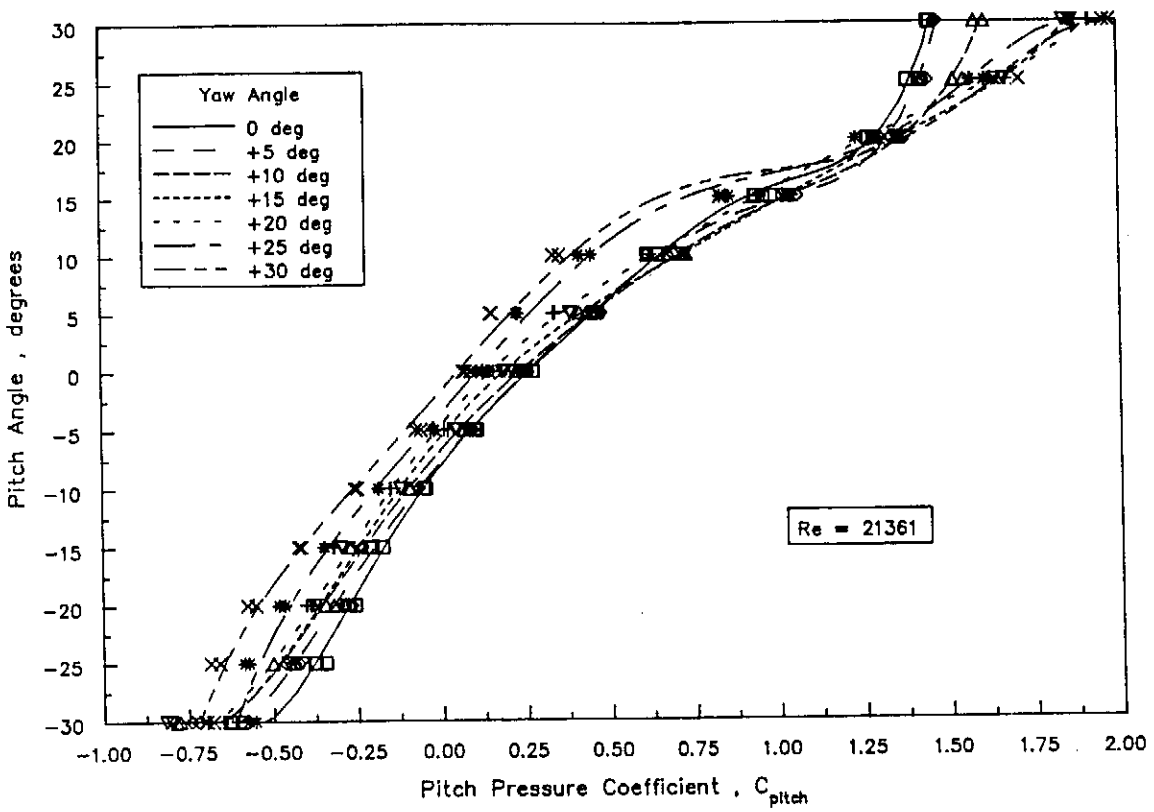

Figure C.5.2.1: Pitch angle for positive yaw angles (Re = 21361)

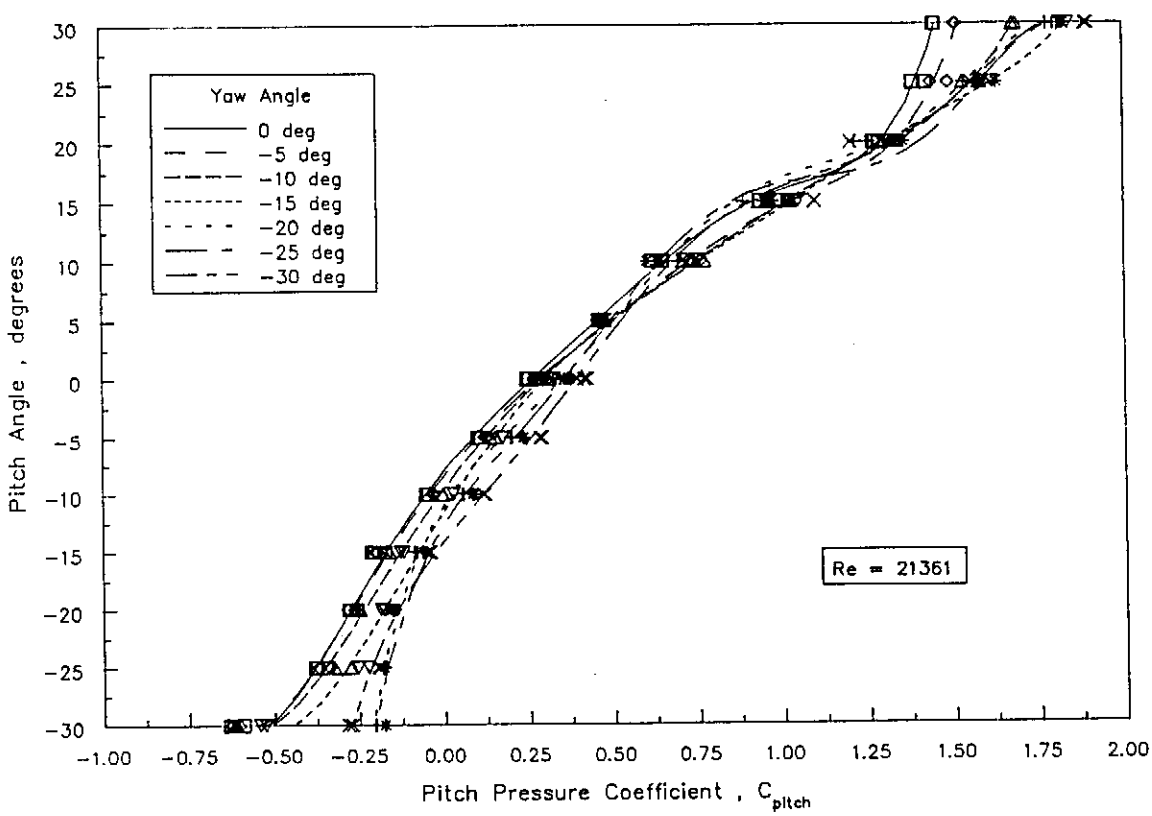

Figure C.5.2.2: Pitch angle for negative yaw angles (Re = 21361)

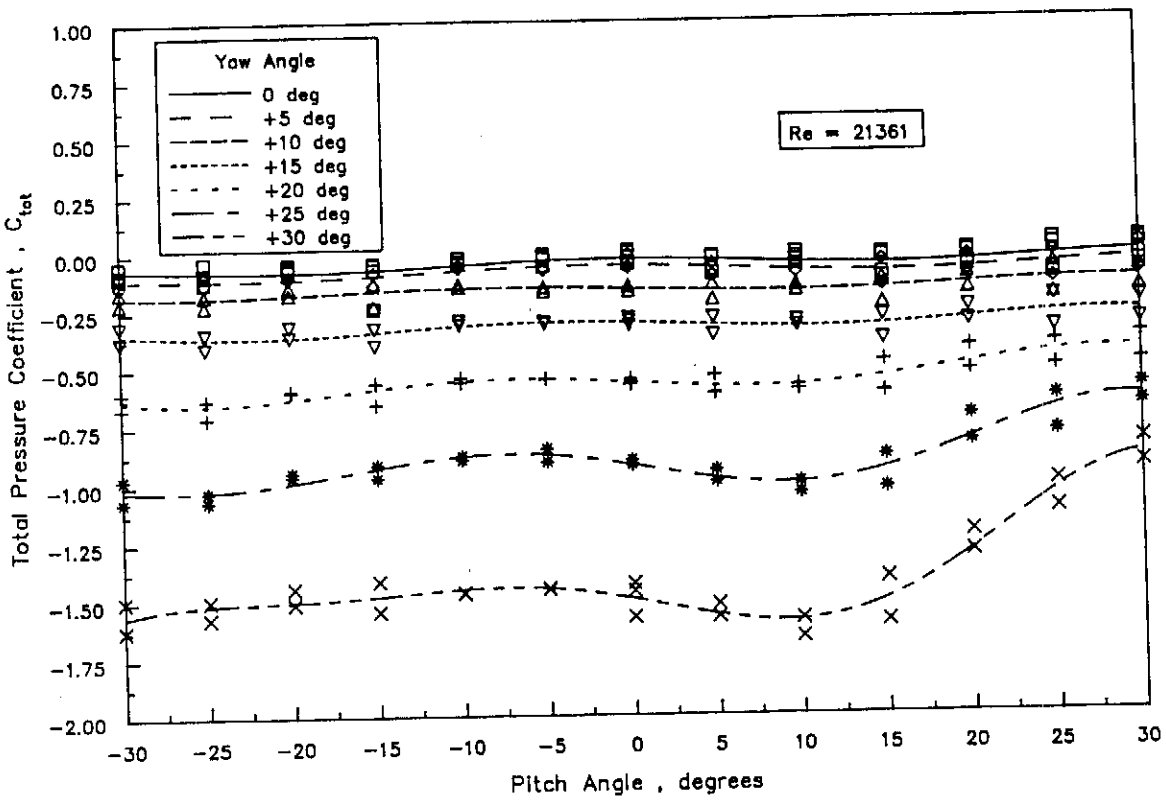

Figure C.5.3.1: C_{tot} for positive yaw angles (Re = 21361)

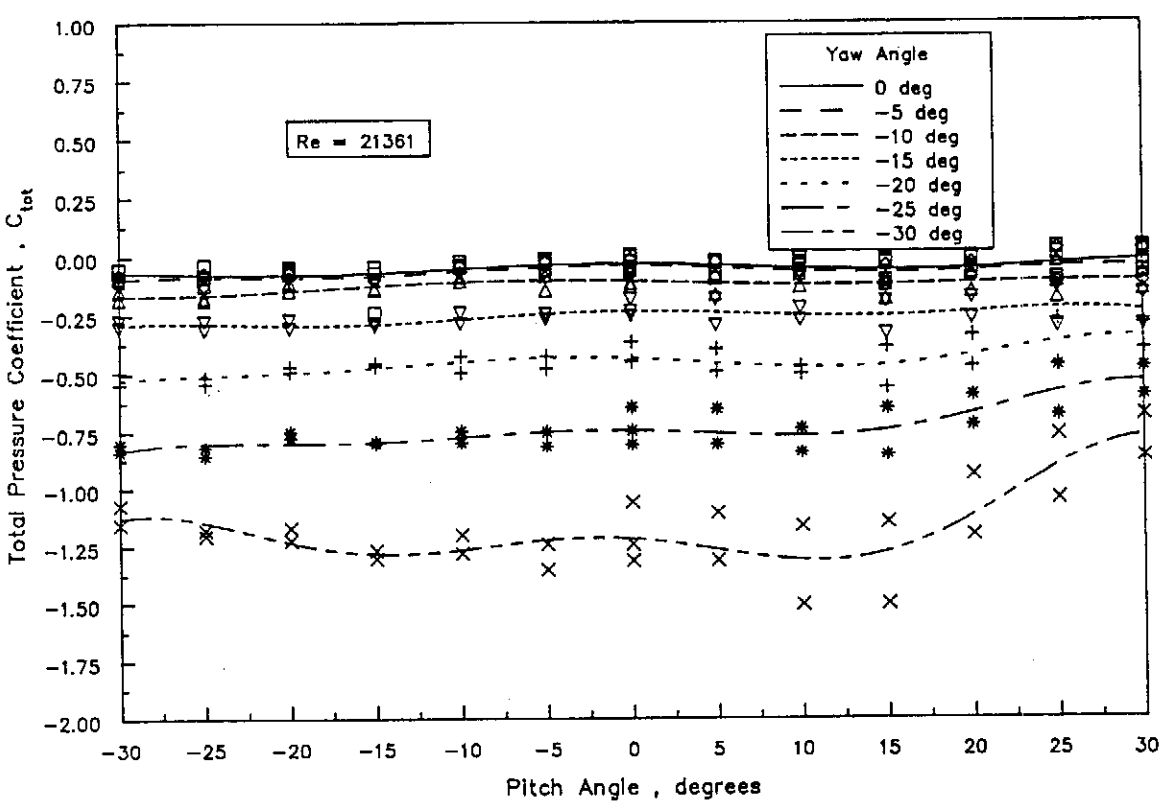

Figure C.5.3.2: C_{tot} for negative yaw angles (Re = 21361)

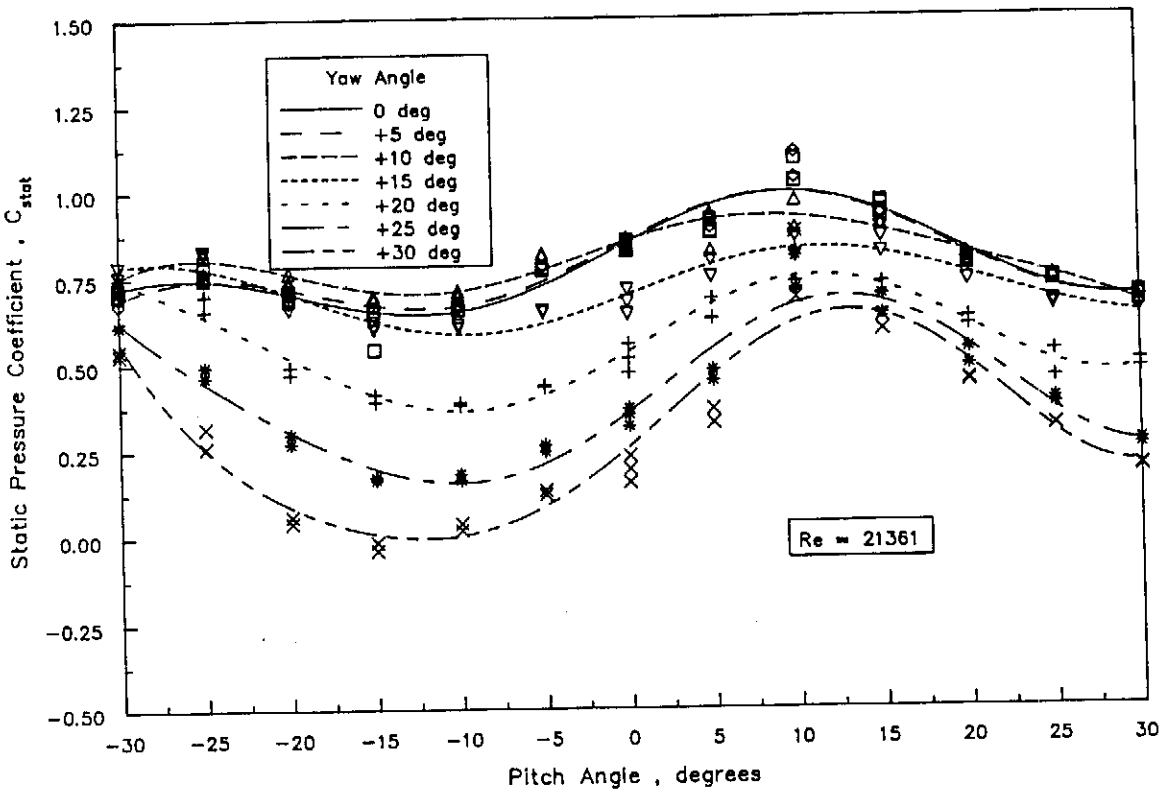

Figure C.5.4.1: C_{stat} for positive yaw angles (Re = 21361)

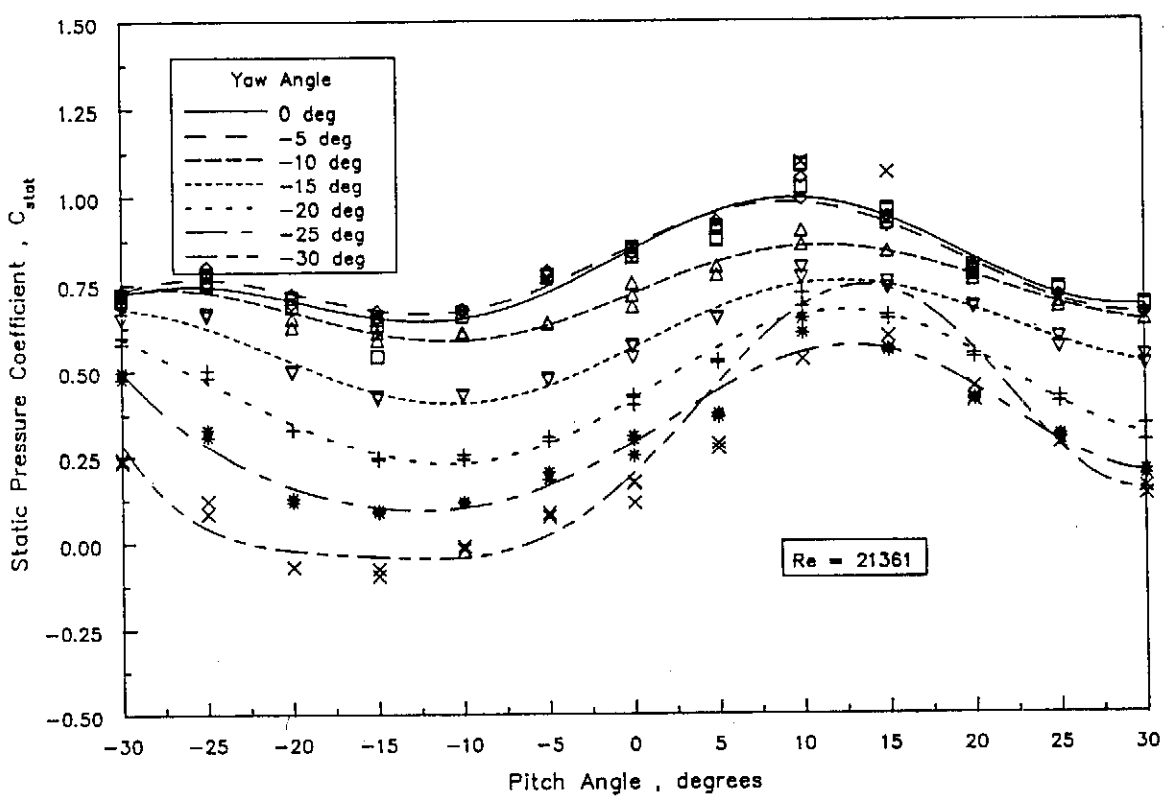

Figure C.5.4.2: C_{stat} for negative yaw angles (Re = 21361)

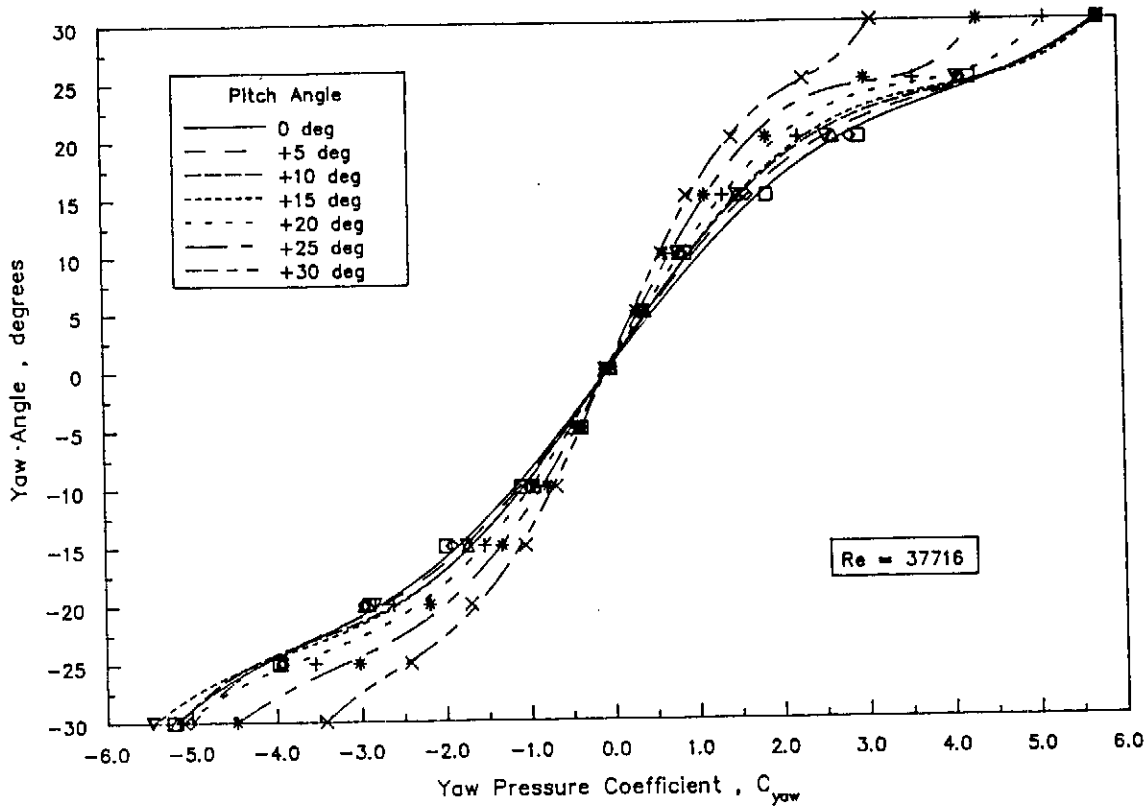

Figure C.6.1.1: Yaw angle for positive pitch angles (Re = 37716)

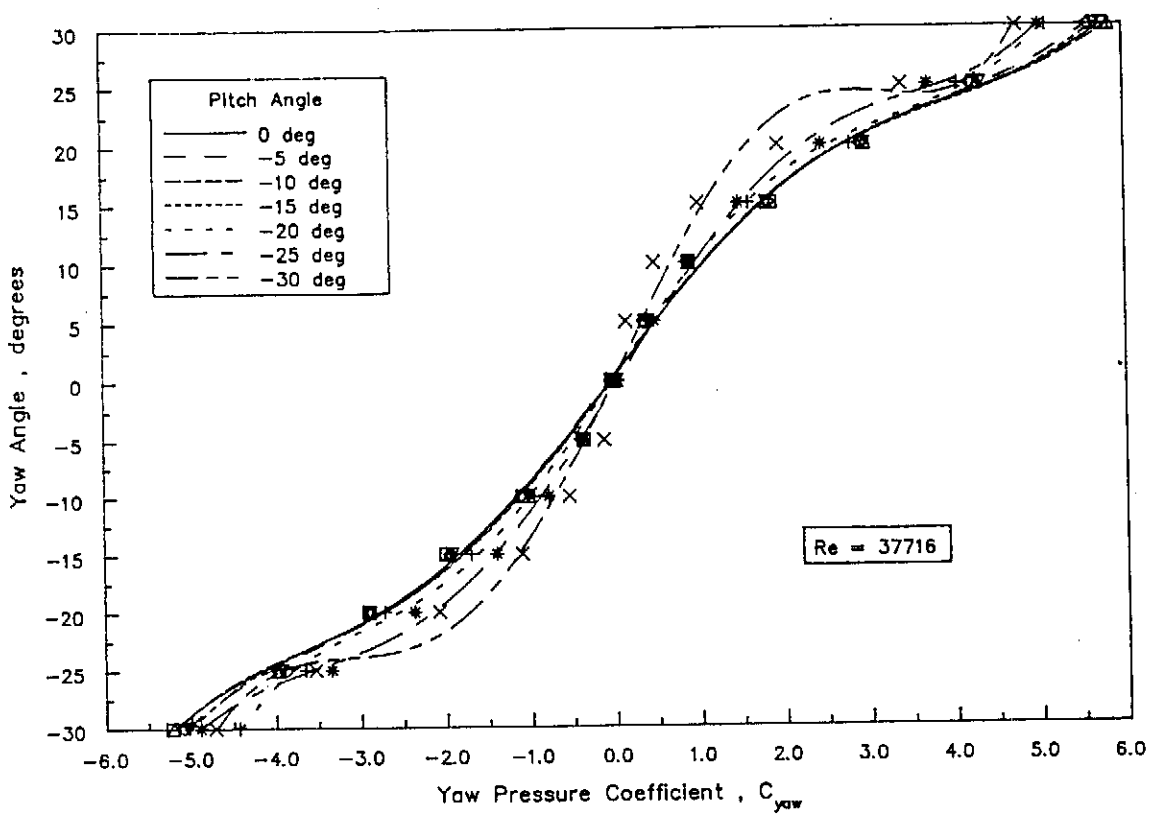

Figure C.6.1.2: Yaw angle for negative pitch angles (Re = 37716)

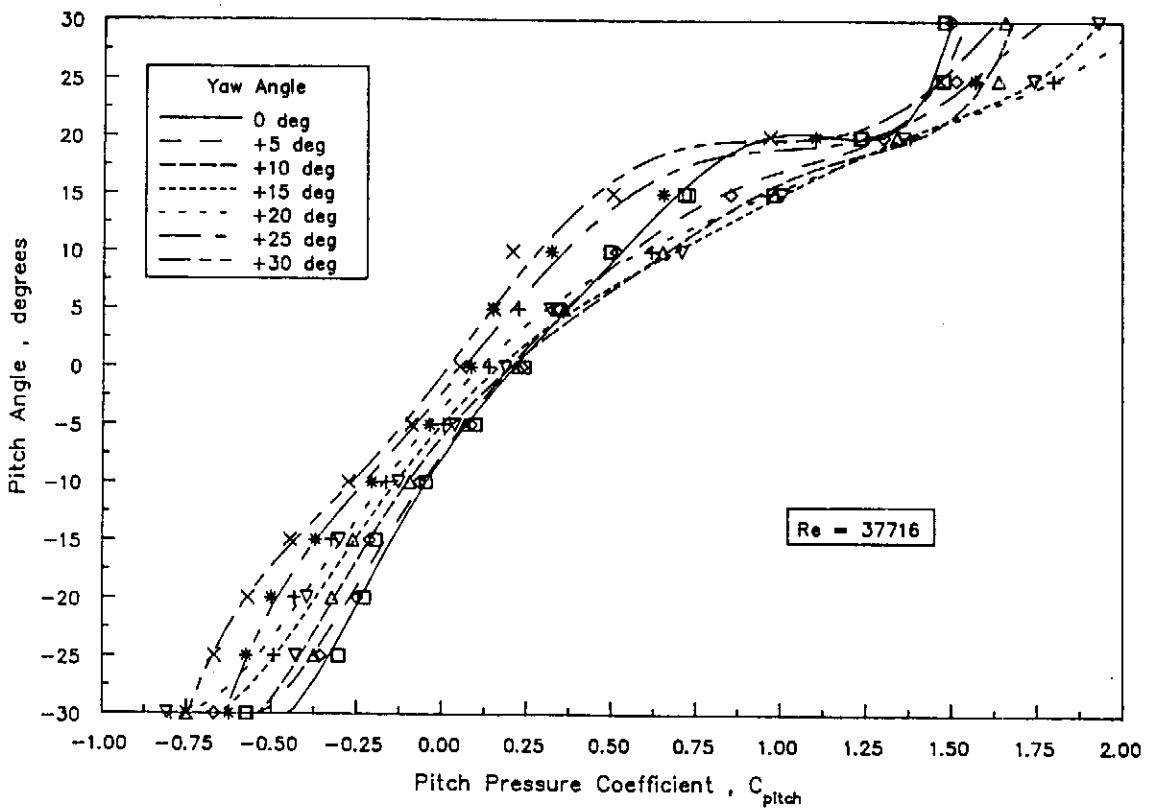

Figure C.6.2.1: Pitch angle for positive yaw angles (Re = 37716)

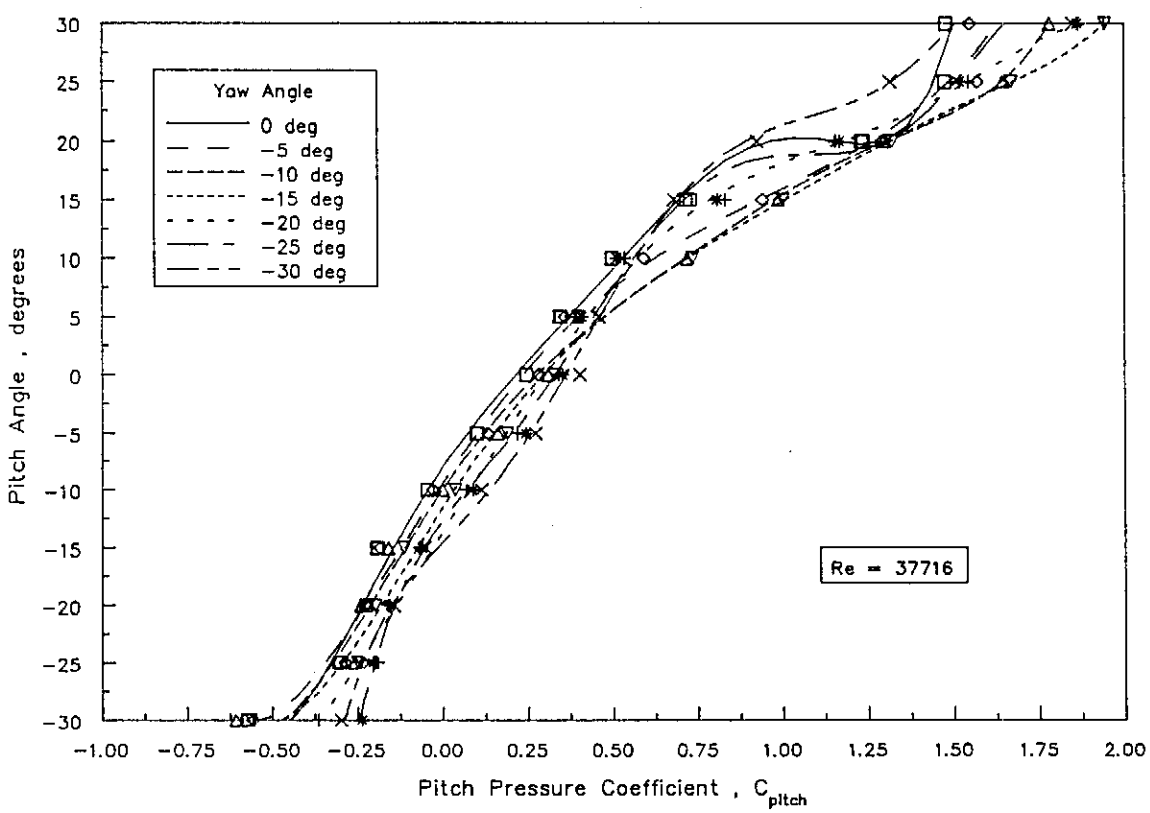

Figure C.6.2.2: Pitch angle for negative yaw angles (Re = 37716)

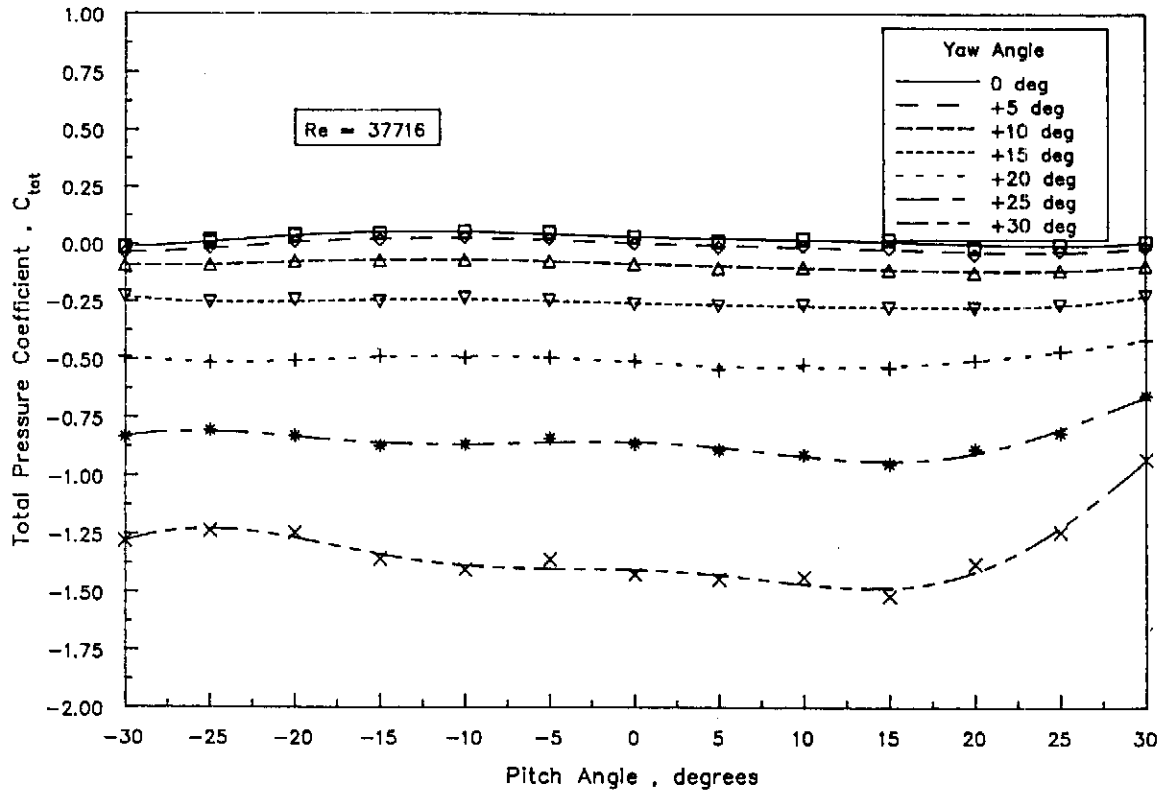

Figure C.6.3.1: C_{tot} for positive yaw angles (Re = 37716)

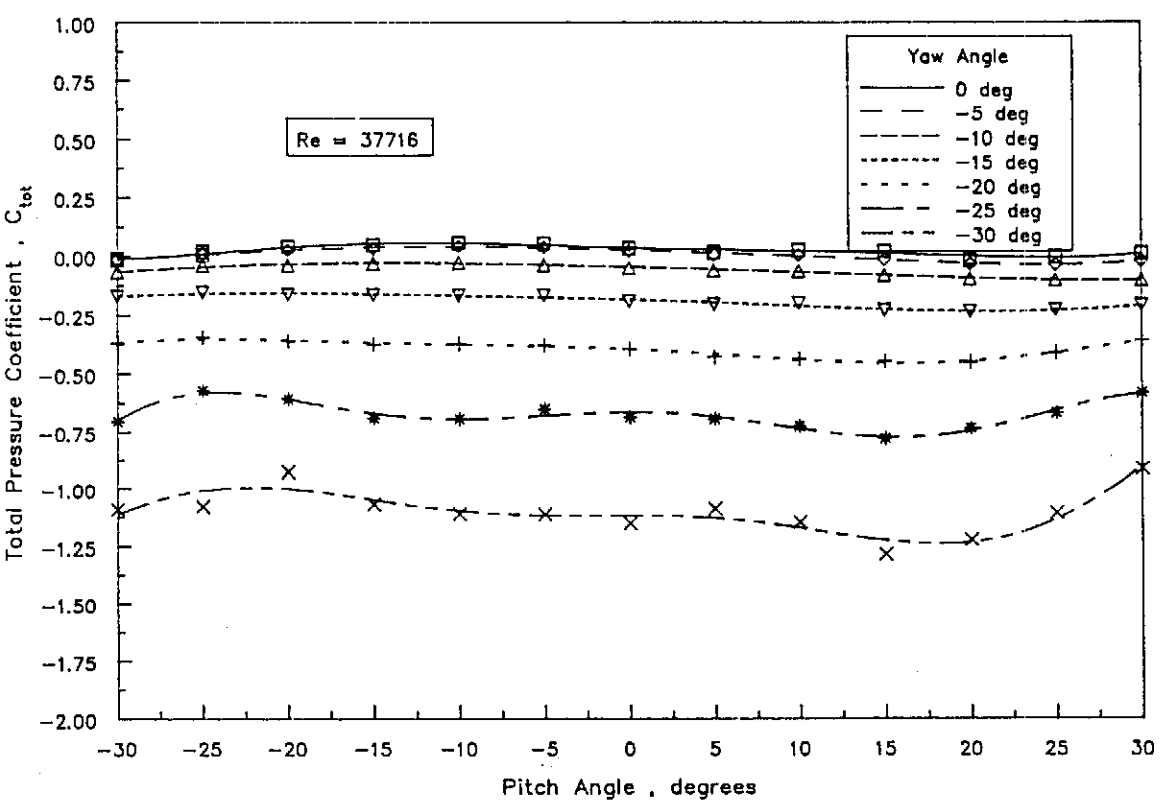

Figure C.6.3.2: C_{tot} for negative yaw angles (Re = 37716)

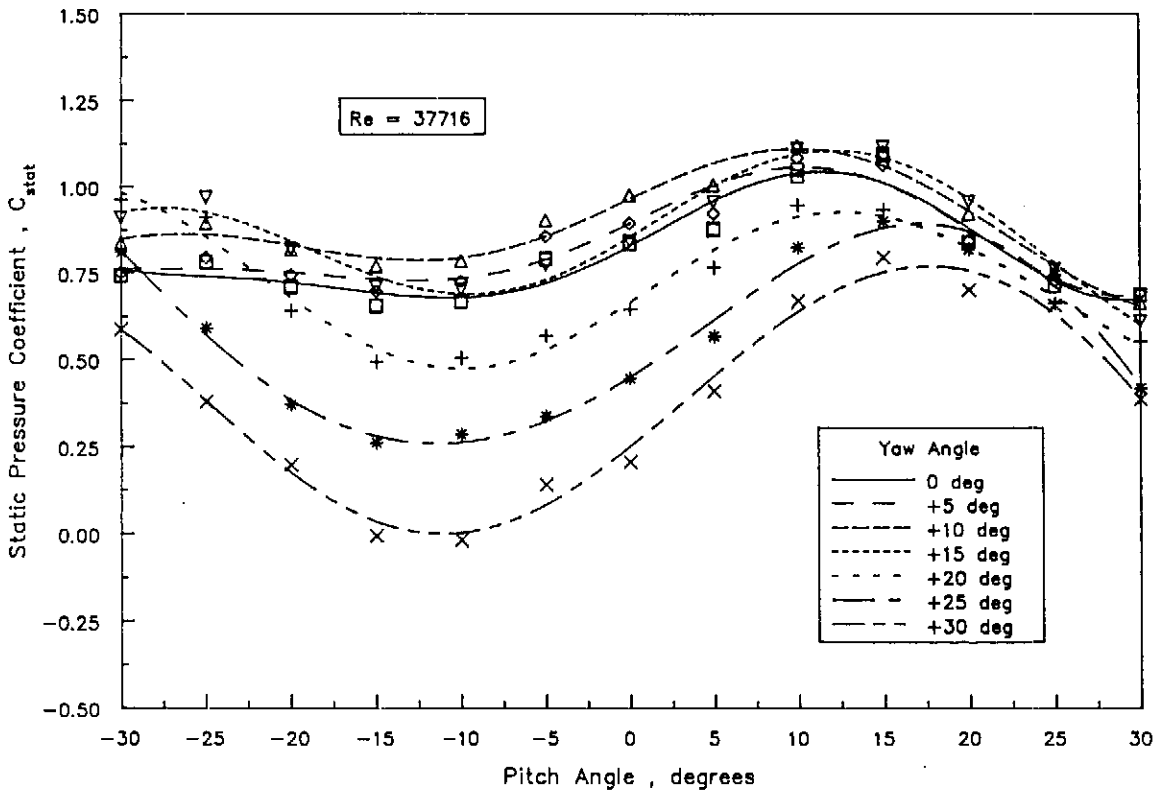

Figure C.6.4.1: C_{stat} for positive yaw angles ($Re = 37716$)

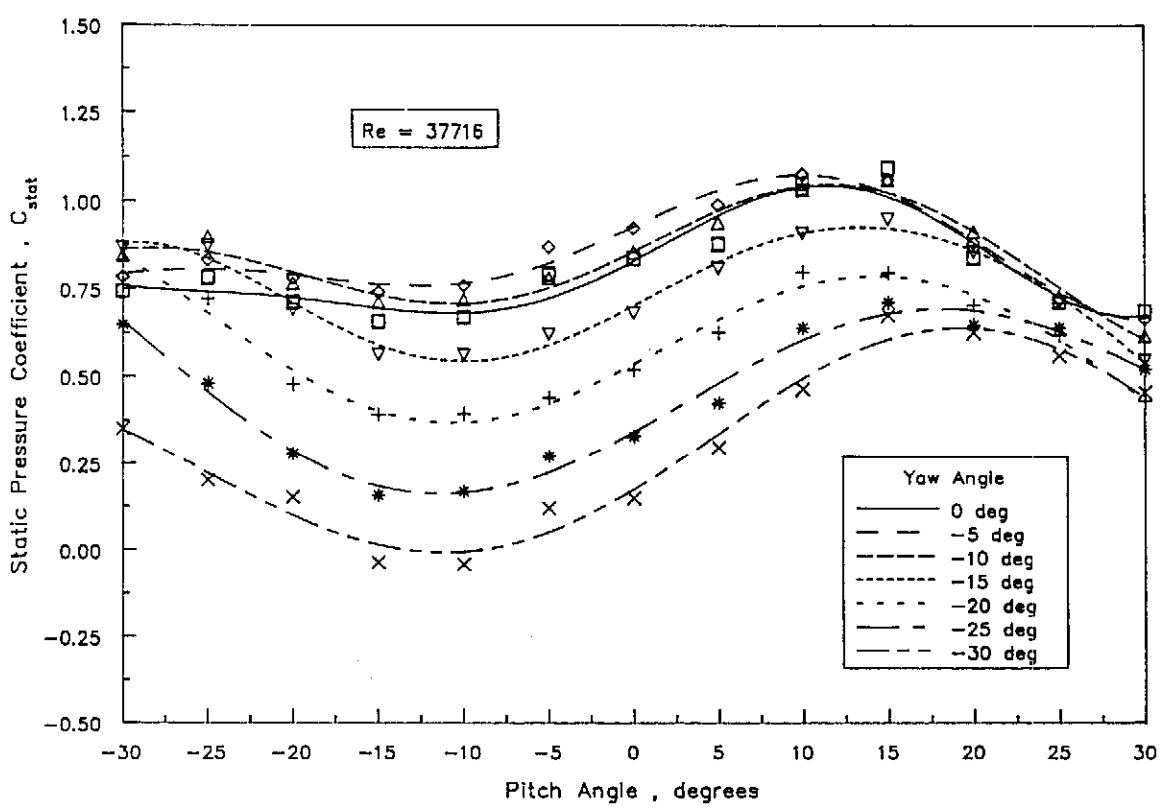

Figure C.6.4.2: C_{stat} for negative yaw angles ($Re = 37716$)

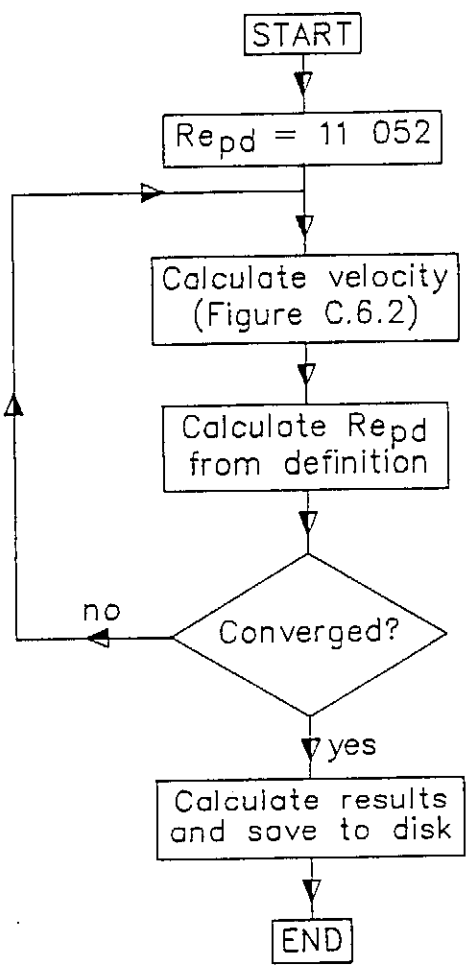

Figure C.7.1: Main program

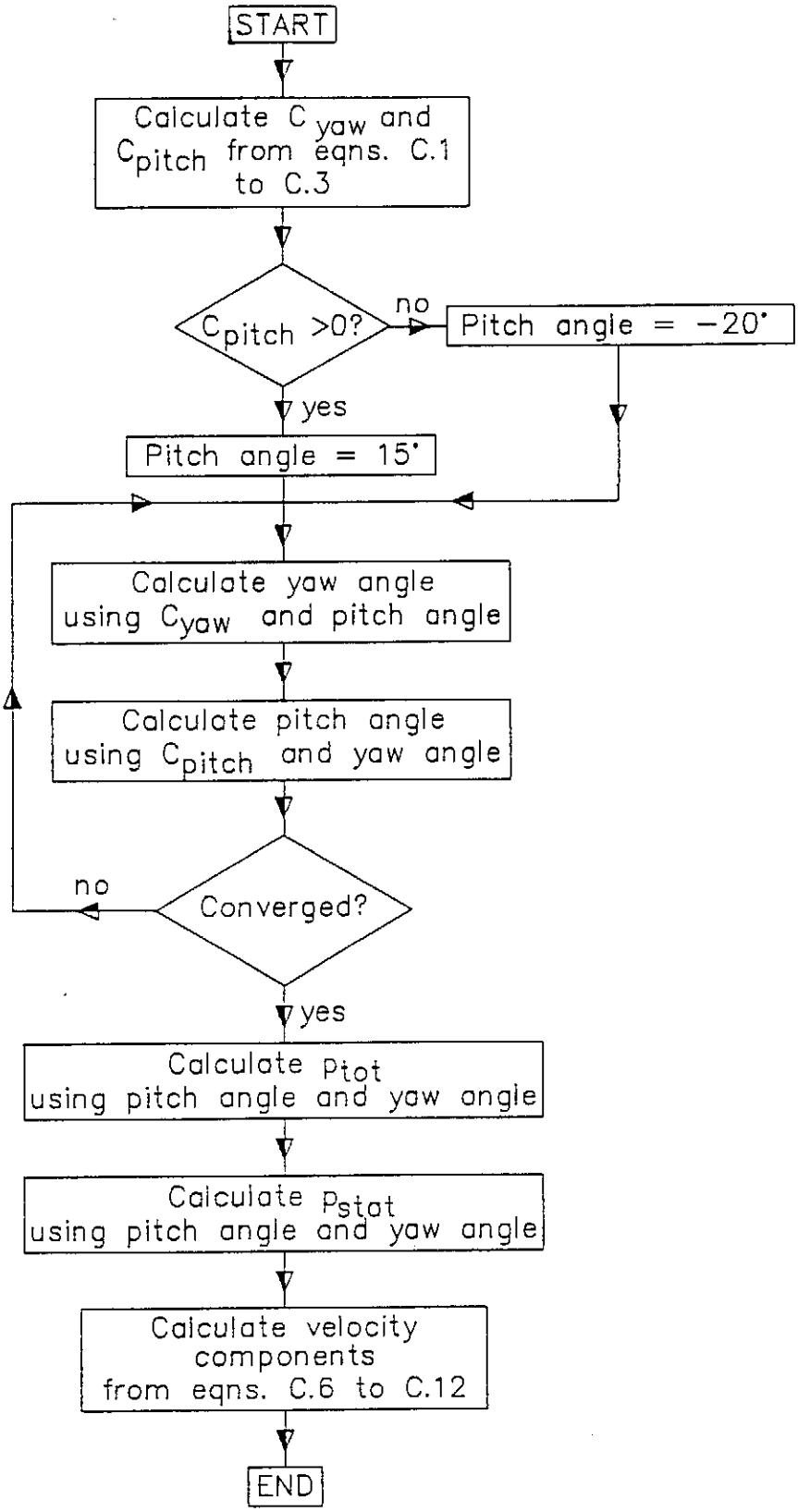

Figure C.7.2: Velocity calculation procedure

Appendix D - Calibration of fan test facility

A detailed description of the fan test facility used to generate experimental data discussed in this report is given in section 3.1.3. The influence of individual parameters on the operation of the test facility had to be assessed before any valid data could be generated.

D.1 Calibration of inlet bellmouth

The air volume flow rate through the test facility is considered to be one of the primary parameters that has to be monitored (refer to the graphs in appendix A).

The different alternatives to measure air flow rate that were considered include

- pitot tube traverse
- inline venturi nozzle
- conical inlet
- calibrated inlet bellmouth or free inlet venturi nozzle.

The latter option was selected because it is more economical to manufacture than an inline venturi meter and is also more reliable than a conical inlet. A calibrated inlet bellmouth is also easier to use than traversing with a pitot tube since a single pressure difference reading is directly related to the volumetric flow rate, compared to at least 30 pressure readings required for a single pitot tube traverse [80BS01]. The pressure losses ("compound flow coefficients" according to BS 1042 [81BS01]) associated with a conical inlet is typically of the order 0,96 for Reynolds numbers based on an inlet diameter in excess of 300 000, compared to 0,985 for an inlet bellmouth (according to BS 848 [80BS01]).

The inlet is manufactured in accordance with BS 848 specifications (drawing F.2.1) with an inlet diameter of 1,008 m. The total included angle of the transformation section used to increase the channel diameter from 1,008 m to 1,5 m is 18°. This angle is smaller than the maximum included angle of 30° specified by BS 848. The specified minimum overall length of the transformation is 3 inlet diameters which corresponds to a length of 3,024 m. Due to limited space, this length is reduced to 1,5 m and the inlet bellmouth is then calibrated once it has been installed.

The inlet bellmouth is calibrated using pitot tube traversing. The compound flow coefficient is found from the area under the average velocity distribution measured in a plane through the bellmouth static pressure tappings. The middle section of the inlet is traversed using a 12 mm diameter NPL type pitot tube, whilst the average shape of the

boundary layer was determined with a 3 mm diameter pitot tube. The average of ten sets of data measured at different velocities is used to determine the calibration constant for the inlet bellmouth (table D.1). A second order curve fit is used to describe the part of the velocity distribution where the slope approximates zero, with a third order curve fit applied to the boundary layer region. A curve combining these sets of data is attached as figure D.1. The resulting equations are

for $0,0 <= r <= 0,45$:

$$v^*(r) = 1,00603 + 0.043648\, r - 0,13331\, r^2 \tag{D.1}$$

for $0,45 <= r <= 0,504$:

$$v^*(r) = 161,0535 - 1067,62\, r + 2374,53\, r^2 - 1761,09\, r^3 \tag{D.2}$$

where $v^*(r) = \sqrt{\dfrac{\Delta p_{pitot}(r)}{\Delta p_{bell}}}$

and
- r - bellmouth radius in $[m]$
- $v^*(r)$ - dimensionless velocity
- $\Delta p_{pitot}(r)$ - measured pitot tube gauge pressure as a function of radius in $[N/m^2]$
- Δp_{bell} - measured bellmouth gauge pressure in $[N/m^2]$

Equations D.1 and D.2 are used to determine the compound flow coefficient from the average velocity which is defined as

$$\bar{v} = \frac{\int_A v(r)dA}{\int_A dA} \tag{D.3}$$

The compound flow coefficient is defined by the following relation

$$\bar{v} = \alpha\epsilon\sqrt{\frac{2\Delta p_{bell}}{\rho}} \tag{D.4}$$

The velocity integral in equation D.3 can be solved as follows

$$\begin{aligned}\int_A v(r)dA &= \int_0^{2\pi}\int_0^R v(r)rdrd\theta \\ &= 2\pi\int_0^R v(r)rdr \\ &= 2\pi\sqrt{\frac{2}{\rho}}\int_0^R \sqrt{\Delta p_{pitot}}rdr \end{aligned} \tag{D.5}$$

which is valid only for incompressible flow (refer to chapter 2).

Substituting equation (D.5) into equation (D.3) gives

$$\bar{v} = \frac{2\pi\sqrt{\frac{2}{\rho}}\int_0^R \sqrt{\Delta p_{pitot}}\; r\; dr}{A} \tag{D.6}$$

The average velocity $\bar{v}$ is determined from equation (D.4) and substituted into the previous equation

$$\alpha\epsilon\pi R^2 = 2\pi\int_0^R v^*(r)rdr \tag{D.7}$$

where $A = \pi R^2$

Reshuffling and substitution results in

$$\alpha\epsilon = \frac{2\int_0^{0,504} v^*(r)rdr}{(0,504)^2} \tag{D.8}$$

The velocity integral in equation (D.6) is evaluated by dividing it into two regions, namely for r between 0 and 0,45 and for r between 0,45 and 0,504.

$$\int_0^{0,45}(1,000603 + 0,043648r - 0,13331r^2)rdr = 0,10127$$

and $$\int_{0,45}^{0,504}(161,0535 - 1067,62r + 2374,53r^2 - 1761,09r^3)rdr = 0,02323$$

Equation (D.6) can therefore be solved to give

$$\alpha\epsilon = \frac{2(0,10127 + 0,02323)}{(0,504)^2}$$

$$= 0,9802 \qquad \text{(D.9)}$$

The deviation of this value from 0,985 as recommended by BS 848 can be attributed to modifications to the transformation piece, and to slight deviations from the prescribed physical dimensions of the inlet.

D.2 Calibration of the torque transducer

A resistive type strain gauge torque transducer is used to indicate input torque to the fan impeller. Rotational speed is monitored by an electro-magnetic device counting the number of pulses generated by a toothed metal disc.

The torque transducer is statically calibrated using a set of stainless steel weights, each having an individual mass of 100 $\pm$ 0,1 g. The mass of the cradle used to support the weights is 0,787 g. A 2 100 mm long 50 mm x 10 mm flat bar, notched at two points 50 mm from each tip, is used as support beam. The center of gravity of the beam corresponds with the axis of the torque transducer. A bridge amplifier (Höttinger KWS 3703) is used to supply an excitation voltage and to amplify the output signal from the strain gauges. The calibration curve shown as figure D.5 reveals a good relationship between applied torque and output signal (table D.2). The calibration constant determined from the average gradient of the curve is 33,659 Nm/V compared to a value of 33,3333 Nm/V supplied by Höttinger. In view of the fact that these two values are almost equal a value 33,3333 Nm/V, as engraved on the transducer, is accepted to eliminate possible future uncertainties.

Both zero and full scale outputs from the rotational speed indicator are adjustable. A pulse generator is used to generate a 100 Hz square wave signal for which the full scale output is adjusted to read 10 V. A frequency output of 100 Hz corresponds to a rotational speed of 857,1 rpm because there are 7 teeth on the metal disk used to activate the pick up sensor. The linearity of the unit is verified by measuring output voltages at different input frequencies. Output voltages of 8 V and 5 V were measured for input signals of 80 Hz and 50 Hz respectively.

D.3 Estimation of air leakage to or from the facility

Due to the large dimensions of the facility (settling chamber of 4 m x 4 m x 7 m) it is necessary to construct it from a large number of smaller panels. Although extensive precautions were taken to produce an airtight system, the joints are still considered a possible threat. Air leaking into or out of the system can result in inaccurate volume flow rate and fan static pressure measurements.

The magnitude of leakages is investigated by sealing all access holes in the unit. A centrifugal fan, equipped with a throttle and mass flow rate measuring device (calibrated in line orifice), is used to evacuate the facility. The mass flow rate of air evacuated for different negative chamber pressures is shown in figure D.3. Figure D.4 shows the effect of leaking air on a typical fan static pressure curve and proves that the influence of air leakages can be ignored.

D.4 Velocity profile inside settling chamber

Data reported upon in this work has been generated in a test facility adhering to the British Standard Institution's BS 848 fan test codes. Accordingly the velocity distribution inside the settling chamber has to be determined. Figure D.3 is a presentation of the velocities measured in the same plane as the four static pressure tappings used to measure fan inlet pressure. It is clear that nowhere does the flow exceed 1,25 times the average velocity or 2,5 m/s as required by BS 848. The free areas of wire mesh screens used to obtain these conditions are 62%, 48% and 48% respectively in a downstream direction.

D.5 Repeatability of results

Most of the data presented in this thesis concerns the effect of different structural additions on the performance of axial flow fans. The complete performance characteristic of a fan is described by fan static pressure, fan static efficiency and fan power consumption graphically displayed against volumetric flow rate of air passing through the fan. Due to the importance of the above parameters, it was decided to investigate the repeatability of measuring each parameter individually.

Data for a specific fan (1,542 m diameter V-fan at 16^o blade angle in this case) was generated on a number of different occasions during experimentation. Results obtained are displayed according to date and time at which each set was generated and are graphically represented as figures D.6 to D.8. A maximum deviation of 4,20 N/m^2 in fan static pressure, 1,50% in fan static efficiency and 80 W in fan power consumption is noted.

D.6 Calibration of pressure transducers

The fan inlet total pressure, pressure drop across the inlet bellmouth and five hole probe pressures are all monitored. Static pressure at the fan outlet as well as static pressure at the inlet to the bellmouth are assumed equal to ambient pressure. This is in accordance with BS 848.

The method used to obtain a continuous pressure trace was to use inductive type differential pressure transducers (Höttinger PD 1) with a maximum range of 1 000 N/m^2 (0,01 bar). The pressure transducers were calibrated against a Betz-manometer with 0,2 $mmWg$ divisions to indicate 100 N/m^2 as 1 V DC output from the bridge amplifier. Temperature effects of less than 0,6% in sensitivity and less than 2,0% in zero drift for a 10 K temperature variation is guaranteed. The linearity of the pressure transducers are better than 1,0% of their nominal operating range as quoted by the manufacturers. An accurate output signal is to be expected from an instrument with such good specifications.

Table D.1

Calibration results for inlet bellmouth

Radius m	Dimensionless radius r^*	Pressure ratio -	Velocity ratio -
0,123	0,122	1,009	1,0044
0,152	0,150	1,007	1,0033
0,266	0,264	1,010	1,0049
0,295	0,293	1,001	1,0005
0,329	0,327	1,001	1,0003
0,359	0,356	0,997	0,9985
0,406	0,403	0,994	0,9969
0,434	0,431	0,993	0,9963
0,450	0,447	0,969	0,9845
0,456	0,453	0,953	0,9762
0,457	0,454	0,988	0,9938
0,465	0,461	0,949	0,9744
0,472	0,468	0,894	0,9454
0,479	0,475	0,845	0,9192
0,482	0,478	0,854	0,9242
0,486	0,483	0,808	0,8989
0,491	0,487	0,739	0,8596
0,494	0,490	0,603	0,7762
0,499	0,495	0,590	0,7681

Table D.2

Calibration results for torque transducer

Mass g	Torque Nm	Voltage set 1 V	Voltage set 2 V	Predicted torque Nm	Predicted torque Nm
787	7,705	0,226	0,233	7,607	7,843
1 787	17,495	0,503	0,519	16,937	17,469
2 787	27,285	0,812	0,812	27,337	27,331
3 787	37,075	1,113	1,103	37,467	37,126
4 787	46,865	1,391	1,403	46,818	47,223
5 787	56,655	1,692	1,684	56,957	56,682
6 787	66,445	1,968	1,978	66,247	66,577
7 787	76,235	2,255	2,268	75,907	76,338
8 787	86,025	2,553	2,569	85,937	86,470
9 787	95,815	2,837	2,843	95,497	95,692
10 787	105,605	3,130	3,141	105,357	105,723
11 787	115,395	3,429	3,433	115,417	115,551
12 787	125,185	3,714	3,730	125,007	125,548
13 787	134,975	4,005	4,022	134,807	135,376
14 787	144,765	4,295	4,293	144,567	144,498

Table D.3

Air leakage results for fan test facility

Static pressure inside settling chamber N/m^2	Measured mass flow rate of leaking air kg/s	Predicted mass flow rate of leaking air kg/s
197,88	0,0170	0,01770
206,86	0,0163	0,01842
242,84	0,0229	0,02122
289,87	0,0262	0,02470
342,46	0,0280	0,02835
482,17	0,0364	0,03682
562,94	0,0410	0,04090

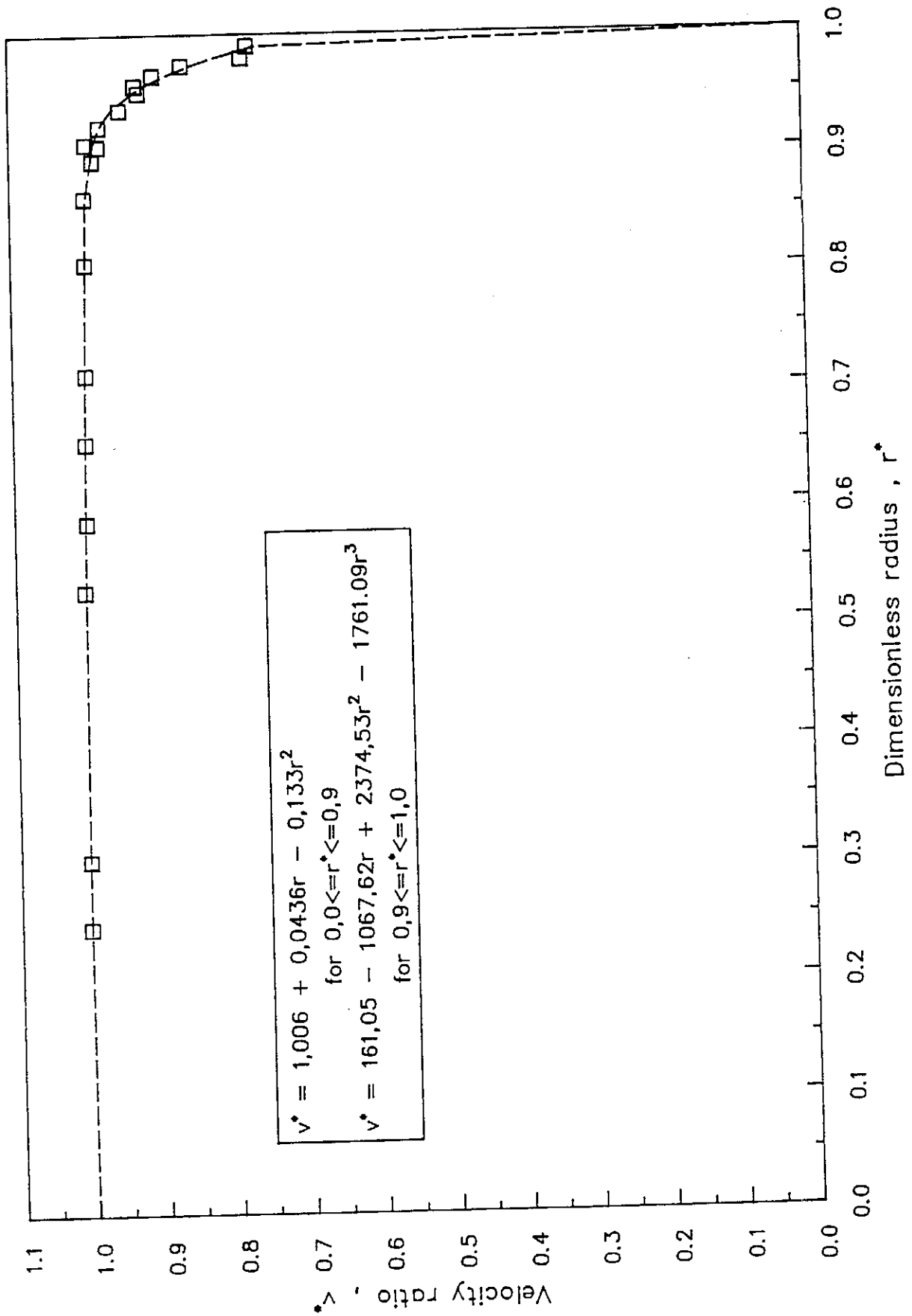

Figure D.1: Velocity profile of inlet bellmouth

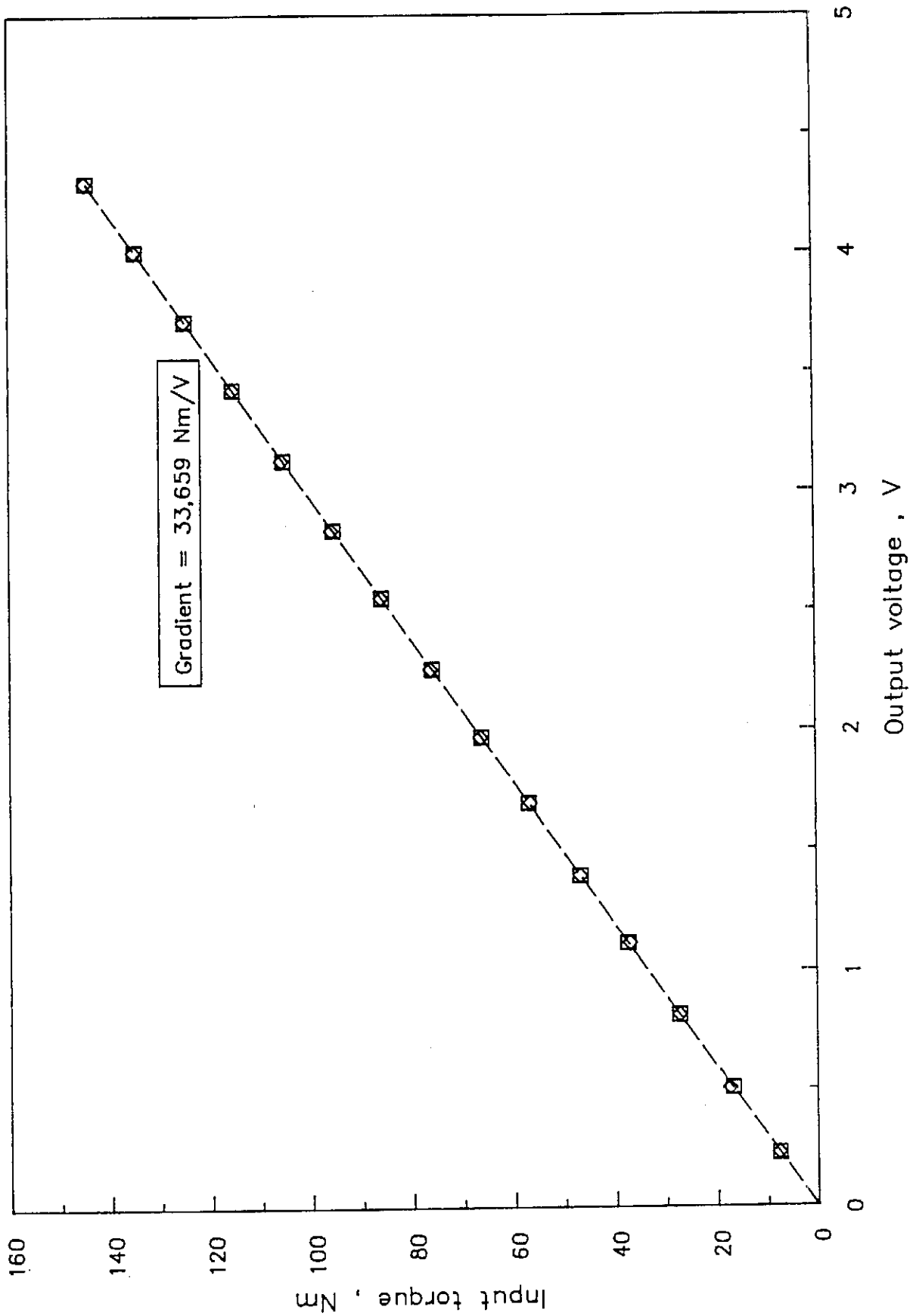

Figure D.2: Calibration curve for torque transducer

1,6 m/s	1,7 m/s	1,3 m/s	1,0 m/s
1,8 m/s	1,7 m/s	1,9 m/s	1,6 m/s
1,7 m/s	1,9 m/s	1,8 m/s	1,7 m/s
1,2 m/s	1,8 m/s	1,7 m/s	1,4 m/s

Figure D.3: Velocity distribution inside settling chamber

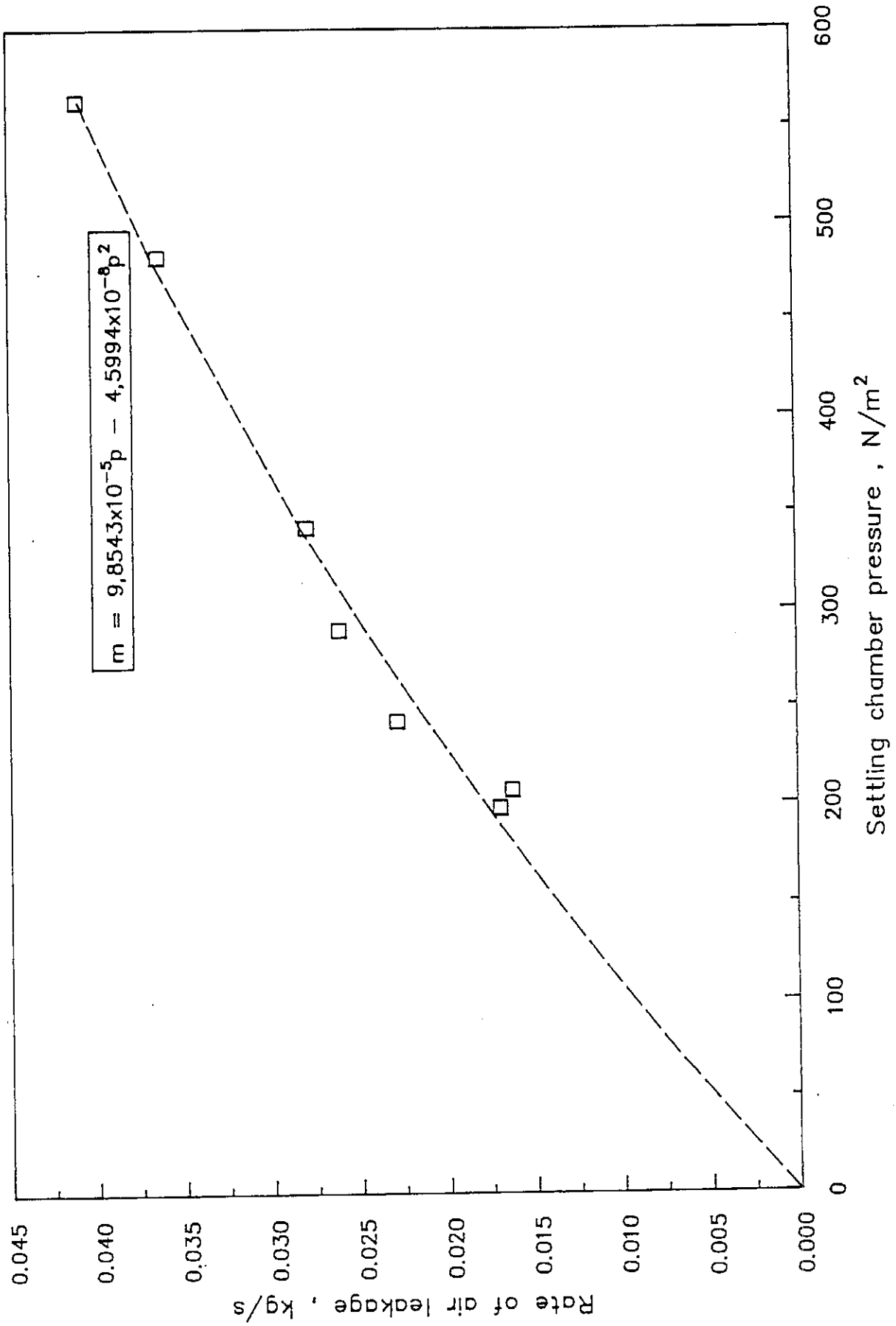

Figure D.4: Air leakage into test facility

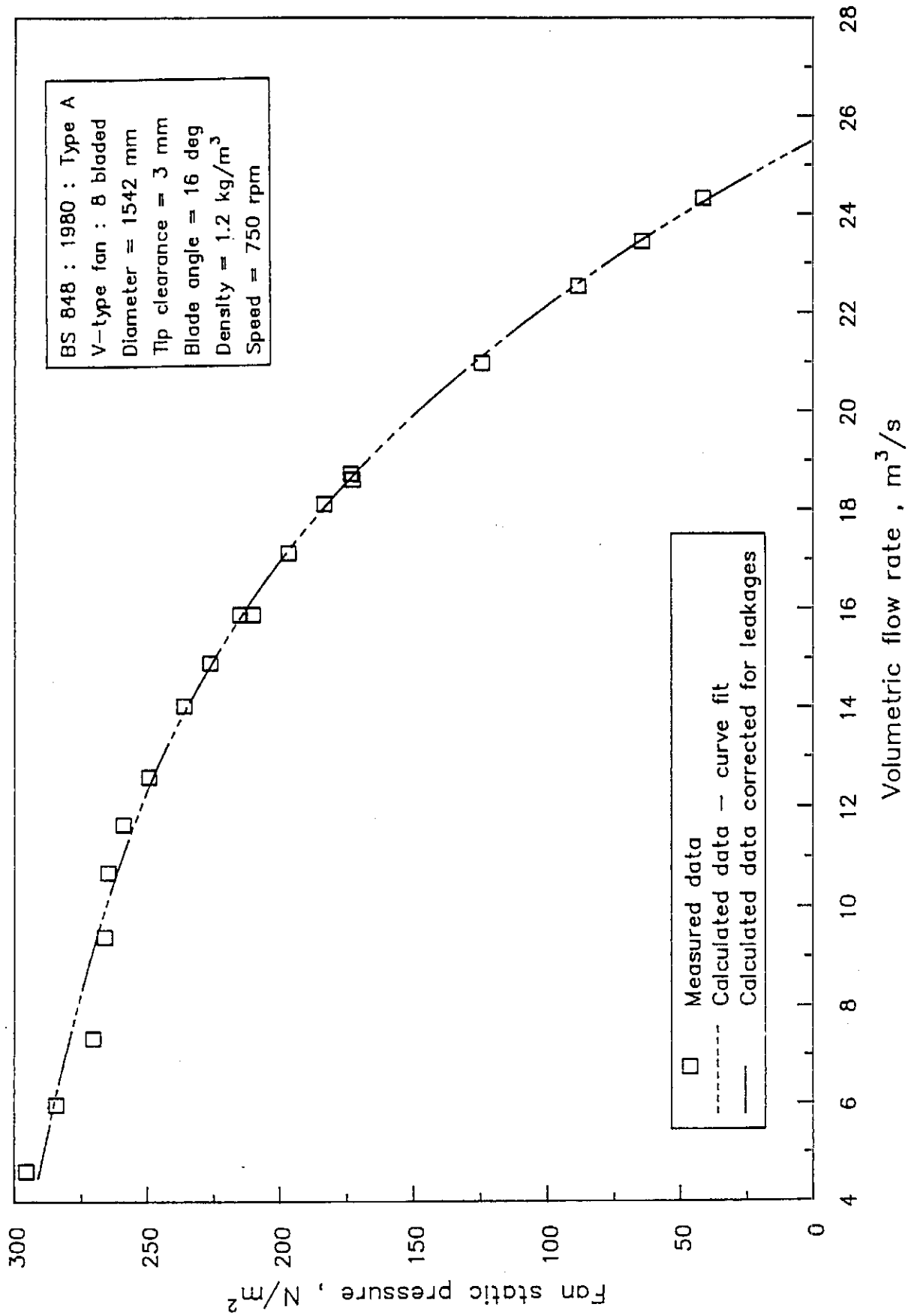

Figure D.5: Effect of air leakage on fan characteristic

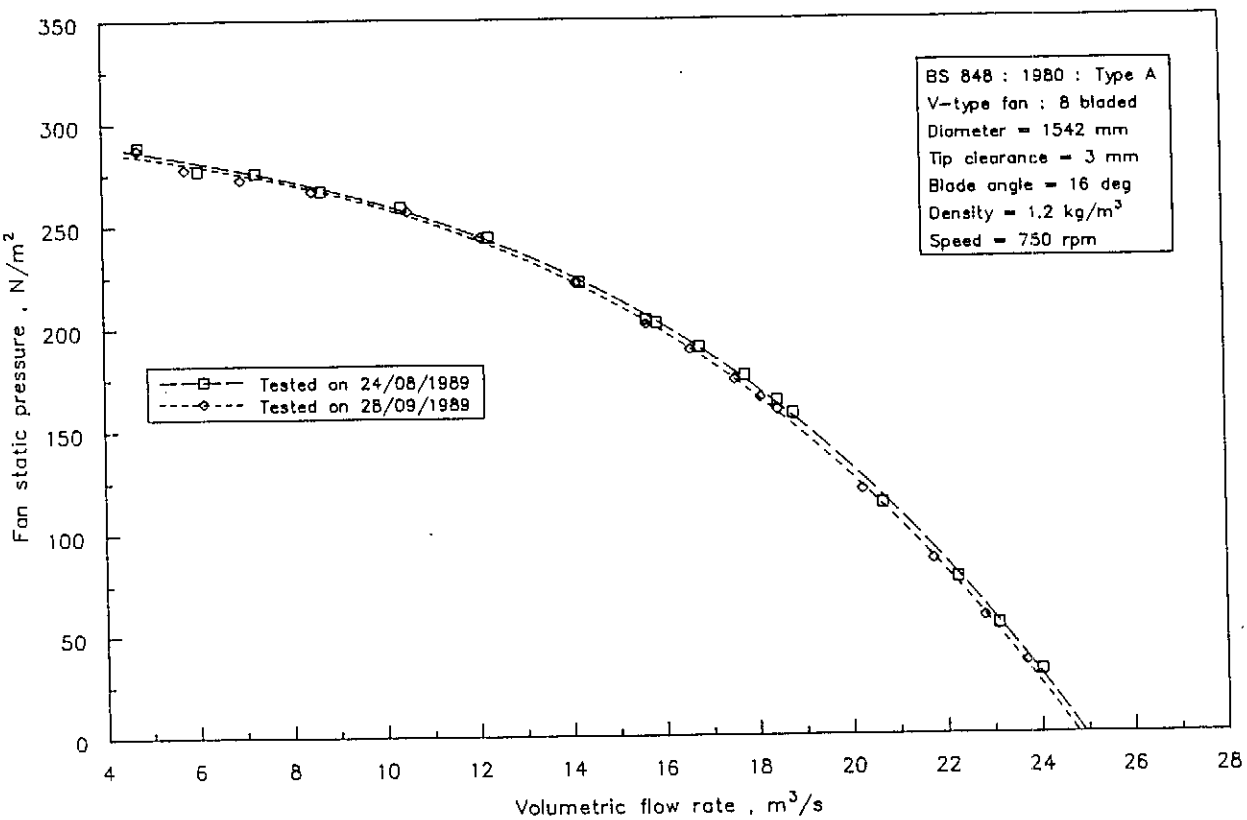

Figure D.6: Fan static pressure : Repeatability

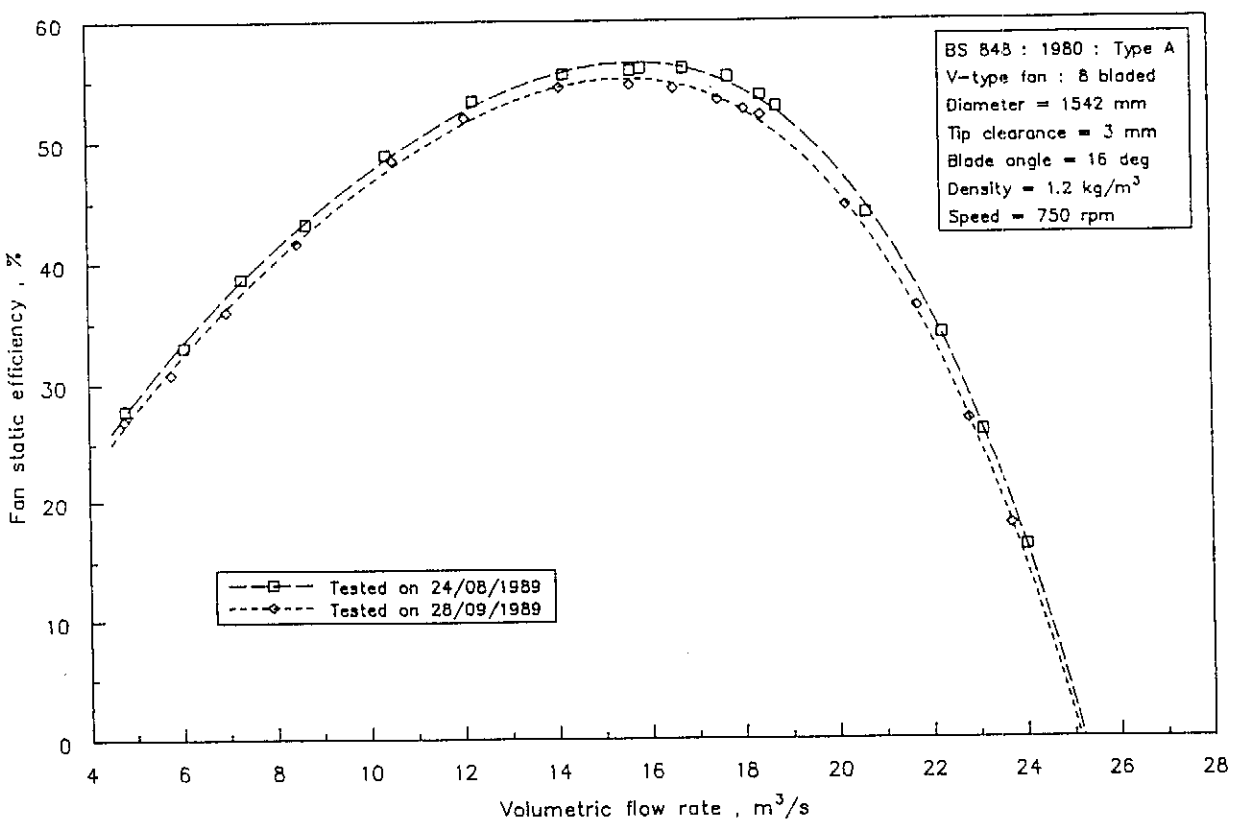

Figure D.7: Fan static efficiency : Repeatability

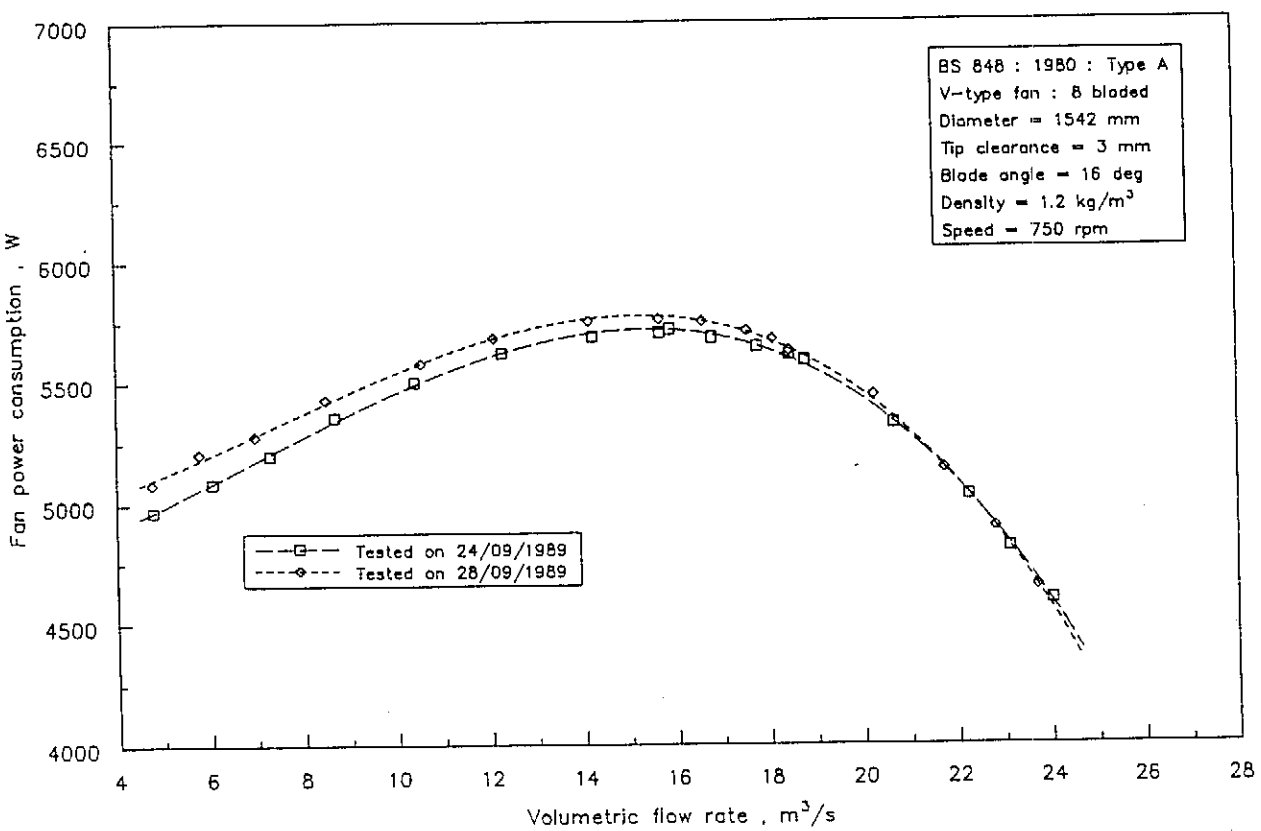

Figure D.8: Fan power consumption : Repeatability

Appendix E - Comparison between model and full scale experiments

Results obtained from the scale model unit are compared with data generated on location at the full scale plant during operation. The scale model is designed so that the prevailing air flow conditions approximate the same conditions as for the full scale unit.

Although the dimensions of most components in the scale model correspond to their scaled counterparts of the full scale unit, the following deviations are present:

- The fan blades used in the scale model are different from those present in the full scale unit (refer to figures F.6.1 to F.6.10).
- No steam pipes (either at the apex or inside the plenum) are included in the scale model.
- The effective tube length of the model heat exchanger corresponds to the scaled tube length of the condenser unit, but is not representative of the same for the dephlegmator units of the full scale plant.
- The heat exchanger and walkway are manufactured from the same components as in the case of the full scale unit. This means that the dimensions of the tube bundles and the "recta grid" of the walkway correspond with the same dimensions as the full scale unit are used. The pressure loss across such components could be influenced by the fact that these dimensions are not scaled correctly. The $75 \times 75 \times 5\ mm$ mesh attached to the safety grid of the full scale unit, is not included in the scale model.
- The full scale unit is attached to a fully operational electricity generating plant. The operating conditions can not always be altered to suit the requirements of specific test procedures. This means that some tests which are performed under non-isothermal conditions should ideally have been performed under isothermal conditions.

E.1 Velocity maps

The velocity maps at the inlet to the full scale fans are presented as figures E.1 to E.11. These maps are measured utilizing the rotating beam (figure F.4.1). The prevailing ambient conditions for each fan are tabulated in table E.1. From these it is obvious that the wind velocity influences the volumetric flow rate through the fans. This conclusion is based upon the comparison between figures E.3 and E.4 for which the wind velocity increases from 1,30 m/s to 4,27 m/s. The effect of wind direction is also clearly illustrated by comparing figures E.1 and E.2. The reverse flow region at the windwall side of fan AN060 test series 1 is associated with the higher wind velocity than for test series 2 of the

Table E.1

Operating conditions relevant to figures E.1 to E.8

Test Number	Ambient Pressure $[mbar]$	Ambient Temperature $[^oC]$	Relative Humidity [%]	Wind Speed $[m/s]$	Wind Direction [-]	Volume Flow Rate $[m^3/s]$
AN060 - #1	923,2	13,0	83	5,10	E	523,06
AN060 - #2	922,3	16,6	61	2,39	ENE	556,24
AN050 - #2	921,5	23,0	36	1,30	NE	612,83
AN040 - #2(a)	919,8	24,8	21	4,27	WSW	447,61
AN040 - #2(b)	919,8	24,8	21	4,27	WSW	431,05
AN030 - #3	925,2	14,3	34	0,53	N	532,28
AN020 - #3	925,0	18,5	30	0,88	N	600,05
AN010 - #3	924,5	22,5	20	2,39	SSW	537,46

same fan. The reverse flow is also partially attributed to the location of fan AN060 next to the windwall.

Figures E.10 and E.9 present the average dimensionless velocity profiles for fan AN060 on the one hand, and the remaining tests on the other, respectively. These profiles are determined by dividing the circumferentially averaged velocities, measured at different locations, by the overall average velocity through the fan. The inlet velocity profiles related to the scale model, measured with the aid of the five hole probe, are compared to the full scale profiles in figure E.11. The full scale velocity profiles compare favorably with those measured in the model facility with an ambient inlet pressure. The profile for throttled conditions (i.e. a fan inlet pressure of below atmospheric) deviate from these profiles. This implies that the kinetic energy flux coefficient is only related to the fan inlet pressure conditions, and is not dependent on the specific flow rate through the fan. It correlates with the assumptions concerning total inlet pressure characteristics in the determination of the pressure loss coefficients associated with the inlet safety grid (refer to section 4.9).

The dimensionless velocity profiles on the outlet face of the heat exchanger (figure E.12) exhibit a good correlation between the model and the full scale unit. The only discrepancy between these graphs is towards the base of the A-frames. At the point furthest from the apex, the velocity profile related to the scale model is lower than for the corresponding values of the full scale unit. This discrepancy in the velocity profiles is attributed to the

dimensional and operational changes between the full scale unit and the scale model (refer to the introduction to this appendix). The large number of different aspects highlighted in that section, makes it intractable to attempt to isolate the individual effects of each parameter.

The velocity distributions at the exit from the unit (at the apex of the heat exchangers) show that the model profile correlates better with the corresponding profile of the dephlegmator unit than the condenser unit (figure E.13). The reason is that the thickness of the heat exchangers are the same for both the model and the full scale unit. The scaled area of zero flow at the apex of the model is therefore representative of the larger zero flow region of the full scale dephlegmator rather than the condenser.

It is concluded that the velocity distributions observed in the scale model are fair approximations of those present in the full scale unit. Deviations are attributed to dimensional changes and variations in ambient and operating conditions listed in the introduction to this appendix.

E.2 System resistances

The system resistances presented in figures 4.8 and 4.9 are used to correlate the actual resistances to those predicted by the manufacturers of the full scale unit. The results presented in these figures show that the bulk method of prediction equals the measured system resistance in the vicinity of 16 m^3/s (corresponding to the maximum fan static efficiency). In addition to the resistances listed in section 4.4, the resistance of the mesh attached to the inlet safety grid needs to be accounted for. The effect of the steam pipes and the smaller inter-plenum distances are also included in the average downstream loss coefficient. Comparative results are listed in table E.2 based on fan inlet shroud area.

The downstream losses of the full scale unit are presented by van Aarde [90VA1].

Absent from the list presented in table E.2 are the pressure loss coefficients associated with the heat exchangers. The reason is that they are not constant for the complete range of volume flow rates. The analytical evaluation of the operating point of a system for which both the correlations of the fan static pressure curve, and the system resistance curve are known is illustrated in the remainder of the section. The influence of the heat exchanger pressure loss coefficient and the velocity through the tube bundles are also highlighted.

Typical relations for fan static pressure and heat exchanger resistance are:

$$\Delta p_{sF} = A\,V^3 + B\,V^2 + C\,V + D \tag{E.1}$$

Table E.2

Comparative results of model vs. full scale pressure loss coefficients : Bulk method

Component	Loss coefficient (Model)	Loss coefficient (Full scale unit)
Inlet safety grid	0,17	0,30
Support beams	0,14	0,14
Walkway	0,21	0,21
Downstream losses	0,43	1,09
Total	0,95	1,74

$$\Delta p_{tS} = F(v_{HX})\,\frac{1}{2}\rho v_{HX}^2 + M\,\frac{1}{2}\rho v_{HX}^2 + N\,\frac{1}{2}\rho v_{fan}^2 \qquad \text{(E.2)}$$

where $F(v_{HX}) = p\,(Ry_{HX})^q$ (typically for the normal flow losses).

Equation (E.2) is rewritten in terms of only the volume flow rate through the fan.

$$\begin{aligned}\Delta p_{tS} &= p\left(\frac{\rho}{\mu}\right)^q \frac{1}{2}\rho(v_{HX})^{(2+q)} + M\,\frac{1}{2}\rho v_{HX}^2 + N\,\frac{1}{2}\rho v_{fan}^2 \\ &= p\left(\frac{\rho}{\mu}\right)^q \frac{1}{(A_{HX})^{(2+q)}}\,\frac{1}{2}\rho V^{(2+q)} + \left[\frac{M}{(A_{HX})^2} + \frac{N}{\left(A_{fan}\right)^2}\right]\frac{1}{2}\rho V^2 \qquad \text{(E.3)}\end{aligned}$$

The following values are valid for the V-type model fan under investigation:

$$\begin{aligned}A_{fan} &= \frac{\pi}{4}\,(1,542)^2 \\ &= 1,8675\ m^2 \\ A_{cond} &= 2\,(1,960)\,(1,610) \\ &= 6,3112\ m^2 \\ A_{deph} &= 0,8395\ A_{cond}\end{aligned}$$

$= \quad 5,2983\, m^2$

The kinematic viscosity ($\nu = \frac{\mu}{\rho}$) for standard air at $20^{\circ}C$ is $1,5 \times 10^{-5}\ N/m^2 s$ and the density of air at these conditions is 1,2 kg/m^3 [77DA1].

The pressure loss coefficient for normal flow approaching the heat exchangers is presented in equation (B.100) as

$$F(v_{HX}) = 4464,83\ (Ry_{HX})^{-0,439} \tag{E.4}$$

The effect of oblique flow approaching the heat exchanger is accounted for by putting M in equation (E.3) equal to 3,038 (refer to equation B.98).

The values of the constants in equation (E.1) are determined by linear regression through the data points. They are found to be

$A \quad = \quad -0,020600$

$B \quad = \quad 0,200179$

$C \quad = \quad -4,42808$

$D \quad = \quad 304,807$

All the numerical values listed above, are substituted into equations (E.1) and (E.3). The operating point of the system is where $\Delta p_{tS} = \Delta p_{sF}$. The following equations result:

Dephlegmator :

$$-0,020600\, V^3 + 1,6375\, V^2 - 4,42808\, V + 304,807 - 1,510\, V^{1,56} = 0 \tag{E.5}$$

Condenser :

$$-0,020600\, V^3 + 1,6566\, V^2 - 4,42808\, V + 304,807 - 1,149\, V^{1,56} = 0 \tag{E.6}$$

The roots of equations (E.5) and (E.6) are determined utilizing a numerical method (Newton method) which states that

Table E.3

Operating points of the condenser and dephlegmator units

Unit	Fan static pressure	Volume flow rate
Condenser	190,12	16,74
Dephlegmator	203,37	15,81

$$x_{n+1} = x_n - \frac{f'(x_n)}{f(x_n)} \tag{E.7}$$

The resulting fan static pressures and volume flow rates from equations (E.5) and (E.6) are presented in table E.3. The same results are graphically presented in figure E.14.

E.3 Fan applications in practice

A practical method which can be used to compare the effect of different system parameters on the performance of an axial flow fan is highlighted in this section. The primary assumption for these comparisons is that the fan power consumption remains the same for the ideal and the altered fan applications. The effect of different initial fan installations is also highlighted. As illustration the system resistances of the condensers and dephlegmators of the full scale unit are compared.

The discrete correlations for the system resistances of the model condenser and dephlegmator units are (refer to section E.2):

Dephlegmator:

$$\Delta p_{tS} = 1,510V^{1,56} + 0,364V^2 \tag{E.8}$$

Condenser:

$$\Delta p_{tS} = 1,149V^{1,56} + 0,345V^2 \tag{E.9}$$

The intercept of these system resistances and the ideal fan characteristics (tip clearance $= 3\ mm$) is determined from the correlations used to generate figure 4.1. For blade angles between 12^o and 20^o (every 2^o), the predicted operating points are tabulated in table E.7. The performance characteristics are presented by the following:

$$\Delta p_{sF} = A_{FSP} + B_{FSP}\,V + C_{FSP}\,V^2 + D_{FSP}\,V^3$$

$$\eta_{sF} = A_{FSE} + B_{FSE}\,V + C_{FSE}\,V^2 + D_{FSE}\,V^3 + E_{FSE}\,V^4$$

$$P_{fan} = A_{Pow} + B_{Pow}\,V + C_{Pow}\,V^2 + D_{Pow}\,V^3$$

Table E.4

Fan static pressure coefficients

Blade Angle	A_{FSP}	B_{FSP}	C_{FSP}	D_{FSP}
12	320.988	-10.03275	0.415228	-0.0282412
14	315.838	-7.47664	0.351126	-0.0253735
16	325.034	-10.62826	0.798078	-0.0359767
18	309.879	-3.12643	0.182708	-0.0186475
20	283.443	1.73204	-0.031469	-0.0130780

Table E.5

Fan static efficiency coefficients

Blade Angle	A_{FSE}	B_{FSE}	C_{FSE}	D_{FSE}	E_{FSE}
12	-14.54	15.180	-1.4750	0.083720	-0.0021060
14	-10.08	11.680	-0.9739	0.052720	-0.0013330
16	6.65	3.919	0.0208	-0.000506	-0.0002590
18	-1.28	6.066	-0.2182	0.008675	-0.0003227
20	-1.48	4.891	-0.0861	0.001605	-0.0001473

The different volume flow rates listed in table E.7 are used to determine the corresponding power consumptions for the two installations. The correlations for the power consumption follow from the previously defined graphs in figure 4.2. The power consumption ratios (r_P) are referred to the ideal power consumption of the fan.

Using a linear regression, the following relations for the power consumption ratios as functions of blade angle (β) are determined:

Table E.6

Fan power consumption coefficients

Blade Angle	A_{Pow}	B_{Pow}	C_{Pow}	D_{Pow}
12	3899	-2.64	11.98	-0.6236
14	4790	-65.41	16.32	-0.6549
16	5389	-60.34	17.01	-0.6387
18	6093	-76.91	16.99	-0.5764
20	7171	-121.40	18.58	-0.5398

Table E.7

Operating points for different blade angles

Blade Angle [°]	Dephlegmator		Condenser	
	V $[m^3/s]$	Δp_{sF} $[N/m^2]$	V $[m^3/s]$	Δp_{sF} $[N/m^2]$
12	14,556	175,831	15,344	162,780
14	15,323	192,422	16,191	179,131
16	16,121	210,373	17,080	197,057
18	16,643	222,492	17,654	209,029
20	17,246	236,876	18,345	223,885

Dephlegmator:

$$r_P = -0,08663 + 0,06749\,\beta \tag{E.10}$$

Condenser:

$$r_P = -0,11415 + 0,06928\,\beta \tag{E.11}$$

Table E.8

Power consumption and power consumption ratios for different blade angles

Blade Angle [°]	Dephlegmator		Condenser	
	P $[m^3/s]$	r_P $[N/m^2]$	P $[m^3/s]$	r_P $[N/m^2]$
12	4475,70	0,7265	4426,32	0,7211
14	5263,40	0,8543	5229,52	0,8520
16	6161,01	1,0000	6138,22	1,0000
18	6861,87	1,1138	6858,98	1,1174
20	7834,64	1,2716	7864,19	1,2812

E.3.1 Tip clearance

The effect of tip clearance on the system performance where the shaft power requirements remains constant, is evaluated. The required power consumption ratios are calculated from the change in shaft power associated with an adjustment in blade tip clearance. The correlations presented in figures 4.6 and 4.7 are:

$$r_{\Delta p_{sF}} = 1 - 0,0266 \left[1000 \left(\frac{s}{D}\right) - 1,945\right] \tag{E.12}$$

$$r_{\eta_{sF}} = 1 - 0,0189 \left[1000 \left(\frac{s}{D}\right) - 1,945\right] \tag{E.13}$$

$$r_V = \sqrt{r_{\Delta p_{sF}}} \tag{E.14}$$

As an example, a reduction in fan tip clearance from 40 mm to 18 mm for the full scale unit is evaluated. The corresponding change in tip clearance of the scaled model is from 6,7 mm to 3,0 mm. The ratios presented in equations (E.12) to (E.14) are all referred to the ideal operating conditions for a tip clearance ratio of 0,1945 %. Substituting for (s/D) equal to 0,43 % into these equations results in:

$$r_{\Delta p_{sF}} = 1 - 0,0266\ (4,3 - 1,945) = 0,9374 \tag{E.15}$$

$$r_{\eta_{sF}} = 1 - 0,0189\ (4,3 - 1,945) = 0,9554 \tag{E.16}$$

$$r_V = \sqrt{0,9374} = 0,9682 \tag{E.17}$$

The corresponding power ratio is

$$r_P = \frac{\frac{\Delta p_{sF_{red}} V_{red}}{\eta_{sF_{red}}}}{\frac{\Delta p_{sF_{id}} V_{id}}{\eta_{sF_{id}}}} = \frac{r_{\Delta p_{sF}} r_V}{r_{\eta_{sF}}} = 0,9500 \tag{E.18}$$

Equation (E.18) is substituted into equations (E.10) and (E.11) to obtain the required blade angle setting for the power consumption ratio to remain the same if the tip clearance ratio is reduced from 0,43 % to 0,1945 %. This means that the higher power requirements, associated with a smaller tip clearance ratio ($s/D = 0,1945$ %), is counteracted by reducing the blade angle. The reduction in power due to the smaller blade angle corresponds to the increase in power consumption of a smaller tip clearance.

Dephlegmator:

$$r_P = 0,9500 = -0,08663 + 0,06749\,\beta$$

$$\text{thus } \beta = 15,36^\circ$$

Condenser:

$$r_P = 0,9500 = -0,11415 + 0,06928\,\beta$$

$$\text{thus } \beta = 15,36^\circ$$

A linear interpolation is used to determine the operating parameters at this angle from the operating conditions listed in table E.7.

The final results, for a tip clearance ratio of 0,1945 %, are compared to the initial operating conditions for a tip clearance ratio of 0,43 %. The respective blade angle settings for these two cases are 15,36° and 16,00°.

It is important to note that one German fan test code [66VD1] proposes a correction factor to be used when scaling tip clearance effects from a model to a full scale fan. The relative boundary layer thickness is smaller in a full scale unit than in a scaled model (provided that their entrance lengths are geometrically similar). The tip clearance ratio of the full scale unit is required to be smaller than the corresponding ratio for the scaled model to achieve the same operating conditions in both cases. Thus, the tip clearance ratio for the full scale model which results in the same fan static efficiency as measured for the scale model, is presented by:

Table E.9

Operating parameters at new blade angle

Blade Angle [°]	Dephlegmator		Condenser	
	V $[m^3/s]$	Δp_{sF} $[N/m^2]$	V $[m^3/s]$	Δp_{sF} $[N/m^2]$
14,00	15,323	192,422	16,191	179,131
16,00	16,121	210,373	17,080	197,057
15,36	15,866	204,629	16,800	191,321

Table E.10

Comparative results for different tip clearance ratios

Tip clearance Ratio [%]	Blade Angle [°]	Dephlegmator		Condenser	
		V $[m^3/s]$	Δp_{sF} $[N/m^2]$	V $[m^3/s]$	Δp_{sF} $[N/m^2]$
0,4300	16,00	15,464	195,523	16,407	183,404
0,1945	15,36	15,866	204,629	16,800	191,321
Improvement		2,60 %	4,66 %	2,40 %	4,32 %

$$\frac{s'}{D'} = \frac{s}{D}\left(\frac{D}{D'}\right)^{0,2}\left(\frac{\Delta p_{sF}}{\Delta p'_{sF}}\right)^{0,1} \tag{E.19}$$

where the accents refer to the full scale unit and the normal symbols to the measured results from the scaled model.

Equation (E.19) is derived from the boundary layer thickness growth relationships for a flat plate. In the case of negligible inlet lengths (as for fans having inlet shrouds) equation (E.19) needs careful consideration because the boundary layer growth is limited due to accelerating flow in the inlet shroud.

E.3.2 Solid disc

The addition of a solid disc upstream of the fan rotor results in an improved fan performance in the normal operating range of the fan (figures A.2.6 to A.2.10). To evaluate the exact magnitude of the improvement, the same method as employed in the previous section is proposed. It is important to note that the ideal operating conditions in this case are those associated with the system after the disc has been attached. This is different from the ideal operating conditions being only the fan rotor with the tip clearance at its smallest, as used in section E.3.1.

The operating conditions associated with the systems described by equations (E.8) and (E.9) are:

Table E.11

Operating parameters associated with the solid disc

Fan Application	Dephlegmator			Condenser		
	V $[m^3/s]$	Δp_{sF} $[N/m^2]$	η_{sF} [%]	V $[m^3/s]$	Δp_{sF} $[N/m^2]$	η_{sF} [%]
Excluding solid disc	15,921	205,790	55,50	16,865	192,643	55,12
Including solid disc	16,125	210,448	57,06	17,029	196,007	56,26

The respective operating parameters for the dephlegmator unit are calculated, utilizing the derivations stated previously in this section.

$$r_{\Delta p_{sF}} = 1,0226$$

$$r_V = 1,0129$$

$$r_{\eta_{sF}} = 1,0281$$

$$\text{thus } r_P = 1,0075$$

The power ratio is inverted before it is substituted into equation (E.10). This is to compensate for the fact that the effect of blade angle is known only for the fan excluding the disc, and not if a solid disc is added to the upstream plane of the fan. The resulting blade angle is therefore the angle at which the bare fan rotor needs to be set to ensure that its

power consumption is the same as the power consumption of the fan, including the solid disc, set at an angle of 16^o.

$$r_P = 0,9926 = -0,08663 + 0,06749\,\beta$$

$$\text{thus } \beta = 13,42^o$$

Exactly the same arguments are followed to determine the blade angle of the fan, excluding the disc, installed in the condenser. This blade setting corresponds to the power consumption of the fan, including the disc, set at a 16^o blade angle.

$$r_{\Delta p_{sF}} = 1,0175$$

$$r_V = 1,0097$$

$$r_{\eta_{sF}} = 1,0207$$

$$\text{thus } r_P = 1,0065$$

The power ratio is again inverted before it is substituted into equation (E.11).

$$r_P = 0,9935 = -0,11415 + 0,06928\,\beta$$

$$\text{thus } \beta = 15,99^o$$

The reference values referred in table E.12 is determined by assuming the same fractional change in volume flow rate and fan static pressure applied to the reference curve valid for the solid disc experiments. This follows from the differences between the reference curves presented in figures A.2.1 and A.2.5.

E.3.3 Number of blades

The effect of different numbers of fan blades is illustrated using the fan data supplied by a specific manufacturer. The fans for which the data are available, are designated the name "S-type" fans. The same system resistances as presented in equations (E.10) and

Table E.12

Comparative results for the effect of a solid disc upstream of the fan rotor

Operating Conditions [–]	Blade Angle [°]	Dephlegmator		Condenser	
		V $[m^3/s]$	Δp_{sF} $[N/m^2]$	V $[m^3/s]$	Δp_{sF} $[N/m^2]$
Excluding solid disc	14,00	15,323	192,422	16,171	179,131
	16,00	16,121	210,373	18,345	223,885
	15,99	16,117	210,283	18,334	223,661
Reference	15,99	15,917	205,702	16,855	192,450
Including solid disc	16,00	16,125	210,448	17,028	196,007
Improvement		1,31 %	2,31 %	0,85 %	1, 85 %

(E.11) are used to determine the effect of different system resistances. The intercepts of these system resistances and the fan characteristic curves for an 8 bladed fan tabulated (table E.13). The power consumption and power consumption ratios are also obtained from the graphs presented by the manufacturer. The parameters for a 16^o blade angle listed in tables E.13 and E.14 are determined by linear interpolation between the 14^o and 18^o blade angle settings.

The power consumption ratios are determined similarly to equations (E.10) and (E.11).

Dephlegmator:

$$r_P = -0,01992 + 0,06417\,\beta \tag{E.20}$$

Condenser:

$$r_P = -0,07462 + 0,06778\,\beta \tag{E.21}$$

The power consumption of the fans, having different numbers of blades, as well as the power consumption ratios referred to the 8 bladed fan are presented in table E.15. The blade angle for all these fans is the same at 14^o.

The power requirements of the different fans are kept constant by assuming that the fan blades are adjusted to a blade angle which results in the same power consumption as the

Table E.13

Operating parameters for different blade angles (8 bladed S-type fan)

Blade	Dephlegmator		Condenser	
Angle	V	Δp_{sF}	V	Δp_{sF}
[°]	$[m^3/s]$	$[N/m^2]$	$[m^3/s]$	$[N/m^2]$
10,00	15,016	185,690	15,806	171,602
14,00	16,640	222,425	17,645	208,835
18,00	17,951	254,220	19,211	208,835
22,00	18,870	277,633	20,420	271,251
16,00	17,340	238,823	18,467	226,281

reference fan (8 bladed). The power consumption ratios listed in table E.15 are substituted into equations (E.20) and (E.21) to obtain the various blade angle settings.

Table E.14

Power consumption and power consumption ratios for different blade angles (8 bladed S-type fan)

Blade Angle [°]	Dephlegmator		Condenser	
	P $[m^3/s]$	r_P $[N/m^2]$	P $[m^3/s]$	r_P $[N/m^2]$
10	4093,56	0,633	4025,40	0,619
14	5582,77	0,864	5569,23	0,856
18	7365,82	1,140	7467,96	1,148
22	9028,95	1,397	9269,25	1,425
16	6463,42	1,000	6502,50	1,000

Table E.15

Power consumption and power consumption ratios for 14° S-type fan

Number of blades [−]	Dephlegmator		Condenser	
	P $[m^3/s]$	r_P $[N/m^2]$	P $[m^3/s]$	r_P $[N/m^2]$
6	4440,82	1,257	4478,59	1,244
7	5174,99	1,079	5202,49	1,070
8	5582,77	1,000	2269,23	1,000
9	6246,85	0,894	6239,15	0,893

Table E.16

Comparative results for the effect of different numbers of fan blades

Comments	Blade Angle [°]	Dephlegmator		Condenser	
		V $[m^3/s]$	Δp_{sF} $[N/m^2]$	V $[m^3/s]$	Δp_{sF} $[N/m^2]$
Six	18,00	16,539	220,050	17,708	210,168
blades	22,00	17,273	237,527	18,578	229,006
	19,90	16,888	228,350		
	19,45			18,023	217,000
Seven	14,00	16,170	211,497	17,256	200,692
blades	18,00	17,447	241,779	18,660	230,797
	17,13	17,169	235,190		
	16,89			18,270	222,440
Nine	14,00	17,326	238,840	18,359	224,180
blades	18,00	18,673	272,550	19,967	260,570
	14,24	17,407	240,863		
	14,28			18,470	226,730
Reference	16,00	17,340	238,823	18,467	226,281
Improvement					
6 bladed		-2,61 %	-4,39 %	-2,40 %	-4,10 %
7 bladed		-0,99 %	-1,52 %	-1,07 %	-1,70 %
9 bladed		+0,39 %	+0,85 %	+0,02 %	+0,20 %

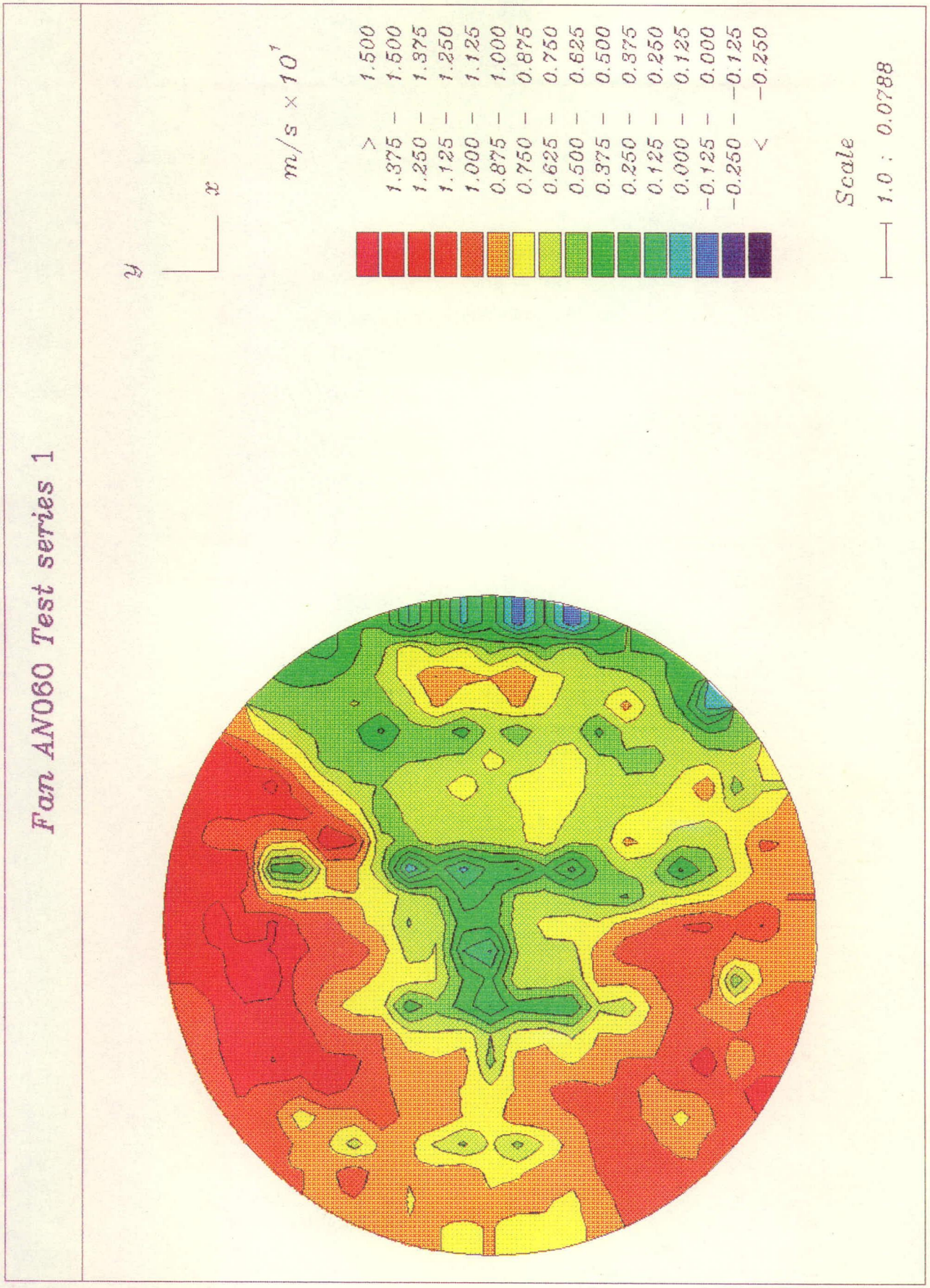

Figure E.1: Velocity profile at full scale fan inlet : Fan AN060 test series 1

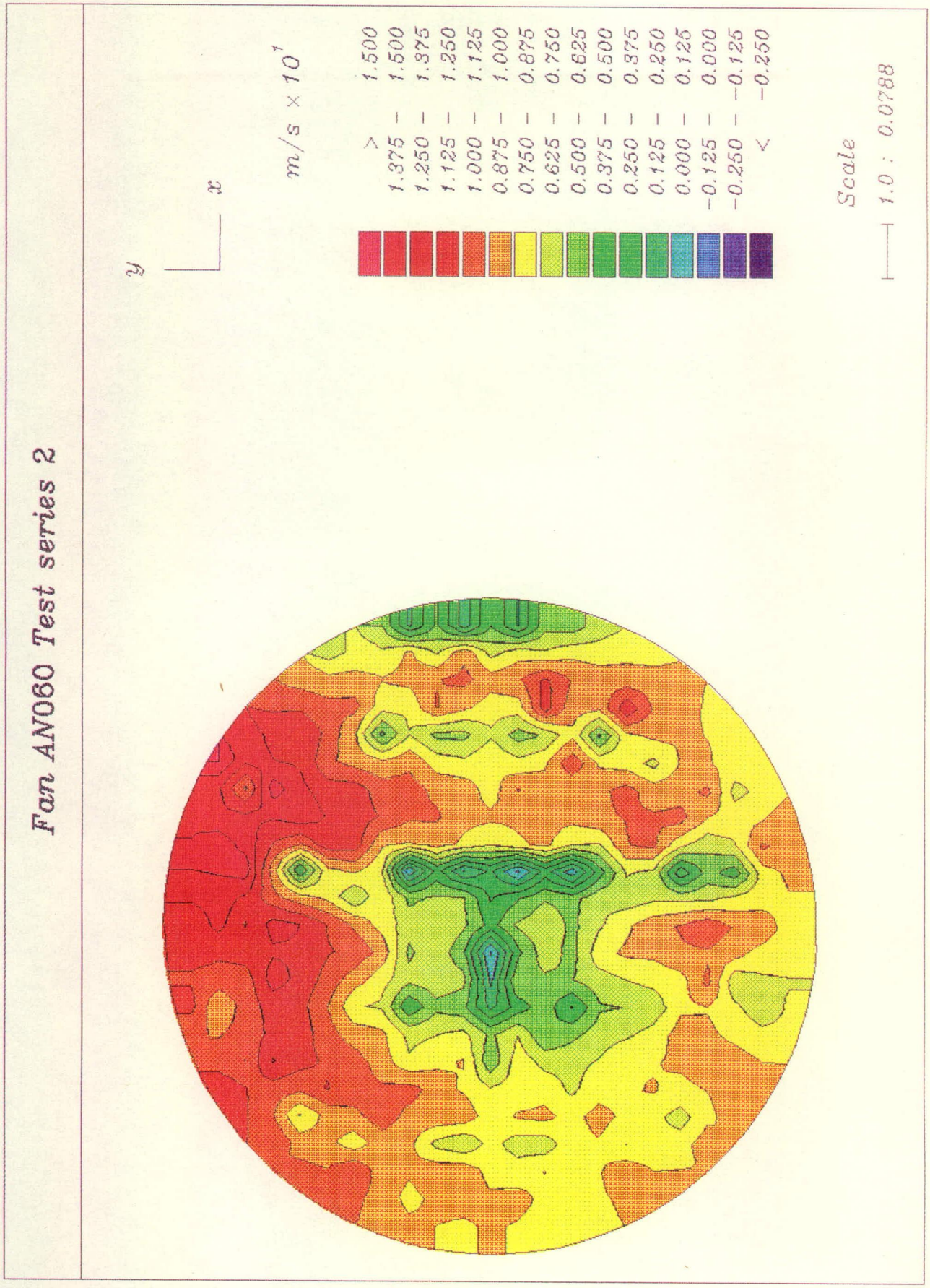

Figure E.2: Velocity profile at full scale fan inlet : Fan AN060 test series 2

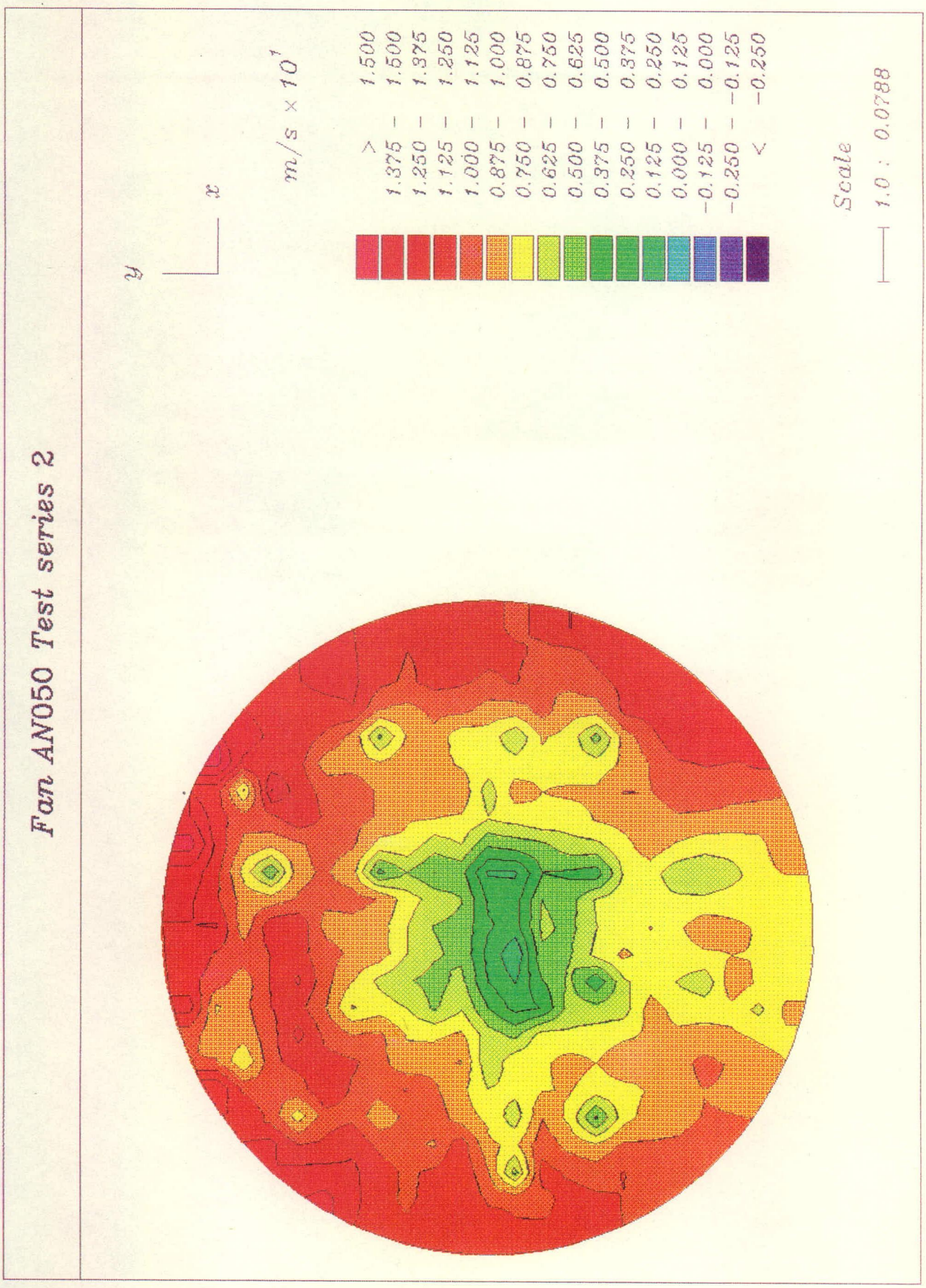

Figure E.3: Velocity profile at full scale fan inlet : Fan AN050 test series 2

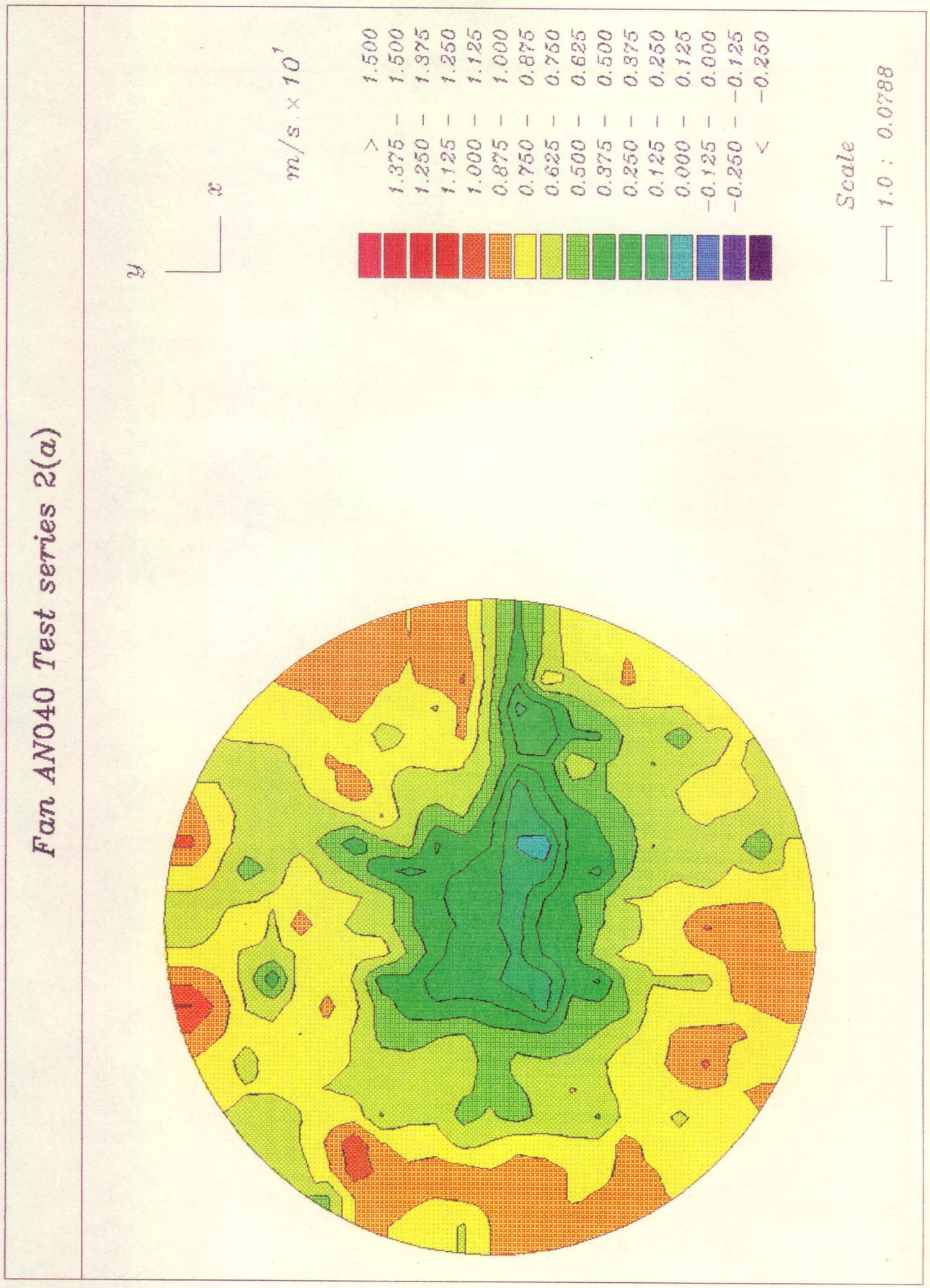

Figure E.4: Velocity profile at full scale fan inlet : Fan AN040 test series 2(a)

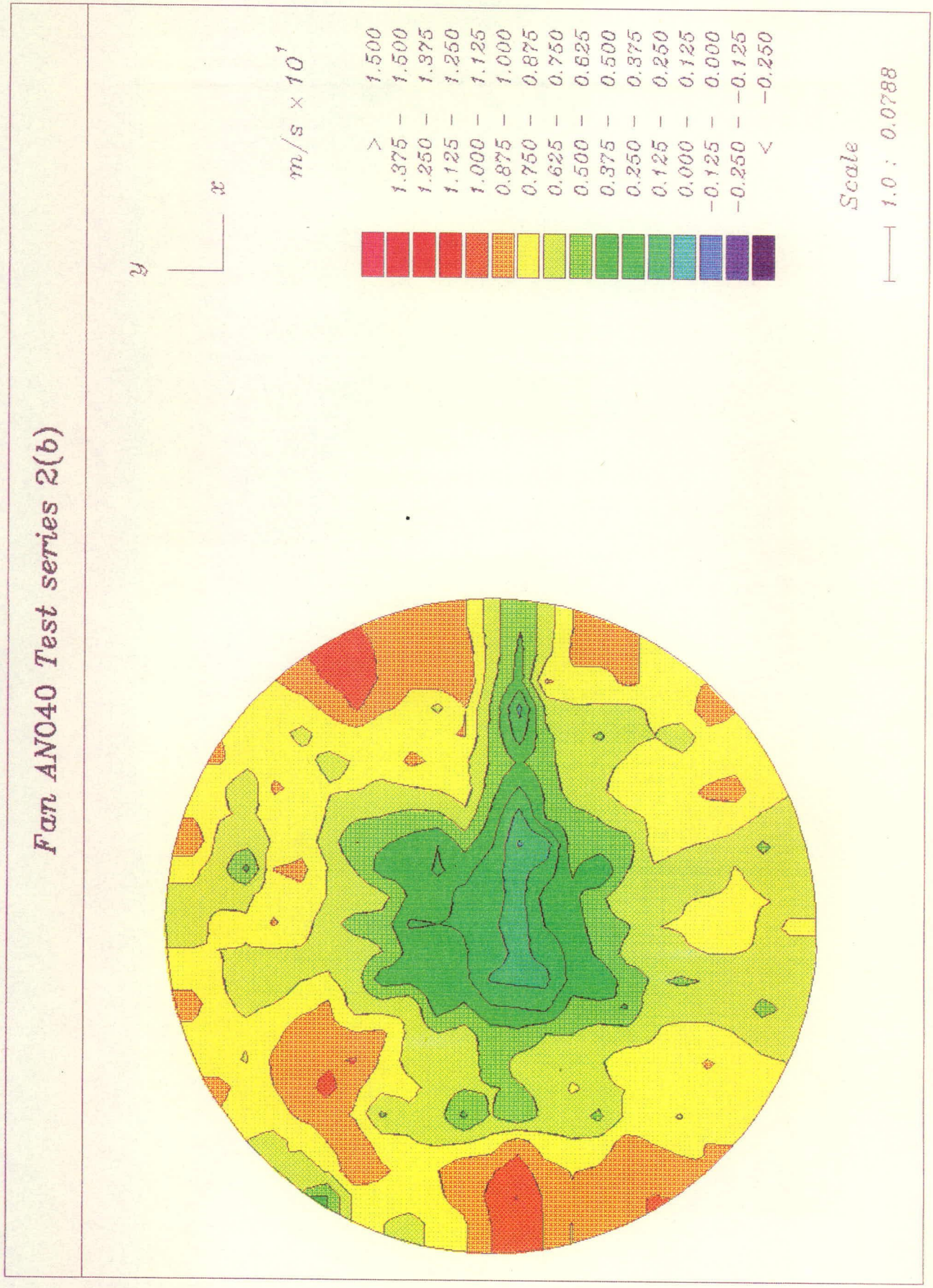

Figure E.5: Velocity profile at full scale fan inlet : Fan AN040 test series 2(b)

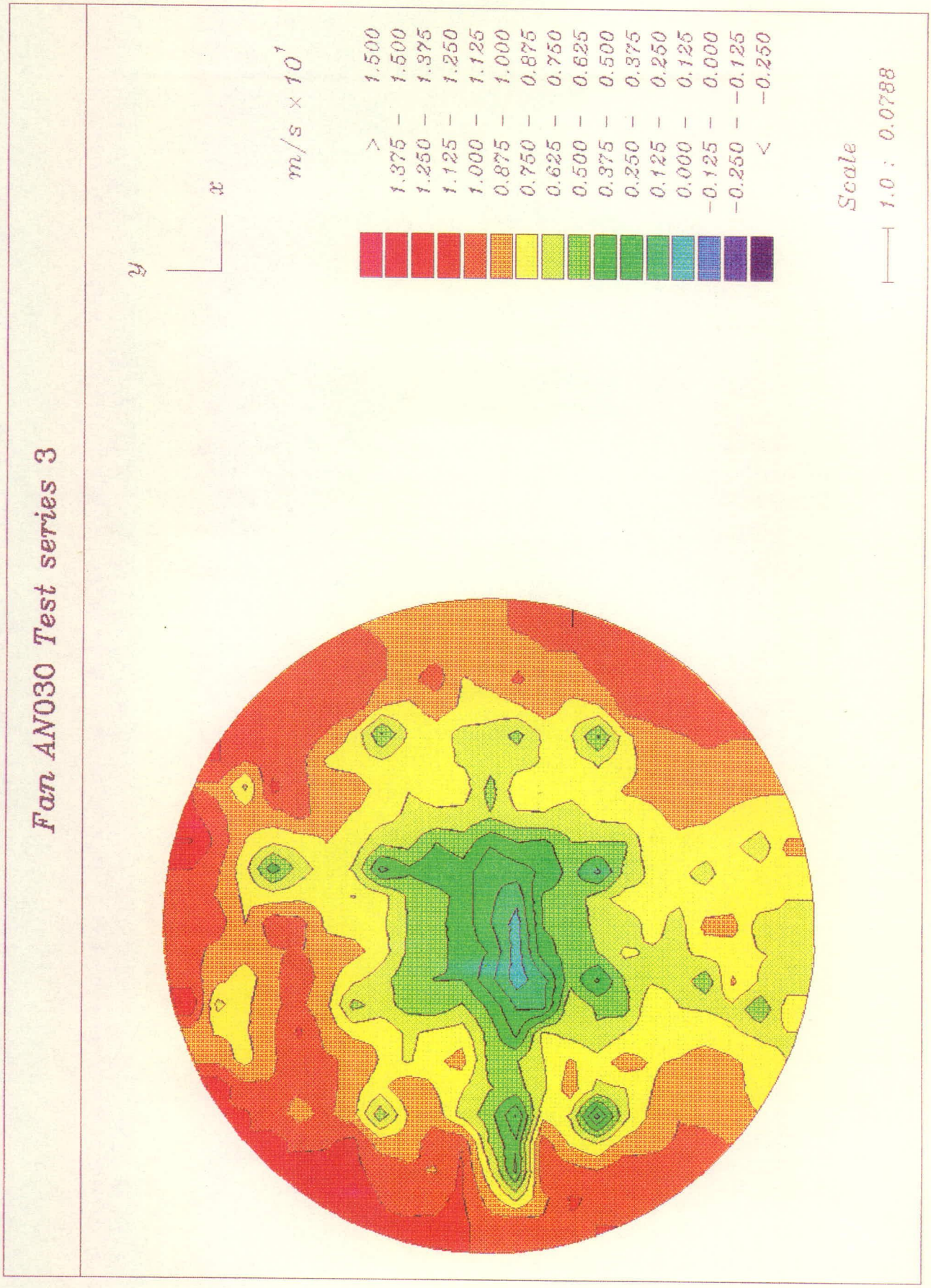

Figure E.6: Velocity profile at full scale fan inlet : Fan AN030 test series 3

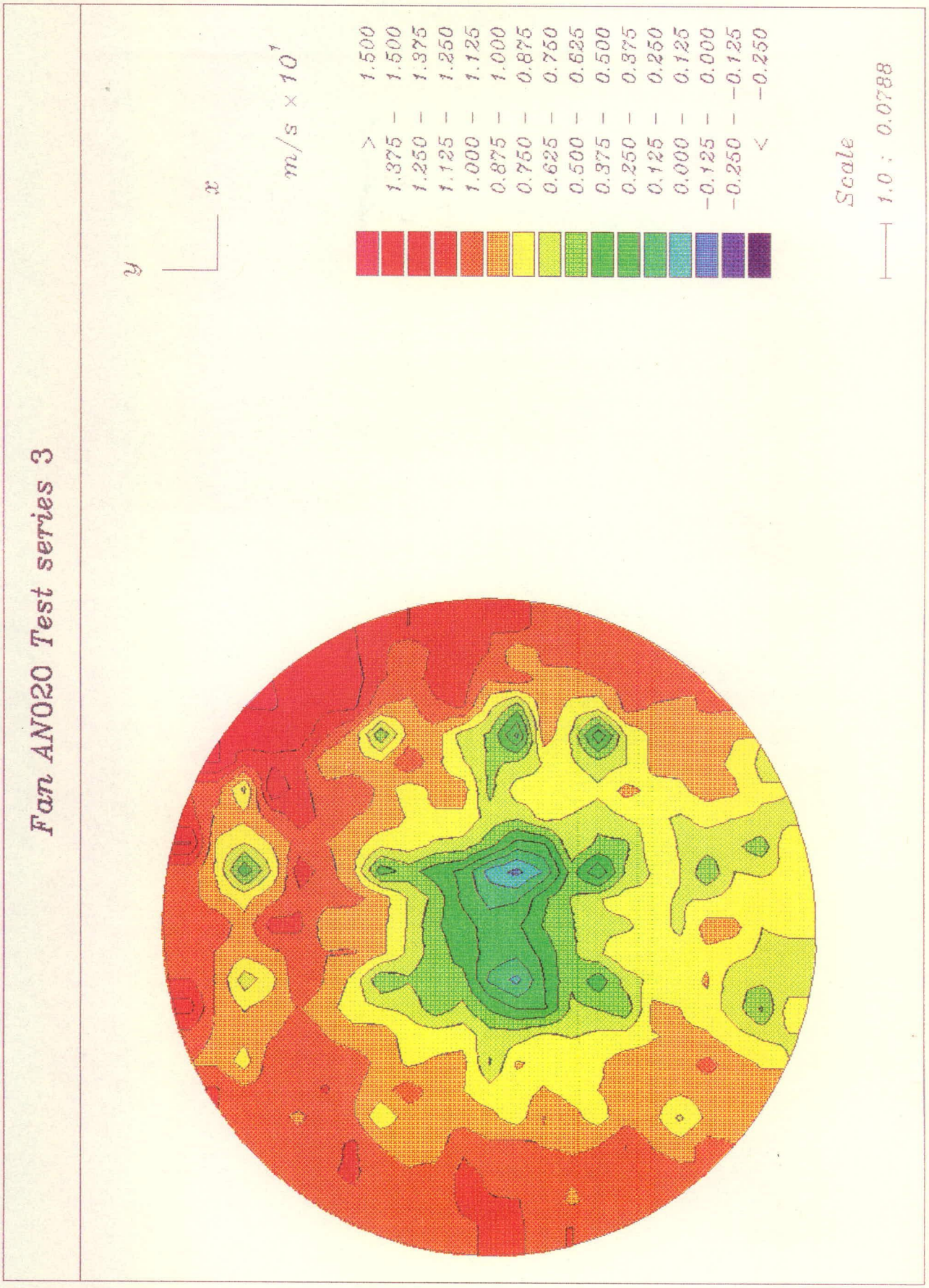

Figure E.7: Velocity profile at full scale fan inlet : Fan AN020 test series 3

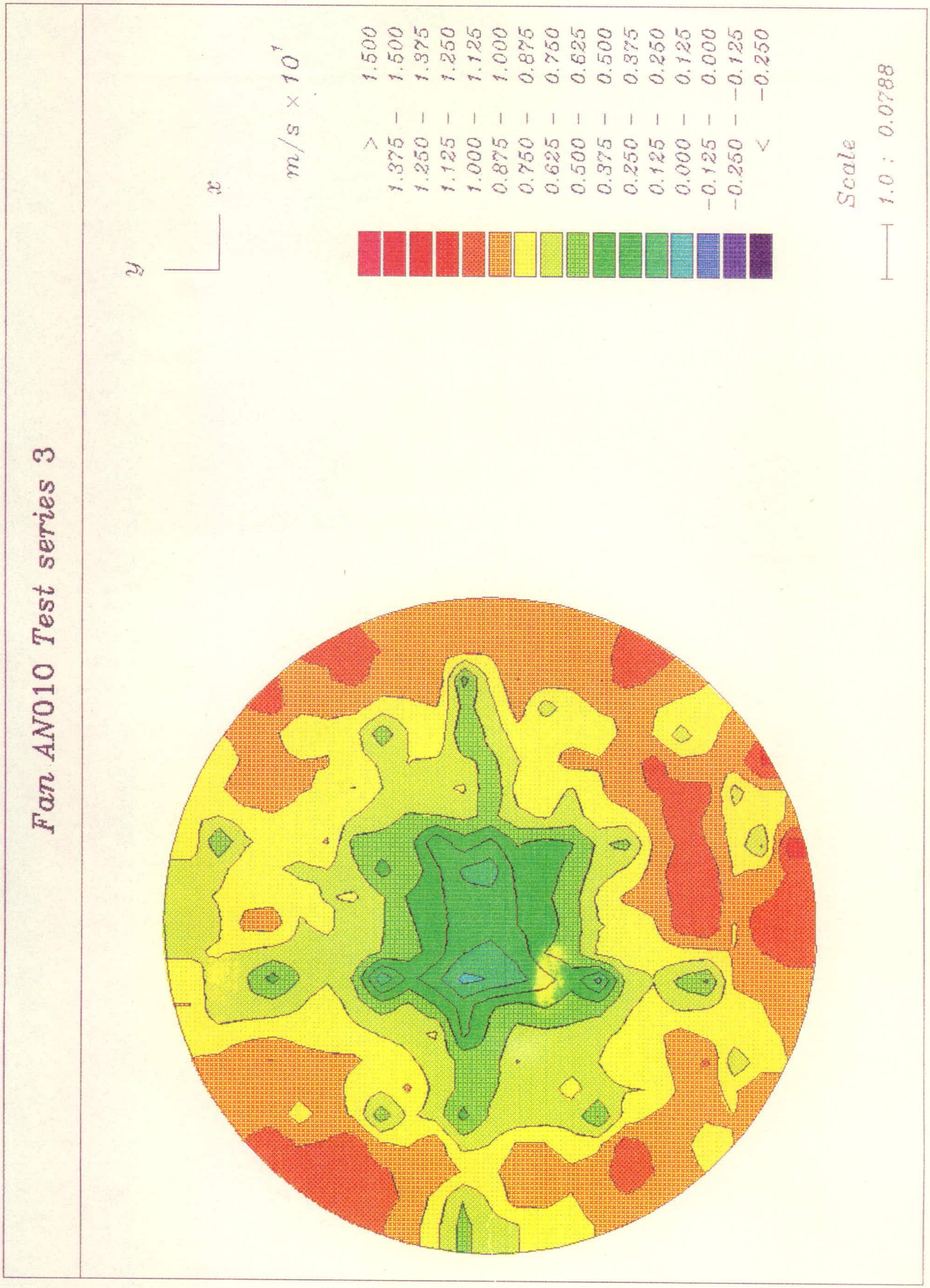

Figure E.8: Velocity profile at full scale fan inlet : Fan AN010 test series 3

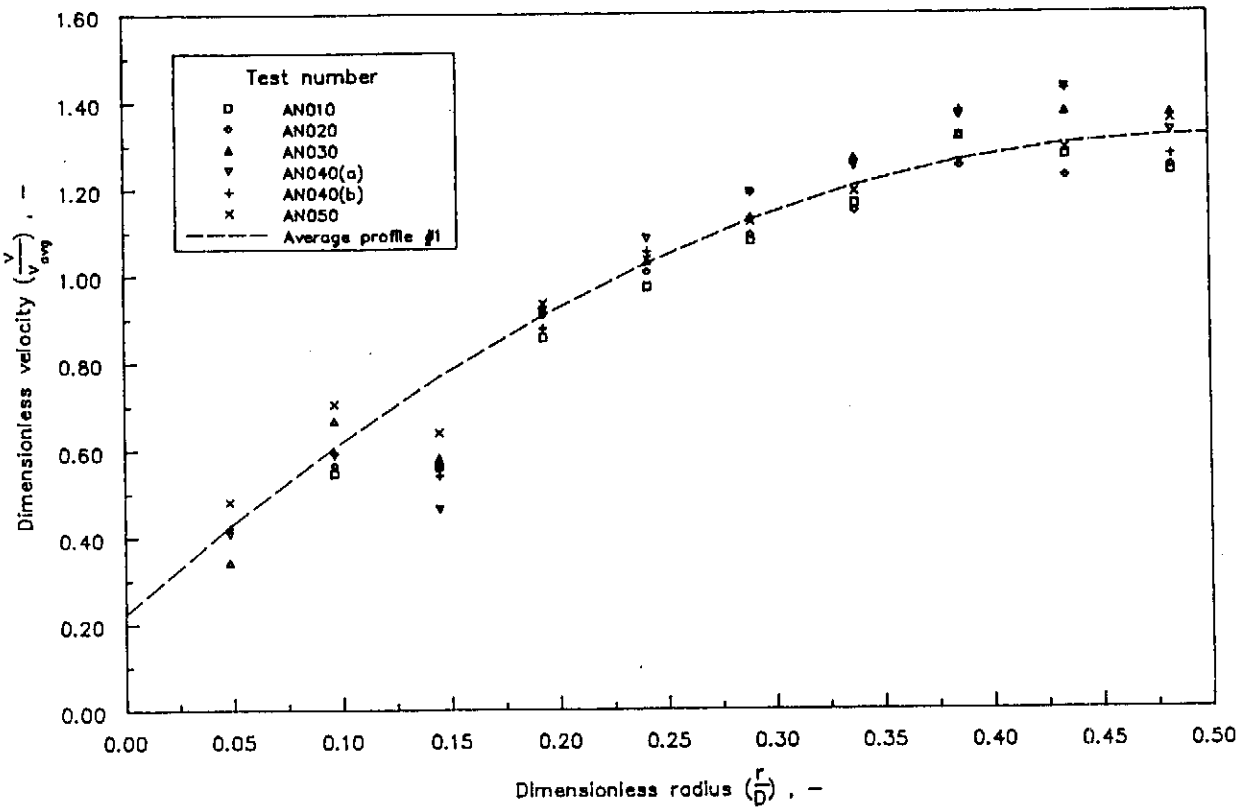

Figure E.9: Velocity profile at fan inlet : Fan AN010 to AN050

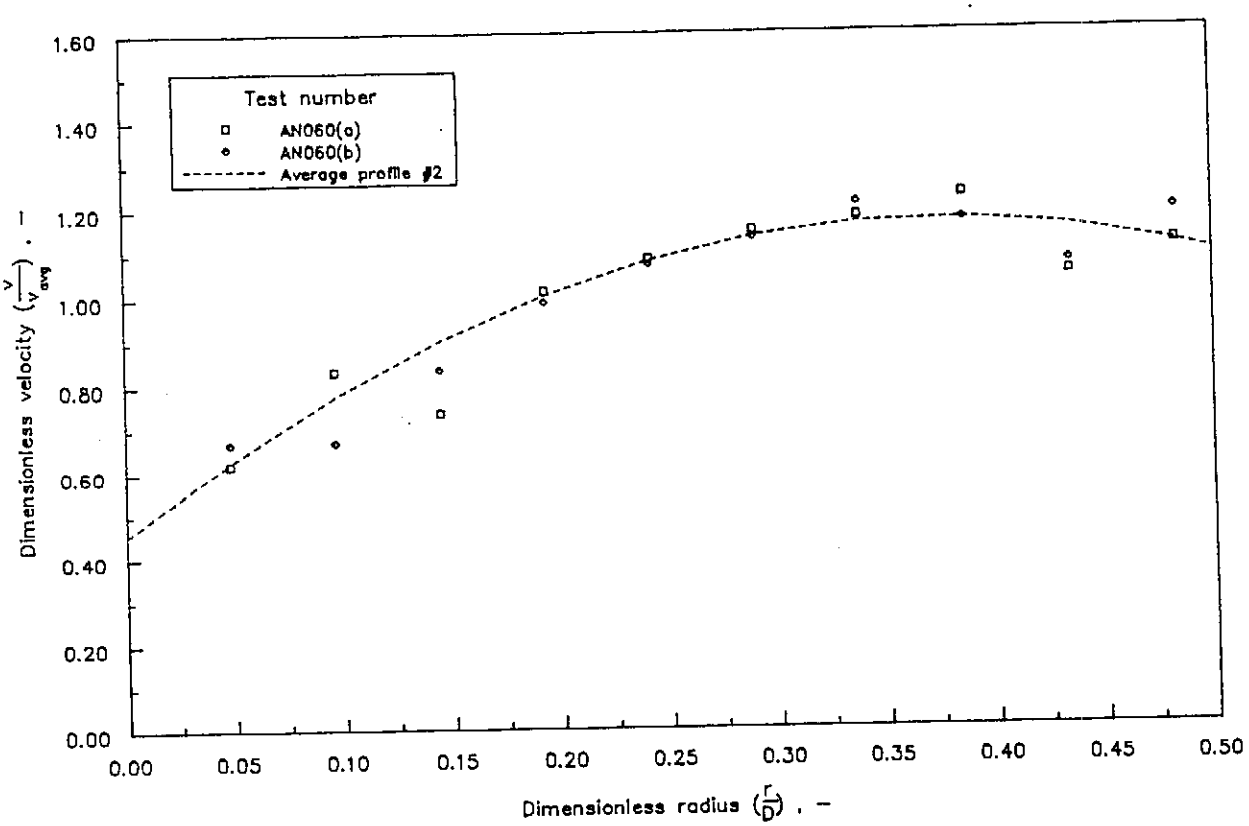

Figure E.10: Velocity profile at fan inlet : Fan AN060

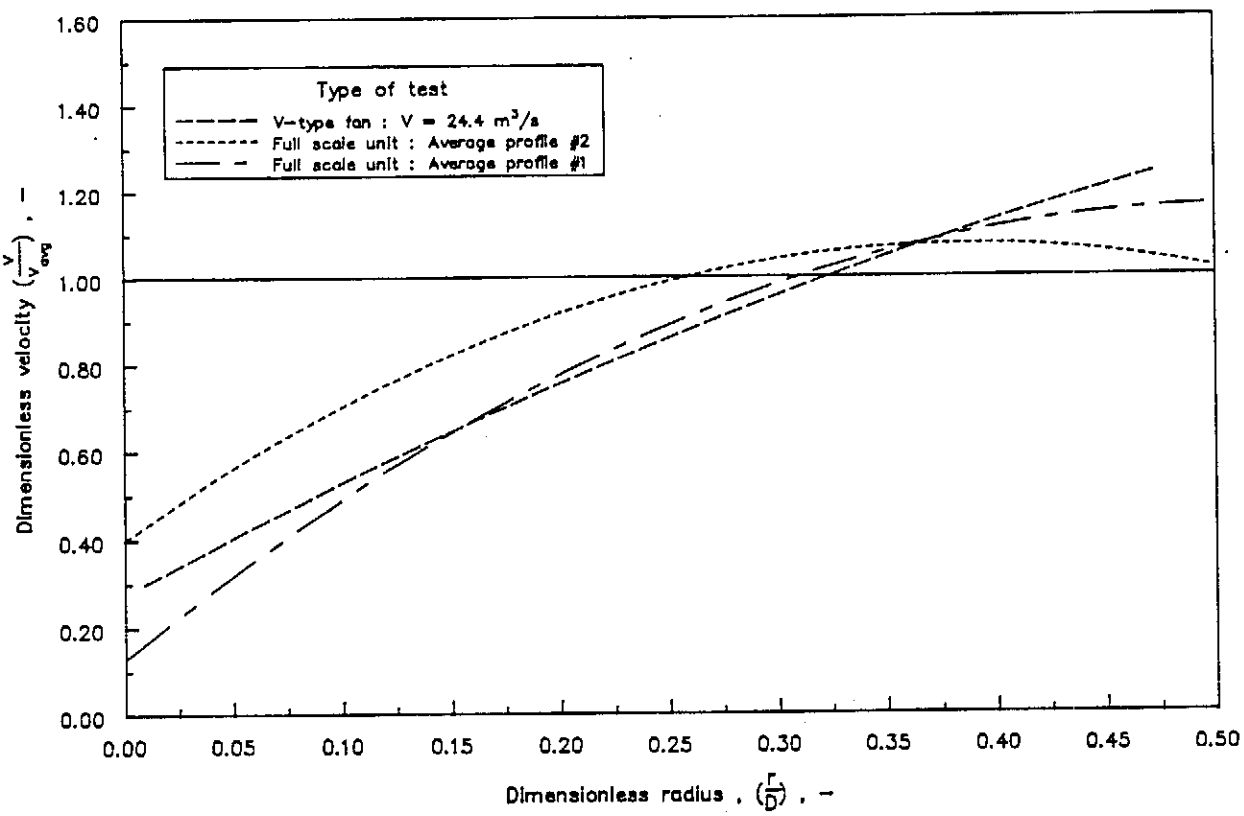

Figure E.11: Velocity profile at fan inlet : Model vs. Full scale

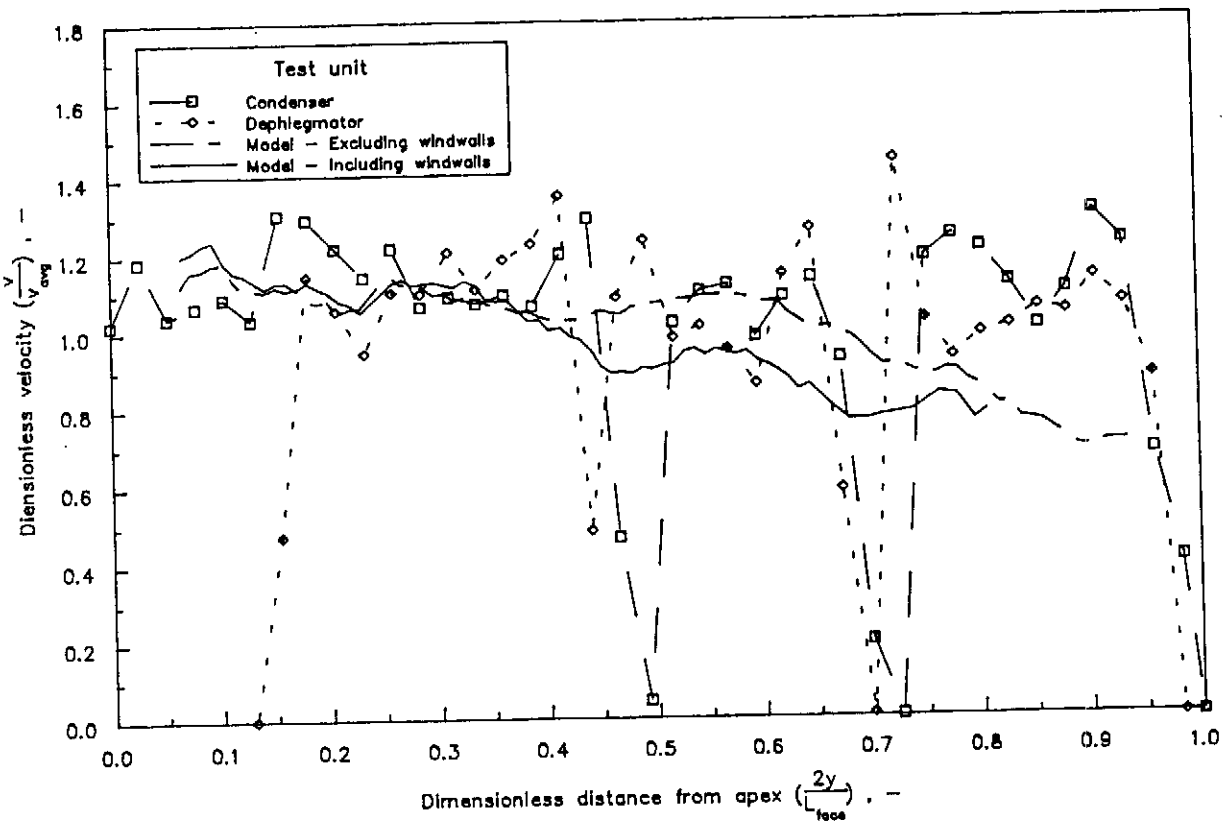

Figure E.12: Velocity profile at heat exchanger surface : Model vs. Full scale

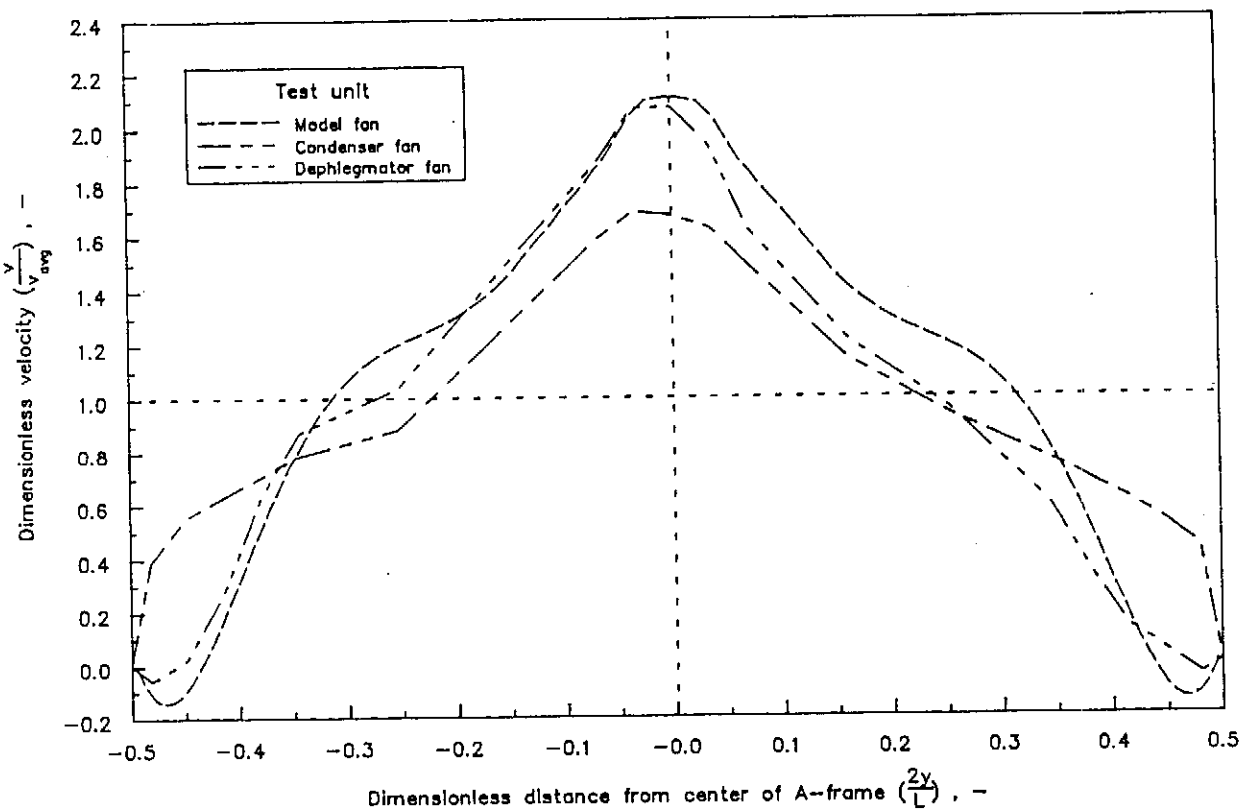

Figure E.13: Velocity profile at apex of unit : Model vs. Full scale

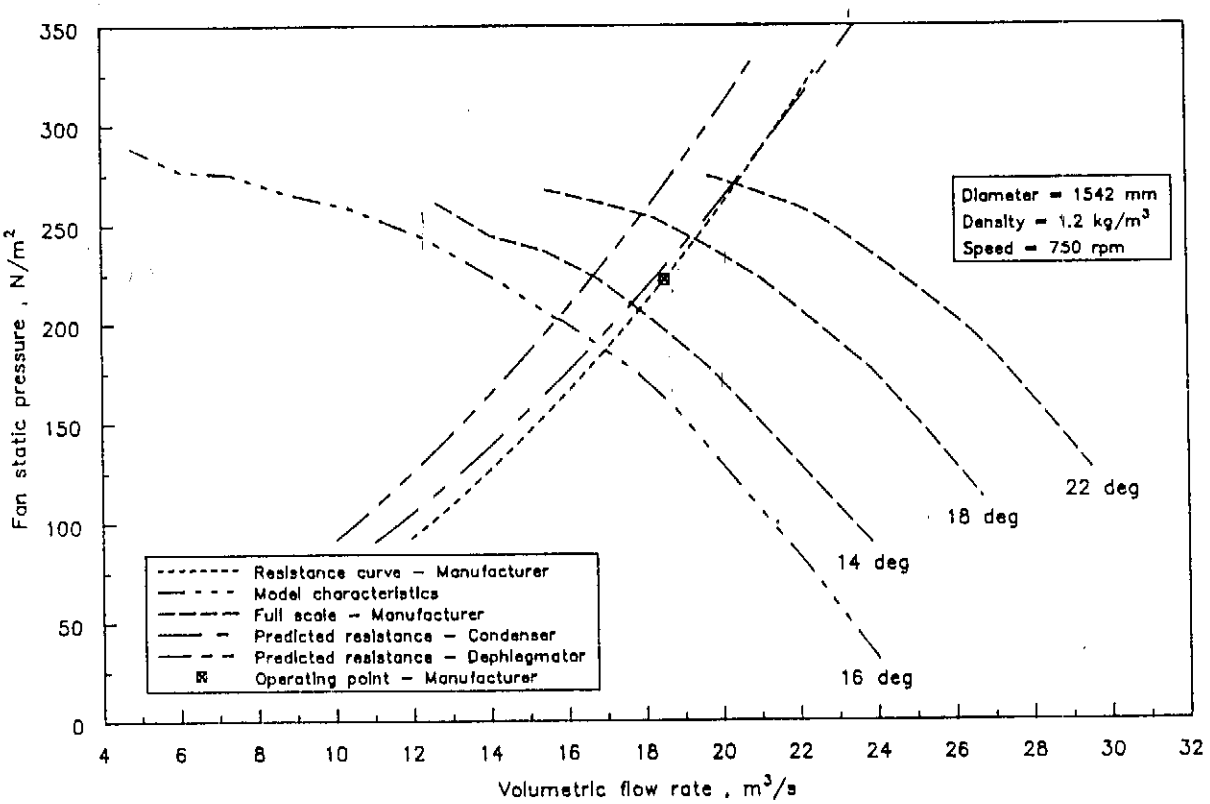

Figure E.14: Fan static pressure : Model vs. Manufacturer's predictions

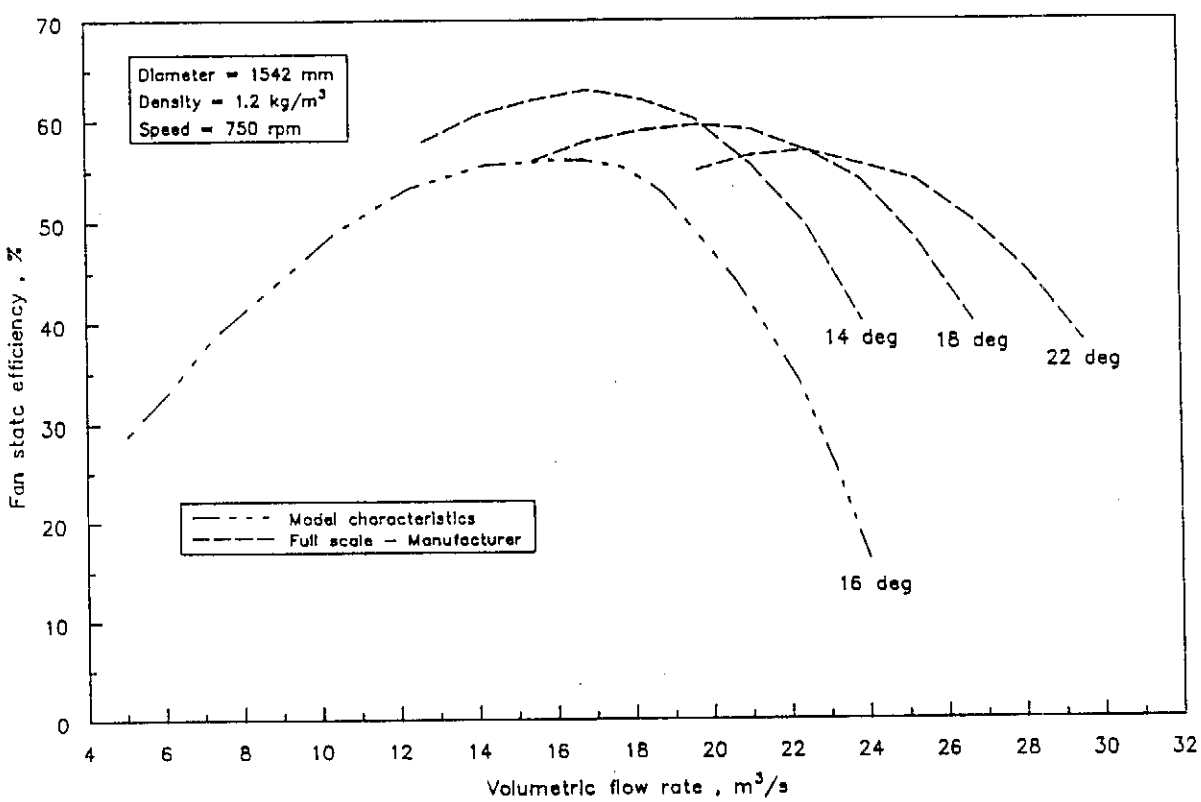

Figure E.15: Fan static efficiency : Model vs. Manufacturer's predictions

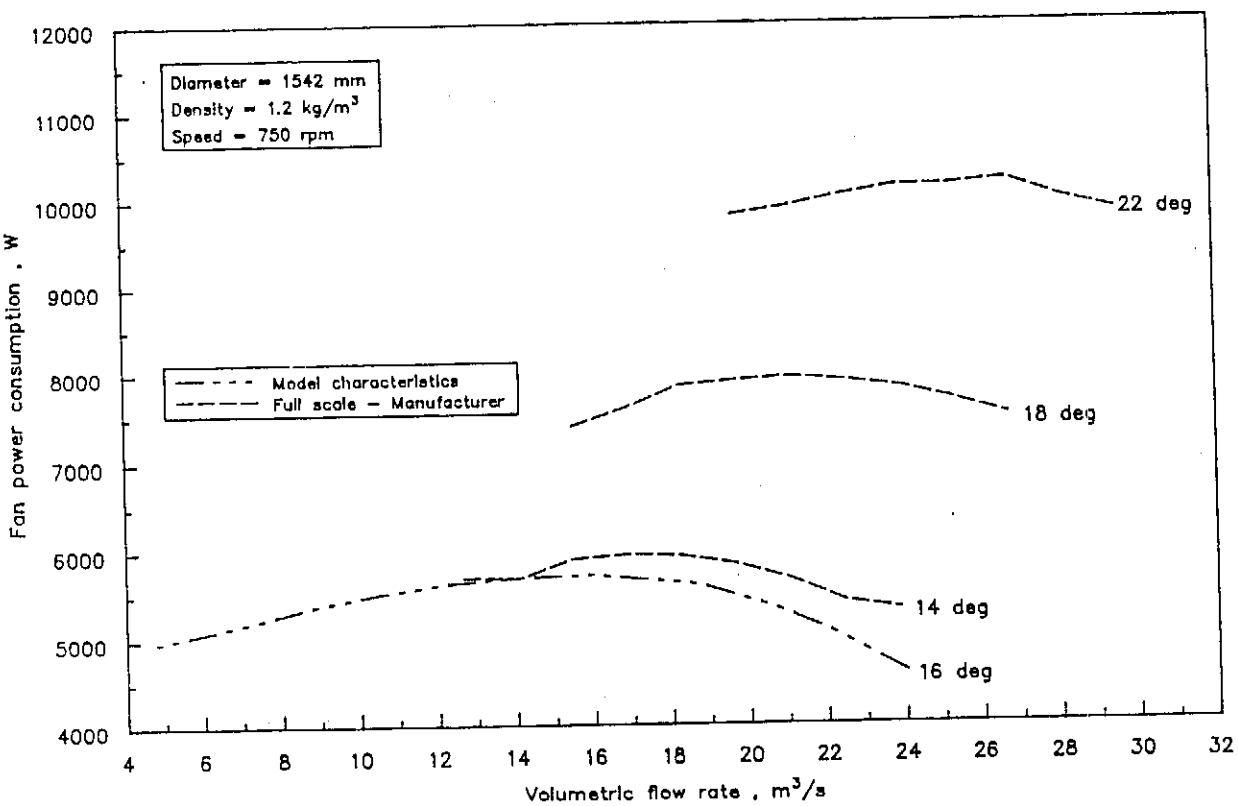

Figure E.16: Fan power consumption : Model vs. Manufacturer's predictions

Appendix F - Drawings

A number of drawings are attached in this appendix to indicate the physical dimensions of all test facilities. Also attached are drawings of the rotating beam and five hole pressure probe used to measure velocity profiles in the full scale and model facilities respectively. The contents of individual sections incorporated into this appendix are first summarized before the items are included.

F.1 Full scale unit

Figure F.1.1 - Full scale installation
Figure F.1.2 - A-frame detail
Figure F.1.3 - Weather mast location

F.2 Scaled model facility

Figure F.2.1 - Composite drawing of scaled model
Figure F.2.2 - Heat exchanger support frame
Figure F.2.3 - Heat exchanger detail : Part 1
Figure F.2.4 - Heat exchanger detail : Part 2
Figure F.2.5 - Internal support detail
Figure F.2.6 - Elliptical fan inlet
Figure F.2.7 - Fan inlet grid
Figure F.2.8 - Walkway
Figure F.2.9 - Support beams : Part 1
Figure F.2.10 - Support beams : Part 2

F.3 Code fan test facility

Figure F.3.1 - Inlet bellmouth according to BS 848
Figure F.3.2 - Transformation piece (Bellmouth)
Figure F.3.3 - Flow throttling device
Figure F.3.4 - Transformation piece (Throttling device)
Figure F.3.5 - Channel duct
Figure F.3.6 - Flow measuring section : Type A
Figure F.3.7 - Flow measuring section : Type B
Figure F.3.8 - Flow straightener : Type A
Figure F.3.9 - Flow straightener detail : Type A

F.4 Instruments

F.5 Measuring positions

F.6 Blade profiles

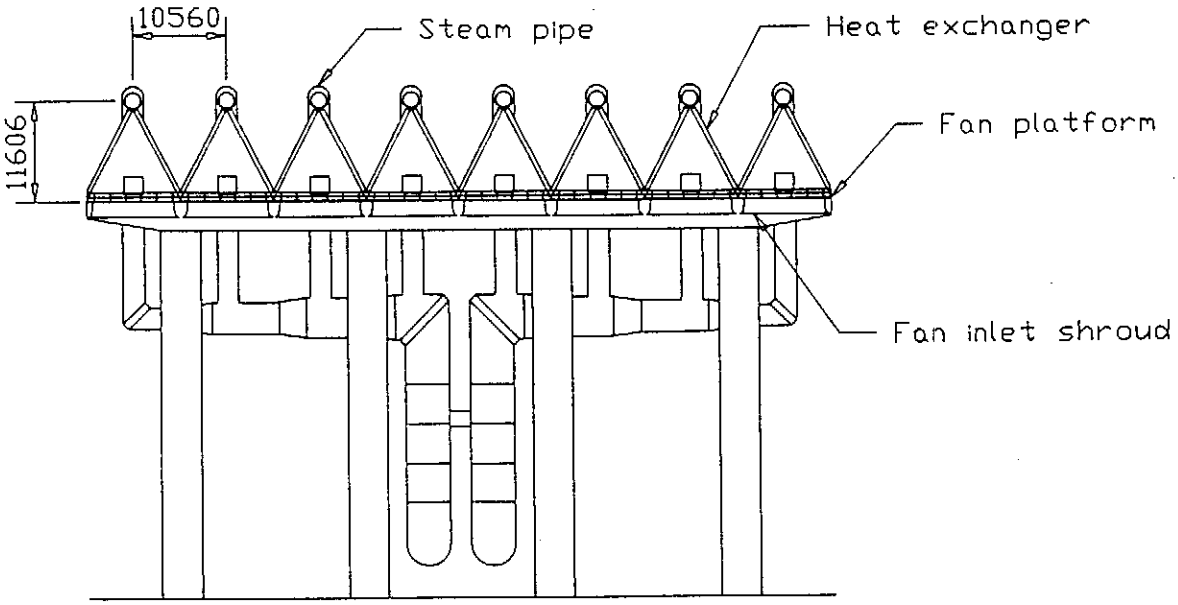

Frontal elevation

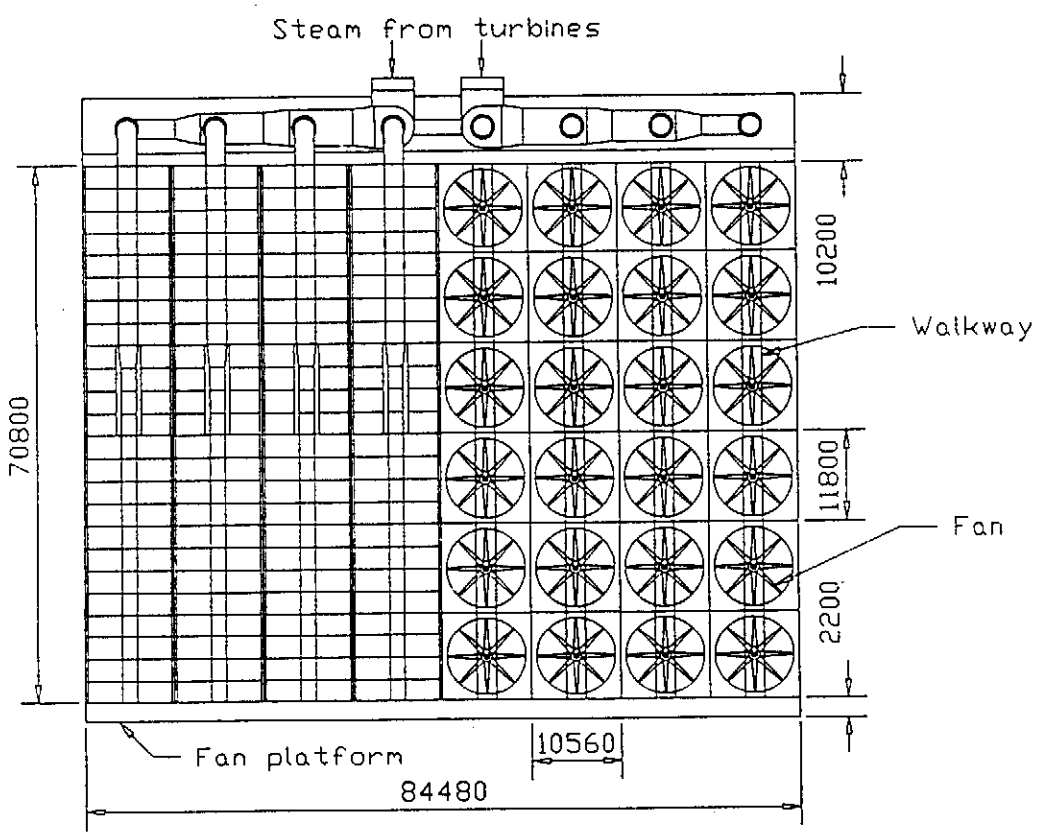

Plan

Figure F.1.1: Full scale installation

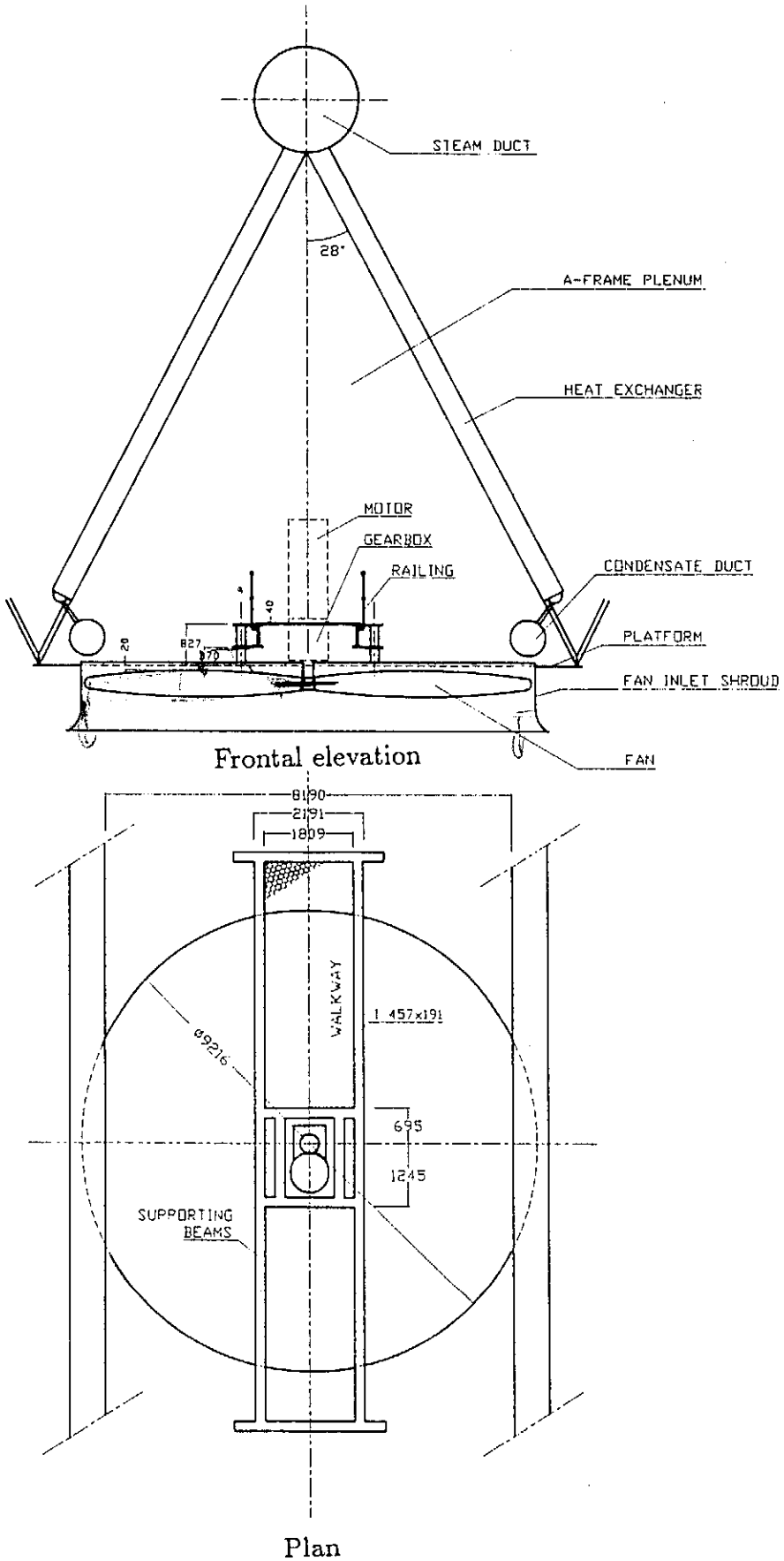

Figure F.1.2: A-frame detail

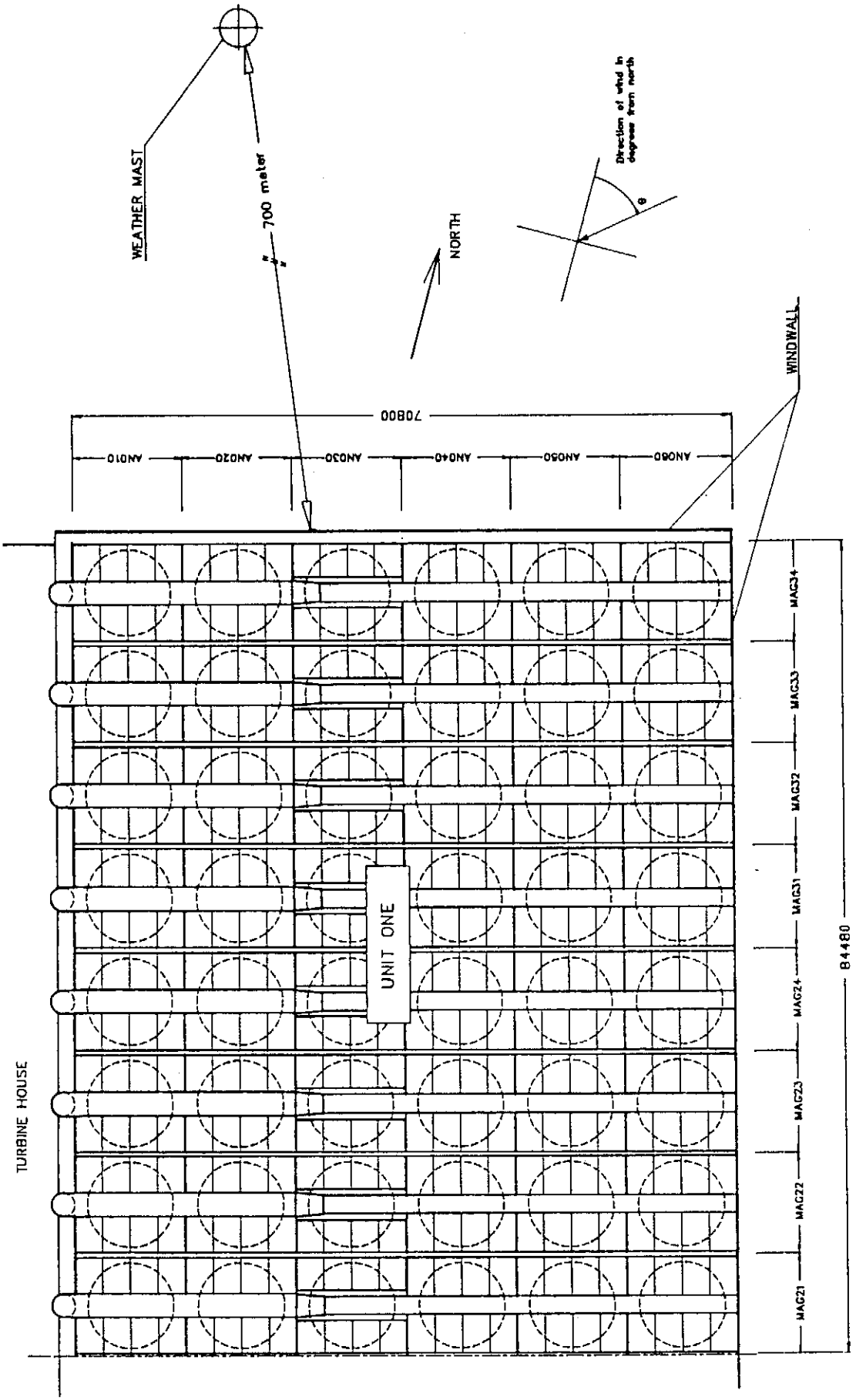

Figure F.1.3: Weather mast location

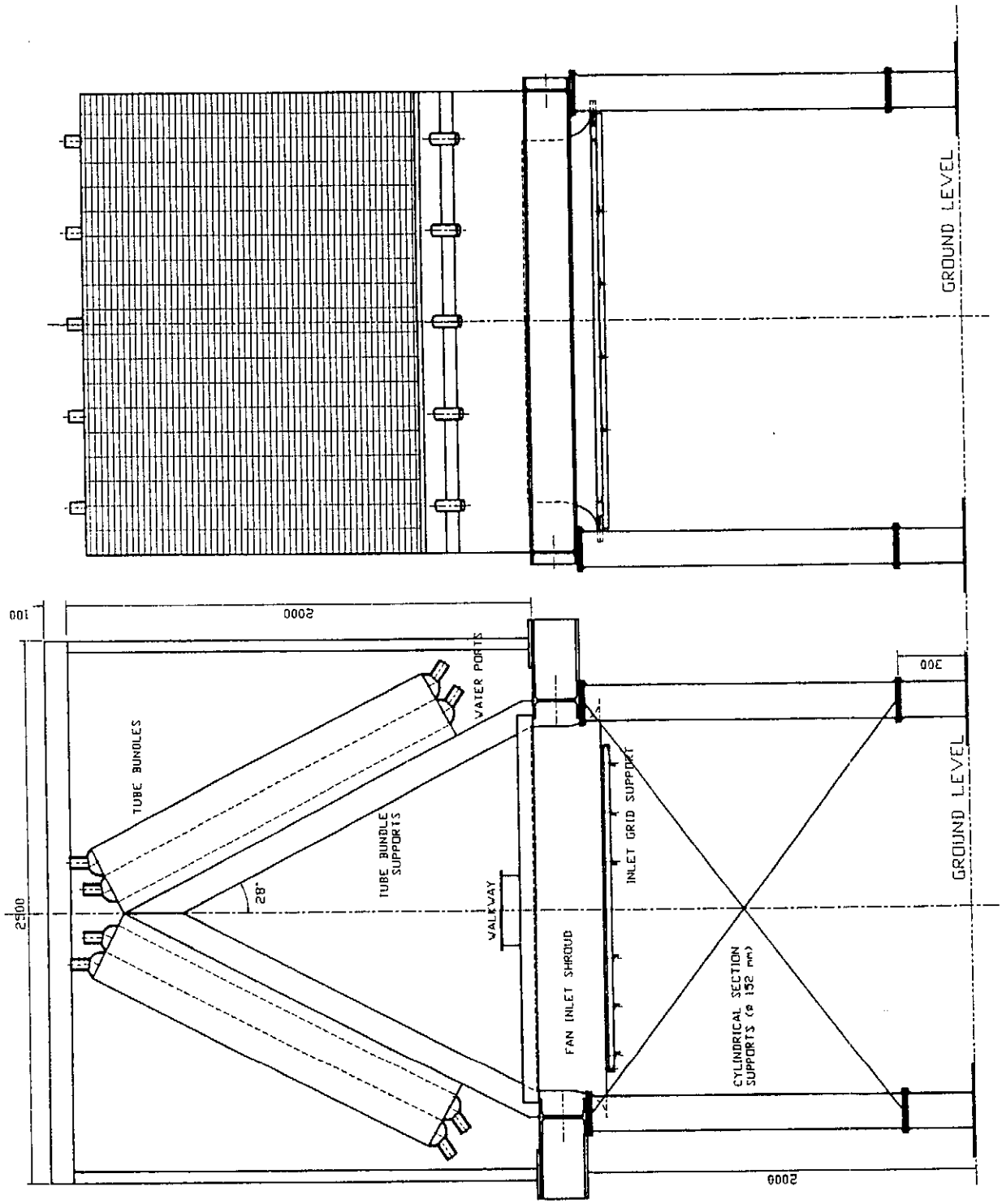

Figure F.2.1: Composite drawing of the scaled model

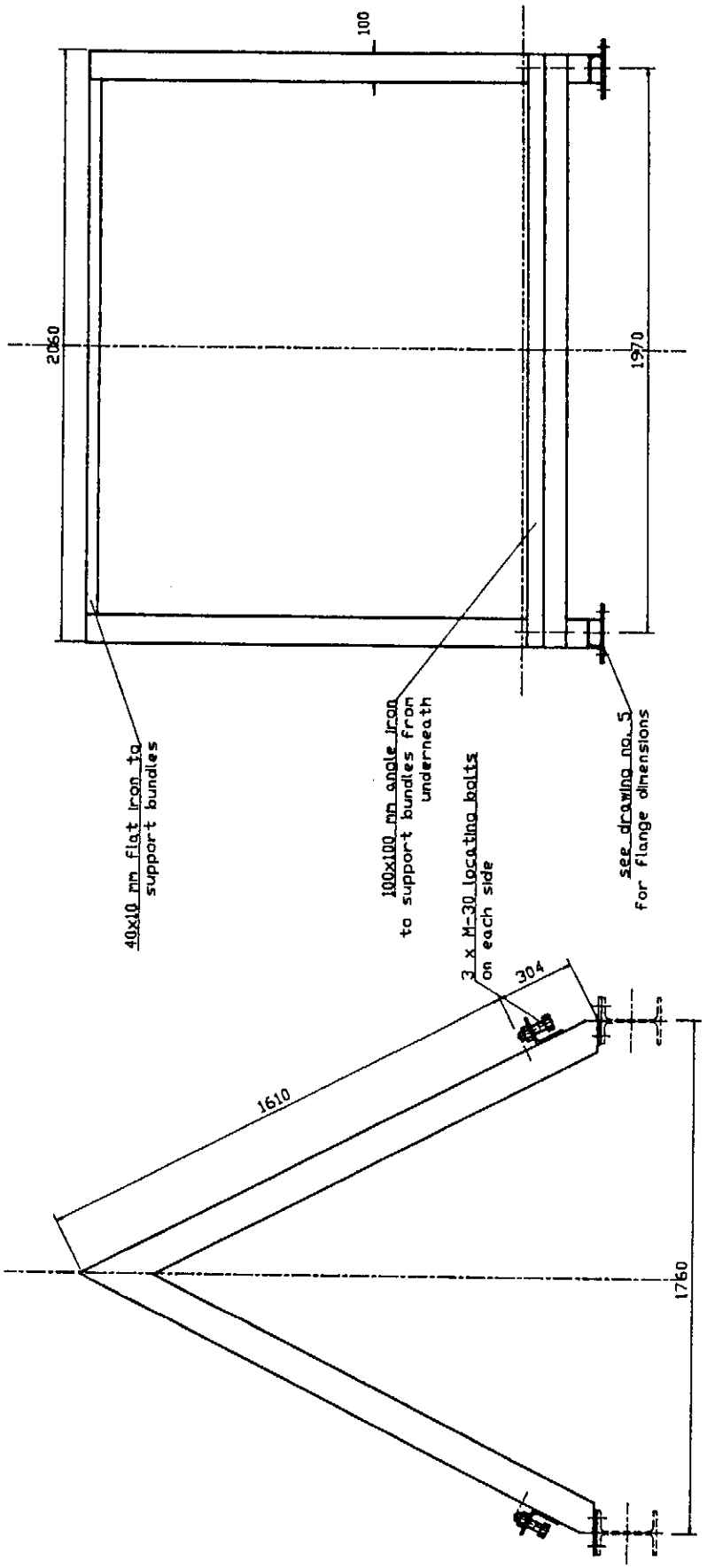

Figure F.2.2: Heat exchanger support frame

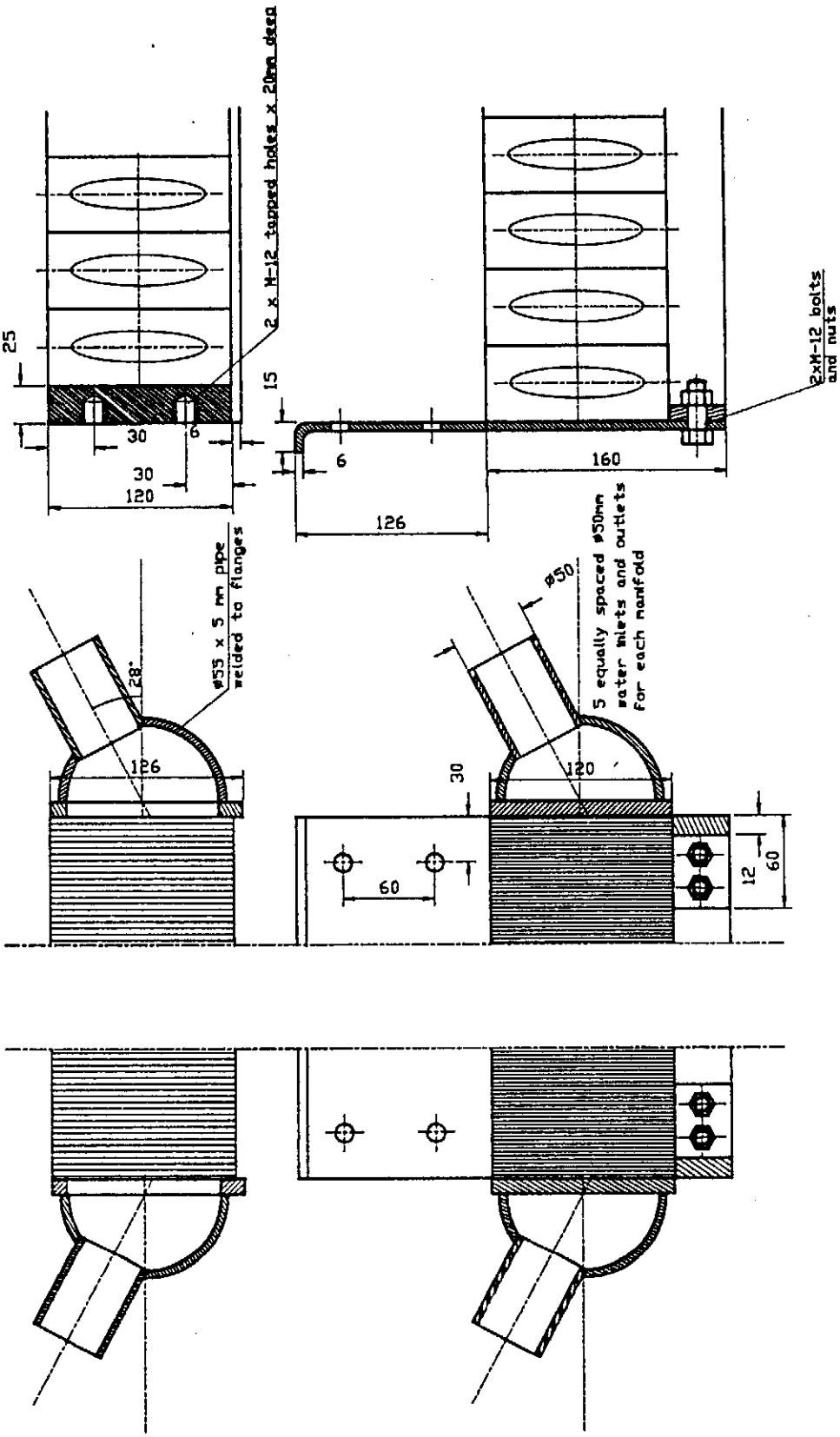

Figure F.2.3: Heat exchanger detail : Part 1

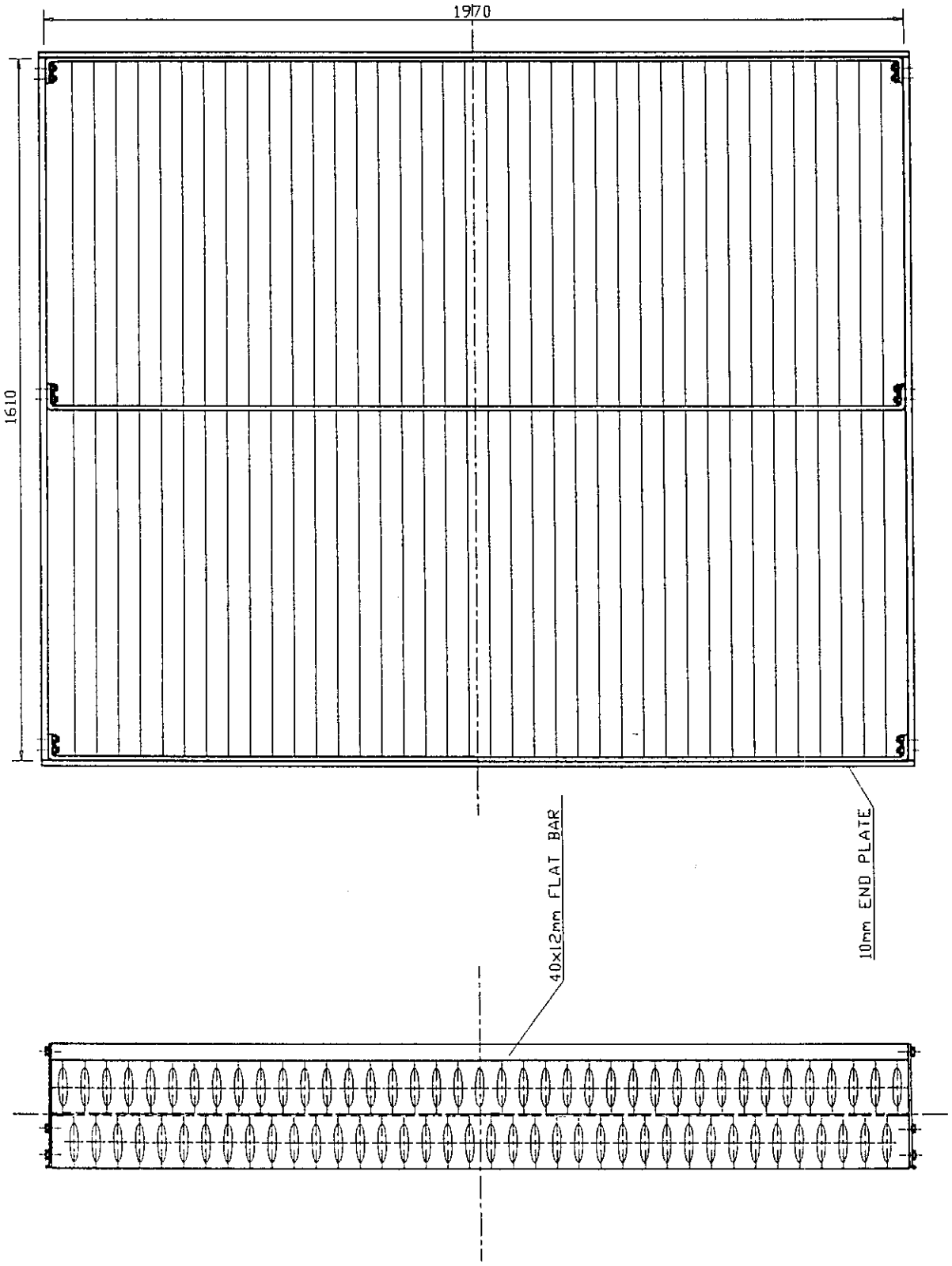

Figure F.2.4: Heat exchanger detail : Part 2

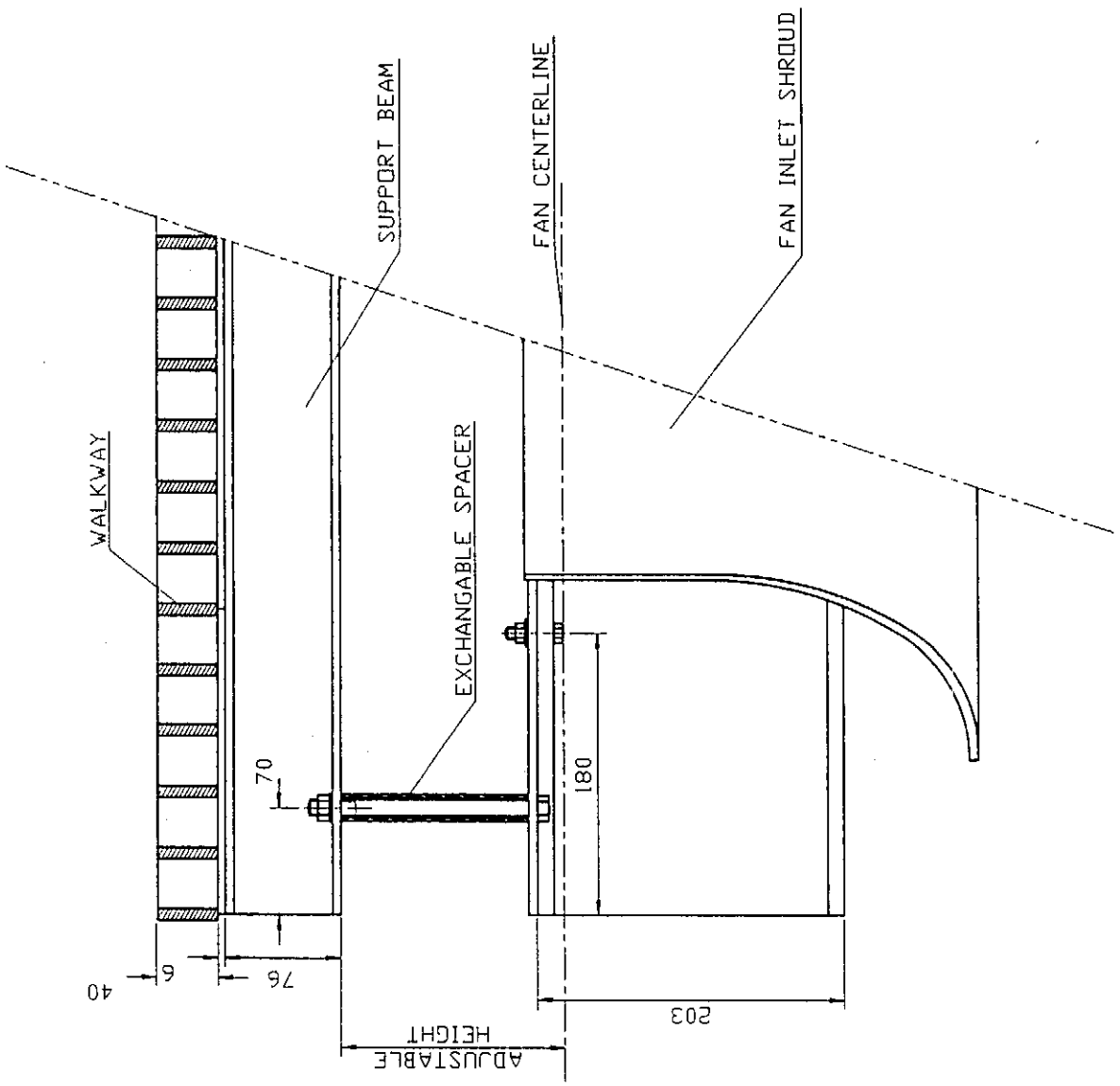

Figure F.2.5: Internal support detail

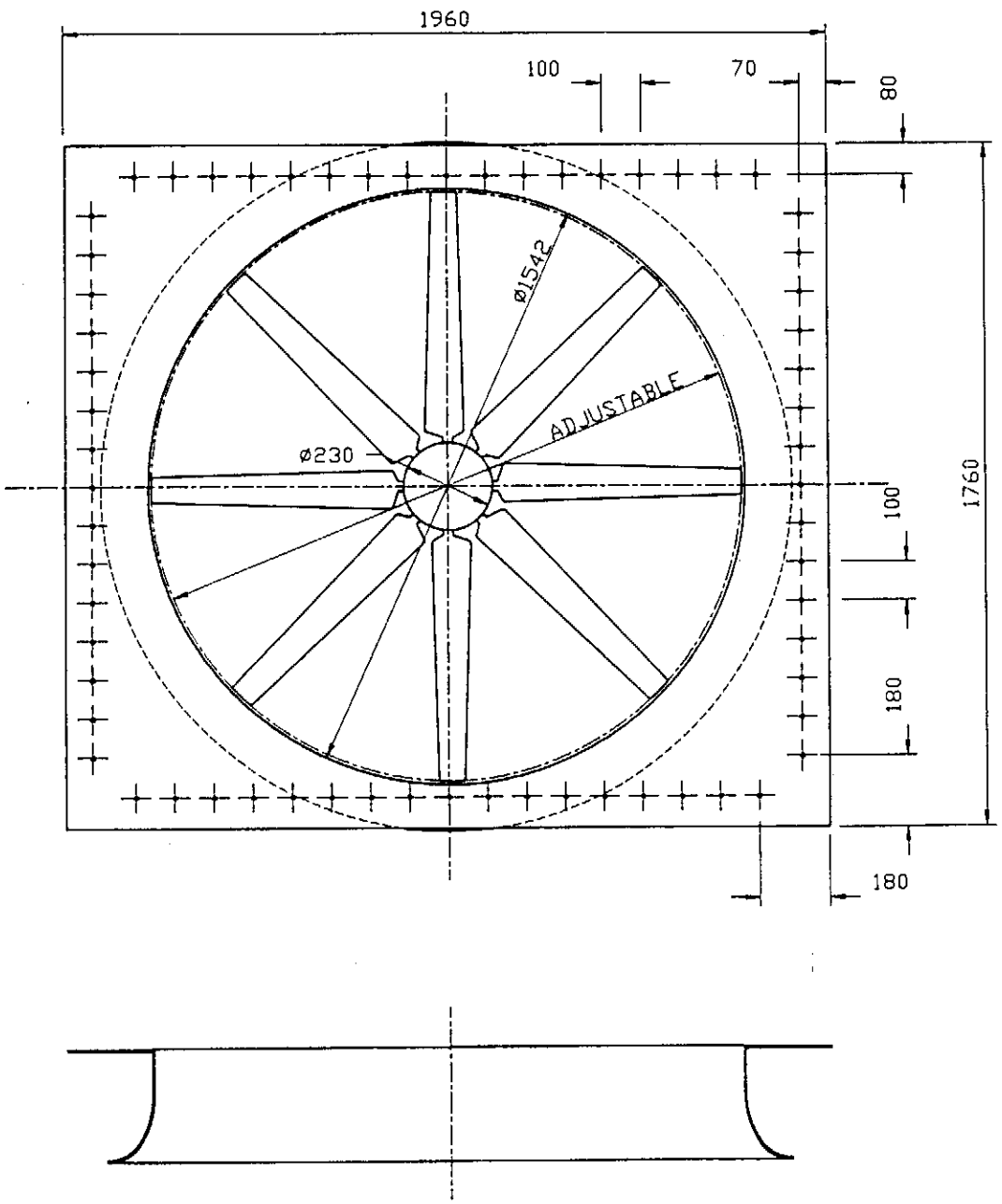

Figure F.2.6: Elliptical fan inlet shroud

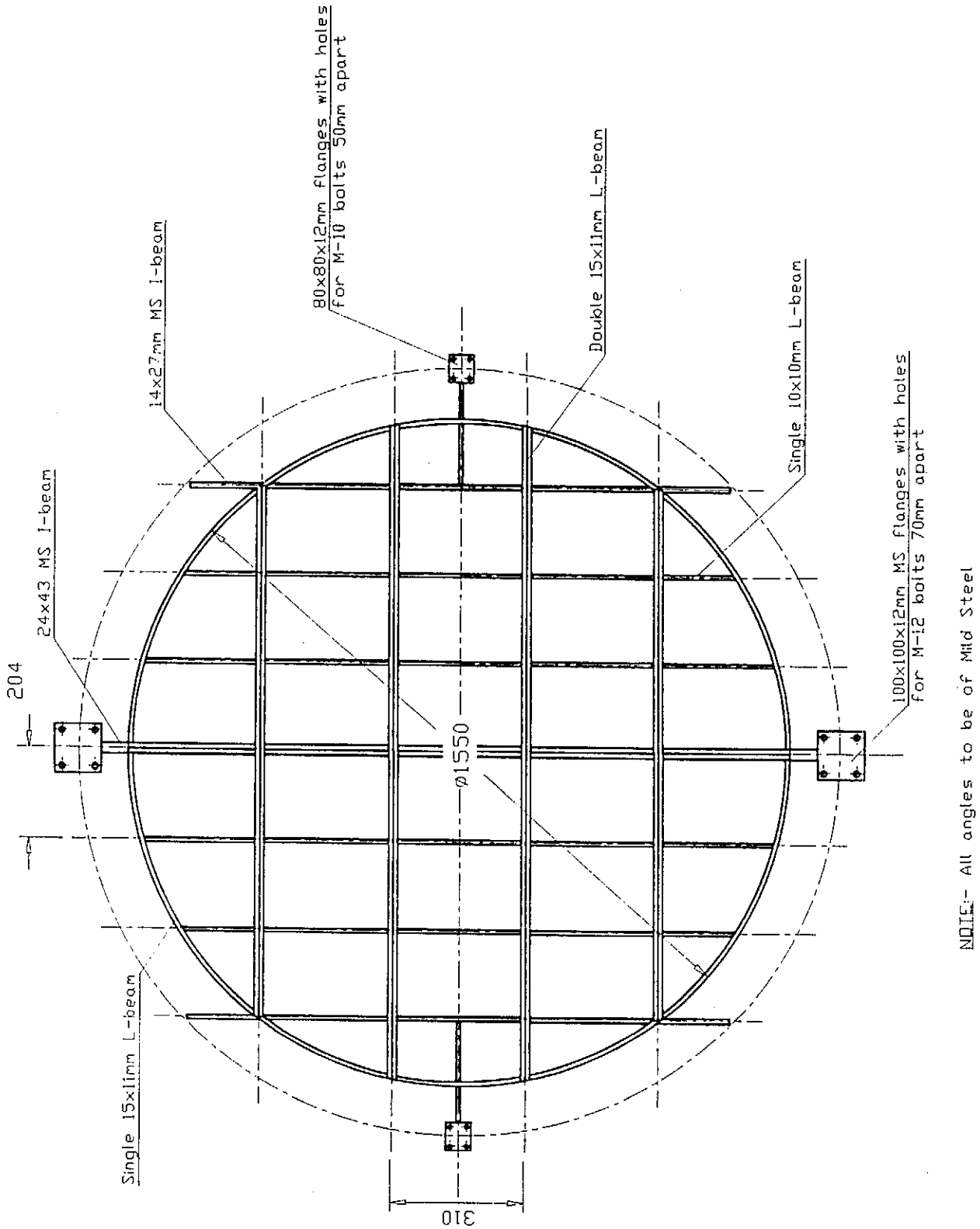

Figure F.2.7: Fan inlet grid

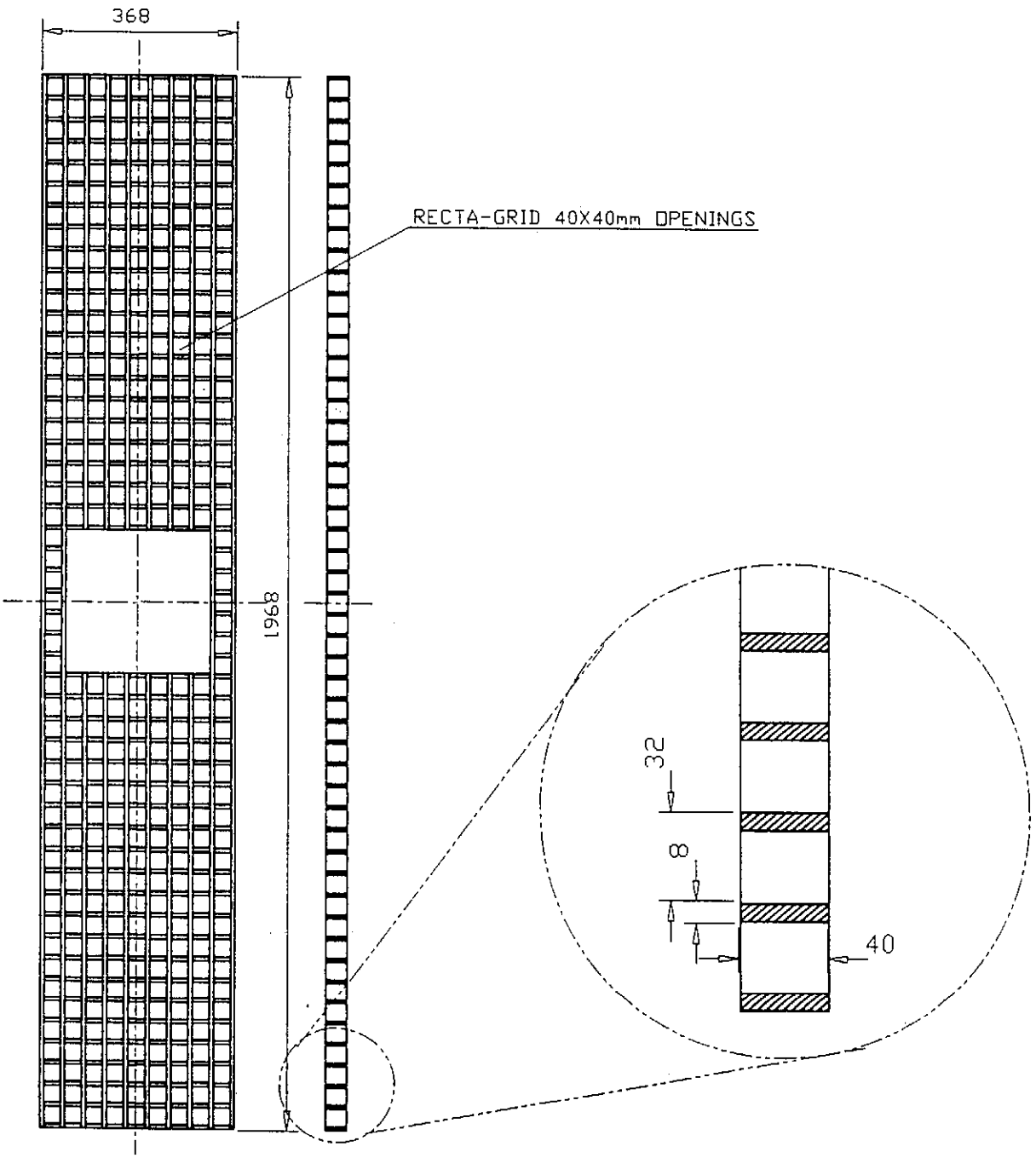

Figure F.2.8: Walkway

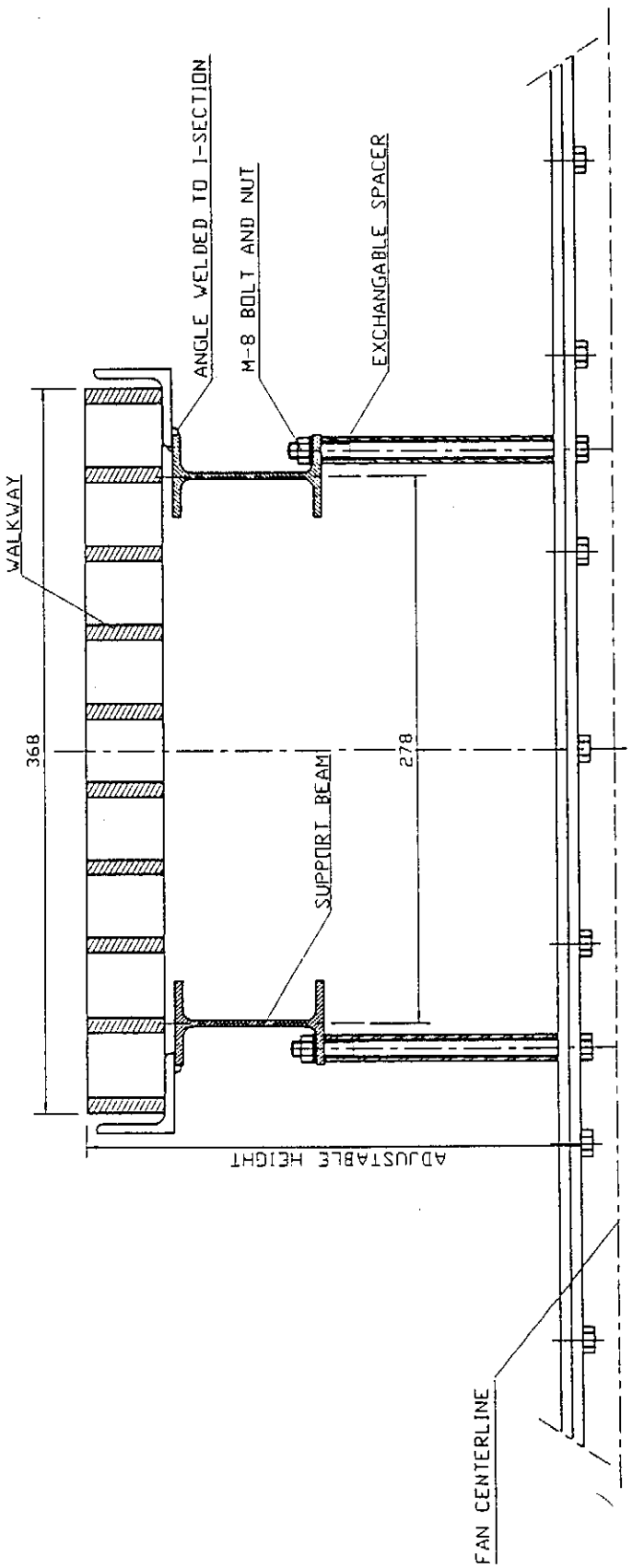

Figure F.2.9: Support beams : Part 1

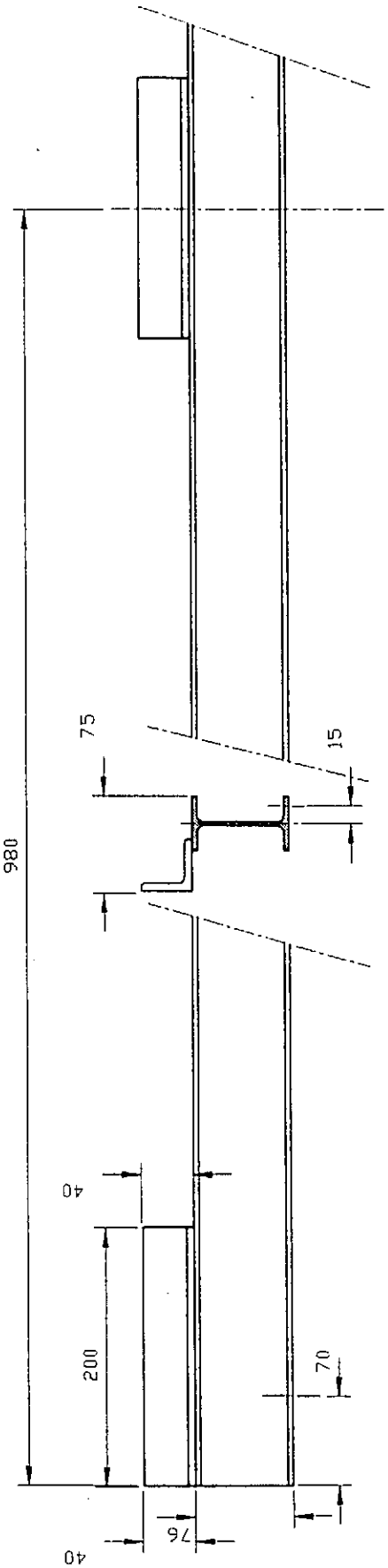

Figure F.2.10: Support beams : Part 2

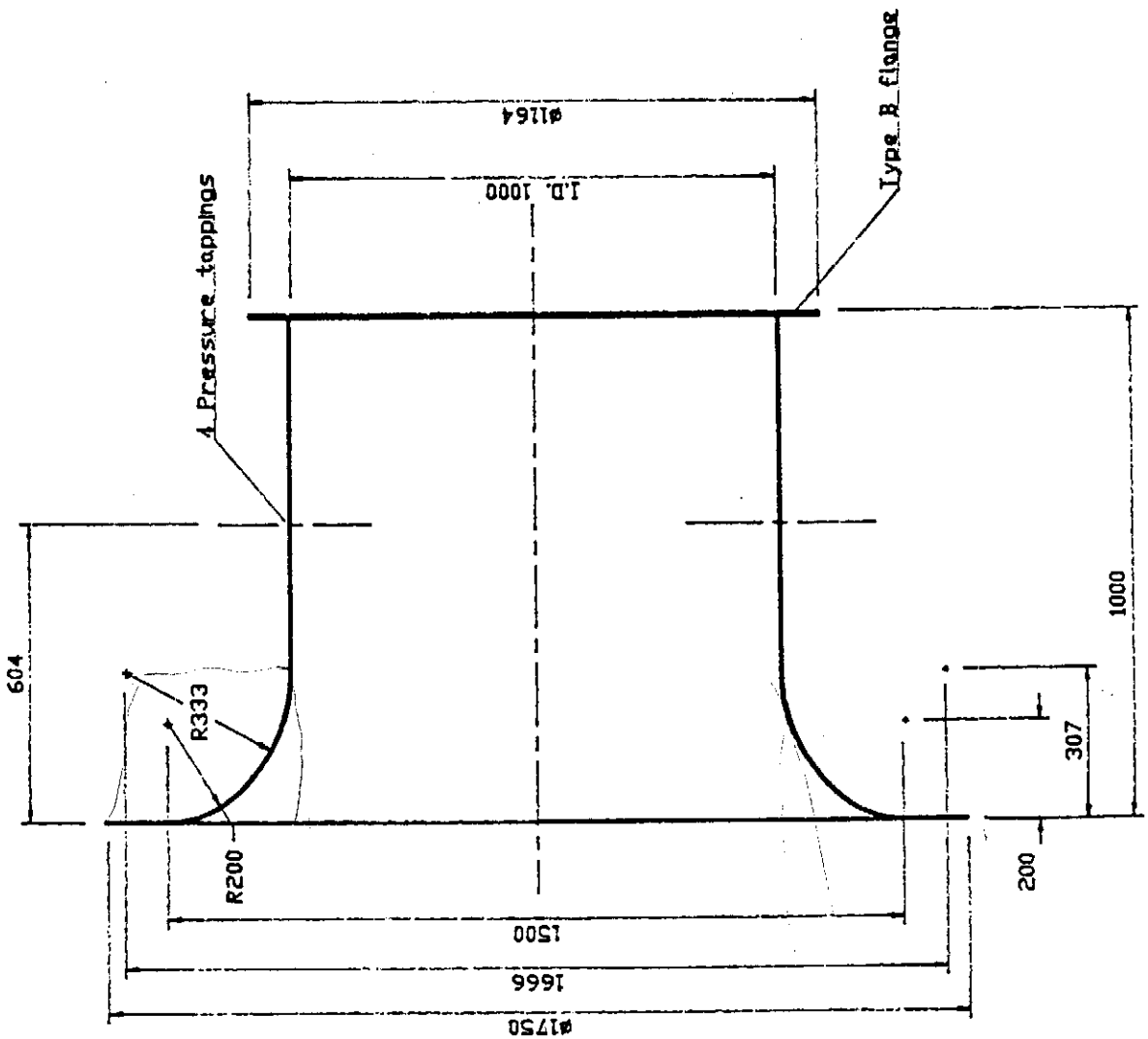

Figure F.3.1: Inlet bellmouth according to BS 848 [80BS1]

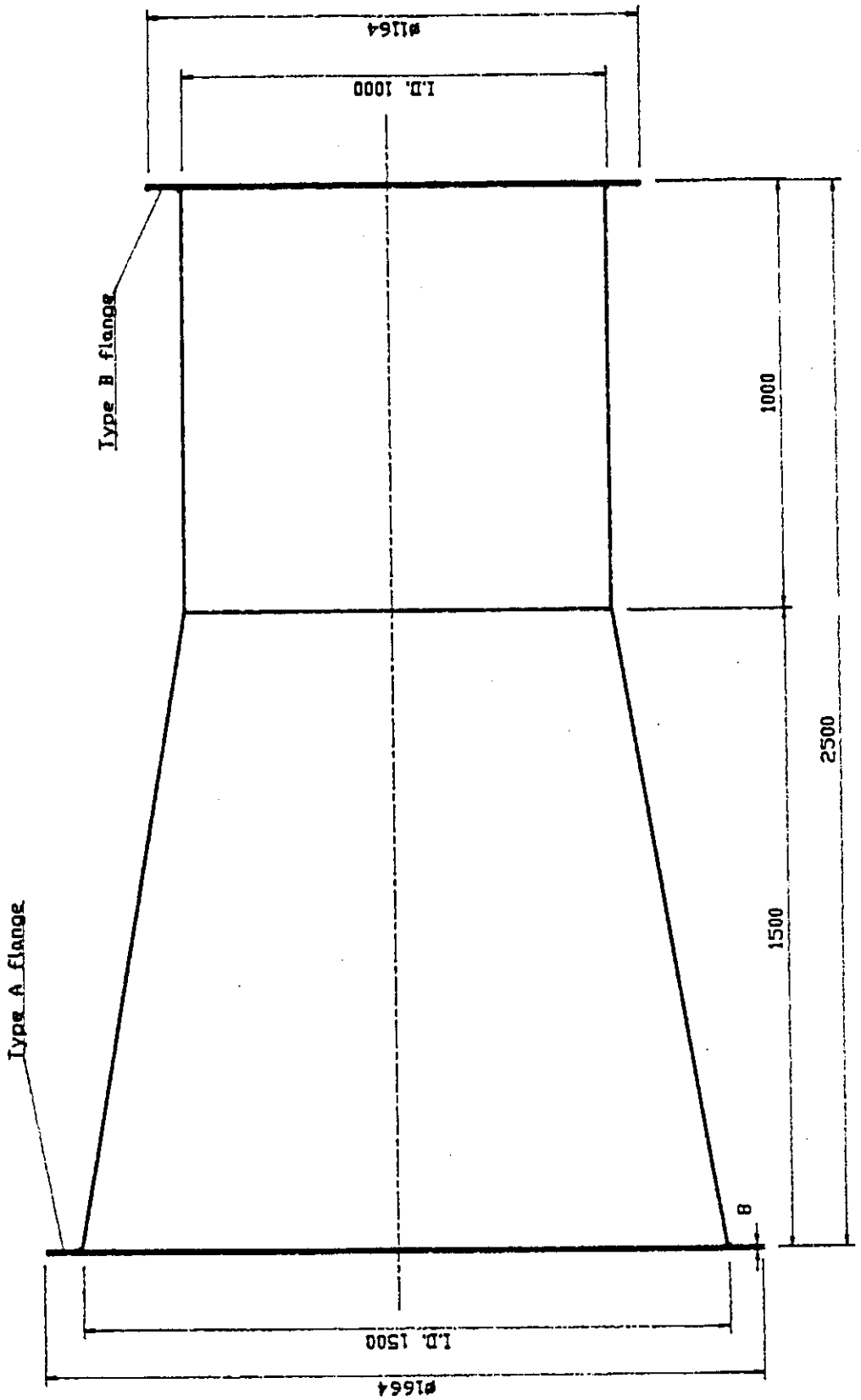

Figure F.3.2: Transformation piece (Bellmouth)

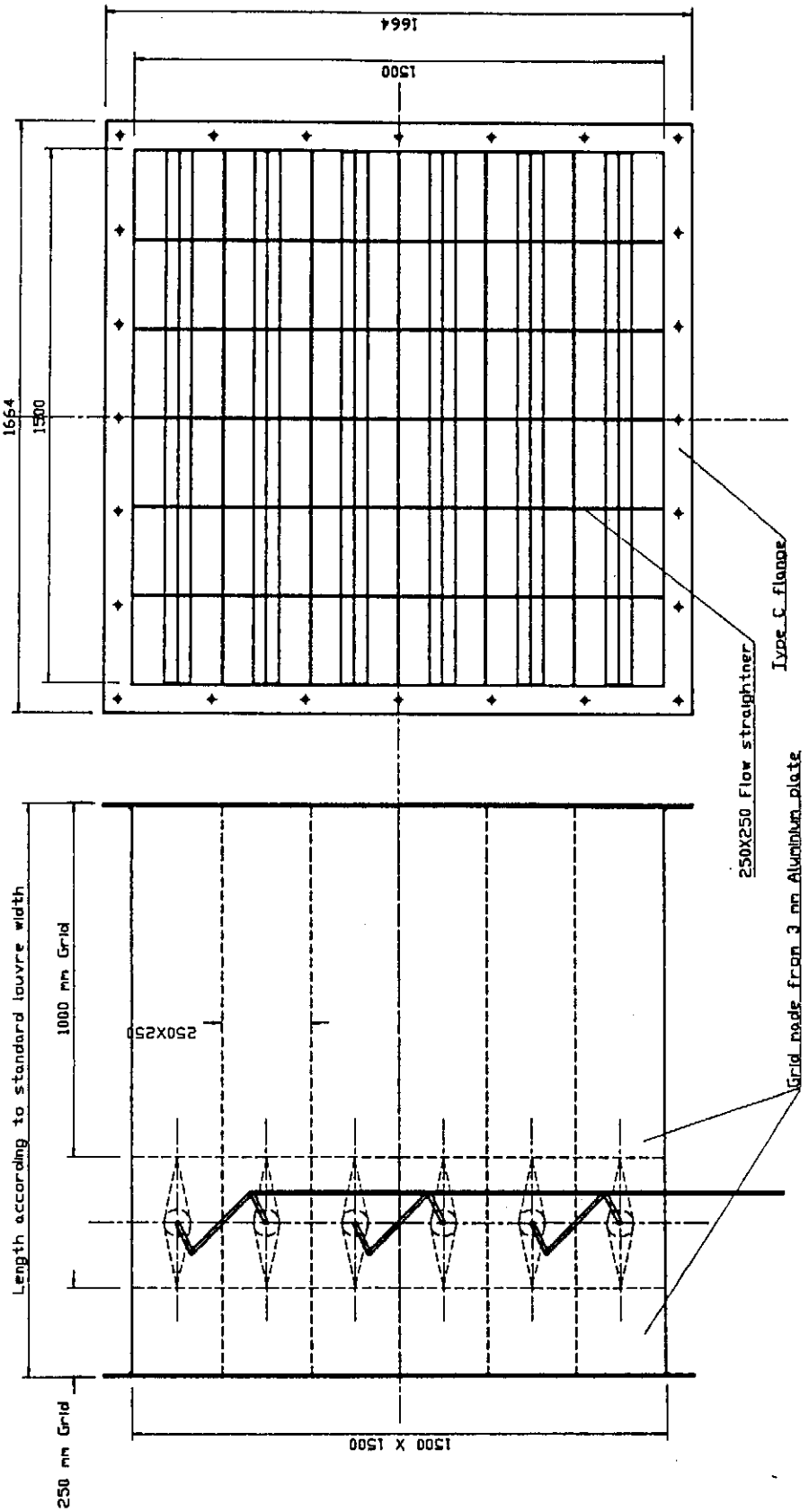

Figure F.3.3: Flow throttling device

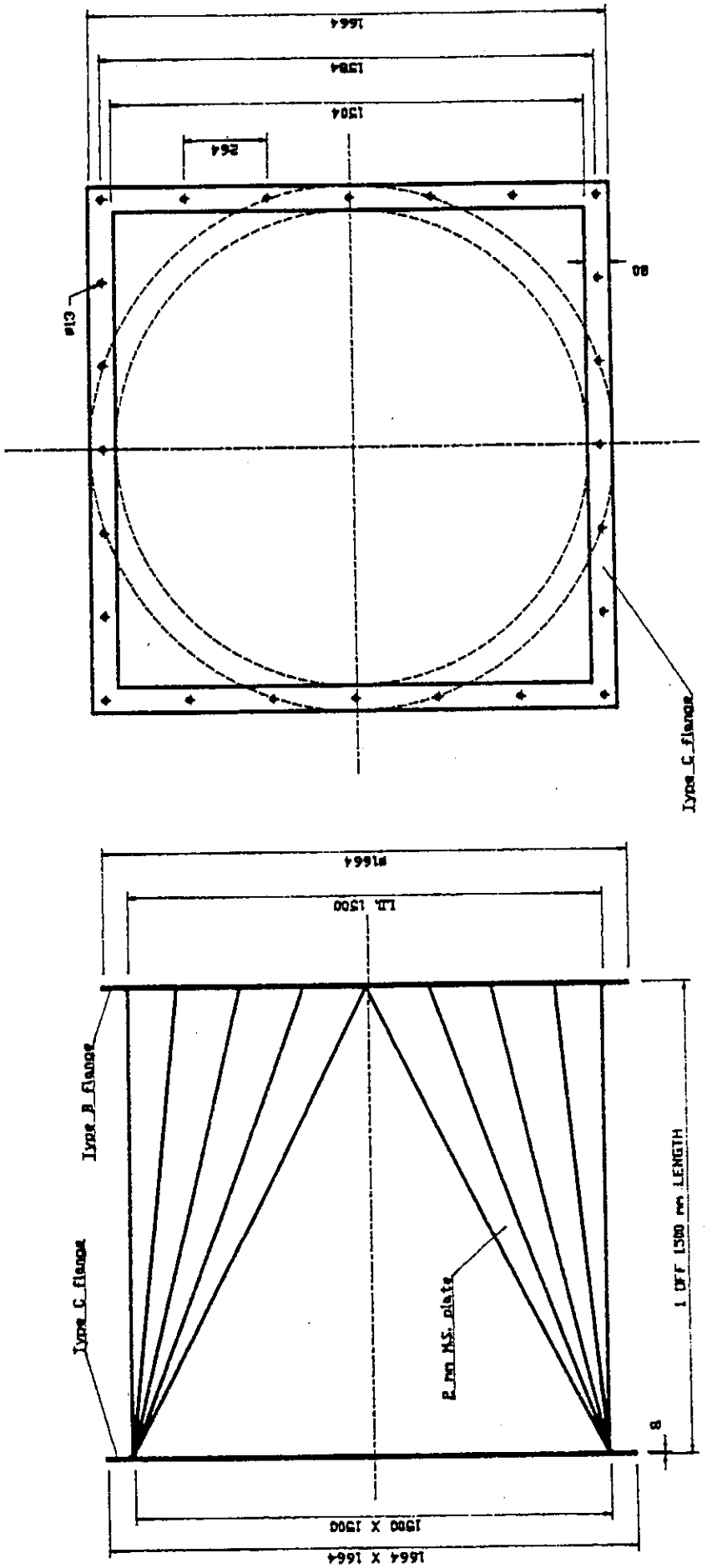

Figure F.3.4: Transformation piece (Throttling device)

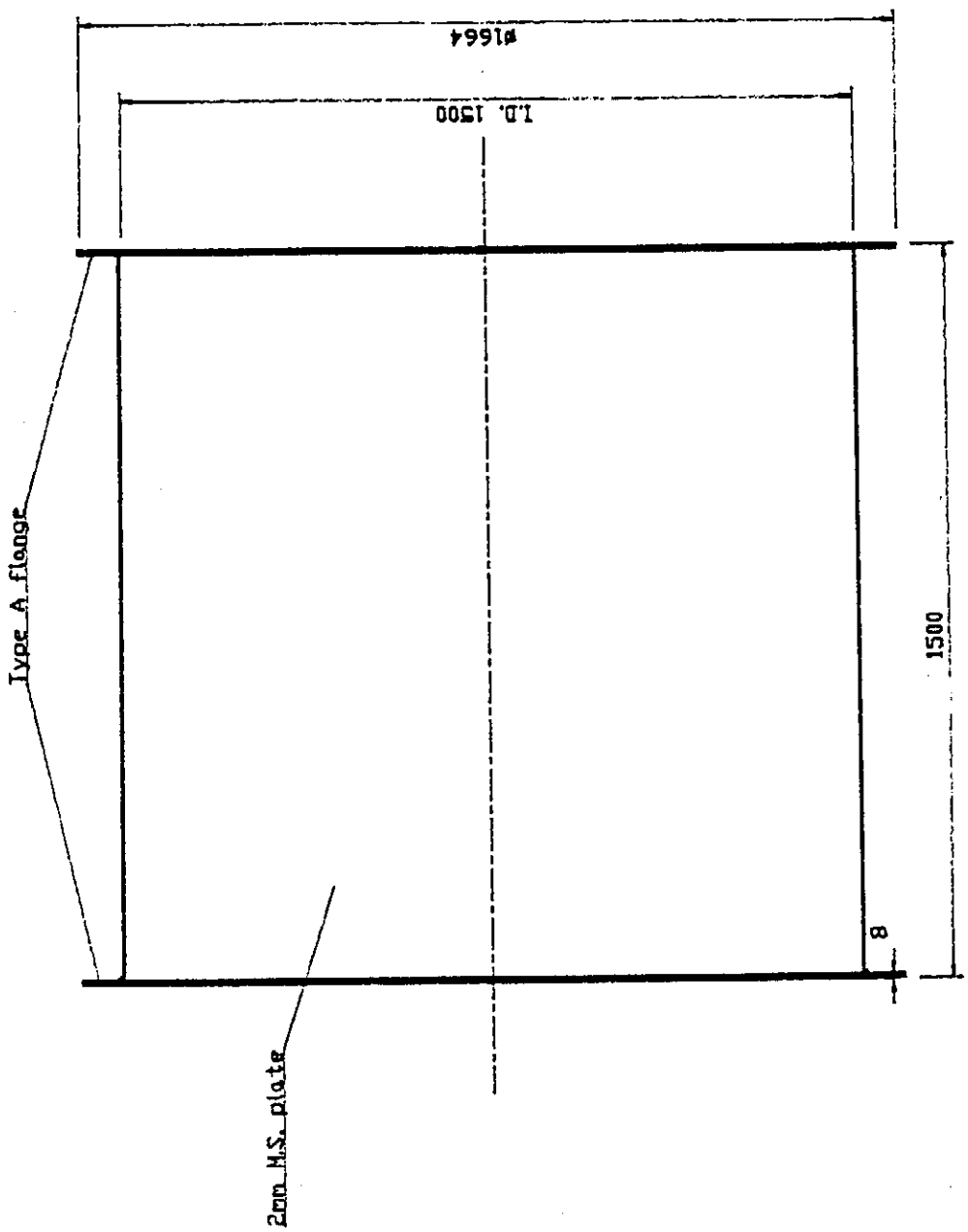

Figure F.3.5: Channel duct

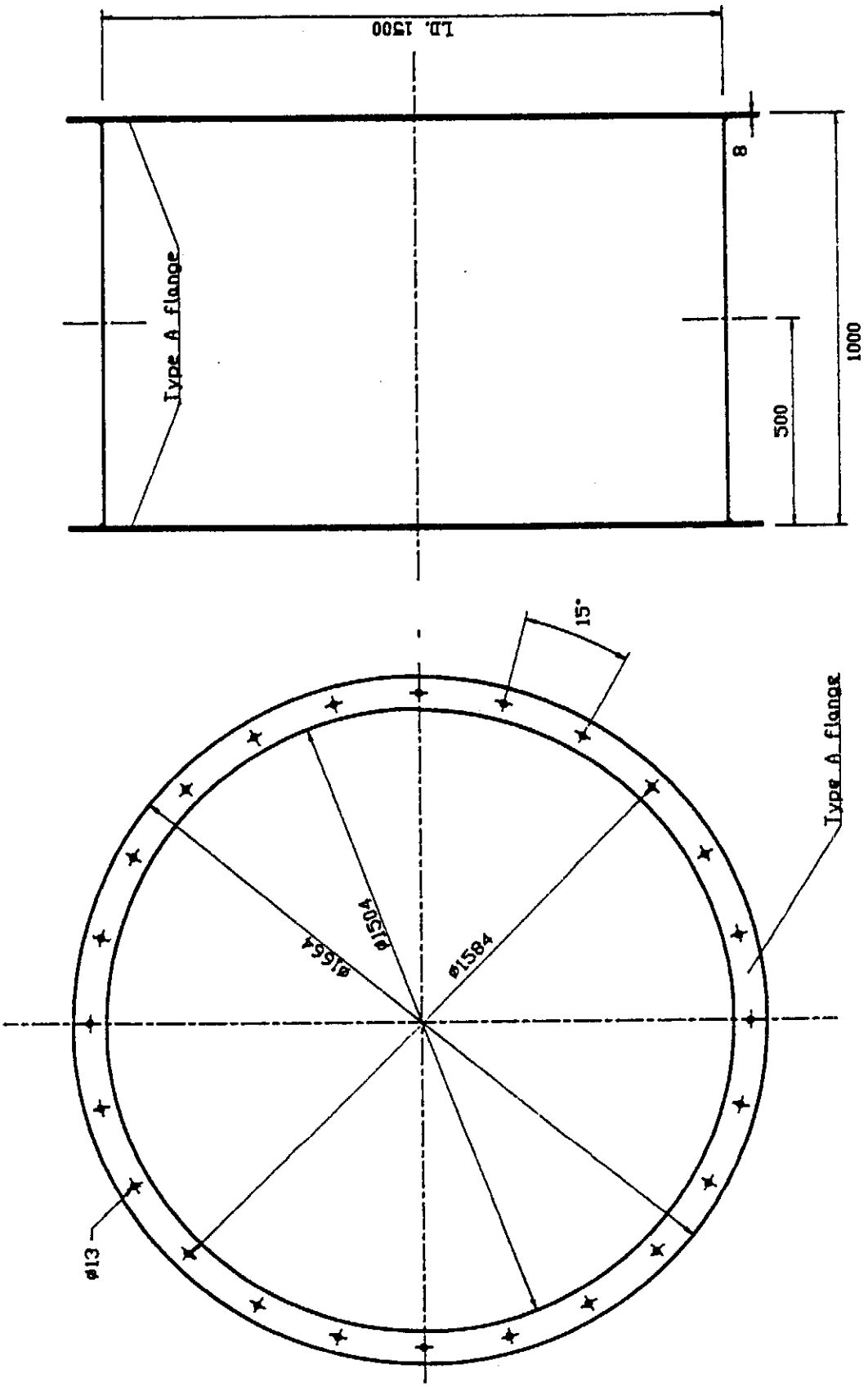

Figure F.3.6: Flow measuring section : Type A

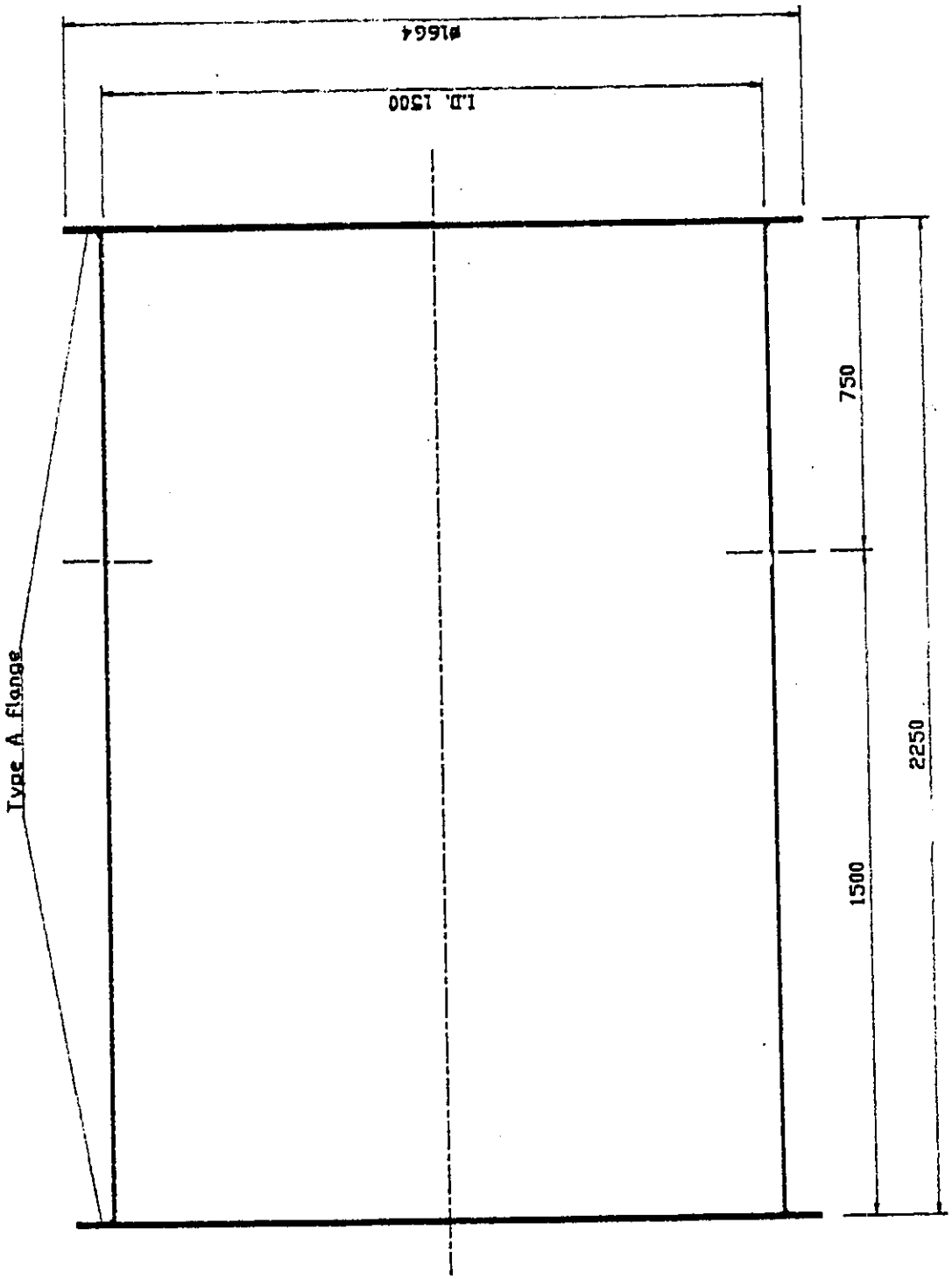

Figure F.3.7: Flow measuring section : Type B

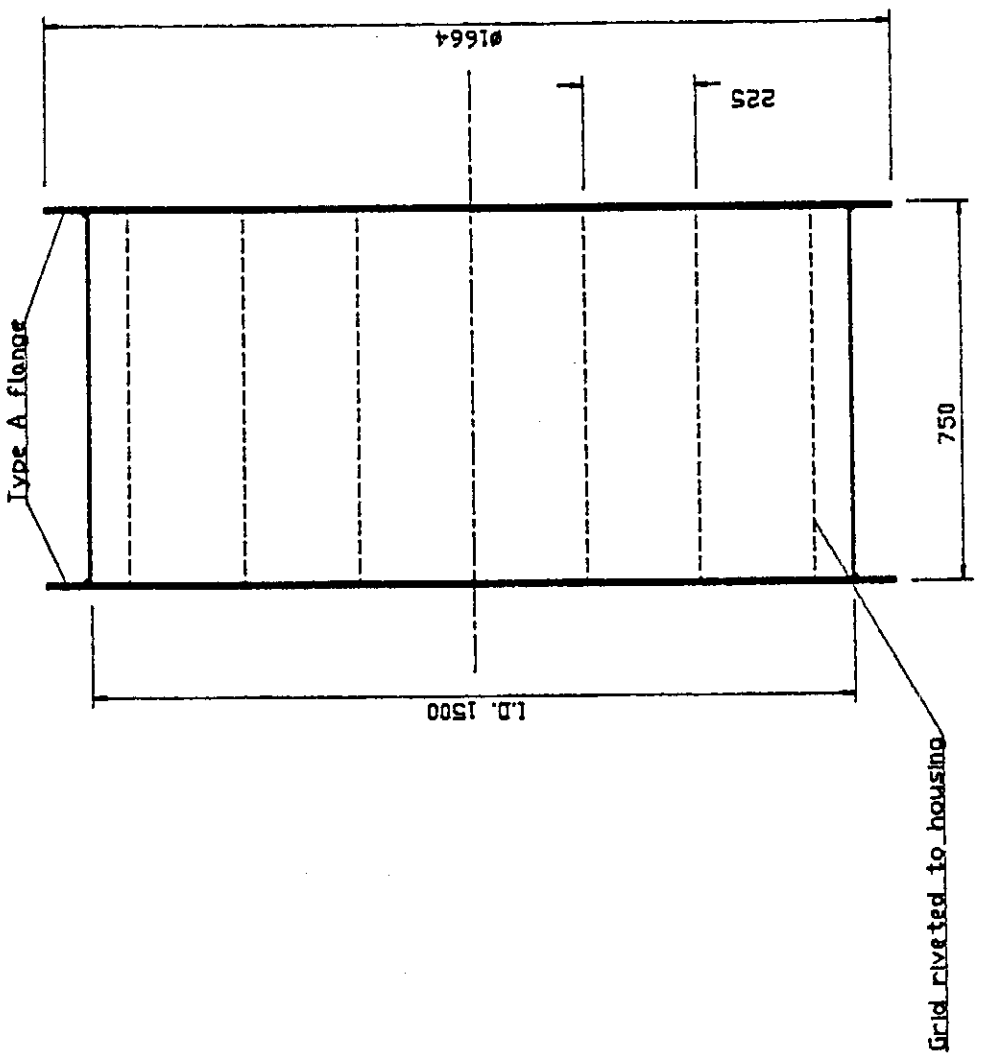

Figure F.3.8: Flow straightener : Type A

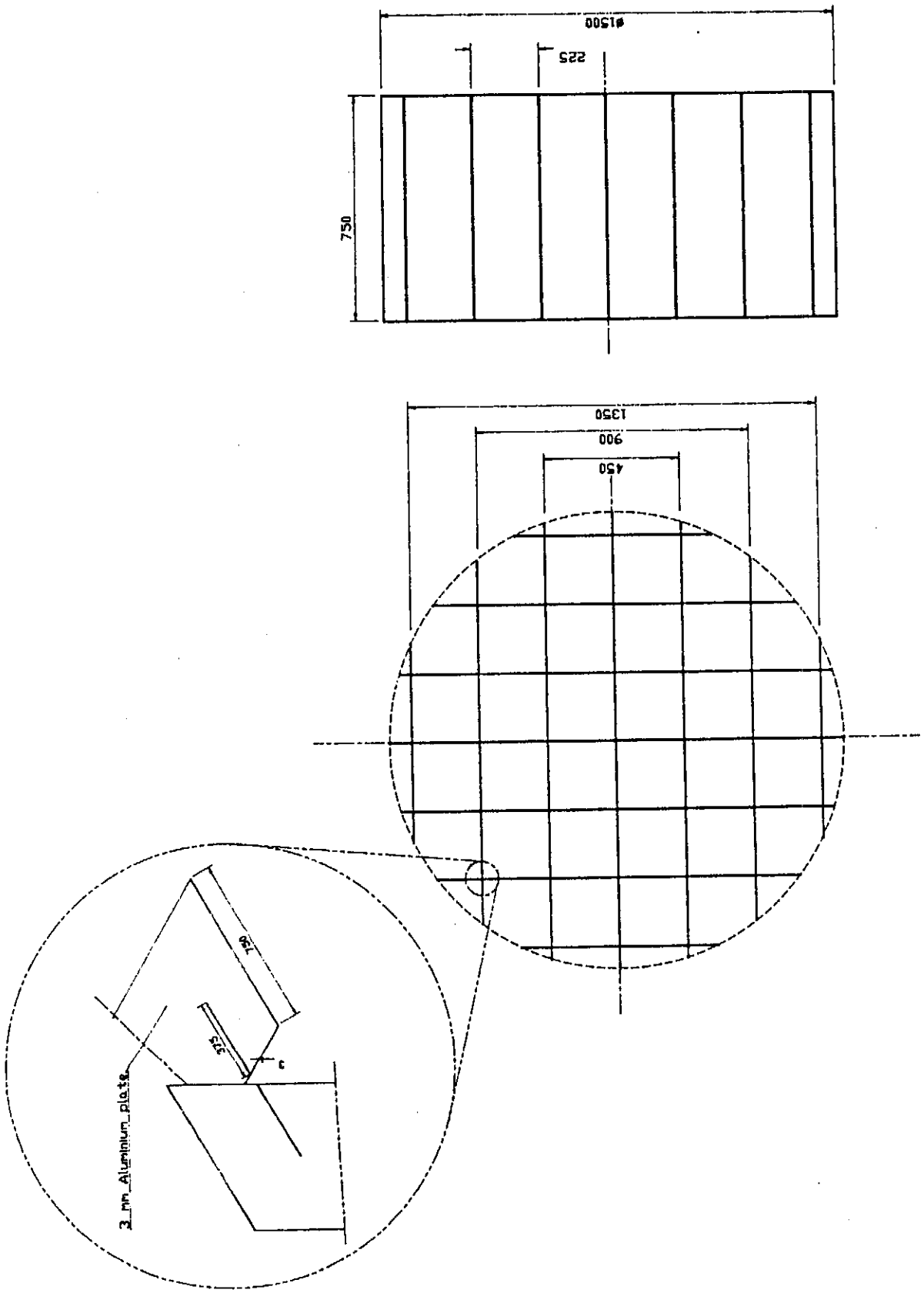

Figure F.3.9: Flow straightener detail : Type A

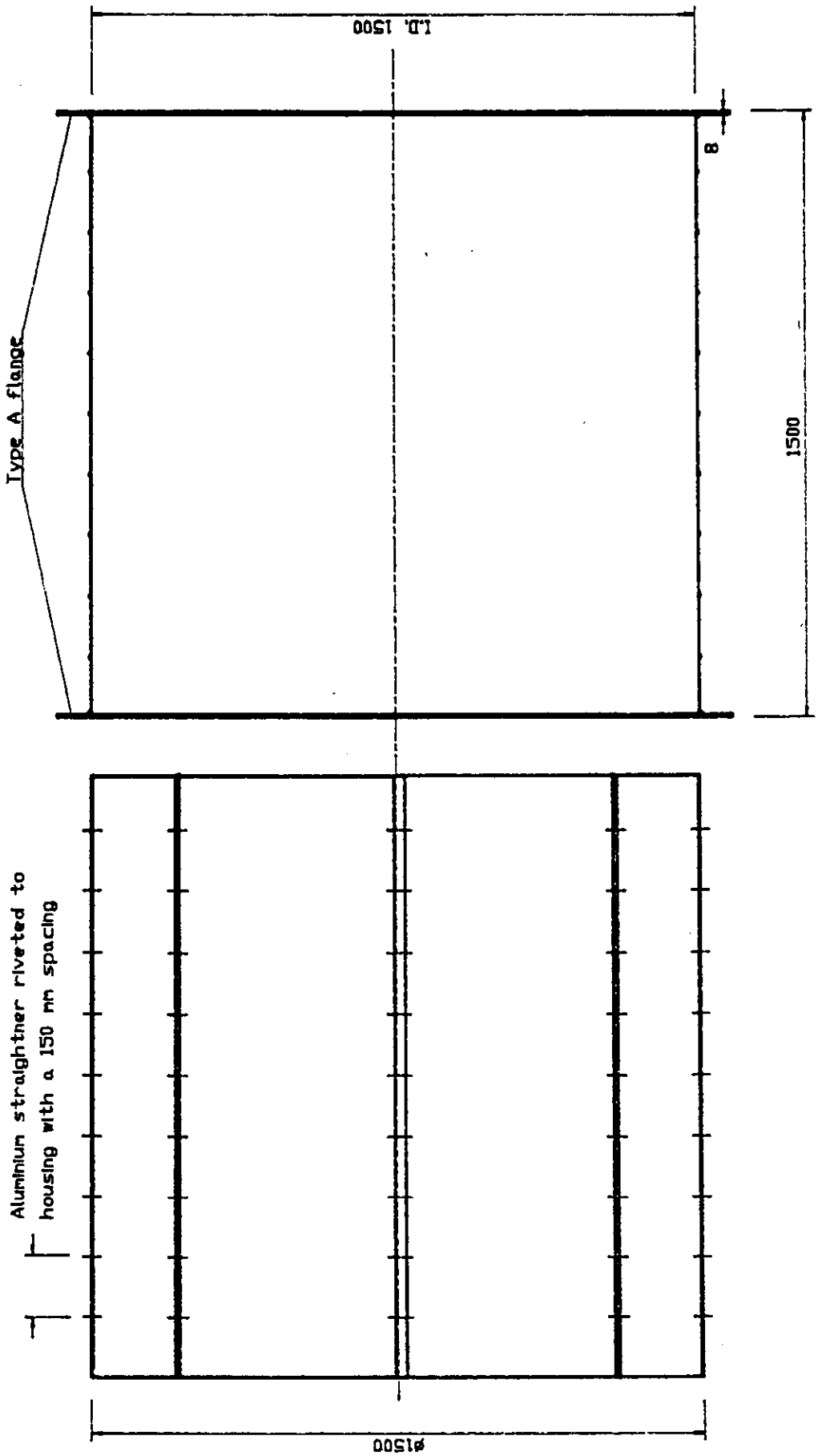

Figure F.3.10: Flow straightener : Type B

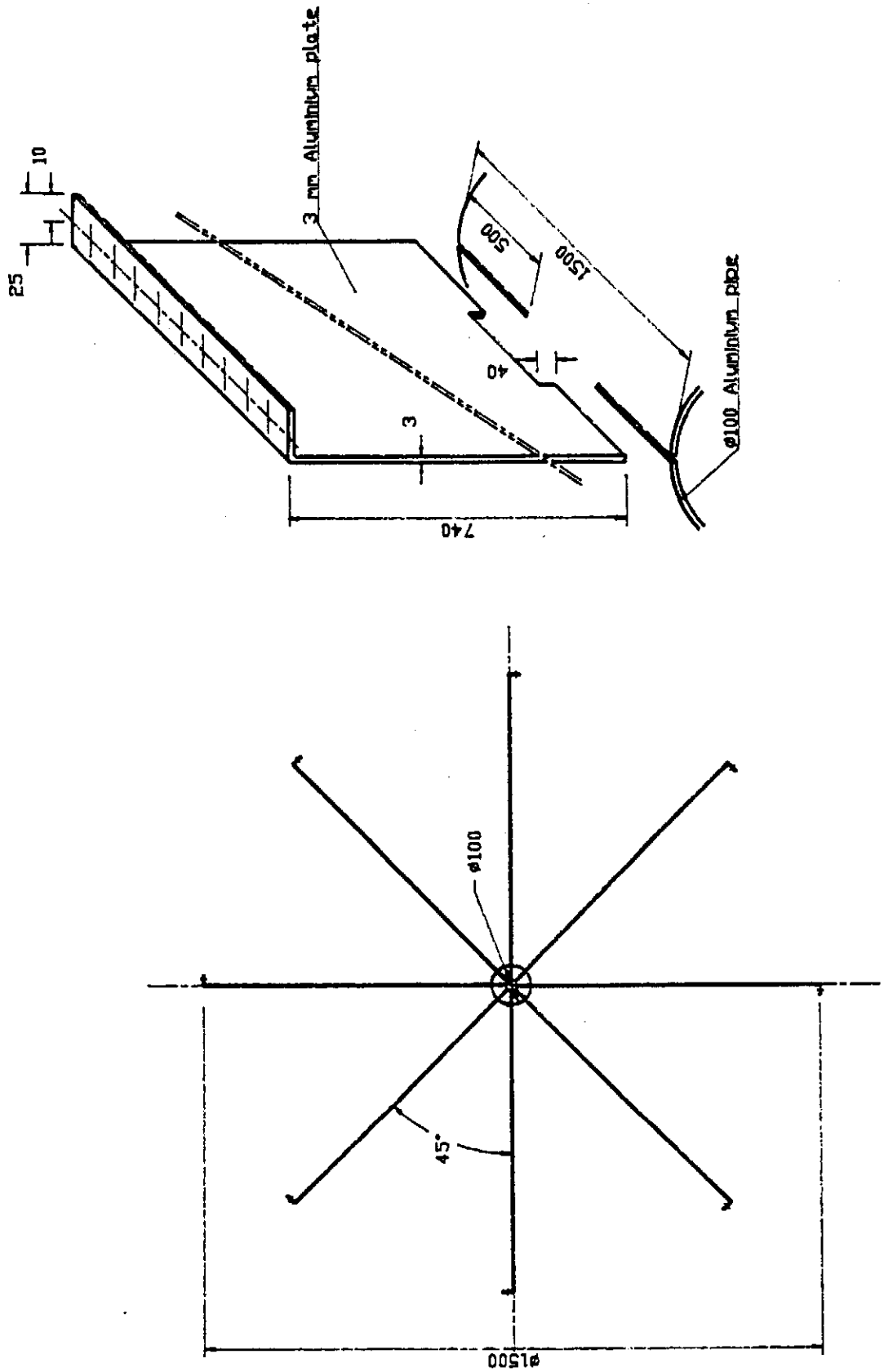

Figure F.3.11: Flow straightener detail : Type B

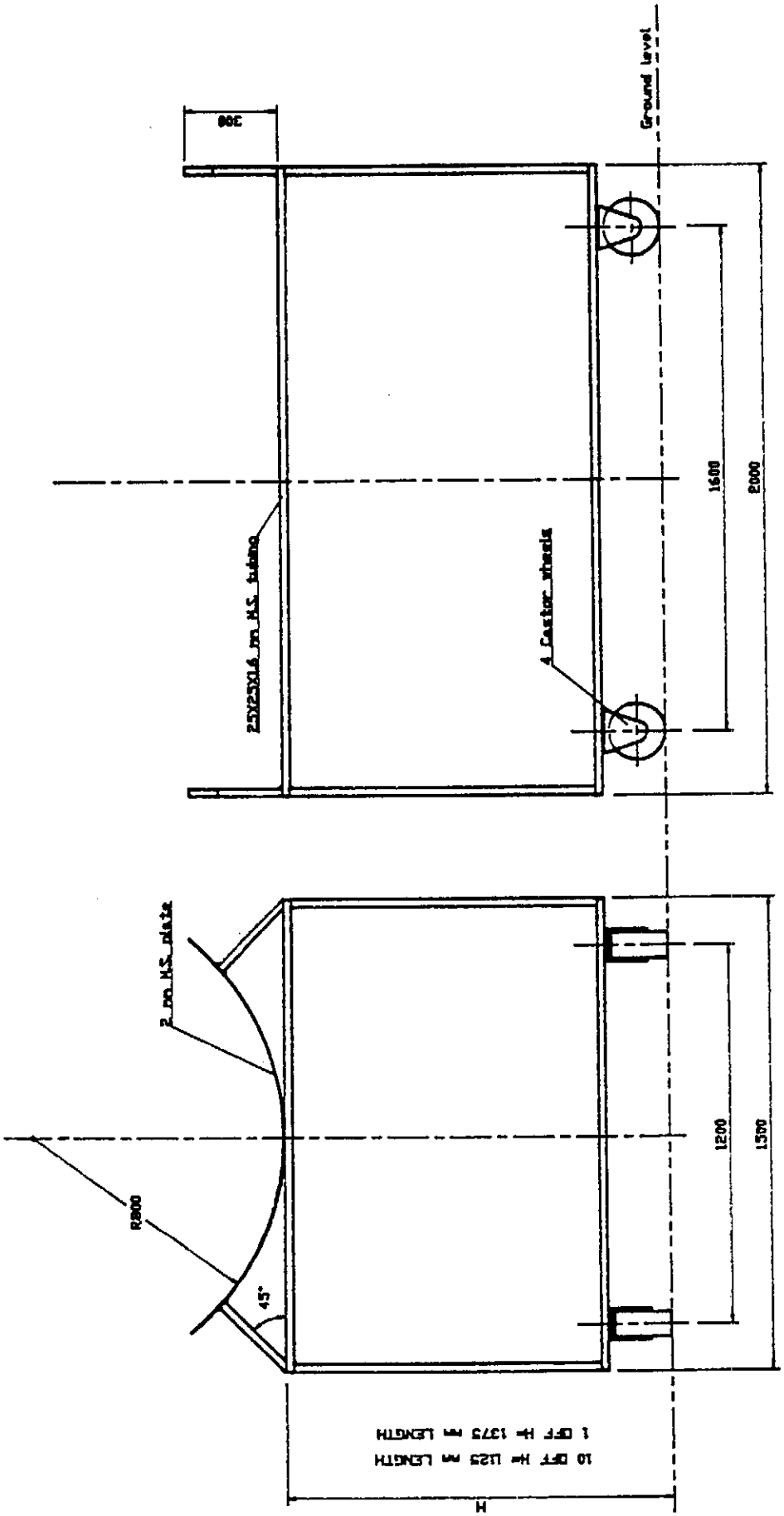

Figure F.3.12: Trolley

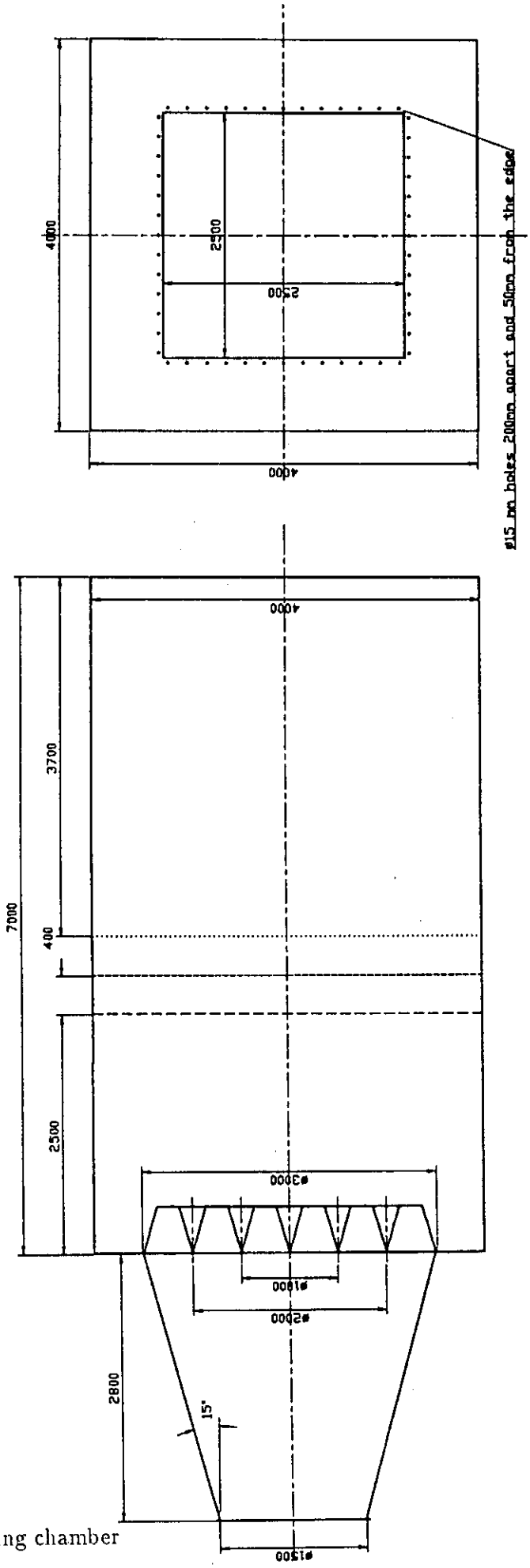

Figure F.3.13: Settling chamber

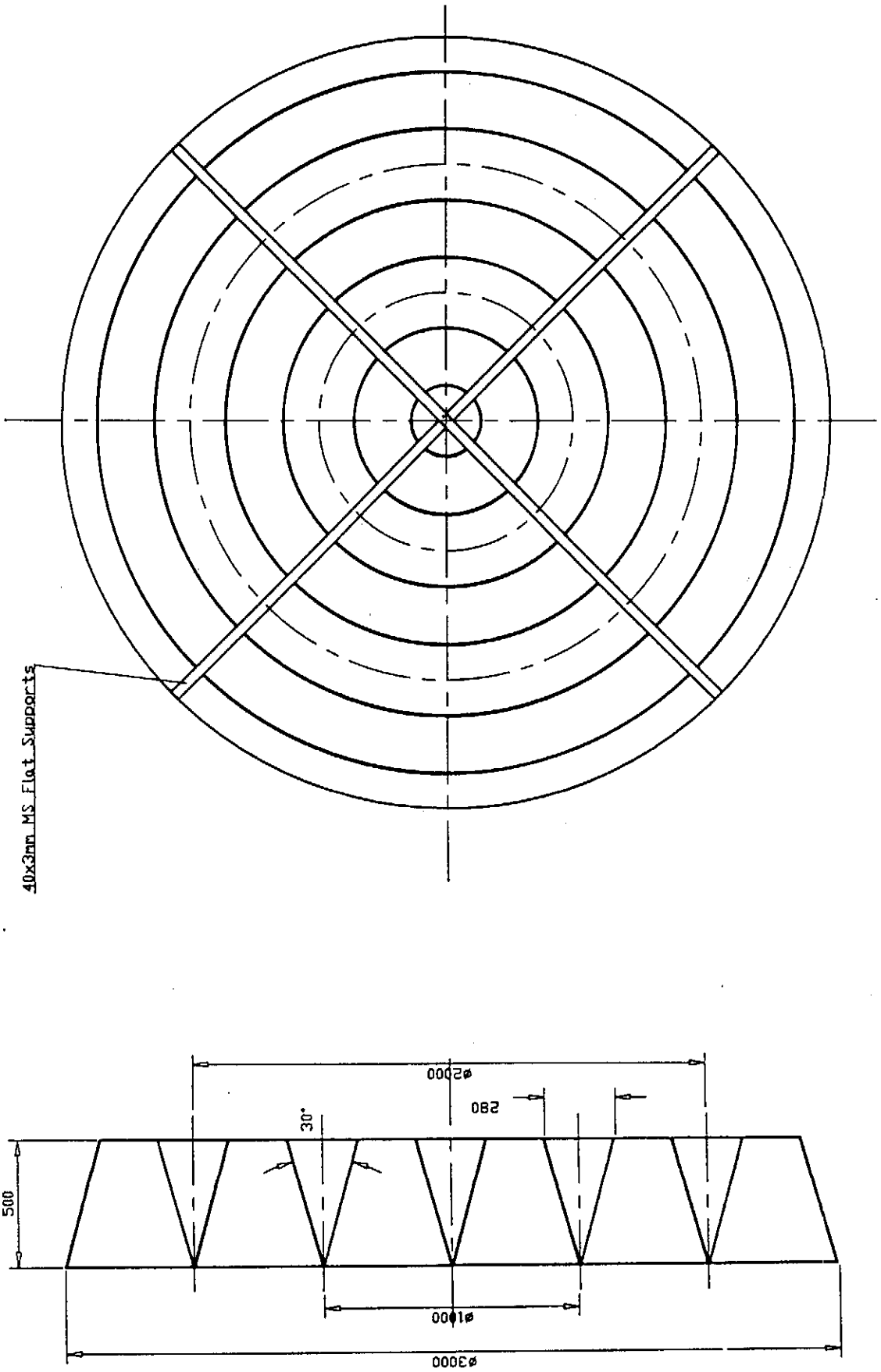

Figure F.3.14: Settling chamber detail

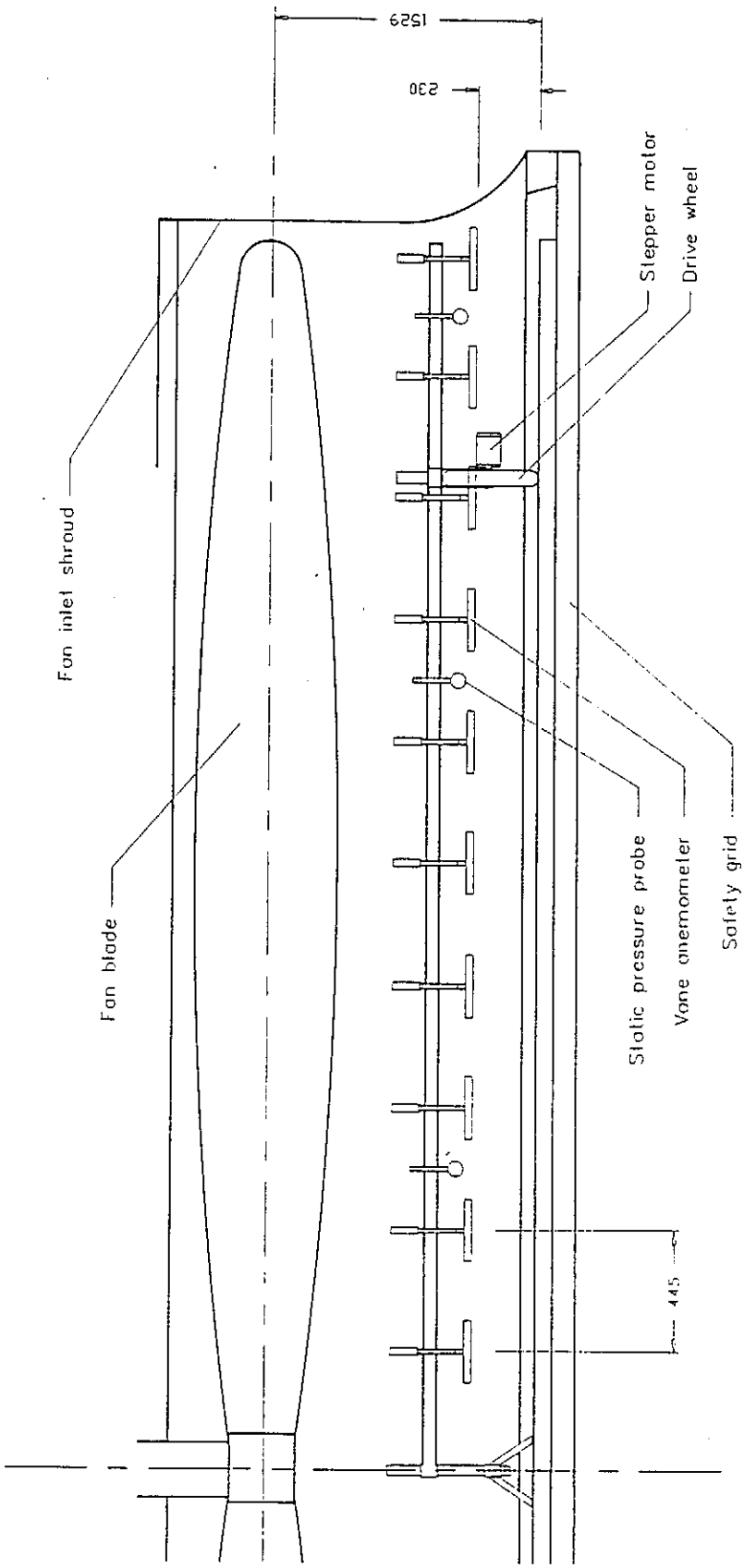

Figure F.4.1: Rotating beam

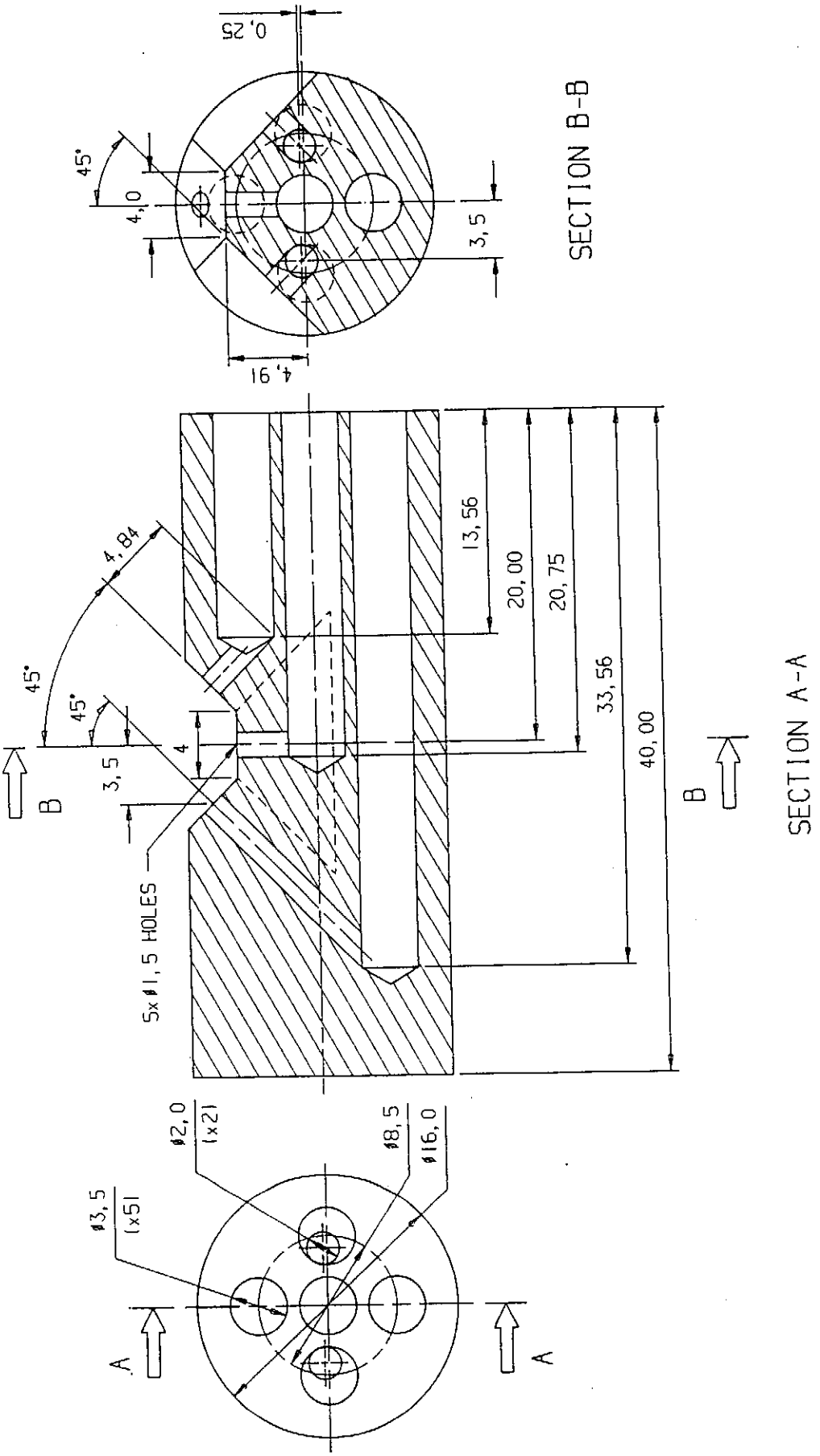

Figure F.4.2: Five hole probe

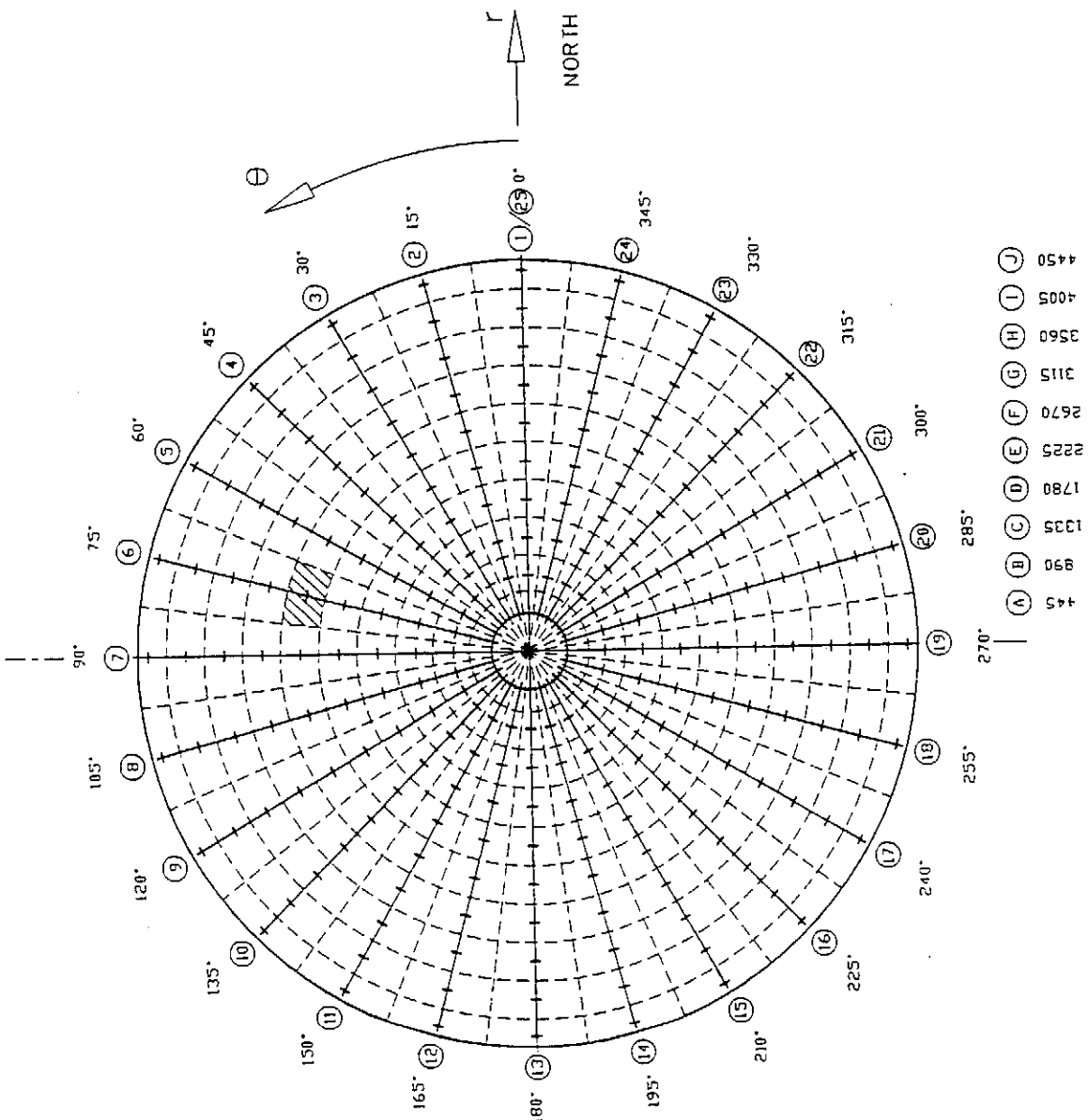

Figure F.5.1: Measuring grid at fan inlet

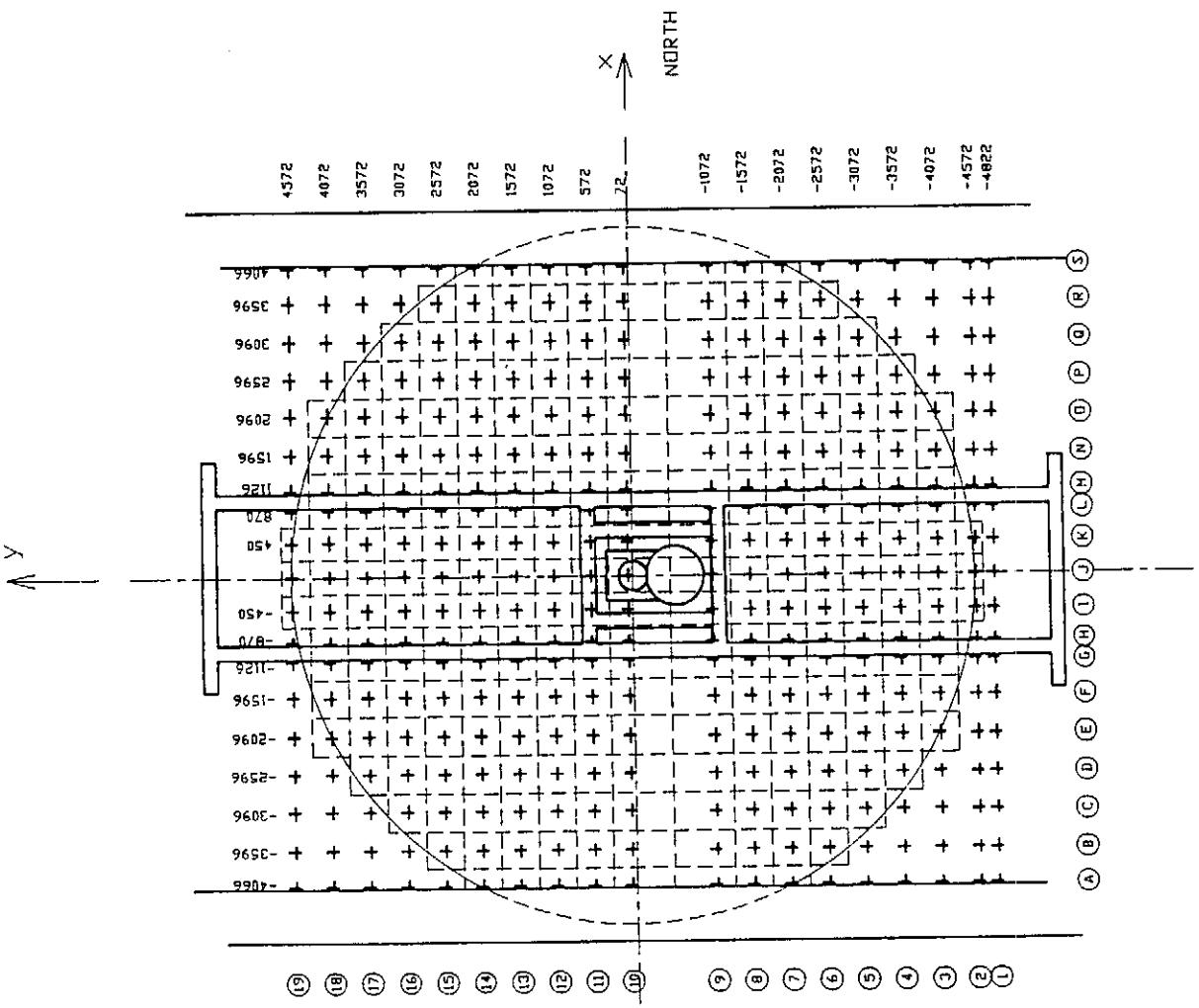

Figure F.5.2: Measuring grid at fan outlet

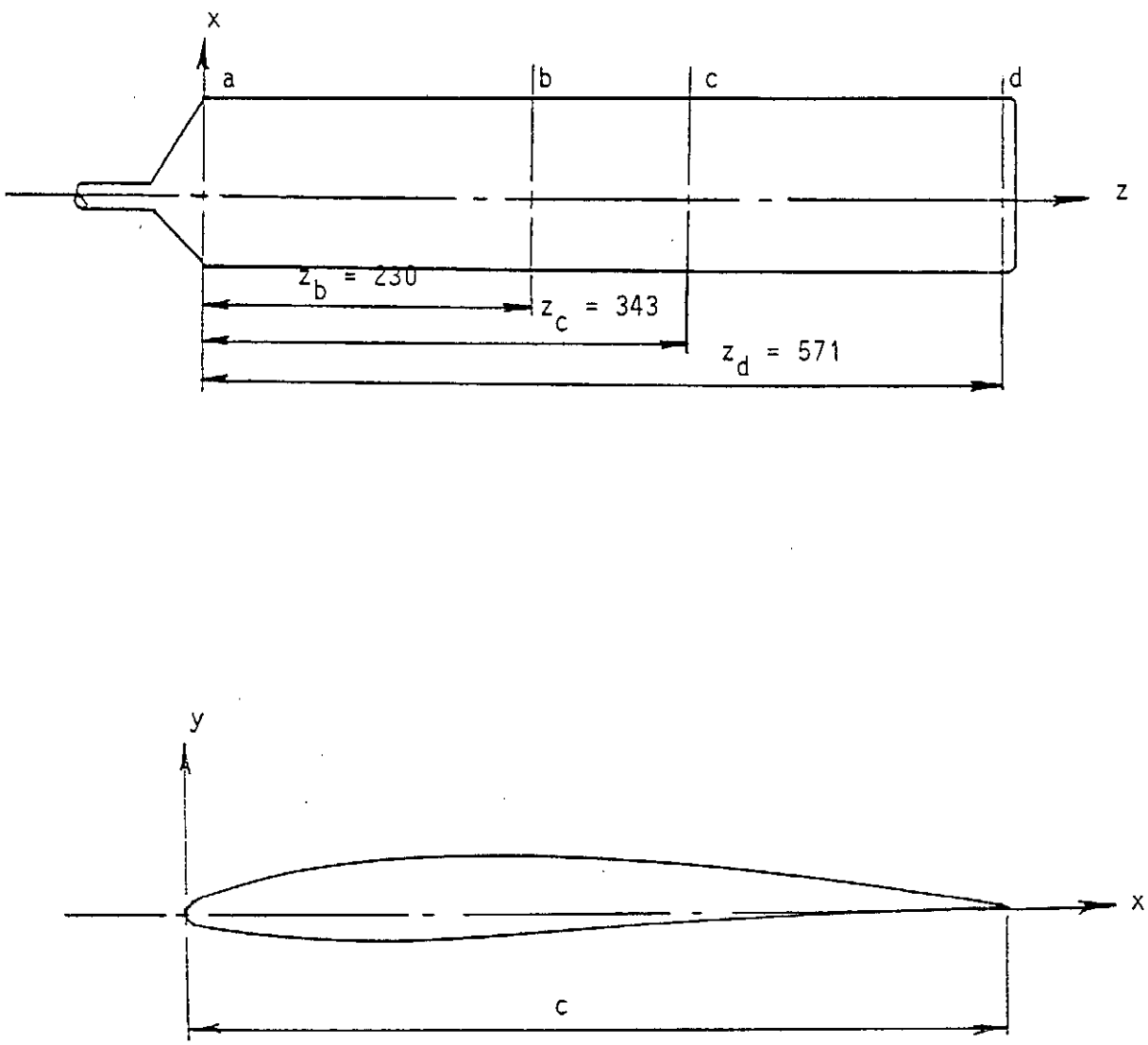

Approximate chord c = 119 mm for section a, b, c, and d.

Figure F.6.1: Model V-fan blade profile locations

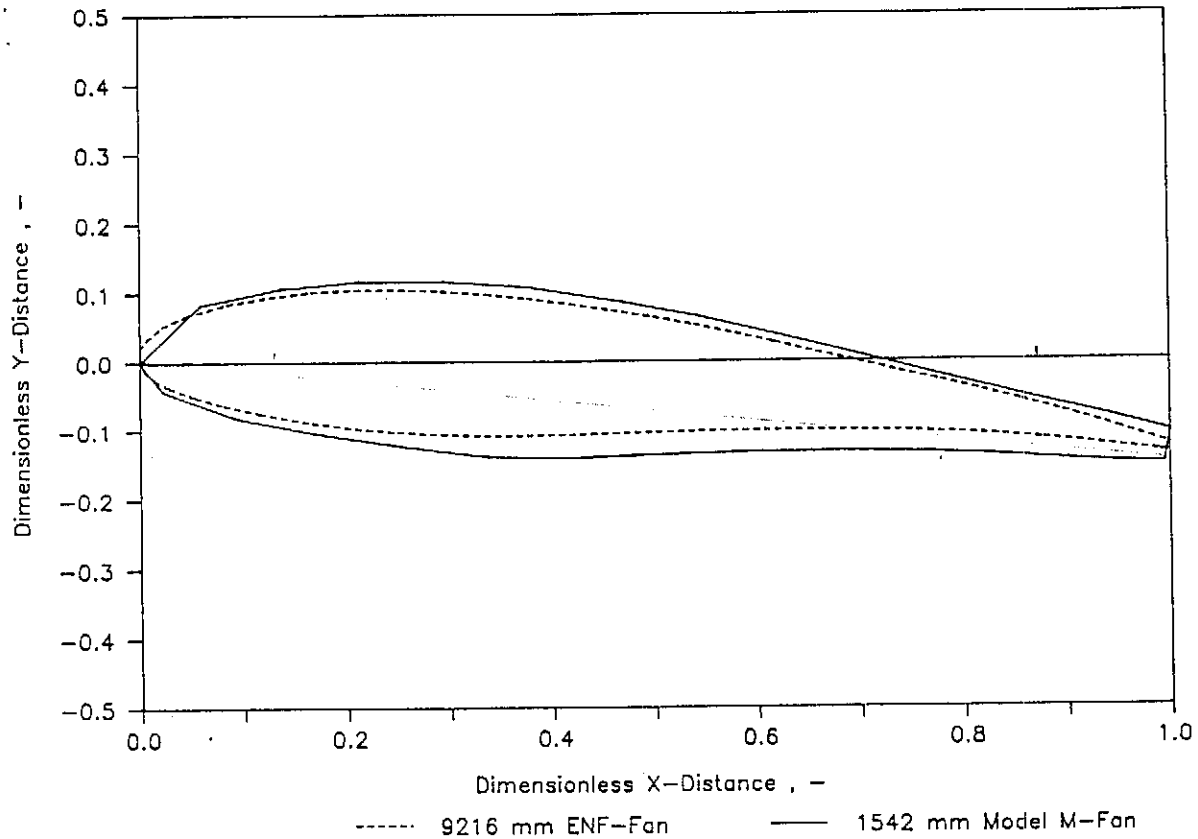

Figure F.6.2: Model V-fan : Position (a)

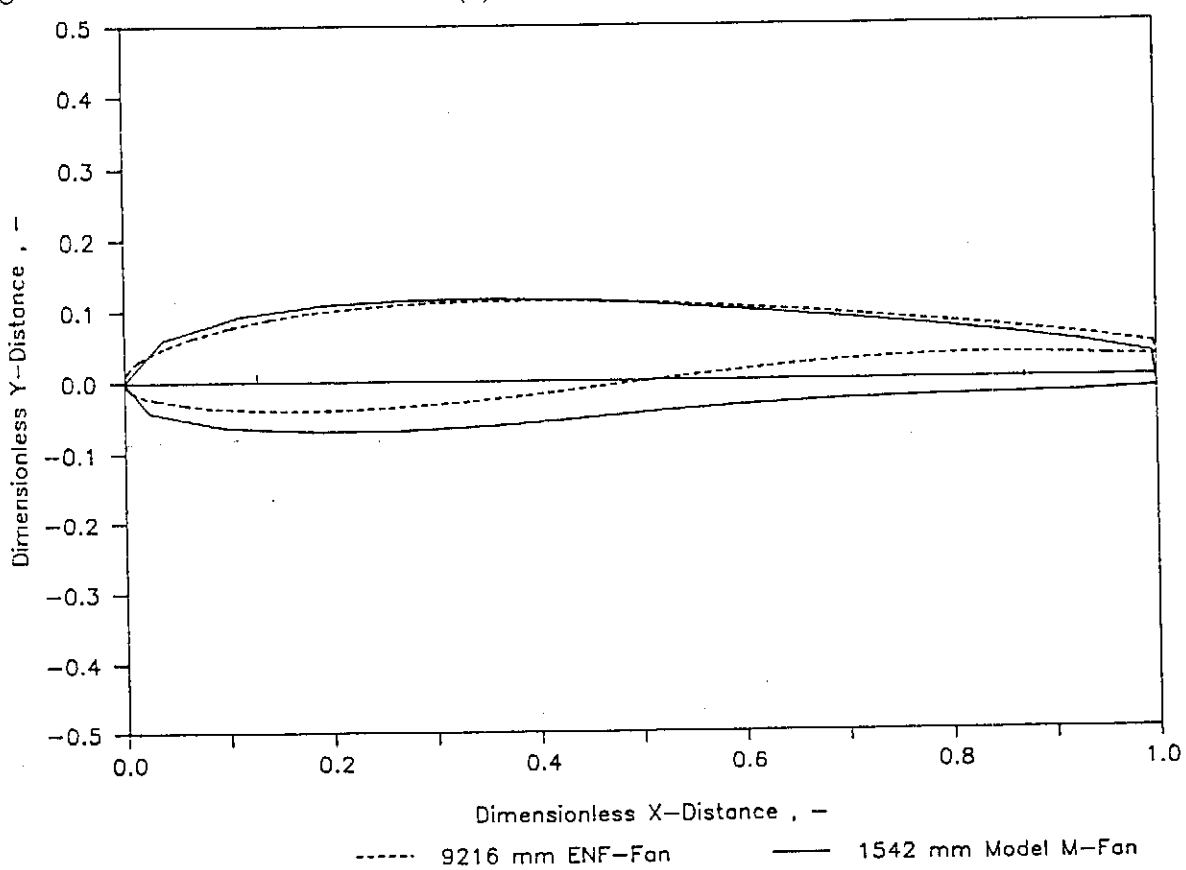

Figure F.6.3: Model V-fan : Position (b)

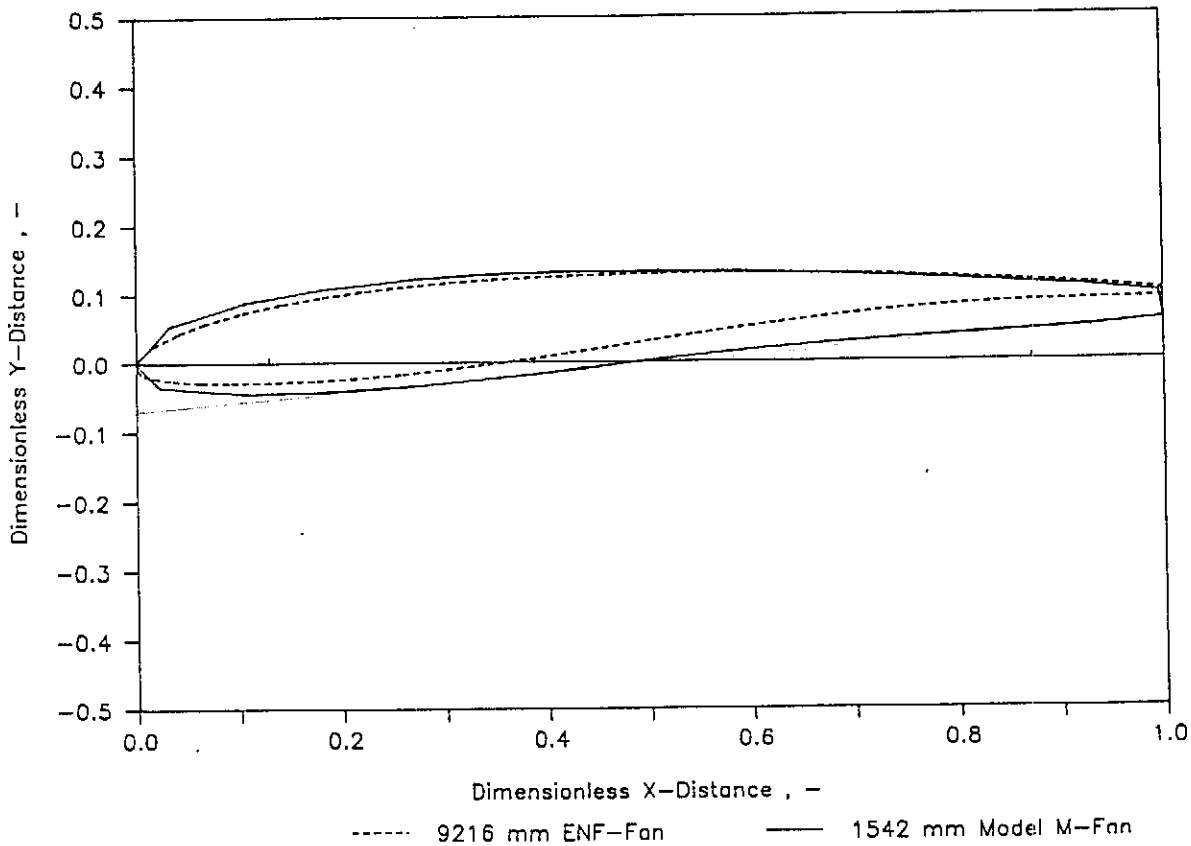

Figure F.6.4: Model V-fan : Position (c)

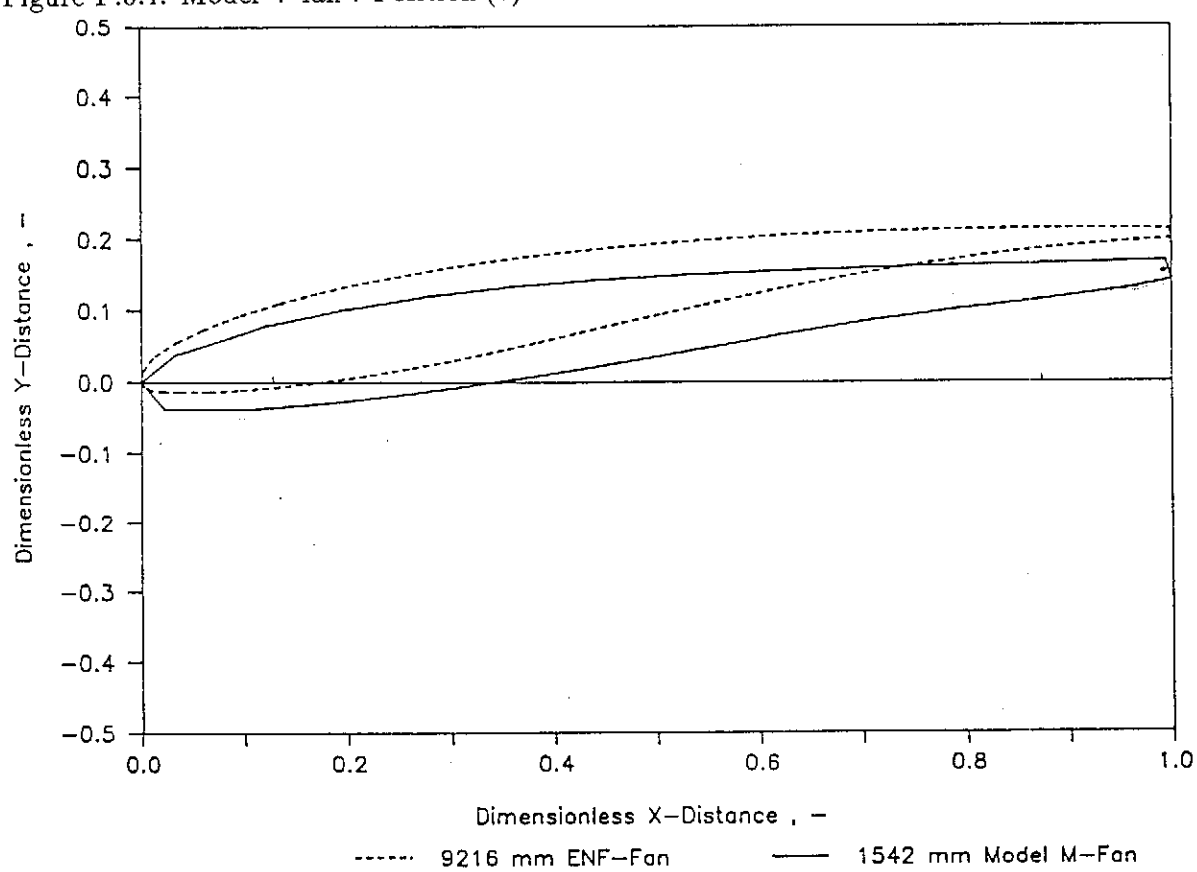

Figure F.6.5: Model V-fan : Position (d)

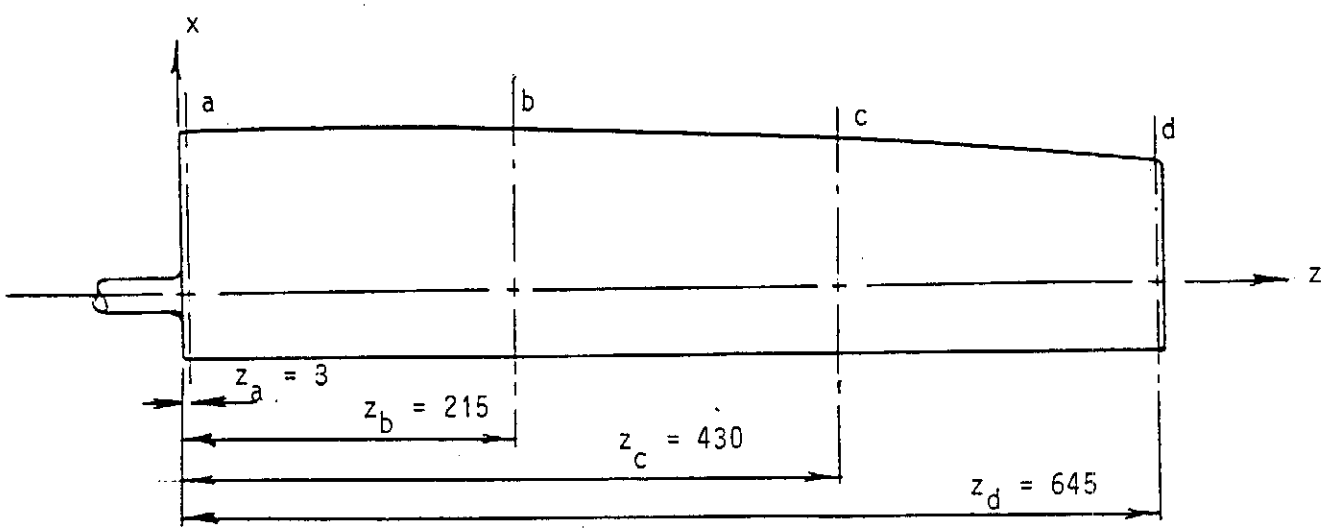

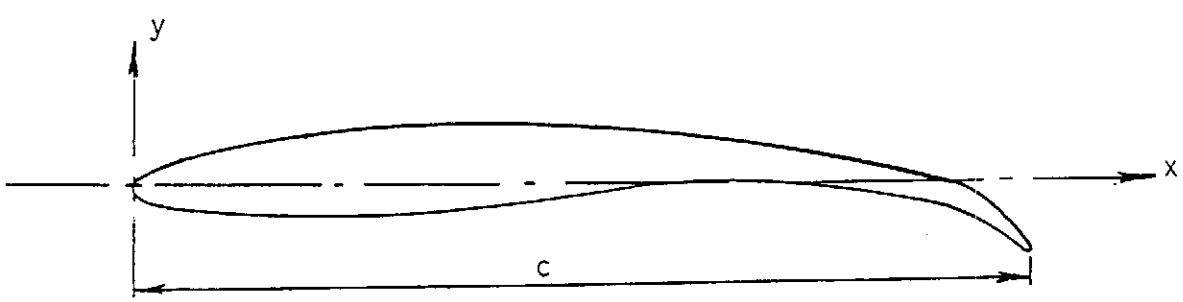

Position	Approximate Chord c
a	145 mm
b	146 mm
c	138 mm
d	122 mm

Figure F.6.6: Model GH-fan blade profile locations

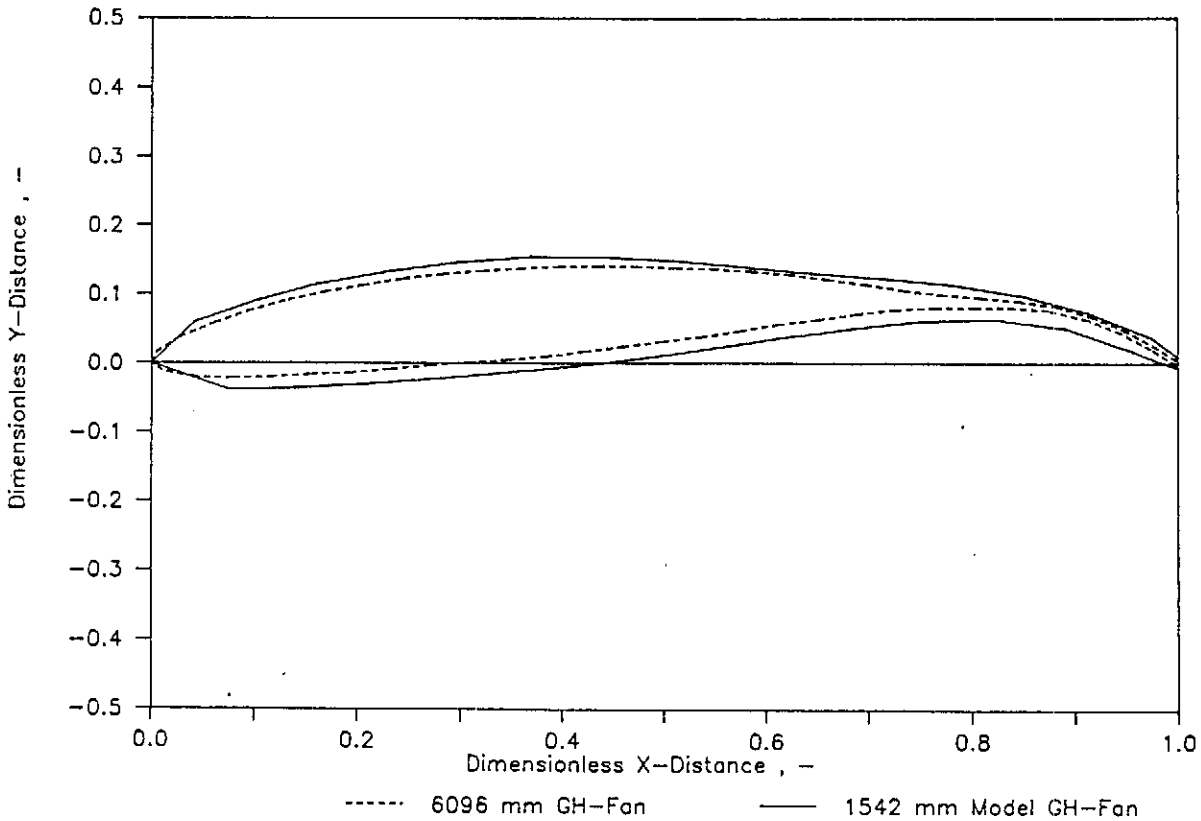

Figure F.6.7: Model GH-fan : Position (a)

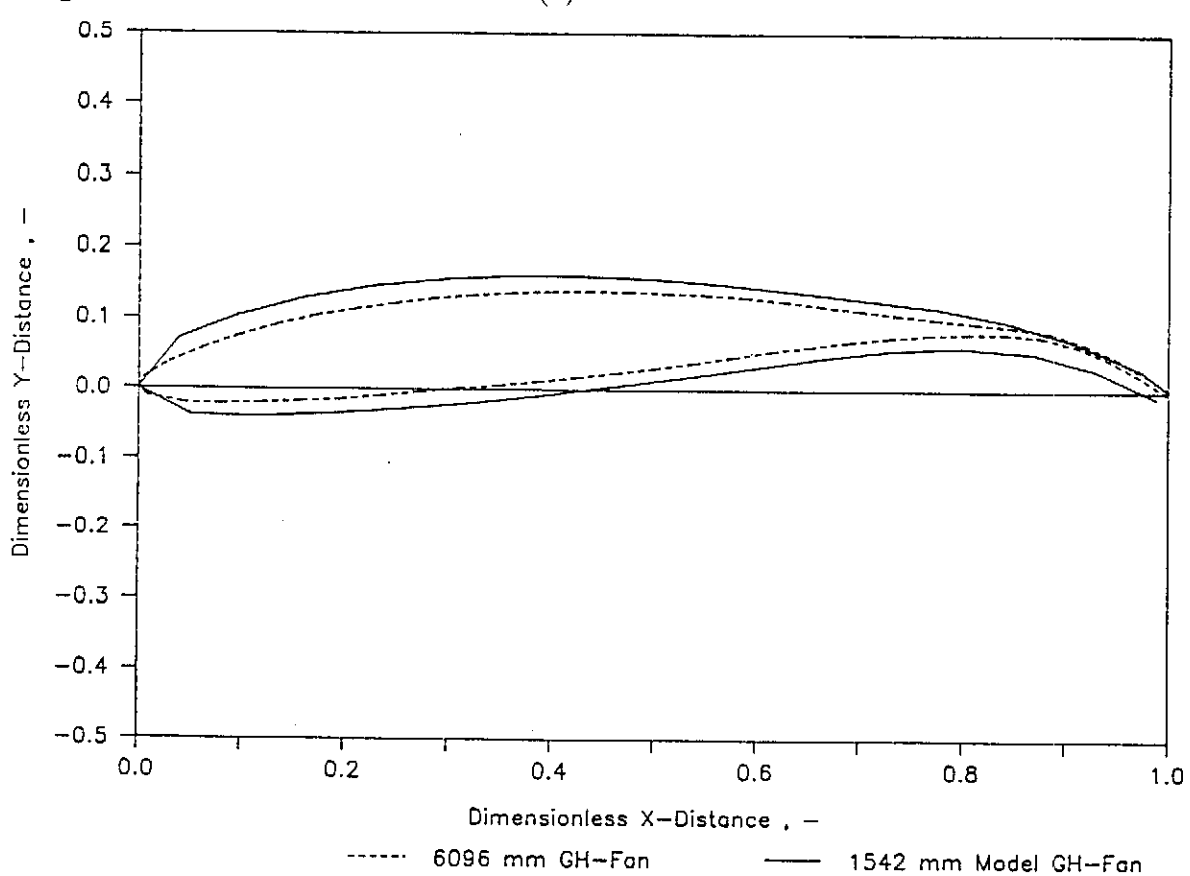

Figure F.6.8: Model GH-fan : Position (b)

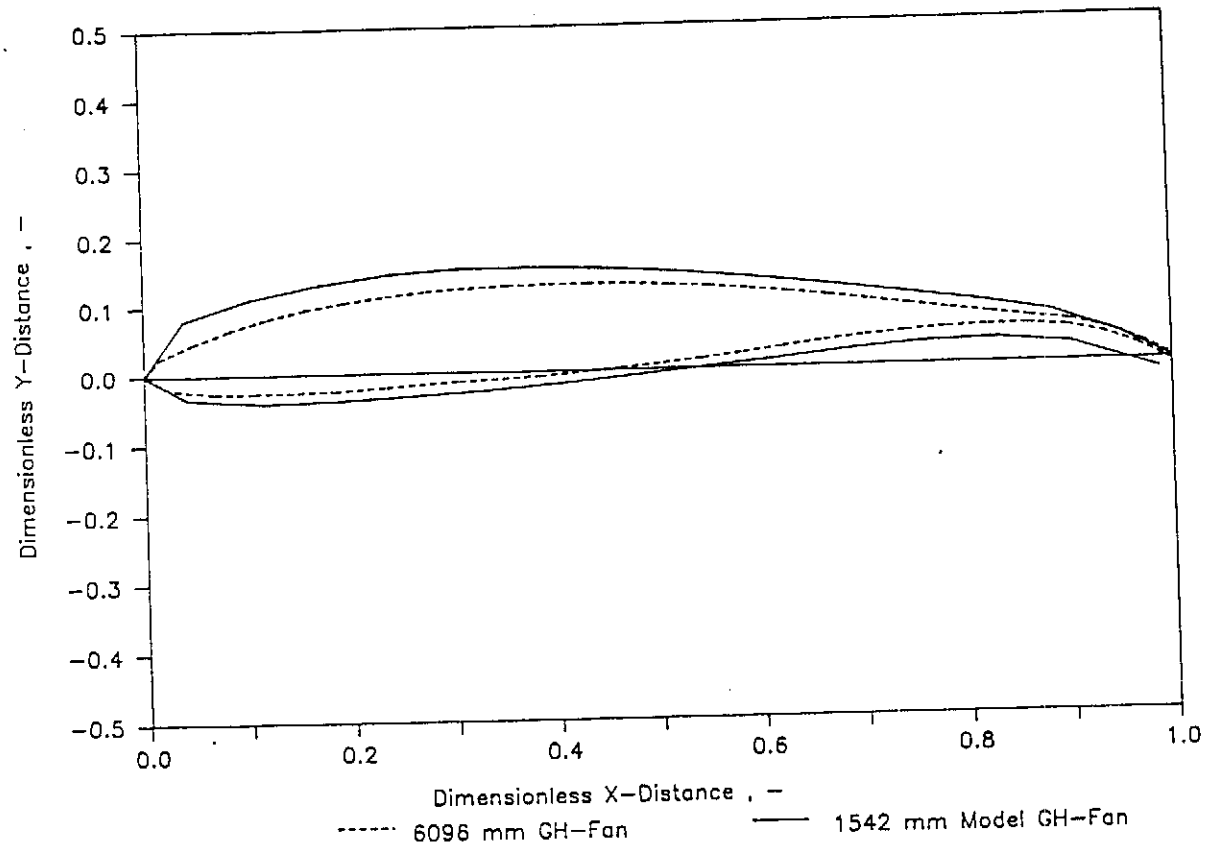

Figure F.6.9: Model GH-fan : Position (c)

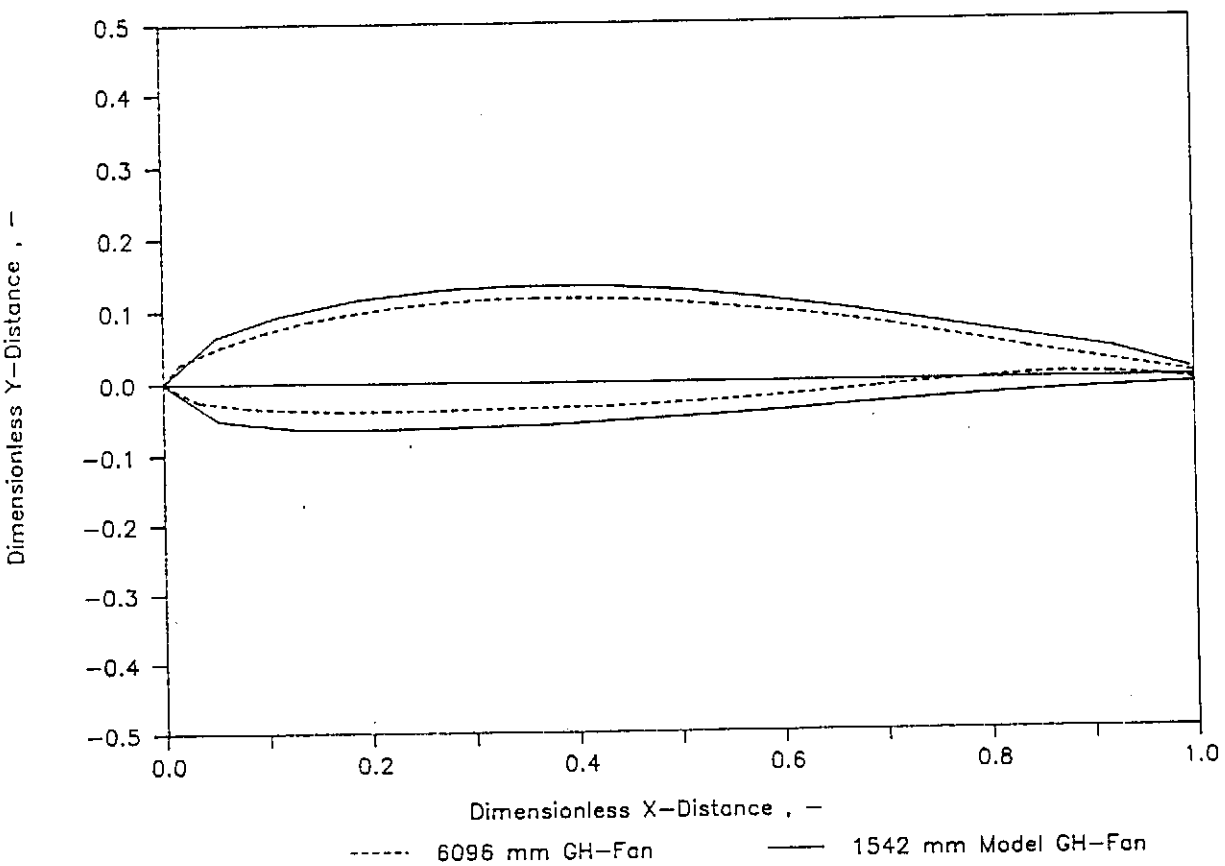

Figure F.6.10: Model GH-fan : Position (d)